Technische Universität München
TUM School of Natural Sciences

The Devil lies in the Tails: Improving the Predictions for BSM Signals at the LHC

Luc Schnell

Vollständiger Abdruck der von der TUM School of Natural Sciences der Technischen Universität München zur Erlangung eines

Doktors der Naturwissenschaften (Dr. rer. nat.)

genehmigten Dissertation.

Vorsitz: Prof. Dr. Bastian Märkisch

Prüfende der Dissertation:

1. Prof. Dr. Andreas Weiler
2. Prof. Dr. Björn Garbrecht

Die Dissertation wurde am 20.06.2024 bei der Technischen Universität München eingereicht und durch die TUM School of Natural Sciences am 24.09.2024 angenommen.

The devil lies in the tails:

Improving the predictions for

BEYOND-THE-SM SIGNALS

at the

LARGE HADRON COLLIDER

Luc Schnell

Supervised by Dr. Ulrich Haisch

MAX PLANCK INSTITUTE
FOR PHYSICS

Gewidmet meinen Eltern Simone und Dieter,
meiner Schwester Anne
und meiner Frau Viktoriia

In liebevoller Erinnerung an
Rosmarie Schnell-Kammermann (1930-2023)
und Urs Schnell (1932-2022)

ABSTRACT

The upcoming HL-LHC run at CERN will allow the search for BSM signals in the tails of kinematic distributions with an unprecedented level of statistics. In this thesis, we investigate how corresponding state-of-the-art theoretical predictions for BSM collider signals are obtained, focusing on two approaches.
The first, the *precision* approach, assumes that signals of multi-TeV BSM physics are hidden within the current uncertainty bands of generic LHC measurements. This creates a need for precise theoretical predictions for BSM signals, which, in this context, are most effectively described in an EFT approach. We review both the POWHEG framework, allowing for the consistent matching of fixed-order calculations to PS generators, and the SMEFT in the precision context. We then present our NNLO+PS-accurate event generator for SMEFT effects in $pp \to Vh$ production based on the POWHEG MiNNLO$_{\text{PS}}$ method, and perform a detailed phenomenological analysis of the $pp \to Zh \to \ell^+\ell^-$ channel.
In the second, the *novel signatures* approach, we investigate two UV models that lead to non-standard signatures at the LHC, which stand out from the SM backgrounds in targeted searches. First, we calculate the contributions of the VLQ that arises in the 4321 gauge completion to $pp \to \tau^+\tau^-$ production at NLO+PS accuracy. The additional requirement of a b-tagged jet in the final state greatly increases the sensitivity to the signatures of the bottom-philic VLQs. Second, in the 2HDM+a model, an interesting LLP phenomenology can arise in the limit of minimal mixing between the DM mediator and the extended scalar sector. We present the constraints from LLP searches of the ATLAS and CMS experiments, demonstrating their distinctive role in constraining such feebly interacting DM mediator scenarios.

ZUSAMMENFASSUNG

Der bevorstehende HL-LHC-Run am CERN wird die Suche nach BSM-Signalen in den Randbereichen kinematischer Verteilungen mit einer noch nie dagewesenen statistischen Genauigkeit ermöglichen. In dieser Dissertation untersuchen wir, wie entsprechende theoretische Vorhersagen für BSM-Signale auf dem neuesten Stand der Technik gewonnen werden können.
Der erste, *Präzisionsansatz*, geht davon aus, dass die BSM-Physik innerhalb der derzeitigen Unsicherheitsbänder von Standardmessungen am LHC verborgen ist. Daraus ergibt sich der Bedarf an präzisen theoretischen Vorhersagen für BSM-Signale, die in diesem Kontext am effektivsten durch einen EFT-Ansatz beschrieben werden können. Wir diskutieren sowohl die POWHEG-Methode, die eine konsistente Kombination von Berechnungen fester Ordnung mit PS-Generatoren ermöglicht, als auch die SMEFT im Präzisionskontext. Anschliessend stellen wir unseren NNLO+PS-präzisen Ereignisgenerator für SMEFT-Effekte in der $pp \to Vh$ Produktion vor, der auf der POWHEG MiNNLO$_{\text{PS}}$-Methode basiert, und führen eine detaillierte phänomenologische Analyse für den Kanal $pp \to Zh \to \ell^+\ell^-$ durch.
Im zweiten Teil, dem Ansatz der *neuartigen Signaturen*, diskutieren wir zwei UV-Modelle, die zu ungewöhnlichen Signaturen am LHC führen. Erstens berechnen wir die Effekte der VLQs, die aus dem 4321-Eichmodell resultieren, auf die $pp \to \tau^+\tau^-$ Produktion mit NLO+PS Genauigkeit. Die zusätzliche Forderung nach einem b-Jet im Endzustand erhöht die Sensitivität gezielter Analysen auf die Signaturen der hauptsächlich an b-Quarks gekoppelten VLQs erheblich. Zweitens kann im 2HDM+a-Modell eine interessante LLP-Phänomenologie im Grenzfall minimaler Mischung zwischen dem pseudoskalaren DM-Mediator und dem erweiterten Skalarsektor auftreten. Wir stellen die Limits aus LLP-Suchen der ATLAS- und CMS-Experimente vor und demonstrieren ihre besondere Rolle bei der Eingrenzung solcher schwach wechselwirkender DM-Mediatoren.

PUBLICATIONS

The following publications are included in this thesis:

[LS1] Rhorry Gauld, Ulrich Haisch, and Luc Schnell. "SMEFT at NNLO+PS: Vh production." In: *JHEP* 01 (2024), p. 192. DOI: 10.1007/JHEP01(2024)192. arXiv: 2311.06107 [hep-ph].

[LS2] Ulrich Haisch and Luc Schnell. "Long-lived particle phenomenology in the 2HDM+a model." In: *JHEP* 04 (2023), p. 134. DOI: 10.1007/JHEP04(2023)134. arXiv: 2302.02735 [hep-ph].

[LS3] Ulrich Haisch, Luc Schnell, and Stefan Schulte. "Drell-Yan production in third-generation gauge vector leptoquark models at NLO+PS in QCD." In: *JHEP* 02 (2023), p. 070. DOI: 10.1007/JHEP02(2023)070. arXiv: 2209.12780 [hep-ph].

Further publications completed during my PhD include:

[LS4] Ulrich Haisch, Luc Schnell, and Stefan Schulte. "On Drell-Yan production of scalar leptoquarks coupling to heavy-quark flavours." In: *JHEP* 11 (2022), p. 106. DOI: 10.1007/JHEP11(2022)106. arXiv: 2207.00356 [hep-ph].

[LS5] Ulrich Haisch, Luc Schnell, and Joachim Weiss. "LHC tau-pair production constraints on a_τ and d_τ." In: *SciPost Phys.* 16.2 (2024), p. 048. DOI: 10.21468/SciPostPhys.16.2.048. arXiv: 2307.14133 [hep-ph].

CONTENTS

ACRONYMS

ADM	anomalous dimension matrix
ALICE	A Large Ion Collider Experiment
ATLAS	A Toroidal LHC ApparatuS
BSM	beyond the SM
CERN	Conseil Européen pour la Recherche Nucléaire
CKKW	Catani-Krauss-Kuhn-Webber
CKM	Cabibbo-Kobayashi-Maskawa
CL	confidence level
CM	calorimeter
CMS	Compact Muon Solenoid
CS	Catani-Seymour
DGLAP	Dokshitzer-Gribov-Lipatov-Altarelli-Parisi
DM	dark matter
DY	Drell-Yan
EFT	effective field theory
EW	electroweak
FASER	ForwArd Search ExpeRiment
FCC	Future Circular Collider
FKS	Frixione-Kunszt-Signer
FSC	final-state collinear
ggF	gluon-gluon fusion
GIM	Glashow-Iliopoulos-Maiani
HL-LHC	High-Luminosity LHC
IBP	integration by parts
ID	inner detector
IR	infrared

ISC	initial-state collinear
KLN	Kinoshita-Lee-Nauenberg
LEP	Large Electron-Positron Collider
LFU	lepton flavor universality
LHC	Large Hadron Collider
LHCb	LHC beauty
l.h.s	left-hand side
LLP	long-lived particle
LL	leading logarithmic
LO	leading order
LQ	leptoquark
MATHUSLA	MAssive Timing Hodoscope for Ultra-Stable neutraL pArticles
MC	Monte Carlo
MilliQan	Search for milli-charged particles at the LHC
MoEDAL	Monopole and Exotic particle Detector At the LHC
MS	minimal subtraction
MS	muon spectrometer
NLL	next-to-leading logarithm
NLO	next-to-leading order
NNLO	next-to-next-to-leading order
N^3LO	next-to-next-to-next-to-leading order
OS	on-shell
PDF	parton distribution function
PDG	Particle Data Group
PS	parton shower
RG	renormalization group
RGE	RG equation
r.h.s	right-hand side
QCD	Quantum Chromodynamics

QED	Quantum Electrodynamics
S	soft
SD	spin-dependent
SI	spin-independent
SLAC	Stanford Linear Accelerator Center
SLC	SLAC Linear Collider
SLD	SLC Large Detector
SM	Standard Model
SMEFT	SM effective field theory
SND@LHC	Scattering and Neutrino Detector at the LHC
SR	signal region
STXS	simplified template cross sections
UV	ultraviolet
VEV	vacuum expectation value
VLQ	vector LQ
2HDM	two-Higgs-doublet model
2HDM+a	two-Higgs-doublet plus pseudoscalar dark matter mediator model
4321	$SU(4)^{[3]} \times SU(3)^{[12]} \times SU(2)_L \times U(1)_X$

1 INTRODUCTION

This is the Jurassic Park for particle physicists...
Some of the particles they are making now or are about to make
haven't been around for 14 billion years.

— Phil Schewe, on the LHC

The LHC

It all begins with a small bottle of hydrogen gas, approximately the size of a human hand. It is located on the premises of the Conseil Européen pour la Recherche Nucléaire (CERN), situated on the Franco-Swiss border near Geneva. This is the world's largest particle physics laboratory. Here, the hydrogen atoms contained in the bottle are ionized, and the resulting protons accelerated to 450 GeV. At this energy, the protons are fed into a 27 km long circular accelerator ring known as the Large Hadron Collider (LHC). The LHC is the world's highest-energy particle accelerator. The protons circulate it in two oppositely running beams and are bunched into 2808 groups of 2×10^{11} particles. They reach energies close to 7 TeV. At four interaction points along the ring, the beams are brought to intersect, and some of the protons collide at energies close to 14 TeV [1]. This process occurs 40 000 000 times per second, recreating the conditions that prevailed in our Universe split-seconds after the Big Bang. At the interaction points, large detectors are placed to measure the collision products. The four detectors are named ATLAS, ALICE, CMS, and LHCb. Each has a distinct setup and targets (slightly) different particle interactions. Of the 40 MHz of collisions, the detectors' triggering systems select up to 1 kHz of particularly interesting events, which, in the cases of ATLAS and CMS, corresponds to 1 GB of data collected every second [2]. By analyzing this data and comparing it to theoretical predictions, particle physicists can test their theories on the fundamental particles and interactions in our Universe.

The SM and the Higgs mechanism

The current best theory is the Standard Model (SM), which up to date describes all interactions among fundamental particles observed at the LHC. Its theoretical formulation was completed in the 1970s, building on important ideas developed by numerous scientists. In the context of LHC physics, an idea known as *spontaneous symmetry breaking* or the *Higgs mechanism* is particularly relevant. The concept was independently conceived by Brout–Englert [3], Higgs [4], and Guralnik–Hagen–Kibble [5] in 1964. The three groups realized that gauge symmetries could be symmetries of the Lagrangian but not of the vacuum, which allows to incorporate non-vanishing gauge boson masses without having to abandon gauge symmetries *per se*. This is achieved by introducing a scalar field that is charged under the gauge symmetry and a corresponding scalar potential with non-trivial minima. As the scalar field vacuum arbitrarily falls into one of these minima, the gauge symmetry is broken. Furthermore, for each gauge group symmetry direction (generator) broken by the vacuum, there must be a corresponding massless mode in the particle

spectrum. These are known as *Goldstone bosons*, after the corresponding theorem published by Goldstone in 1961 [6]. The convincing feature of the Higgs mechanism is that these Goldstone bosons turn into the longitudinal modes of the gauge bosons, explaining both how the massive gauge bosons acquire the additional polarization and why the Goldstone bosons have not been observed experimentally as massless modes [7]. In contrast, all remaining scalar degrees of freedom are physical. The formulation of the SM electroweak (EW) sector by Glashow [8], Salam–Ward [9] and Weinberg [10] between 1961 and 1967 revealed the necessity of at least one Higgs doublet to impart mass to the Z and $W^{\pm}$ gauge bosons. Of the four real degrees of freedom of the doublet, three are absorbed into the longitudinal gauge boson modes, leaving one physical scalar particle. It is referred to as *Higgs boson*, and while its mass is a free parameter of the theory, its couplings to the other SM particles are clearly defined by the Higgs mechanism. The experimental hunt for a scalar particle fitting the bill of the Higgs boson was on.

The discovery of the Higgs boson

This hunt was successfully concluded at the LHC. From fits to EW precision data, where the mass of the Higgs boson m_h enters logarithmically through loop contributions, it was anticipated that m_h would be situated within [40, 180] GeV at 95% confidence level (CL) [11, Fig. 10.5]. Given that the Large Electron-Positron Collider (LEP) and the Tevatron, two earlier collider experiments, were able to exclude the parameter space up to around 110 GeV in direct searches, it was anticipated that a significant discovery would be near. This was corroborated by the fact that, in the absence of the Higgs mechanism, the EW SM would break down at scales of approximately 1.2 TeV due to unitarity-violating longitudinal contributions from the gauge bosons [12]. Consequently, any mechanism responsible for restoring the symmetry would have to be discernible at the LHC. This argument was coined the *no-lose theorem*. And indeed, the LHC did not lose. In July 2012, the ATLAS and CMS collaborations announced the discovery of a new particle in the mass range of 125 GeV, which was consistent with the Higgs boson. Further analyses [13] have since demonstrated that the 125 GeV scalar exhibits all the properties of the SM Higgs, at least within the experimental precision achieved. The discovery of this particle represents the final piece of evidence required to establish the SM. It appears evident that any theory that most accurately describes the fundamental interactions within our Universe must be constructed on top of the SM.

Going beyond the SM

Yet, paradoxically, while the 125 GeV scalar was a smoking gun for the SM, it also lies at the heart of many arguments and searches for physics beyond the SM (BSM). Firstly, this is due to the fact that the Higgs boson couples to all other known massive fundamental particles by virtue of the Higgs mechanism. If new particles exist at a scale Λ far above the EW scale and couple to the Higgs boson, then loop corrections on the order of the scale Λ would affect the Higgs mass. Indeed, as a scalar particle, there is no symmetry that protects the Higgs mass against such contributions. The $\mathcal{O}(\Lambda)$ terms must largely cancel out in order to arrive at $m_h \ll \Lambda$, which physicists do not consider to be *natural*, barring an explanation. Many BSM models with additional symmetries have been proposed to address this *hierarchy problem*. These models typically require additional structures at the TeV scale to shield the Higgs mass from the ultraviolet (UV). Additionally, given the astrophysical evidence for the presence of non-baryonic dark matter (DM) in our

In the context of Quantum Gravity, one for example expects new structures to appear at the Planck scale $\Lambda \sim 10^{19}$ GeV.

Universe, which at most interacts weakly with the SM particles, it is plausible that the Higgs may act as a portal to new massive dark states. This is also motivated by the special role of the Higgs in the SM. Experimental collaborations are investigating Higgs portal scenarios by searching for final states that include SM particles in conjunction with invisible dark states. Secondly, the addition of one Higgs doublet to the SM spectrum is based on simplicity rather than experimental evidence – we are only just now beginning to probe the scalar potential. Therefore, considering models with extended Higgs sectors seems well motivated. The two-Higgs-doublet model (2HDM), the most well-known realization of these extended sectors, has been the subject of numerous theoretical and experimental analyses. It would manifest generically in the presence of heavier scalar modes in the TeV range. Thirdly, the couplings of the Higgs boson to the SM fermions, which are implemented *ad hoc* in the SM via the addition of the Yukawa terms, appear to have a highly non-trivial structure. In particular, they exhibit an approximate flavor symmetry that distinguishes the third generation of fermions from the first two. This structure is not motivated in the SM and can be considered a preliminary indication of the existence of flavor-dependent BSM physics. Interesting BSM models with additional complexity on the TeV scale have also been developed in this direction.

Searching for BSM physics at the LHC

In light of this, the direct evidence for BSM physics has become one of the main physics objectives of the LHC [14]. Numerous searches for well-motivated BSM theories have been conducted, resulting in competitive constraints on their parameter spaces. To date, no clear deviation from the SM has been found. Does this mean that there is no BSM physics within the reach of the LHC? Not necessarily. The previous runs have demonstrated that if new physics is to be discovered at the LHC, it must be better concealed than expected. There are a multitude of potential explanations for this, and indeed a multitude of potential explanations are being pursued within the BSM community. We focus on two of these, which we consider to be particularly motivated:

(I) The first layer of BSM physics lies in the multi-TeV range, so that the small indirect signals it induces currently hide within the uncertainty bands.

(II) The BSM physics is non-standard and its signals are easily missed unless targeted in dedicated analyses.

We broadly define *non-standard* as any particle that does not couple to light partons or that does not produce high (missing) transverse momentum signatures [15]. Examples of such particles include those exclusively coupled to the heavy fermion flavors or weakly coupled light particles.

The High-Luminosity LHC (HL-LHC)

In the forthcoming years, the LHC experiments will continue to focus on both of these possibilities. In the context of scenario (I), the upcoming runs of the High-Luminosity LHC (HL-LHC) will play a pivotal role. These are projected to commence in 2029 and conclude in 2041 [16]. The HL-LHC will be equipped with an instantaneous luminosity that is five times higher than the current one. It is projected to provide a total integrated luminosity of $3\,\text{ab}^{-1}$, extending the current $140\,\text{fb}^{-1}$ by a factor of 20 [14]. In terms of the relevant Higgs couplings, it is projected that the uncertainties will be reduced from the current order of magnitude of $\mathcal{O}(15\text{-}30\%)$ to $\mathcal{O}(2\text{-}5\%)$. For the first time in history, the HL-LHC will thus provide access to

the Higgs interactions with appreciable precision, which will facilitate the search for BSM physics therein. In order to explore possibility (II), a broad search must be conducted. This can be achieved through the use of smaller LHC experiments, which have been designed with this purpose in mind. These include FASER, MATHUSLA, MilliQan, MoEDAL and SND@LHC. Additionally, the larger LHC collaborations are continuously working on improving the sensitivity of their detectors to exotic signatures. The projects presented in part (II) discuss non-standard signatures that could be observed by the ATLAS and CMS detectors in dedicated analyses.

The need for improved BSM predictions

In order to facilitate the search for BSM physics, it is essential to provide support from the theoretical side. In the context of scenario (I), in order to meet the precision requirements of the HL-LHC, the predictions for SM backgrounds and BSM signals must be improved. It is frequently argued that the precision requirements for BSM signals are less stringent than for the SM backgrounds, as the former must be at least an order of magnitude smaller than the latter at the energies accessible at the LHC. Otherwise, they would have been discovered already. While this is true, we argue that the probability of finding the needle in the haystack is significantly enhanced when both the hay and the needle are precisely defined. In particular, the potential to construct improved signal discriminators through the application of machine learning or matrix element techniques necessitates a precise modelling of BSM physics in order to tune our searches to the right signatures. We therefore argue that enhancing the precision of BSM signal predictions for well-motivated scenarios is a worthwhile pursuit.

Precise predictions for BSM signals

This is accomplished by incorporating higher-order perturbative corrections to theoretical predictions, extending to the next-to-leading order (NLO) or even next-to-next-to-leading order (NNLO) in the SM coupling constant expansions for the BSM contributions. With the enhanced precision, the complexity of the calculations is markedly increased. Nowadays, numerical tools are employed to evaluate the parton distribution functions (PDFs), to perform the phase-space integration, to simulate the splittings of partonic final states into high-multiplicity final states and more. In Section 2, we review the basic ingredients necessary for obtaining NLO-accurate theoretical predictions matched to parton shower (PS) systems. In part (I), we will then examine how the precision of these predictions can be enhanced, with a particular focus on the predictions for BSM signals. The SM effective field theory (SMEFT) plays an essential role in this regard, as it enables the incorporation of the indirect effects of *arbitrary* high-scale new physics into a systematically improvable framework. In Chapter 3.1, we introduce the SMEFT. In Section 4, we review the methods required to improve the SMEFT predictions by including higher-order perturbative corrections. Finally, in Section 5, we exemplify this with the calculation of NNLO+PS-accurate predictions for SMEFT effects in the Higgsstrahlungs process.

"Arbitrary" needs some fine print – the EW symmetry breaking must be realized linearly, i.e. SM-like.

Improved searches for BSM physics targeting non-standard signatures

In the context of scenario (II), two fully specified BSM UV models are presented in Chapters 3.2 and 3.3. The first is a vector LQs (VLQs) model arising in the $SU(4)^{[3]} \times SU(3)^{[12]} \times SU(2)_L \times U(1)_X$ (4321) gauge unification (the superscripts refer to the fermion generations that are charged under the corresponding gauge group). The second features an extended scalar sector coupled to the dark sector via a pseudoscalar DM mediator, the so-called two-Higgs-doublet plus pseudoscalar

dark matter mediator model (2HDM+a). Both models are connected to open questions regarding the SM Higgs sector: where does the highly nongeneric flavor structure of the SM come from, and why is the SM Higgs the only scalar particle realized in nature? In Sections 6 and 7, we present details of non-standard LHC signatures induced by these models, which provide a special handle to search for them. In the former model, the VLQs are primarily coupled to fermions of the third family, which gives rise to effects in $pp \to \tau^+\tau^-$ in association with b-quarks. By implementing these in the POWHEG framework at NLO+PS accuracy, we provide support for corresponding analyses searching for signals in $pp \to \tau^+\tau^-$ in association with b-tagged jets. As will be demonstrated, the latter 2HDM+a model can exhibit a long-lived particle (LLP) phenomenology if the pseudoscalar DM mediator only mixes minimally with the extended scalar sector. Then, conventional missing transverse energy searches for DM mediators at the LHC are inadequate, and instead targeted analyses for LLP signatures represent the optimal approach.

2

THEORETICAL PREDICTIONS FOR THE LHC

Our work is a delightful game.
I am frequently astonished
that it so often results in correct predictions
of experimental results.

— Murray Gell-Mann

In order to predict new effects in proton collisions at the LHC, a comprehensive understanding of a vast range of phenomena is required. This encompasses the physics of the proton, hard scatterings between constituents of the proton (the partons), the transformation of individual partons into high-multiplicity final-state jets, and many other phenomena. Over the course of several decades, significant research has been conducted with the objective of developing theoretical predictions for the LHC that are both *precise* and *accurate*. This chapter presents the fundamentals of these techniques. We consider proton-proton collisions of the form

Proton-proton collisions

$$\boldsymbol{P}_{\oplus}(K_{\oplus})\,\boldsymbol{P}_{\ominus}(K_{\ominus}) \to \boldsymbol{F}\,, \tag{2.1}$$

where $\boldsymbol{P}_{\oplus}, \boldsymbol{P}_{\ominus}$ are the incoming protons with momenta $K_{\oplus}, K_{\ominus}$ and $\boldsymbol{F}$ is an arbitrary (hadronic) final state. The subscripts $\oplus$ and $\ominus$ indicate the direction in which the protons enter the collision along the beam axis. A schematic representation of this process is provided in Figure 2.1. In this explanation, we will start at the center of Figure 2.1 and move outward. The light green circle represents a hard collision event among partons, which are constituents of the proton. One incoming parton from $\boldsymbol{P}_{\oplus}$ (illustrated in Figure 2.1 as a gluon) scatters with one incoming parton from $\boldsymbol{P}_{\ominus}$ (also a gluon), resulting in a small number of outgoing daughter particles. The hard parton scatterings are described by fixed-order calculations, which will be introduced in Subchapter 2.1.1. As more and more orders in perturbation theory are included, the resulting descriptions become increasingly *precise*, capturing the physics occurring at the hardest scale Q.

Note that there is no distinguished beam direction in pp collisions, therefore the assignment of $\oplus$ and $\ominus$ is somewhat arbitrary.

At the other end of the energy spectrum, at the scale Λ_{QCD}, resides the physics occurring inside the protons. The incoming protons $\boldsymbol{P}_{\oplus}$ and $\boldsymbol{P}_{\ominus}$ are depicted as two dark rectangles in Figure 2.1. They transform into three narrow arrows, reflecting the composite nature of protons. Finally, they provide the partons that undergo the hard scatterings. The probability of finding a parton at a given energy fraction inside the proton is described by the PDFs, which will be introduced in Subchapter 2.1.2.

In order to bridge the gap between the scales Q and Λ_{QCD}, which are usually separated by several orders of magnitude, PS generators are employed. These generators model the splittings of partons into the high-multiplicity final state $\boldsymbol{F}$,

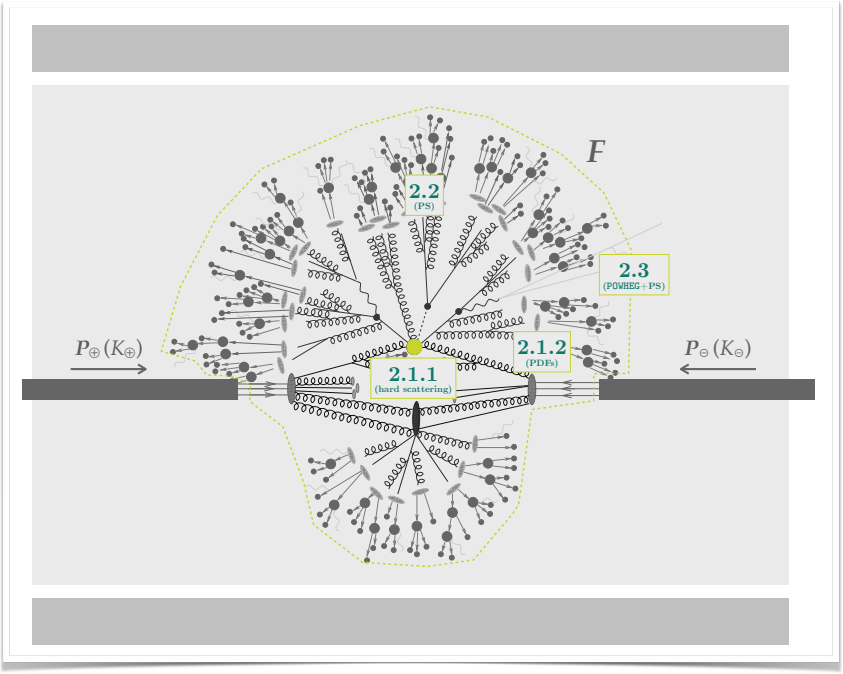

Figure 2.1: A schematic representation of proton-proton collisions at the LHC. The fundamental process is the hard scattering of partons (see Subchapter 2.1.1), which is described by fixed-order calculations. These partons originate from the incoming protons (depicted as dark rectangles), whose physics is described by the PDFs (see Subchapter 2.1.2). The splitting of the partons into high-multiplicity jets (see Chapter 2.2) outside the hard scattering process is modelled by the PS. The POWHEG framework (see Chapter 2.3) finally allows for the consistent matching of fixed-order matrix elements to PS generators. Figure adapted from [17].

which is depicted by the tree-like branchings of the particles in Figure 2.1. The theoretical predictions made by the PS are *accurate*, in the sense that the modeled events closely resemble final states observed at the LHC. Ideally, the fixed-order description and the PS modelling should go hand in hand. This is accomplished by the POWHEG framework, which will be introduced in Chapter 2.3.

2.1 Fixed-Order Predictions

This chapter draws upon the review of NLO calculations presented in [18]. Further details on automated NLO calculations in the POWHEG framework can be found there.

The underlying partonic hard scattering process

High-energy collisions between protons at the LHC originate from underlying hard scattering events between constituent partons. These are of the form

$$p_{i,\oplus}(k_\oplus)\, p_{j,\ominus}(k_\ominus) \to F(k_1, \ldots, k_n)\,, \tag{2.2}$$

where $p_{i,\oplus}, p_{j,\ominus}$ are the partons originating from $\boldsymbol{P}_\oplus, \boldsymbol{P}_\ominus$ and F represents a partonic final state. We assume that F is composed of n particles with momenta $k_1, \ldots, k_n$. The subscripts i, j of the partons reflect the fact that different underlying parton

configurations can contribute to the overall $\boldsymbol{P}_\oplus \boldsymbol{P}_\ominus \to \boldsymbol{F}$ process. The partons carry a fraction of the total proton momentum, this is expressed as

$$k_\oplus = x_\oplus K_\oplus\,, \qquad k_\ominus = x_\ominus K_\ominus\,, \tag{2.3}$$

with momentum fractions $x_\oplus, x_\ominus \in [0,1]$. Energy and momentum are conserved in elastic scattering processes, therefore

$$x_\oplus K_\oplus + x_\ominus K_\ominus = k_1 + \cdots + k_n\,. \tag{2.4}$$

Given that partons appear to be fundamental particles at the current experimental precision, scatterings between them are necessarily elastic.

The cross section $\sigma(\boldsymbol{P}_\oplus \boldsymbol{P}_\ominus \to F)$ can be expressed as

$$\boxed{\sigma(\boldsymbol{P}_\oplus \boldsymbol{P}_\ominus \to F) = \sum_{ij} \int dx_\oplus x_\ominus\, \mathcal{L}_{ij}(x_\oplus, x_\ominus, \mu_F)\, \sigma_{ij,F}(x_\oplus, x_\ominus, \mu_R, \mu_F)\,,} \tag{2.5}$$

where the indices i, j label the possible combinations of initial-state parton flavors, the parton luminosity $\mathcal{L}_{ij}$ describes the probability to find partons $p_{i,\oplus}, p_{j,\ominus}$ with momentum fractions $x_\oplus, x_\ominus$ inside the protons, and $\sigma_{ij,F} \equiv \sigma(p_{i,\oplus} p_{j,\ominus} \to F)$ is the partonic cross section. Eq. (2.5) is the result of a fundamental concept known as *factorization* [19], which allows us to separate the low-energy proton physics contained in $\mathcal{L}_{ij}$ (occurring at Λ_{QCD}) from the high-energy parton scattering physics contained in $\sigma_{ij,F}$ (occurring at the hard scale Q). This is crucial, as it allows us to calculate $\sigma_{ij,F}$ with a procedure known as *perturbation theory*, while non-perturbative effects are encapsulated in $\mathcal{L}_{ij}$, which are determined once-and-for-all in experiments. This approach is valid as long as the typical scale Q of the considered process is large compared to the scale Λ_{QCD}, which is approximately 0.2 GeV. Below this scale, the perturbative treatment of Quantum Chromodynamics (QCD) becomes invalid. The meanings of the unphysical renormalization scale μ_R and factorization scale μ_F will be elucidated below. We will now discuss the elements of (2.5) in greater detail.

Factorization

2.1.1 *The Partonic Scattering Process*

We write the partonic cross section $\sigma_{ij,F} = \sigma(p_{i,\oplus} p_{j,\ominus} \to F)$ as

Partonic cross section

$$\boxed{\sigma_{ij,F}(x_\oplus, x_\ominus, \mu_R, \mu_F) = \int d\Phi_F(k_\oplus + k_\ominus; k_1, \ldots, k_n) \frac{\left|\mathcal{M}_{ij,F}(\boldsymbol{\Phi}_F, \mu_R, \mu_F)\right|^2}{2\, s_{\oplus\ominus}}\,,} \tag{2.6}$$

where $s_{\oplus\ominus} = (k_\oplus + k_\ominus)^2$, $\boldsymbol{\Phi}_F = \{x_\oplus, x_\ominus; k_1, \ldots k_n\}$ is the so-called n-particle phase space, and

Phase space element

$$\boxed{d\Phi_F \equiv d\Phi_F(q; k_1, \ldots, k_n) = (2\pi)^d\, \delta^d\left(q - \sum_{i=1}^n k_i\right) \prod_{i=1}^n \frac{d^{d-1}k_i}{(2\pi)^{d-1}\, 2k_i^0}\,.} \tag{2.7}$$

Here, d is the number of spacetime dimensions (usually $d = 4$). The functions $\mathcal{M}_{ij,F}$ are called matrix elements, we can expand them as a perturbative series. In the context of QCD, this is a series in the strong coupling constant $g_s = \sqrt{4\pi\alpha_s}$.

Matrix elements

Perturbative series

One writes

$$\mathcal{M}_{ij,F} = \mathcal{M}^{(0)}_{ij,F} + \frac{g_s^2}{16\pi^2}\mathcal{M}^{(1)}_{ij,F} + \mathcal{O}\left(g_s^4\right) , \tag{2.8}$$

the series in the squared matrix elements of (2.6) then becomes

$$\left|\mathcal{M}_{ij,F}\right|^2 = \left|\mathcal{M}^{(0)}_{ij,F}\right|^2 + \frac{\alpha_s}{2\pi}\mathrm{Re}\left\{\mathcal{M}^{(0)*}_{ij,F}\mathcal{M}^{(1)}_{ij,F}\right\} + \mathcal{O}\left(\alpha_s^2\right) . \tag{2.9}$$

$\left|\mathcal{M}^{(0)}_{ij,F}\right|^2$ is called the leading order (LO) contribution, whereas $\mathrm{Re}\left\{\mathcal{M}^{(0)*}_{ij,F}\mathcal{M}^{(1)}_{ij,F}\right\}$ constitutes the corresponding NLO virtual correction.

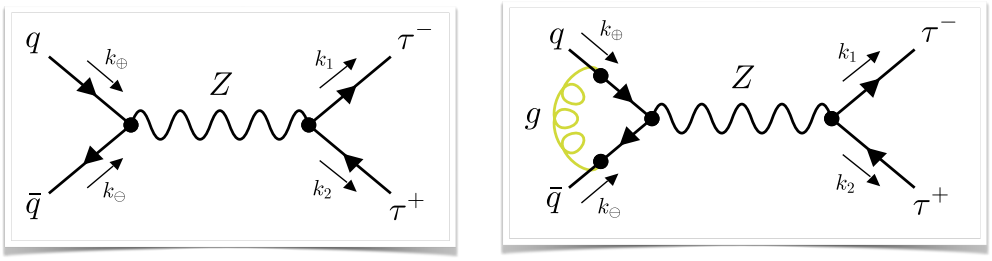

(a) LO diagram (b) NLO virtual diagram

Figure 2.2: Feynman diagrams for the partonic scattering processes $q\bar{q} \to \tau^+\tau^-$ with a Z boson exchange.

EXAMPLE: DRELL-YAN (DY) To illustrate, let us consider the case of DY production $pp \to \tau^+\tau^-$. One of the partonic scattering processes contributing to this is $q\bar{q} \to \tau^+\tau^-$ with a Z boson exchange. The corresponding LO and NLO virtual correction Feynman diagrams are shown in Figure 2.2. The LO squared matrix element is given by

$$\boxed{\left|\mathcal{M}^{(0)}_{q\bar{q},\tau\tau}\right|^2 = \frac{\left(g^-_{Zq}\right)^2\left(\left(g^-_{Z\tau}\right)^2 t^2_{\ominus 1} + \left(g^+_{Z\tau}\right)^2 t^2_{\oplus 1}\right)}{N_c\left((s_{\oplus\ominus} - m_Z)^2 + \Gamma_Z^2 m_Z^2\right)} + \left(g^+_\bullet \leftrightarrow g^-_\bullet\right) ,} \tag{2.10}$$

where the Mandelstam variables

$$s_{ij} = \left(k_i + k_j\right)^2 , \qquad t_{ij} = \left(k_i - k_j\right)^2 \tag{2.11}$$

have been introduced. The Z boson is assumed to have mass m_Z, width Γ_Z, and SM fermion couplings g^h_{Zf}, where $h = \pm$ is the fermion helicity (see (A.2)). It should be noted that (2.10) is averaged over the spins and colors of the fermions. It is convenient to express (2.10) in terms of the Mandelstam variables (2.11), given that these are Lorentz-invariant quantities and therefore do not depend on the chosen frame. The NLO virtual diagram in Figure 2.2b involves integrals over the loop momentum, which we will refer to as q.

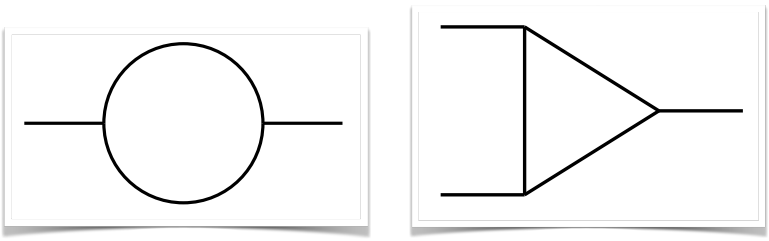

(a) $B_{2,1}$ (b) $C_{3,1}$

Figure 2.3: Scalar one-loop integrals.

In four spacetime dimensions, the integrals that occur are of the form

$$\int \frac{d^4q}{q^4}\,, \qquad \int \frac{d^4q}{q^2(q+k)^2}\,, \qquad \int \frac{d^4q}{q^2(q+k_1)^2(q+k_1+k_2)^2}\,, \tag{2.12}$$

and are in fact divergent. In order to address the divergences, it is necessary to *regularize* them. This entails the introduction of a procedure that allows to isolate the singularities and to derive analytical expressions for (2.12). The most commonly employed regularization scheme is based on the fact that (2.12) are only divergent in four spacetime dimensions, not however in general d dimensions. The integrals may therefore be rendered finite by generalizing them to d dimensions, a procedure known as *dimensional regularization*. By subsequently setting $d = 4 - 2\epsilon$, the divergences are recovered as poles of the form $1/\epsilon$ or $1/\epsilon^2$. It is important to ensure that all objects of the theory are changed consistently. This includes the introduction of an unphysical *renormalization scale*, μ_R, which ensures that the dimensionality of the integrals remains the same. We define

$$\begin{aligned} B_{2,1}(k^2) &\equiv \mu_R^{4-d} \int \frac{d^dq}{(2\pi)^d} \frac{1}{q^2(q+k)^2}\,, \\ C_{3,1}(k_1^2, k_2^2, (k_1+k_2)^2) &\equiv \mu_R^{4-d} \int \frac{d^dq}{(2\pi)^d} \frac{1}{q^2(q+k_1)^2(q+k_1+k_2)^2}\,, \end{aligned} \tag{2.13}$$

with no internal masses. Diagrammatic representations of the scalar one-loop integrals $B_{2,1}, C_{3,1}$ are shown in Figure 2.3. The analytical expressions for the integrals in (2.12) are [20]

$$\begin{aligned} B_{2,1}(0) &= \frac{i\mathcal{N}}{16\pi^2} \left(-\frac{\mu_R^2}{s}\right)^{\epsilon} \left(\frac{1}{\epsilon_{\text{UV}}} - \frac{1}{\epsilon_{\text{IR}}}\right)\,, \\ B_{2,1}(s) &= \frac{i\mathcal{N}}{16\pi^2} \left(-\frac{\mu_R^2}{s}\right)^{\epsilon} \left(\frac{1}{\epsilon_{\text{UV}}} + 2\right)\,, \\ C_{3,1}(0,0,s) &= \frac{i\mathcal{N}}{16\pi^2} \left(-\frac{\mu_R^2}{s}\right)^{\epsilon} \left(\frac{1}{s\,\epsilon_{\text{IR}}^2}\right)\,, \end{aligned} \tag{2.14}$$

which come with two different kinds of ϵ labelled $\epsilon_{\text{UV}}, \epsilon_{\text{IR}}$. They indicate the different origins of the poles, which can either be the infrared (IR) or the UV regions. We will discuss these different divergences and how to handle them in more detail below.

First, we wish to provide a brief commentary on the normalization in (2.14). We have employed the conventions of the POWHEG-BOX [21] with

$$\boxed{\mathcal{N} = (4\pi)^\epsilon / \Gamma(1-\epsilon)\,,} \tag{2.15}$$

where Γ is the gamma function. This convention will be followed throughout the thesis. Another frequent normalization of loop integrals involves the factor

$$\boxed{S_\epsilon = (4\pi)^\epsilon e^{-\gamma_E \epsilon}\,,} \tag{2.16}$$

with γ_E the Euler-Mascheroni constant. At the one-loop level, the two are identical, since

$$\boxed{\left(\frac{S_\epsilon}{\mathcal{N}}\right)^2 = 1 + \zeta_2\,\epsilon^2 + \frac{2\,\zeta_3\,\epsilon^3}{3} + \frac{7\,\zeta_2^2\,\epsilon^4}{10} + \mathcal{O}(\epsilon^5)} \tag{2.17}$$

only starts to deviate from unity at $\mathcal{O}(\epsilon^2)$. In above expression, ζ_1, ζ_2 are values of the Riemann zeta function. At the two-loop level, however, expressions based on the different conventions start to differ, necessitating the inclusion of (2.17).

Let us now return to the virtual diagram depicted in Figure 2.2b. It can be demonstrated that the (unrenormalized) NLO virtual matrix element, derived from the Feynman diagram depicted in Figure 2.2b, is proportional to the LO one. Using the integrals in (2.14), it reads

$$\frac{\alpha_s}{4\pi}\mathcal{M}^{(1)}_{0,\,q\bar{q},\tau\tau} = \underbrace{\frac{C_F\,\alpha_s}{4\pi}\left((d-7)\,B_{2,1}(s) - 2s\,C_{3,1}(0,0,s) + 4\,B_{2,1}(0)\right)}_{\equiv K_0^{(1)}}\mathcal{M}^{(0)}_{q\bar{q},\tau\tau}\,, \tag{2.18}$$

where $C_F = 4/3$ is the Casimir invariant of the fundamental representation of $SU(3)$. In (2.18), we introduced the factor $K_0^{(1)}$ that is multiplied in the NLO virtual amplitude. It contains divergences both of the IR and UV type

$$K_0^{(1)} = \frac{C_F\,\alpha_s}{4\pi}\,\mathcal{N}\left(-\frac{\mu_R^2}{s}\right)^\epsilon\left(-\frac{2}{\epsilon_{\text{IR}}^2} - \frac{4}{\epsilon_{\text{IR}}} + \frac{1}{\epsilon_{\text{UV}}} - 8 + \mathcal{O}(\epsilon)\right). \tag{2.19}$$

Let us first address the UV pole. The divergences $1/\epsilon_{\text{UV}}$ in (2.14) originate from the regions in (2.13) where the momentum q grows large. These regions are detached from those where q is on the order of the momenta produced at the LHC. As only the latter are relevant to experimentally measurable quantities, we may absorb the UV divergences into redefinitions of our theory parameters, without affecting the physical regions. This process is referred to as *renormalization*. We write

$$\psi_0 = \underbrace{\sqrt{1+\delta Z_\psi}}_{Z_\psi^{1/2}}\psi\,, \qquad A_0 = \underbrace{\sqrt{1+\delta Z_A}}_{Z_A^{1/2}}A\,, \qquad g_0 = \underbrace{(1+\delta Z_g)}_{Z_g}g\,, \tag{2.20}$$

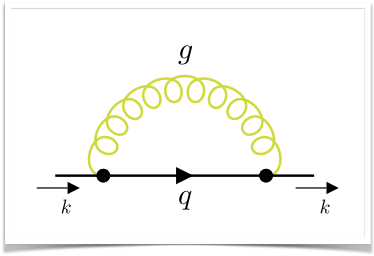

Figure 2.4: Self-energy diagram for the quark fields q that contributes to Γ_q.

where ψ, A and g generically represent fermion fields, vector fields and coupling strengths, respectively. The unrenormalized parameters, designated by the subscript 0, are equal to the renormalized parameters up to the factors Z, which have been introduced to cancel the UV poles. Regarding (2.18), it is sufficient to consider Z_q for the quark fields, which can be determined from the corresponding self-energy Γ_q. Up to $\mathcal{O}(\alpha_s)$, we find

$$\Gamma_q(s) = \left(1 - \frac{(2-d)\, C_F\, \alpha_s\, B_{2,1}(s)}{8\pi} + \mathcal{O}(\alpha_s^2)\right)\left(1 + \delta Z_q\right) , \tag{2.21}$$

where $s = k^2$ with k the quark momentum and expressed in terms of the renormalized parameters, adding the factor $(1 + \delta Z_q)$. The term proportional to α_s originates from the Feynman diagram depicted in Figure 2.4. The poles of this expression must be cancelled by δZ_q. While this uniquely specifies the $\mathcal{O}(\epsilon^{-1})$ terms of δZ_q, there is some freedom associated with the choice of its constant parts $\mathcal{O}(\epsilon^0)$. Different renormalization schemes exist, which correspond to different constant parts being absorbed into δZ_q. In our case, these are

$$\begin{aligned} \delta Z_q^{\text{OS}} &= \frac{(2-d)\, C_F\, \alpha_s\, B_{2,1}(0)}{8\pi} , && (\text{OS}) , \\ \delta Z_q^{\overline{\text{MS}}} &= \frac{C_F\, \alpha_s}{4\pi}\left(\frac{\mathcal{N}}{\epsilon_{\text{IR}}} - \frac{\mathcal{N}}{\epsilon_{\text{UV}}}\right) , && (\overline{\text{MS}}) . \end{aligned} \tag{2.22}$$

The on-shell (OS) scheme is predicated on the requirement $\Gamma(s)|_{s=m^2} = 1$, where m is the mass of the corresponding particle. In other words, all higher-order corrections are cancelled when the particle is on-shell. The minimal subtraction (MS) schemes only subtract the $1/\epsilon$ poles, in the case of the standard $\overline{\text{MS}}$ scheme up to the normalization factor $\mathcal{N}$, which transforms $1/\epsilon$ into $1/\epsilon + \log(4\pi) - \gamma_E$, where γ_E is the Euler gamma. Given that the factor $\mathcal{N}$ is always encountered in loop expressions, its multiplication to δZ_q serves to considerably simplify the expressions. All dependence on the renormalization scheme is unphysical and drops out in the limit of infinite orders in perturbation theory. It is acknowledged that in the example at hand, the distinction in (2.22) is a rather academic exercise, as the two expressions are in fact identical and vanish for $\epsilon_{\text{IR}} = \epsilon_{\text{UV}}$. Nevertheless, we thought it appropriate to introduce the renormalization schemes at this point.

Finally, the renormalized virtual NLO matrix element in the $\overline{\text{MS}}$ scheme is

$$\begin{aligned}\frac{\alpha_s}{2\pi}\text{Re}\left\{\mathcal{M}^{(0)*}_{q\bar{q},\tau\tau}\mathcal{M}^{(1)}_{q\bar{q},\tau\tau}\right\} &= 2\,\text{Re}\Big\{\underbrace{K_0^{(1)}+\delta Z_q}_{K^{(1)}}\Big\}\left|\mathcal{M}^{(0)}_{q\bar{q},\tau\tau}\right|^2 \\ &= \frac{C_F\,\alpha_s}{2\pi}\mathcal{N}\,\text{Re}\left\{\left(\frac{-\mu_R^2}{s}\right)^{\epsilon}\left(-\frac{2}{\epsilon_{\text{IR}}^2}-\frac{3}{\epsilon_{\text{IR}}}-8\right)\right\}\left|\mathcal{M}^{(0)}_{q\bar{q},\tau\tau}\right|^2 \\ &= \frac{C_F\,\alpha_s}{2\pi}\mathcal{N}\left(-\frac{2}{\epsilon_{\text{IR}}^2}-\frac{2L_\mu+3}{\epsilon_{\text{IR}}}+\pi^2-8-3L_\mu-L_\mu^2\right)\left|\mathcal{M}^{(0)}_{q\bar{q},\tau\tau}\right|^2,\end{aligned} \tag{2.23}$$

where we introduced the renormalized one-loop factor $K^{(1)}$ as well as $L_\mu = \log(\mu_R^2/s)$, and used the analytic continuation $\log(-x) = \log(x) + i\pi$ for real x. The only poles that remain now are of IR type. In many calculations, the origin of the poles is inconsequential, and thus, we will often omit the indices IR, UV of the ϵ from now on, unless they are relevant to the specific discussion.

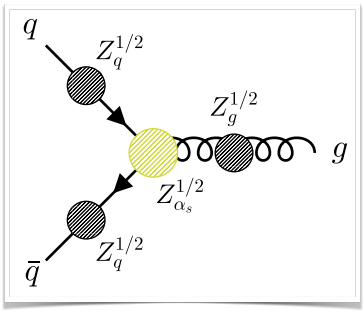

Figure 2.5: Schematic depiction of the $\bar{q}qg$ Green's function including the higher-order coupling corrections (Z_{α_s}) and the higher-order contributions from the wavefunction renormalization (Z_q, Z_g).

Before addressing the IR divergences, let us discuss the UV renormalization of the strong coupling constant α_s. Following (2.20), we may rewrite the Lagrangian expressed in terms of the bare couplings and fields as

$$\sqrt{4\pi\alpha_{s,0}}\;(\bar{q}_0\gamma^\mu T^a q_0)\,G^a_{0,\mu} = \sqrt{4\pi\alpha_s(\mu_R)}\,\mu_R^\epsilon\,Z_{\alpha_s}^{1/2}Z_g^{1/2}Z_q\;(\bar{q}\gamma^\mu T^a q)\,G^a_\mu\,, \tag{2.24}$$

where q are the quark fields and G the gluon. Once the renormalization factors Z_q, Z_g have been determined from the self-energies of the quarks and the gluon, one can use the $\bar{q}qg$ Green's function to find Z_{α_s}. This is illustrated schematically in Figure 2.5. The $\overline{\text{MS}}$ expression for Z_q at $\mathcal{O}(\alpha_s)$ has been determined in (2.22). We refrain from calculating Z_g explicitly, and instead directly quote the well-known $\overline{\text{MS}}$ result for Z_{α_s} [22, 23]

$$Z_{\alpha_s} = S_\epsilon^{-1}\left(1-\frac{\beta_0}{\epsilon}\left(\frac{\alpha_s(\mu_R)}{4\pi}\right)+\left(\frac{\beta_0^2}{\epsilon^2}-\frac{\beta_1}{2\epsilon}\right)\left(\frac{\alpha_s(\mu_R)}{4\pi}\right)^2+\mathcal{O}(\alpha_s^3)\right), \tag{2.25}$$

with

$$\boxed{\beta_0 = \frac{11\,C_A}{3} - \frac{2\,n_f}{3}\,, \qquad \beta_1 = \frac{34\,C_A^2}{3} - \frac{10\,C_A\,n_f}{3} - 2\,C_F\,n_f\,.} \tag{2.26}$$

QCD beta functions β_0, β_1

Here, $C_A = 3$ is the Casimir invariant of the adjoint representation of $SU(3)$ and n_f is the number of (light) quark flavors. In the renormalization (2.24), the unphysical renormalization scale μ_R is once again introduced to ensure the proper dimensionality of the integrals. Consequently, the renormalized coupling constant $\alpha_s(\mu_R)$ exhibits a dependence on μ_R

Of course, the bare coupling constant $\alpha_{s,0}$ is independent of the scale μ_R.

$$\frac{d\alpha_s}{d\log\mu_R} \equiv \beta(\alpha_s, \epsilon)\,, \tag{2.27}$$

which using $\alpha_{s,0} = \alpha_s(\mu_R)\,\mu_R^{2\epsilon}\,Z_{\alpha_s}$ results in [24]

$$\begin{aligned}\beta(\alpha_s,\epsilon) &= \frac{d}{d\log\mu_R}\left(\alpha_{s,0}\,\mu_R^{-2\epsilon} Z_{\alpha_s}^{-1}\right) = \alpha_{s,0}\,\mu_R \frac{d}{d\mu_R}\left(\mu_R^{-2\epsilon} Z_{\alpha_s}^{-1}\right)\\ &= \alpha_{s,0}\left(-2\epsilon\,\mu_R^{-2\epsilon} Z_{\alpha_s}^{-1} - \mu_R^{-2\epsilon+1}\frac{1}{Z_{\alpha_s}^2}\frac{dZ_{\alpha_s}}{d\mu_R}\right)\\ &= -2\epsilon\alpha_s - \alpha_s\frac{1}{Z_{\alpha_s}}\frac{dZ_{\alpha_s}}{d\log\mu_R} \equiv -2\epsilon\alpha_s + \beta(\alpha_s)\,.\end{aligned} \tag{2.28}$$

The function $\beta(\alpha_s)$ is called the *renormalization group (RG) function*. In $\overline{\text{MS}}$, it can be determined directly from the poles in (2.25), since writing $Z_{\alpha_s} = 1 + \sum_{n=1}^{\infty} S_\epsilon^n/\epsilon^n Z_{\alpha_s,n}$ yields [24]

$$\begin{aligned}\beta(\alpha_s)\left(1 + Z_{\alpha_s,1}\frac{S_\epsilon}{\epsilon} + \mathcal{O}(\epsilon^{-2})\right) = \beta(\alpha_s) Z_{\alpha_s} &= -\alpha_s\frac{dZ_{\alpha_s}}{d\log\mu_R}\\ &\overset{(2.27)}{=} -\alpha_s\,\beta(\alpha_s,\epsilon)\frac{dZ_{\alpha_s}}{d\alpha_s}\\ &= -\alpha_s\,\beta(\alpha_s,\epsilon)\left(\frac{dZ_{\alpha_s,1}}{d\alpha_s}\frac{S_\epsilon}{\epsilon} + \mathcal{O}(\epsilon^{-2})\right),\end{aligned} \tag{2.29}$$

and equating the non-singular terms results in

$$\beta(\alpha_s) \overset{(2.28)}{=} 2\alpha_s^2\frac{dZ_{\alpha_s,1}}{d\alpha_s} \overset{(2.25)}{=} -2\beta_0\frac{\alpha_s^2}{4\pi} - 2\beta_1\frac{\alpha_s^3}{(4\pi)^2} + \mathcal{O}(\alpha_s^4)\,. \tag{2.30}$$

Renormalization group running of α_s

The RG equation (RGE) for α_s in $\overline{\text{MS}}$ therefore reads

$$\boxed{\frac{d\alpha_s}{d\log\mu_R} = -2\beta_0\frac{\alpha_s^2}{4\pi} - 2\beta_1\frac{\alpha_s^3}{(4\pi)^2} + \mathcal{O}(\alpha_s^4)\,.} \tag{2.31}$$

Its solution is

$$\boxed{\alpha_s(\mu_R) = \frac{\alpha_s(m_Z)}{v(\mu_R)}\left(1 - \frac{\beta_1}{\beta_0}\frac{\alpha_s(m_Z)}{4\pi}\frac{\log v(\mu_R)}{v(\mu_R)}\right),} \tag{2.32}$$

with

$$v(\mu_R) = 1 + \beta_0\frac{\alpha_s(m_Z)}{2\pi}\log\left(\frac{\mu_R}{m_Z}\right), \tag{2.33}$$

There would have to be $n_f \geq 33/2$ effective quark flavours for β_0 to change sign.

and where the experimental value $\alpha_s(m_Z)$ is assumed to be given as a boundary condition. Since $\beta_0 > 0$, the denominator (2.33) grows with μ_R, meaning that $\alpha_s(\mu_R)$ decreases with increasing μ_R. The change of coupling constants with μ_R is called the RG *running*, the fact that α_s becomes small for large μ_R is known as the *asymptotic freedom* of QCD.

EXAMPLE: DY We will now return to the IR singularities that remained present in (2.23) following the renormalization of the UV poles. To address them, it is essential to recognize that certain partonic contributions to $\boldsymbol{P}_\oplus \boldsymbol{P}_\ominus \to \boldsymbol{F}$ have been overlooked so far. These are of the form

$$\boldsymbol{P}_\oplus \boldsymbol{P}_\ominus \to F \underbrace{J \dots J}_{l \text{ times}} \equiv F J^l \,, \tag{2.34}$$

where the final state FJ^l contains $l \in \mathbb{N}$ additional massles partons J. If these carry very little energy or are collinear to some of the massless partons in F, then the final state FJ^l is experimentally indistinguishable from F. Consequently, these contributions must be included as well.

For our underlying partonic scattering events, we extend (2.2) and consider

$$p_{i,\oplus}(k_\oplus)\, p_{j,\ominus}(k_\ominus) \to F J^l(k_1, \dots, k_n, k_{n+1}, \dots, k_{n+l}) \,, \tag{2.35}$$

Underlying partonic configurations with additional real radiation

where FJ^l is a final state including $l \in \mathbb{N}$ additional massless partons in the final state associated with the momenta $k_{n+1}, \dots, k_{n+l}$ in addition to the partonic final state F introduced earlier. Then

$$\sigma(\boldsymbol{P}_\oplus \boldsymbol{P}_\ominus \to \boldsymbol{F}) = \sum_l \sigma(\boldsymbol{P}_\oplus \boldsymbol{P}_\ominus \to F J^l) \,, \tag{2.36}$$

with the right-hand side (r.h.s) given by (2.6) replacing $n \to n + l$. In practice, since all emissions of additional massless partons are associated with factors g_s in the matrix elements, we have $\sigma(\boldsymbol{P}_\oplus \boldsymbol{P}_\ominus \to F J^l) \propto \alpha_s^l$ in QCD. Consequently, only the first few elements in the sum of (2.36) have to be considered at a given order in α_s.

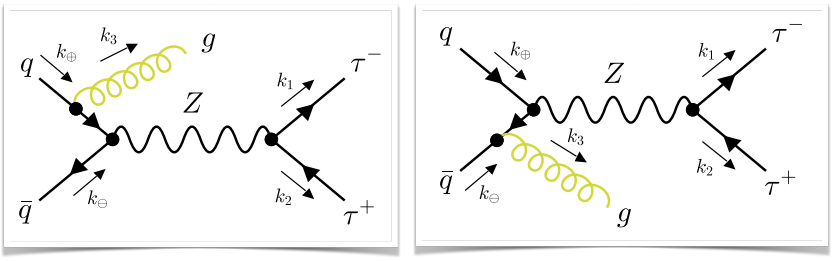

Figure 2.6: Feynman diagrams for the partonic scattering processes $q\bar{q} \to \tau^+\tau^- g$ with a Z boson exchange. Crossings of above diagrams with the gluon in the initial state contribute as well, but we do not discuss these contributions here.

Example: DY In the DY production $pp \to \tau^+\tau^-$ case, we consider NLO real diagrams as those shown in Figure 2.6, with additional gluons in the final state. It should be noted that further contributions arise from crossings of these diagrams with an initial-state gluon, which are not discussed here. The matrix element for the diagrams in Figure 2.6 is given by

$$\begin{aligned}\left|\mathcal{M}^{(0)}_{q\bar{q},\tau\tau g}\right|^2 = &-\frac{8\pi\alpha_s C_F}{N_c}\frac{(s_{\oplus\ominus}+t_{\oplus 3}+t_{\ominus 3})(g^-_{Zq})^2}{t_{\oplus 3}t_{\ominus 3}\left(\Gamma_Z^2 m_Z^2+\left(m_Z^2-s_{\oplus\ominus}-t_{\oplus 3}-t_{\ominus 3}\right)^2\right)}\\ &\Big(\quad (g^-_{Z\tau})^2\left((s_{\oplus\ominus}+t_{\oplus 1}+t_{\oplus 3})^2+t_{\ominus 1}^2\right)\\ &\quad +(g^+_{Z\tau})^2\left((s_{\oplus\ominus}+t_{\ominus 1}+t_{\ominus 3})^2+t_{\oplus 1}^2\right)\Big)+\left(g^+_\bullet \leftrightarrow g^-_\bullet\right).\end{aligned} \tag{2.37}$$

Eq. (2.37) has interesting features: if the momentum k_3 of the additional final-state gluon goes to zero, we observe that $t_{\oplus 3} = t_{\ominus 3} = 0$, resulting in the divergence of (2.37). In a similar manner, if the momentum k_3 becomes collinear to the initial-state parton that emitted it, either $k_\oplus$ or $k_\ominus$, we also have $t_{\oplus 3} \propto k_\oplus^2 = 0$ or $t_{\ominus 3} \propto k_\ominus^2 = 0$. Due to these poles, the phase space integral (2.6) of (2.37) cannot be computed directly in four spacetime dimensions. The divergences are related to the IR poles that we previously encountered in the virtual matrix element. For NLO real diagrams, the divergences can be classified into two categories: *soft* divergences, which occur when a parton momentum approaches zero, and *collinear* divergences, which arise when a parton momentum becomes collinear to another parton momentum. In order to address these divergences, we follow the *subtraction formalism*, which entails the introduction of counterterms that mimick the behavior of the full NLO real matrix element in the singular regions. By subtracting these counterterms from the matrix element, the phase space integral (2.6) can be performed in four dimensions. The integral over the subtraction terms themselves is performed in d dimensions and added back to the total result. It contains IR poles of the form $1/\epsilon_{\text{IR}}$. For so-called *IR-collinear* safe observables (formally introduced below), these poles always cancel against the IR poles we encountered in the NLO virtual matrix element. The cancellation of IR divergences was proven formally by Kinoshita and Lee-Nauenberg in what is now known as the Kinoshita-Lee-Nauenberg (KLN) theorem [25, 26]. Note that for initial-state collinear (ISC) singularities in proton-proton collisions the cancellation is somewhat more intricate, as will be discussed below.

In order to focus on the important aspects of the subtraction formalism, let us simplify our notation. First, we combine (2.5) and (2.6) into

$$\sigma(\boldsymbol{P}_\oplus \boldsymbol{P}_\ominus \to \boldsymbol{F}) = \sum_{ij}\sum_{l}\int d\boldsymbol{\Phi}_{FJ^l}\,\mathcal{L}_{ij}(x_\oplus, x_\ominus)\,\frac{\left|\mathcal{M}_{ij,FJ^l}(\boldsymbol{\Phi}_{FJ^l})\right|^2}{2\,s_{\oplus\ominus}}, \tag{2.38}$$

where $d\mathbf{\Phi}_{FJ^l} = dx_\oplus\, dx_\ominus\, d\Phi_{FJ^l}$ and we have omitted the dependence on the renormalization scales μ_R, μ_F. Furthermore, we will refrain from including indices related to the flavor structure of the process. Strictly speaking, we have already begun to do so. For a given final state F, multiple final states FJ are possible with an additional parton emission. In the case of $pp \to \tau^+\tau^-$, for example, $pp \to \tau^+\tau^- g$ (see (2.37)), $pp \to \tau^+\tau^- q$ and $pp \to \tau^+\tau^-\bar{q}$ are all valid FJ states. Consequently, we should have included not just the sum over l but also over the possible flavor combinations for FJ^l in (2.38). We will continue to omit the summation over flavors to keep our notation simple. To facilitate a straightforward extension to multiple flavor combinations nevertheless, we collect the flavors $\mathcal{F}_F \equiv \{f_\oplus, f_\ominus; f_1, \ldots, f_n\}$ of all particles and pair them with their phase space configuration $\mathbf{\Phi}_F$ into

$$\boldsymbol{P}_F \equiv (\mathbf{\Phi}_F, \mathcal{F}_F)\,, \tag{2.39}$$

and analogous for $\boldsymbol{P}_{FJ}$. This allows us to express the LO, NLO virtual and NLO real contributions as

$$\begin{aligned}
\mathcal{L}\,\mathcal{B}(\boldsymbol{P}_F) &\equiv \sum_{ij} \mathcal{L}_{ij}(x_\oplus, x_\ominus)\, \frac{\left|\mathcal{M}^{(0)}_{ij,F}(\mathbf{\Phi}_F)\right|^2}{2\,s_{\oplus\ominus}}\,, \\
\mathcal{L}\,\mathcal{V}_b(\boldsymbol{P}_F) &\equiv \sum_{ij} \mathcal{L}_{ij}(x_\oplus, x_\ominus)\, \frac{2\,\mathrm{Re}\left\{\mathcal{M}^{(0)*}_{ij,F}(\mathbf{\Phi}_F)\mathcal{M}^{(1)}_{ij,F}(\mathbf{\Phi}_F)\right\}}{2\,s_{\oplus\ominus}}\,, \\
\mathcal{L}\,\mathcal{R}(\boldsymbol{P}_{FJ}) &\equiv \sum_{ij} \mathcal{L}_{ij}(x_\oplus, x_\ominus)\, \frac{\left|\mathcal{M}^{(0)}_{ij,FJ}(\mathbf{\Phi}_{FJ})\right|^2}{2\,s_{\oplus\ominus}}\,,
\end{aligned} \tag{2.40}$$

including the *flux factor* $1/(2\,s_{\oplus\ominus})$ and where the NLO virtual matrix element is renormalized, but still contains IR poles. The fact that it is still divergent in four dimensions is indicated by the subscript b. The NLO cross section then reads

$$\sigma_{\mathrm{NLO}} = \int d\mathbf{\Phi}_F\, \mathcal{L}\left(\mathcal{B}(\boldsymbol{P}_F) + \mathcal{V}_b(\boldsymbol{P}_F)\right) + \int d\mathbf{\Phi}_{FJ}\, \mathcal{L}\,\mathcal{R}(\boldsymbol{P}_{FJ})\,, \tag{2.41}$$

the NLO expectation value for an arbitrary observable $\mathcal{O}$ is

$$\begin{aligned}
\langle\mathcal{O}\rangle_{\mathrm{NLO}} = &\int d\mathbf{\Phi}_F\, \mathcal{L}\,\mathcal{O}(\mathbf{\Phi}_F)\Big(\mathcal{B}(\boldsymbol{P}_F) + \mathcal{V}_b(\boldsymbol{P}_F)\Big) \\
&+ \int d\mathbf{\Phi}_{FJ}\, \mathcal{L}\,\mathcal{O}(\mathbf{\Phi}_{FJ})\mathcal{R}(\boldsymbol{P}_{FJ})\,.
\end{aligned} \tag{2.42}$$

As previously stated, $\mathcal{V}_b$ still contains IR poles and $\mathcal{R}$ diverges in the collinear and soft regions of $\mathbf{\Phi}_{FJ}$. In order to be able to compute (2.41) and (2.42), it is necessary to introduce appropriate subtraction counterterms.

Factorization counterterms

In order to cancel the ISC poles, which correspond to a situation where a final-state parton becomes collinear to the initial-state parton that emitted it, two *factorization*

counterterms, $\mathcal{G}_{\oplus,b}$ and $\mathcal{G}_{\ominus,b}$, must be introduced. They depend on the ISC collinear phase spaces $\mathbf{\Phi}_{F,\oplus}$ and $\mathbf{\Phi}_{F,\ominus}$

$$\begin{aligned}\mathbf{\Phi}_{F,\oplus} &\equiv \left\{\overleftarrow{\mathbf{\Phi}}_F, z\right\} \equiv \{\{zx_\oplus, x_\ominus; k_1, \dots, k_n\}, z\} \quad \text{with} \quad zx_\oplus K_\oplus + x_\ominus K_\ominus = \sum_{i=1}^n k_i\,, \\ \mathbf{\Phi}_{F,\ominus} &\equiv \left\{\overleftarrow{\mathbf{\Phi}}_F, z\right\} \equiv \{\{x_\oplus, zx_\ominus; k_1, \dots, k_n\}, z\} \quad \text{with} \quad x_\oplus K_\oplus + zx_\ominus K_\ominus = \sum_{i=1}^n k_i\,,\end{aligned} \tag{2.43}$$

where z is the momentum fraction of the initial-state parton after radiating off the collinear final-state parton. We further write

$$\begin{aligned}d\mathbf{\Phi}_{F,\oplus} &= d\overleftarrow{\mathbf{\Phi}}_F\, dz = dx_\oplus\, dx_\ominus\, d\Phi_F\left(zk_\oplus + k_\ominus; k_1, \dots, k_n\right)\, dz\,, \\ d\mathbf{\Phi}_{F,\ominus} &= d\overleftarrow{\mathbf{\Phi}}_F\, dz = dx_\oplus\, dx_\ominus\, d\Phi_F\left(k_\oplus + zk_\ominus; k_1, \dots, k_n\right)\, dz\,,\end{aligned} \tag{2.44}$$

with the n-body phase space element $d\Phi_F$ given in (2.7). The corresponding flavor configurations $\mathcal{F}_{F,\circledast}$ are of the n-body type. The factorization counterterms are added to the NLO cross section and expectation values as additional terms

$$\begin{aligned}\sigma_{\text{NLO}} \supset{}& \int d\mathbf{\Phi}_{F,\oplus}\, \mathcal{L}\, \mathcal{G}_{\oplus,b}(\boldsymbol{P}_{F,\oplus}) + \int d\mathbf{\Phi}_{F,\ominus}\, \mathcal{L}\, \mathcal{G}_{\ominus,b}(\boldsymbol{P}_{F,\ominus})\,, \\ \langle\mathcal{O}\rangle_{\text{NLO}} \supset{}& \int d\mathbf{\Phi}_{F,\oplus}\, \mathcal{L}\, \mathcal{O}(\mathbf{\Phi}_{F,\oplus})\, \mathcal{G}_{\oplus,b}(\boldsymbol{P}_{F,\oplus}) \\ &+ \int d\mathbf{\Phi}_{F,\ominus}\, \mathcal{L}\, \mathcal{O}(\mathbf{\Phi}_{F,\ominus})\, \mathcal{G}_{\ominus,b}(\boldsymbol{P}_{F,\ominus})\,.\end{aligned} \tag{2.45}$$

In order to cancel the remaining poles, we introduce *real counterterms* $\mathcal{C}^{(\alpha)}$ for each region α in the $(n+1)$-body phase space where a soft or collinear divergence occurs. For a given singular region α, a mapping $\overleftarrow{\boldsymbol{M}}$ of the form

$$\overleftarrow{\boldsymbol{M}}^{(\alpha)}(\boldsymbol{P}_{FJ}) = \begin{cases} \mathbf{\Phi}_{FJ} \to \left(\overleftarrow{\mathbf{\Phi}}_F^{(\alpha)}, z^{(\alpha)}\right) \\ \mathcal{F}_{FJ} = \{f_\oplus, \dots, a, b, \dots, f_{n+1}\} \to \overleftarrow{\mathcal{F}}_F^{(\alpha)} \equiv \{f_\oplus, \dots, ab, \dots, f_n\} \end{cases}, \tag{2.46}$$

is defined. The input is an $(n+1)$-parton configuration $\boldsymbol{P}_{FJ}$, which is mapped into an n-parton phase space configuration $\overleftarrow{\mathbf{\Phi}}_F$, a real number $z \in [0,1]$ and an n-body flavor configuration $\overleftarrow{\mathcal{F}}_F$. The flavors $a, b, ab \in \{q, \bar{q}, g\}$ are related to splittings of the form $ab \to a\,b$ (i.e. $q \to gq$, $g \to gg$ or $g \to q\bar{q}$). The phase space configuration $\overleftarrow{\mathbf{\Phi}}_F$ is called the *underlying n-body configuration* . The definition of $\overleftarrow{\boldsymbol{M}}$ is contingent upon the nature of the divergence associated with α:

Real counterterms
For readability, we omit the superscripts (α) of the parameters in the body of the text from now on, and only keep them in the main equations as a reminder for the α-dependence.

The underlying n-body configuration

- If it is a soft (S) divergence, $\mathbf{\Phi}_{FJ}$ is first mapped into a configuration where one of the final-state partons has zero momentum. $\overleftarrow{\mathbf{\Phi}}_F$ and $\overleftarrow{\mathcal{F}}_F$ are derived by removing this parton. The value of z is set to 1.
- If it is a final-state collinear (FSC) divergence, $\mathbf{\Phi}_{FJ}$ is first mapped into a configuration where two of the final-state partons have collinear momenta. $\overleftarrow{\mathbf{\Phi}}_F$ ($\overleftarrow{\mathcal{F}}_F$) is then obtained by replacing the corresponding partons by a single parton that carries the combined momentum (flavor) of the original partons. The value of z is set to 1.

- If it is an $\text{ISC}_{\oplus}$ divergence, $\mathbf{\Phi}_{FJ}$ is mapped into a configuration where a final-state parton has a momentum that is collinear to the momentum $k_{\oplus}$ of the initial-state parton $p_{\oplus}$. $\overleftarrow{\bar{\mathbf{\Phi}}}_F$ ($\overleftarrow{\bar{\mathcal{F}}}_F$) is then obtained by removing this final-state parton and replacing the momentum (flavor) of the initial-state parton with the momentum (flavor) after radiation. The value of z is set to the momentum fraction after radiation.

Furthermore, it is required that the configurations of the remaining partons (i.e. those not mentioned in the aforementioned replacement rules) in $\overleftarrow{\bar{\boldsymbol{P}}}_F \equiv (\overleftarrow{\bar{\mathbf{\Phi}}}_F, \overleftarrow{\bar{\mathcal{F}}}_F)$ remain unchanged in the asymptotic limit where $\mathbf{\Phi}_{FJ}$ approaches the singular region α and that

$$\boxed{\mathcal{O}(\mathbf{\Phi}_{FJ})\,\mathcal{R}(\boldsymbol{P}_{FJ}) - \sum_{\alpha} \mathcal{O}\left(\overleftarrow{\bar{\mathbf{\Phi}}}_F^{(\alpha)}\right) \mathcal{C}^{(\alpha)}(\boldsymbol{P}_{FJ})} \tag{2.47}$$

has at most integrable singularities in $\mathbf{\Phi}_{FJ}$ for suitable observables $\mathcal{O}$. In this context, *suitable* means *IR-collinear* safe, i.e. $\mathcal{O}(\mathbf{\Phi}_{FJ}) \to \mathcal{O}\left(\overleftarrow{\bar{\mathbf{\Phi}}}_F\right)$ as $\mathbf{\Phi}_{FJ}$ approaches the singular region α. In other words, $\mathcal{O}$ should not depend on the details of the emitted parton in the collinear limits, since these correspond to low-energy physics that we assumed to be separable from the high-energy parton scattering physics in (2.5). Otherwise, the factorization of the high-energy parton scattering from the low-energy proton physics will not be valid.

IR-collinear safe observables

Using (2.47), we rewrite the NLO real contribution in (2.42) as

$$\begin{aligned}\int d\mathbf{\Phi}_{FJ}\,\mathcal{L}\,\mathcal{O}(\mathbf{\Phi}_{FJ})\,\mathcal{R}(\boldsymbol{P}_{FJ}) = &\underbrace{\sum_{\alpha}\int d\mathbf{\Phi}_{FJ}\,\mathcal{L}^{(\alpha)}\,\mathcal{O}\left(\overleftarrow{\bar{\mathbf{\Phi}}}_F^{(\alpha)}\right)\mathcal{C}^{(\alpha)}(\boldsymbol{P}_{FJ})}_{①} \\ &+ \underbrace{\int d\mathbf{\Phi}_{FJ}\left(\mathcal{L}\,\mathcal{O}(\mathbf{\Phi}_{FJ})\,\mathcal{R}(\boldsymbol{P}_{FJ}) - \sum_{\alpha}\mathcal{L}^{(\alpha)}\,\mathcal{O}\left(\overleftarrow{\bar{\mathbf{\Phi}}}_F^{(\alpha)}\right)\mathcal{C}^{(\alpha)}(\boldsymbol{P}_{FJ})\right)}_{②}.\end{aligned} \tag{2.48}$$

We have introduced

$$\begin{aligned}\mathcal{L}^{(\alpha_{\text{FS}})} &= \mathcal{L}\left(\overleftarrow{x}_{\oplus}^{(\alpha_{\text{FS}})}, \overleftarrow{x}_{\ominus}^{(\alpha_{\text{FS}})}\right) && \text{for} \quad \alpha_{\text{FS}} \in \{\text{FSC}, \text{S}\}\,, \\ \mathcal{L}^{(\alpha_{\oplus})} &= \mathcal{L}\left(\overleftarrow{x}_{\oplus}^{(\alpha_{\oplus})}/z^{(\alpha_{\oplus})}, \overleftarrow{x}_{\ominus}^{(\alpha_{\oplus})}\right) && \text{for} \quad \alpha_{\oplus} \in \{\text{ISC}_{\oplus}\}\,, \\ \mathcal{L}^{(\alpha_{\ominus})} &= \mathcal{L}\left(\overleftarrow{x}_{\oplus}^{(\alpha_{\ominus})}, \overleftarrow{x}_{\ominus}^{(\alpha_{\ominus})}/z^{(\alpha_{\ominus})}\right) && \text{for} \quad \alpha_{\ominus} \in \{\text{ISC}_{\ominus}\}\,.\end{aligned} \tag{2.49}$$

The term ② of (2.48) is integrable in four dimensions, as a consequence of how the counterterms $\mathcal{C}$ have been set up. In contrast, the term ① necessarily diverges. The form (2.48) is nevertheless of use, as the $\mathcal{C}$ can be implemented in a general manner suitable for arbitrary processes. Consequently, the term ① can be calculated once-and-for-all.

In order to determine ①, we introduce the parametrization

$$\mathbf{\Phi}_{FJ} \mathrel{\widehat{=}} \left\{\overleftarrow{\bar{\mathbf{\Phi}}}_F^{(\alpha)}, \Phi_{\text{rad}}^{(\alpha)}\right\} \quad \text{and} \quad d\mathbf{\Phi}_{FJ} \mathrel{\widehat{=}} d\overleftarrow{\bar{\mathbf{\Phi}}}_F^{(\alpha)} d\Phi_{\text{rad}}^{(\alpha)} \tag{2.50}$$

in each singular region α. Here, $\overleftarrow{\bar{\mathbf{\Phi}}}_F$ is the underlying n-body configuration as before, while Φ_{rad} parameterises the phase space of the additional emitted parton. Using this, we define

$$\begin{aligned}
\overleftarrow{\mathcal{C}}^{(\alpha_{\oplus})}\left(\overleftarrow{\bar{\boldsymbol{P}}}_F^{(\alpha_{\oplus})}, z\right) &\equiv \int d\Phi_{\text{rad}}^{(\alpha_{\oplus})}\, \mathcal{C}^{(\alpha_{\oplus})}(\boldsymbol{P}_{FJ})\, z\, \delta\left(z - z^{(\alpha_{\oplus})}\right) \qquad \text{for} \quad \alpha_{\oplus} \in \{\text{ISC}_{\oplus}\}\,, \\
\overleftarrow{\mathcal{C}}^{(\alpha_{\text{FS}})}\left(\overleftarrow{\bar{\boldsymbol{P}}}_F^{(\alpha_{\text{FS}})}\right) &\equiv \int d\Phi_{\text{rad}}^{(\alpha_{\text{FS}})}\, \mathcal{C}^{(\alpha_{\text{FS}})}(\boldsymbol{P}_{FJ}) \qquad \text{for} \quad \alpha_{\text{FS}} \in \{\text{S, FSC}\}\,.
\end{aligned} \tag{2.51}$$

In the former case, term ① becomes

$$\begin{aligned}
&\sum_{\alpha_{\oplus}} \int d\boldsymbol{\Phi}_{FJ}\, \mathcal{L}^{(\alpha_{\oplus})}\, \mathcal{O}\left(\overleftarrow{\bar{\mathbf{\Phi}}}_F^{(\alpha_{\oplus})}\right) \mathcal{C}^{(\alpha_{\oplus})}(\boldsymbol{P}_{FJ}) \\
&\qquad = \sum_{\alpha_{\oplus}} \int d\overleftarrow{\bar{\mathbf{\Phi}}}_F^{(\alpha_{\oplus})} \frac{dz}{z}\, \mathcal{L}^{(\alpha_{\oplus})} \mathcal{O}\left(\overleftarrow{\bar{\mathbf{\Phi}}}_F^{(\alpha_{\oplus})}\right) \overleftarrow{\mathcal{C}}^{(\alpha_{\oplus})}\left(\overleftarrow{\bar{\boldsymbol{P}}}_F^{(\alpha_{\oplus})}, z\right) \\
&\qquad = \sum_{\alpha_{\oplus}} \int d\boldsymbol{\Phi}_{F,\oplus}\, \mathcal{L}\, \mathcal{O}\left(\overleftarrow{\bar{\mathbf{\Phi}}}_F\right) \overleftarrow{\mathcal{C}}^{(\alpha_{\oplus})}\left(\boldsymbol{P}_{F,\oplus}\right)\,.
\end{aligned} \tag{2.52}$$

The last step is non-trivial. We have used the fact that the integration over $d\overleftarrow{\bar{\mathbf{\Phi}}}_F dz$ is equivalent to the integration over $d\boldsymbol{\Phi}_{F,\oplus}$, and the factor $1/z$ on the second line of (2.52) is cancelled by the Jacobian factor from the transformation between $\overleftarrow{x}_{\oplus}/z \,\widehat{=}\, x_{\oplus}$. The latter identity also allowed us to replace $\mathcal{L}^{(\alpha_{\oplus})}$ by $\mathcal{L}$. The total NLO expectation value for $\mathcal{O}$ now reads

$$\begin{aligned}
\langle \mathcal{O} \rangle_{\text{NLO}} = &\int d\boldsymbol{\Phi}_F\, \mathcal{L}\, \mathcal{O}(\boldsymbol{\Phi}_F) \Big(\mathcal{B}(\boldsymbol{P}_F) + \mathcal{V}_b(\boldsymbol{P}_F) \Big) \\
&+ \int d\boldsymbol{\Phi}_{FJ} \left(\mathcal{L}\, \mathcal{O}(\boldsymbol{\Phi}_{FJ}) \mathcal{R}(\boldsymbol{P}_{FJ}) - \sum_{\alpha} \mathcal{L}^{(\alpha)} \mathcal{O}\left(\overleftarrow{\bar{\mathbf{\Phi}}}_F^{(\alpha)}\right) \mathcal{C}^{(\alpha)}(\boldsymbol{P}_{FJ}) \right) \\
&+ \sum_{\alpha_{\text{FS}}} \int d\overleftarrow{\bar{\mathbf{\Phi}}}_F^{(\alpha_{\text{FS}})}\, \mathcal{L}^{(\alpha_{\text{FS}})}\, \mathcal{O}\left(\overleftarrow{\bar{\mathbf{\Phi}}}_F^{(\alpha_{\text{FS}})}\right) \overleftarrow{\mathcal{C}}^{(\alpha_{\text{FS}})}\left(\overleftarrow{\bar{\boldsymbol{P}}}_F^{(\alpha_{\text{FS}})}\right) \\
&+ \int d\boldsymbol{\Phi}_{F,\oplus}\, \mathcal{L}\, \mathcal{O}\left(\overleftarrow{\bar{\mathbf{\Phi}}}_F\right) \left(\sum_{\alpha_{\oplus}} \overleftarrow{\mathcal{C}}^{(\alpha_{\oplus})}\left(\boldsymbol{P}_{F,\oplus}\right) + \mathcal{G}_{\oplus,b}(\boldsymbol{P}_{F,\oplus}) \right) \\
&+ \int d\boldsymbol{\Phi}_{F,\ominus}\, \mathcal{L}\, \mathcal{O}\left(\overleftarrow{\bar{\mathbf{\Phi}}}_F\right) \left(\sum_{\alpha_{\oplus}} \overleftarrow{\mathcal{C}}^{(\alpha_{\oplus})}\left(\boldsymbol{P}_{F,\ominus}\right) + \mathcal{G}_{\ominus,b}(\boldsymbol{P}_{F,\ominus}) \right)\,.
\end{aligned}$$

Moreover, it turns out that one can always write

$$\boxed{\sum_{\alpha_{\oplus}} \overleftarrow{\mathcal{C}}^{(\alpha_{\oplus})}(\boldsymbol{P}_{F,\oplus}) + \mathcal{G}_{\oplus,b}(\boldsymbol{P}_{F,\oplus}) = \mathcal{G}_{\oplus}(\boldsymbol{P}_{F,\oplus}) + \delta(1-z)\, \mathcal{G}_{\oplus}^{\text{div}}\left(\overleftarrow{\bar{\boldsymbol{P}}}_F\right)\,,} \tag{2.53}$$

where $\mathcal{G}_{\oplus}$ is finite in four dimensions, while $\mathcal{G}_{\oplus}^{\text{div}}$ contains divergences that are related to soft gluon emissions. Overall, the quantity

Cancellation of the IR poles

$$\boxed{\mathcal{V}(\boldsymbol{P}_F) \equiv \mathcal{V}_b(\boldsymbol{P}_F) + \sum_{\alpha_{\text{FS}}} \overleftarrow{\mathcal{C}}^{(\alpha_{\text{FS}})}(\boldsymbol{P}_F) + \mathcal{G}_{\oplus}^{\text{div}}(\boldsymbol{P}_F) + \mathcal{G}_{\ominus}^{\text{div}}(\boldsymbol{P}_F)} \tag{2.54}$$

is finite in four dimensions. In the total sum of (2.54), the IR divergences we have found in $\mathcal{V}_b$ are exactly cancelled, as guaranteed by the KLN theorem [25, 26].

The subtraction formalism master formula

It should be noted, however, that some of the ISC divergences have been absorbed by the $\mathcal{G}_{\oplus,b}$ along the way. Finally, we can write the NLO expectation value as

$$\begin{aligned}\langle\mathcal{O}\rangle_{\text{NLO}} &= \int d\mathbf{\Phi}_F\, \mathcal{O}(\mathbf{\Phi}_F)\Big[B(\boldsymbol{P}_F) + V(\boldsymbol{P}_F)\Big] \\ &+ \int d\mathbf{\Phi}_{FJ}\left[\mathcal{O}(\mathbf{\Phi}_{FJ})\, R(\boldsymbol{P}_{FJ}) - \sum_\alpha \mathcal{O}\left(\overleftarrow{\mathbf{\Phi}}_F^{(\alpha)}\right) C^{(\alpha)}(\boldsymbol{P}_{FJ})\right] \\ &+ \int d\mathbf{\Phi}_{F,\oplus}\, \mathcal{O}\left(\overleftarrow{\mathbf{\Phi}}_F\right) G_\oplus(\mathbf{\Phi}_{F,\oplus}) \\ &+ \int d\mathbf{\Phi}_{F,\ominus}\, \mathcal{O}\left(\overleftarrow{\mathbf{\Phi}}_F\right) G_\ominus(\mathbf{\Phi}_{F,\ominus})\,,\end{aligned} \tag{2.55}$$

where we have introduced the abbreviations

$$R = \mathcal{L}\mathcal{R}\,, \quad C^{(\alpha)} = \mathcal{L}^{(\alpha)}\mathcal{C}^{(\alpha)}\,, \quad G_\oplus = \mathcal{L}\mathcal{G}_\oplus\,, \quad B = \mathcal{L}\mathcal{B}\,, \quad V = \mathcal{L}\mathcal{V} \tag{2.56}$$

for ease of notation. Equation (2.55) is finite in four dimensions and can be integrated numerically. It may be viewed as the master formula for NLO subtraction schemes.

EXAMPLE: DY In practice, subtraction formalisms known as Frixione-Kunszt-Signer (FKS) subtraction [27, 28] or Catani-Seymour (CS) subtraction [29] are employed in Monte Carlo (MC) codes. We refrain from explicitly writing down the corresponding counterterms for the DY process. Nevertheless, we wish to outline a subtraction formalism for DY based on the plus distribution. This will allow us to recover the additional IR poles from the NLO real matrix element and demonstrate how they are cancelled. As a first step, we re-express the part of the phase space element (2.7) that pertains to the additional emitted gluon as

$$\frac{d^{d-1}k_3}{2k_3^0(2\pi)^{d-1}} = \left(\frac{\mu^2}{s_{\oplus\ominus}}\right)^\epsilon \frac{s_{\oplus\ominus}}{(4\pi)^{d-1}}(1-z)^{1-2\epsilon}(1-\xi^2)^{-\epsilon}dz\, d\xi\, d\Omega^{d-2}\,, \tag{2.57}$$

where $z = (1 - 2k_3^0/\sqrt{s_{\oplus\ominus}}) \in [0,1]$ parameterises the momentum fraction of the quark after radiating off the gluon and $\xi = \cos\theta \in [-1,1]$ relates to the collinearity of the gluon with θ the angle between the three-momentum of the gluon and the $\oplus$ axis. Using this parametrization, the Mandelstam variables $t_{\oplus 3}, t_{\ominus 3}$ that appear in (2.37) become

$$t_{\oplus 3} = -\frac{s_{\oplus\ominus}}{2}(1-z)(1-\xi)\,, \quad t_{\ominus 3} = -\frac{s_{\oplus\ominus}}{2}(1-z)(1+\xi)\,. \tag{2.58}$$

The singular part in (2.37) behaves as

$$R \propto \frac{1}{t_{\oplus 3}t_{\ominus 3}} \propto \frac{1}{(1-z)^2(1-\xi^2)}\,, \tag{2.59}$$

making the different kinds of IR singularities apparent. For $z \to 1$, the emitted gluon is soft, resulting in a divergence of type S. For $\xi \to 1$, the gluon becomes collinear to the $\oplus$ direction, leading to a divergence of type $\text{ISC}_\oplus$. Finally, for $\xi \to -1$, a divergence of type $\text{ISC}_\ominus$ emerges.

These divergences can be cured by multiplying appropriate factors. The combination $[(1-z)^2(1-\xi)R]$ is finite for $\xi \in [0,1]$, while $[(1-z)^2(1+\xi)R]$ is finite for $\xi \in [-1,0]$. Overall, we rewrite the integral over R as

$$\begin{aligned}\int d\Phi_{\text{rad}}\, R \propto \quad & \int_0^1 d\xi \int_0^1 dz\, (1-z)^{-1-2\epsilon}\, (1-\xi)^{-1-\epsilon} \left[(1-z)^2(1-\xi)R\right] \\ & + \int_{-1}^0 d\xi \int_0^1 dz\, (1-z)^{-1-2\epsilon}\, (1+\xi)^{-1-\epsilon} \left[(1-z)^2(1+\xi)R\right] ,\end{aligned} \tag{2.60}$$

where we have focussed on the divergent parts and included the Jacobian factors from (2.57). The expressions within the square brackets are finite. We proceed by rewriting the factors in front of the square bracket, focusing on the first term in (2.60). The procedure for the second term is analogous. Using

$$\begin{aligned}(1-z)^{-1-2\epsilon} &= -\frac{1}{2\epsilon}\delta(1-z) + \left(\frac{1}{1-z}\right)_+ - 2\epsilon \left(\frac{\log(1-z)}{1-z}\right)_+ + \mathcal{O}(\epsilon^2) , \\ (1-\xi)^{-1-\epsilon} &= -\frac{2^{-\epsilon}}{\epsilon}\delta(1-\xi) + \left(\frac{1}{1-\xi}\right)_+ + \mathcal{O}(\epsilon) ,\end{aligned} \tag{2.61}$$

where the plus distributions are defined as

$$\begin{aligned}\int_0^1 dz \left(\frac{1}{1-z}\right)_+ f(z) &= \int_0^1 dz\, \frac{f(z)-f(1)}{1-z} , \\ \int_0^1 dz \left(\frac{\log(1-z)}{1-z}\right)_+ f(z) &= \int_0^1 dz\, \log(1-z)\, \frac{f(z)-f(1)}{1-z} , \\ \int_0^1 dy \left(\frac{1}{1-y}\right)_+ f(y) &= \int_0^1 dy\, \frac{f(y)-f(1)}{1-y} ,\end{aligned} \tag{2.62}$$

the first term in (2.60) becomes

$$\begin{aligned}&\int_0^1 d\xi \int_0^1 dz\, (1-z)^{-1-2\epsilon}\, (1-\xi)^{-1-\epsilon} g(z,\xi) \\ &\quad = -\frac{1}{2\epsilon}\int_0^1 d\xi\, (1-\xi)^{-1-\epsilon}\, g(1,\xi) \\ &\qquad - \int_0^1 dz \left[\frac{2^{-\epsilon}}{\epsilon}\left(\frac{1}{1-z}\right)_+ - 2\left(\frac{\log(1-z)}{1-z}\right)_+\right] g(z,1) \\ &\qquad + \int_0^1 d\xi \int_0^1 dz \left(\frac{1}{1-z}\right)_+ \left(\frac{1}{1-\xi}\right)_+ g(z,\xi) + \mathcal{O}(\epsilon) .\end{aligned} \tag{2.63}$$

We have abbreviated $g(z,\xi) \equiv \left[(1-z)^2(1-\xi)R\right]$. The last term of (2.63) is finite in four dimensions. It corresponds to the term ② in (2.48). In fact, the plus distribution precisely induces the subtraction terms that are needed in order to cancel the divergences in R. The other two terms, meanwhile, are divergent. They correspond to the term ① in (2.48). To better understand how the cancellation of their singularities with the singularities recovered in the NLO matrix element plays out, let us calculate them explicitly.

We start with the first term on the r.h.s. In the limit $z \to 1$, we have $t_{\oplus 3}, t_{\ominus 3} \to 0$, and $g(z,\xi)$ becomes

$$\begin{aligned} g(1,\xi) &\propto \lim_{z\to 1} (1-z)^2(1-\xi) \left|\mathcal{M}^{(0)}_{q\bar{q},\tau\tau g}\right|^2 \\ &= \frac{4\pi\alpha_s C_F}{N_c} \frac{(g^-_{Zq})^2 \left((g^-_{Z\tau})^2 t^2_{\ominus 1} + (g^+_{Z\tau})^2 t^2_{\oplus 1}\right)}{(1+\xi)\, s_{\oplus\ominus}\left(\Gamma_Z^2 m_Z^2 + \left(m_Z^2 - s_{\oplus\ominus}\right)^2\right)} + \left(g^+_\bullet \leftrightarrow g^-_\bullet\right), \\ &= \frac{4\pi\alpha_s C_F}{(1+\xi)\, s_{\oplus\ominus}} \left|\mathcal{M}^{(0)}_{q\bar{q},\tau\tau}\right|^2 . \end{aligned} \tag{2.64}$$

It is not a coincidence that the LO matrix element appears, as the radiation of the gluon *factorizes* from the remaining process in the soft limit at this order in perturbation theory. This is illustrated schematically in Figure 2.7a. Overall, we obtain

$$\boxed{\frac{\alpha_s C_F}{2\pi} \left|\mathcal{M}^{(0)}_{q\bar{q},\tau\tau}\right|^2 \left(\frac{2}{\epsilon^2_{\text{IR}}} + \frac{2L_\mu}{\epsilon_{\text{IR}}} + \mathcal{O}\left(\epsilon^0_{\text{IR}}\right)\right)} \tag{2.65}$$

for the first term on the r.h.s of (2.63), which exactly cancels the $1/\epsilon^2_{\text{IR}}$ term in the NLO virtual matrix element (2.23). Let us now turn to the divergence in the second term. In the limit $\xi \to 1$, the factor $g(z,\xi)$ becomes

$$\begin{aligned} g(z,1) &\propto \lim_{\xi\to 1} (1-z)^2(1-\xi) \left|\mathcal{M}^{(0)}_{q\bar{q},\tau\tau g}\right|^2 \\ &= \frac{16\pi\alpha_s C_F}{N_c} \left(\frac{z\,(g^-_{Zq})^2 (g^-_{Z\tau})^2 \left((s_{\oplus\ominus} + t_{\oplus 1})^2 + t^2_{\ominus 1}\right)}{s_{\oplus\ominus}\left(\Gamma_Z^2 m_Z^2 + \left(m_Z^2 - z\, s_{\oplus\ominus}\right)^2\right)} \right. \\ &\quad \left. + \frac{z\,(g^-_{Zq})^2 \left((g^+_{Z\tau})^2 (z\, s_{\oplus\ominus} + t_{\ominus 1})^2 + t^2_{\oplus 1}\right)}{s_{\oplus\ominus}\left(\Gamma_Z^2 m_Z^2 + \left(m_Z^2 - z\, s_{\oplus\ominus}\right)^2\right)} \right) + \left(g^+_\bullet \leftrightarrow g^-_\bullet\right) \\ &= \frac{16\pi\alpha_s C_F\,(1+z^2)}{N_c} \frac{(g^-_{Zq})^2 \left((g^-_{Z\tau})^2 \tilde{t}^2_{\ominus 1} + (g^+_{Z\tau})^2 \tilde{t}^2_{\oplus 1}\right)}{\tilde{s}_{\oplus\ominus}\left(\Gamma_Z^2 m_Z^2 + \left(m_Z^2 - \tilde{s}_{\oplus\ominus}\right)^2\right)} + \left(g^+_\bullet \leftrightarrow g^-_\bullet\right), \\ &= \frac{16\pi\alpha_s C_F\,(1+z^2)}{N_c} \left|\mathcal{M}^{(0)}_{q\bar{q},\tau\tau}\right|^2 , \end{aligned} \tag{2.66}$$

where we have used that in the collinear limit $\xi \to 1$ we can rewrite $s_{\oplus\ominus} = \tilde{s}_{\oplus\ominus}/z$, $t_{\oplus 1} = \tilde{t}_{\oplus 1}/z$ and $t_{\ominus 1} = \tilde{t}_{\ominus 1}$ to express the Mandelstams in terms of the momenta $\tilde{k}_\oplus = z k_\oplus$ and $\tilde{k}_\ominus = k_\ominus$ after the radiation of the gluon. Once more, the LO matrix element is recovered, as the emission of the gluon factorizes in the collinear limit, illustrated schematically in Figure 2.7b. Overall, we obtain the pole

$$-\frac{\alpha_s C_F}{\pi} \left|\mathcal{M}^{(0)}_{q\bar{q},\tau\tau}\right|^2 \int_0^1 dz\, \frac{1}{\epsilon} \left(\frac{1+z^2}{1-z}\right)_+ \tag{2.67}$$

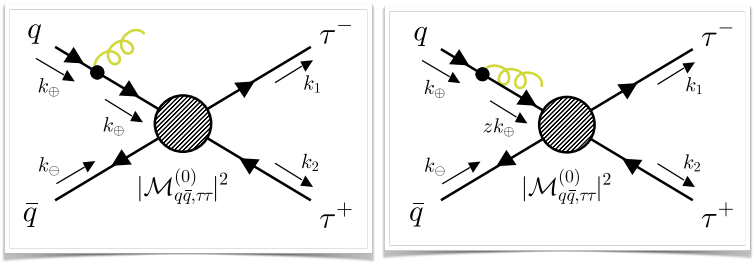

(a) Soft limit (b) Collinear limit

Figure 2.7: Schematic depiction of the factorization of the gluon emission from the remaining diagram in the soft (left) and collinear (right) limits. The physics of the remaining diagram is described by the LO matrix element $|\mathcal{M}^{(0)}_{q\bar{q},\tau\tau}|^2$.

from the second term on the r.h.s of (2.63). Combined with the $1/\epsilon_{\text{IR}}$ pole of the NLO virtual contribution (2.23), it results in

$$-\frac{\alpha_s}{\pi}\left|\mathcal{M}^{(0)}_{q\bar{q},\tau\tau}\right|^2 \int_0^1 dz\, \frac{1}{\epsilon}\, \underbrace{C_F\left[\left(\frac{1+z^2}{1-z}\right)_+ \frac{3}{2}\delta(1-z)\right]}_{\equiv P^{(0)}_{qq}(z)} . \tag{2.68}$$

In this expression, the LO *Altarelli-Parisi splitting function* $P^{(0)}_{qq}(z)$ appeared. The corresponding pole resulted from the $\text{ISC}_\oplus$ divergences of the NLO real and virtual contributions, and is absorbed by the collinear counterterm $\mathcal{G}_{\oplus,b}$. In the language of the subtraction formalism, the term proportional to $3/(2\epsilon)\,\delta(1-z)$ is part of $\delta(1-z)\mathcal{G}^{\text{div}}_\oplus$ and cancels the $1/\epsilon_{\text{IR}}$ poles in the NLO virtual matrix element $\mathcal{V}_b$. To understand where the counterterm $\mathcal{G}_{\oplus,b}$ comes from, it is necessary to discuss the PDFs in greater detail.

2.1.2 *Parton distribution functions*

In (2.5), we introduced the parton luminosity $\mathcal{L}_{ij}(x_\oplus, x_\ominus, \mu_F)$, which encapsulates the low-energy physics of the proton. As previously stated, the latter can be factorized from the high-energy hard scatterings of the partons. One decomposes the $\mathcal{L}_{ij}$ as

Parton luminosity

$$\mathcal{L}_{ij}(x_\oplus, x_\ominus, \mu_F) = f_i(x_\oplus, \mu_F)\, f_j(x_\ominus, \mu_F)\,, \tag{2.69}$$

where the $f_i(x, \mu_F)$ are the PDFs. They describe the probability of finding a parton of type i in the proton, which carries the momentum fraction $x \in [0,1]$ of the total proton momentum.

The PDFs

As previously demonstrated in the DY example, in the case of ISC singularities, not all of the IR divergences are cancelled between the NLO virtual and real matrix elements. There are divergences such as the pole proportional to $P^{(0)}_{qq}(z)$ that remain. These divergences factorize from the hard scattering matrix elements. In the above example, this manifested in the form of the poles being equal to the LO matrix

element, $|\mathcal{M}^{(0)}_{q\bar{q},\tau\tau}|^2$, times additional structure. The latter is general and originates from the soft-collinear part of the process. As such, it should be removed from the hard scattering matrix elements and added to the PDFs, which were designed to contain the low-energy physics. This is achieved in a procedure called *factorization*. The ISC poles are absorbed into the divergent bare PDFs $f_i^{\text{bare}}(x)$, which thereby turn into the finite physical PDFs $f_i(x, \mu_F)$ and gain a dependence on the factorization scale μ_F. Or, expressed differently in the framework of the subtraction formalism, the divergent bare PDFs $f_i^{\text{bare}}(x)$ are replaced by the finite physical PDFs $f_i(x, \mu_F)$ and the collinear counterterms $\mathcal{G}_{\oplus,b}, \mathcal{G}_{\ominus,b}$, which cancel the remaining IR poles from the ISC divergences. The μ_F-dependence of the $f_i(x, \mu_F)$ is described by

Factorization

$$\boxed{\frac{\partial}{\partial \ln \mu_F^2}\begin{pmatrix} f_{q_i}(x,\mu_F) \\ f_g(x,\mu_F)\end{pmatrix} = \frac{\alpha_s}{2\pi}\sum_{q_j}\int_x^1 \frac{dz}{z}\begin{pmatrix} P_{q_iq_j}(\frac{x}{z}) & P_{q_ig}(\frac{x}{z}) \\ P_{gq_j}(\frac{x}{z}) & P_{gg}(\frac{x}{z})\end{pmatrix}\begin{pmatrix} f_{q_j}(z,\mu_F) \\ f_g(z,\mu_F)\end{pmatrix}}\,, \tag{2.70}$$

an equation known as Dokshitzer-Gribov-Lipatov-Altarelli-Parisi (DGLAP) evolution equation. At the LO, the Altarelli-Parisi splitting functions P_{ij} read

DGLAP evolution equation

$$\begin{aligned}
P^{(0)}_{q_iq_j}(z) &= \delta_{ij} C_F \left(\left(\frac{1+z^2}{1-z}\right)_+ + \frac{3}{2}\delta(1-z)\right)\,, \\
P^{(0)}_{gq_i}(z) &= C_F\left(\frac{1+(1-z)^2}{z}\right)\,, \\
P^{(0)}_{q_ig}(z) &= \frac{1}{2}\left(z^2+(1-z)^2\right)\,, \\
P^{(0)}_{gg}(z) &= 2C_A\left(\left(\frac{z}{1-z}\right)_+ + (1-z)\left(z+\frac{1}{2}\right) + \frac{11C_A-2n_f}{6}\delta(1-z)\right)\,.
\end{aligned} \tag{2.71}$$

The splitting functions $P_{ij}(z)$ represent the probability that a parton j emits a parton i with a momentum fraction z, as we have seen in the DY example. In contrast, the x-dependence of the PDFs must be determined based on experimental data. The corresponding distributions for the light parton flavors are shown in Figure 2.8 for the PDF set `NNPDF40_nnlo_as_01180` [30]. The distributions of the valence quarks u and d show bumps around $x \sim 1/3$, as expected from the parton model. In contrast, the sea quarks $\bar{u}, \bar{d}$ and the gluon PDFs do not exhibit this bump and instead grow monotonously towards smaller x.

Altarelli-Parisi splitting functions

x-dependence of the PDFs

This concludes our discussion of the fixed-order predictions. We have demonstrated how the high-energy hard scatterings of partons are described by LO, NLO virtual and NLO real matrix elements, and how the divergences that appear therein are cancelled. In particular, we have delineated the framework of the subtraction formalism and demonstrated how the ISC divergences are absorbed into the PDFs, thereby factorizing the hard scattering from the low-energy proton physics.

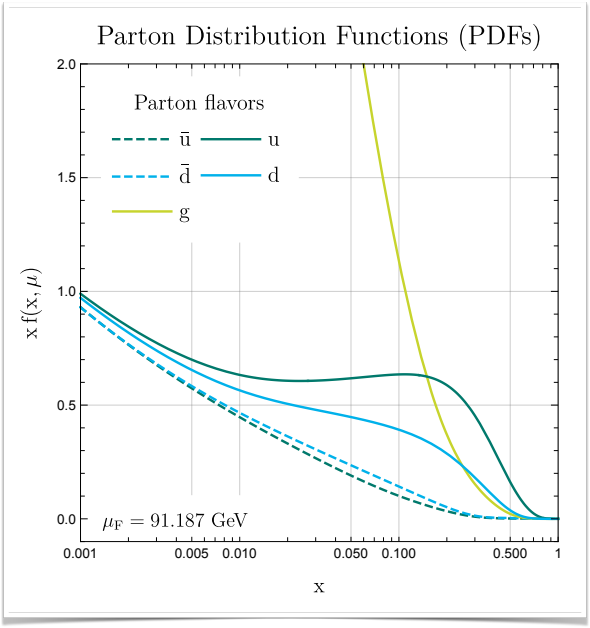

Figure 2.8: This plot illustrates the x-dependence of the parton distribution functions (PDFs) at a factorization scale $\mu_F = 91.187\,\text{GeV}$. The distributions are shown for the light parton flavors only. The data was derived from the PDF set `NNPDF40_nnlo_as_01180` [30], extracted using the `Mathematica` package `ManeParse` [31].

2.2 Parton Showers

This chapter draws upon the lecture notes on PS event generators in reference [17]. An extensive yet pedagogical introduction into the topic can be found there.

Thus far, we have described the hard scatterings of initial-state partons $p_{i,\oplus}(k_\oplus)$, $p_{j,\ominus}(k_\ominus)$ into final states $FJ^l(k_1,\ldots,k_n,k_{n+1},\ldots,k_{n+l})$ that include l additional partonic emissions. We have demonstrated how cross sections for such interactions can be calculated by combining real contributions with virtual ones that include up to l additional loops. However, the fixed-order description is only accurate in describing the physics that occurs at the high scale, $Q \gg \Lambda_{\text{QCD}}$. In order to include physics at lower scales, in particular the final-state particles that interact with the material of the LHC detectors, it is necessary to employ PSs to bridge the gap between the hard scale Q and Λ_{QCD}. In this chapter, we will elucidate the main concepts of PS generators.

A final-state parton produced in the hard scattering process and with an energy on the order of Q can undergo a splitting into two daughter partons, of the form $ab \to a\,b$ with $ab, a, b \in \{q, g\}$ (i.e. $q \to gq$, $g \to gg$ or $g \to q\bar{q}$). The daughter partons have lower energies, but may also subsequently split into two partons. And so on. The splitting process continues until the resulting partons have energies on the order of Λ_{QCD}, at which point the shower terminates and hadronization begins. The spray of particles produced in this manner is called a final-state shower. In a similar manner, the partons in the initial state of the hard scattering process may have

originated from a long sequence of initial-state splittings occurring at progressively higher energies, starting at the energy scale of the proton, Λ_{QCD}, and extending to the scale of Q. The corresponding spray of particles is called an initial-state shower. Both types of showers are depicted schematically in Figure 2.1.

It is evident that attempting to describe the large number of parton shower splittings in a full fixed-order prescription is unfeasible. Fortunately, the factorization of the real NLO matrix element in the soft and collinear limits, which we have observed in (2.64), (2.64), and which is shown schematically in Figure 2.7, allows us to describe the parton shower in an approximate manner. In (2.46), we have introduced a mapping $\overleftarrow{\boldsymbol{M}}(\boldsymbol{P}_{FJ})$ between an $(n+1)$-body parton configuration $\boldsymbol{P}_{FJ}$ and its underlying n-body configuration $\overleftarrow{\boldsymbol{P}}_F$ for singular regions α. PSs are based on an analogous mapping, but in the reverse direction. Given an n-body parton configuration $\boldsymbol{P}_F$, the parton shower selects possible singular regions α and corresponding $(n+1)$-body configurations of the form

The inverse map $\overrightarrow{\boldsymbol{M}} : \boldsymbol{P}_F \to \overrightarrow{\boldsymbol{P}}_{FJ}$

$$\overrightarrow{\boldsymbol{M}}^{(\alpha)}(\boldsymbol{P}_F) = \begin{cases} \boldsymbol{\Phi}_F \to \overrightarrow{\boldsymbol{\Phi}}_{FJ}^{(\alpha)} \mathrel{\widehat{=}} \left(\boldsymbol{\Phi}_F, \Phi_{\text{rad}}^{(\alpha)}\right) \\ \mathcal{F}_F = \{f_1, \ldots, ab, \ldots, f_n\} \to \overrightarrow{\mathcal{F}}_{FJ}^{(\alpha)} = \{f_1, \ldots, a, \ldots, f_n, b\} \end{cases}, \tag{2.72}$$

with $d\overrightarrow{\boldsymbol{\Phi}}_{FJ} = d\boldsymbol{\Phi}_F\, d\Phi_{\text{rad}}$ and where $ab \to a\,b$ is the splitting associated with α. In this case, several splittings are possible for a given emitter parton, which must be chosen on a statistical basis using MC methods. Consequently, each α is associated with a specific flavor choice, which we again collect together with the momenta as $\overrightarrow{\boldsymbol{P}}_{FJ} = (\overrightarrow{\boldsymbol{\Phi}}_{FJ}, \overrightarrow{\mathcal{F}}_{FJ})$.

The one-particle emission phase-space

The one-particle emission phase-space, $d\Phi_{\text{rad}}$, can be described in terms of three variables: the evolution variable t, the splitting variable z and an azimuthal angle ϕ, i.e.

$$d\Phi_{\text{rad}}^{(\alpha)} = \frac{1}{16\pi^2}\, dt^{(\alpha)}\, dz^{(\alpha)}\, \frac{d\phi^{(\alpha)}}{2\pi}\, \mathcal{J}(t^{(\alpha)}, z^{(\alpha)}, \phi^{(\alpha)})\,, \tag{2.73}$$

where $\mathcal{J}$ is the Jacobian factor associated with the variable transformation. We have previously encountered z, which represents the momentum fraction after radiation in the collinear limit. There exist various formally equivalent definitions for t in the literature. For the most well-known PS generator systems `Pythia` [32, 33], `Herwig` [34, 35] and `Sherpa` [36, 37], these include the energy-weighted emission angle (`Herwig`), the virtuality (early versions of `Pythia` and `Sherpa`) or the transverse momentum (current versions of `Pythia` and `Sherpa`). In the following, we do not specify t precisely, but assume that it has the dimensions of an energy squared and can be related to the transverse momentum of the radiated parton. Let us now recall the real counterterms $\mathcal{C}$ that we introduced in Subchapter 2.1.1 in order to cancel the IR divergences. The $\mathcal{C}$ model the behavior of the full real matrix element R in the singular regions α, where, as previously demonstrated, R decomposes into the Born matrix element B and a *universal* splitting function. The latter can be uncovered by writing

$$\begin{aligned} \int d\overrightarrow{\boldsymbol{\Phi}}_{FJ}^{(\alpha)}\, R\left(\overrightarrow{\boldsymbol{P}}_{FJ}^{(\alpha)}\right) \mathcal{O}\left(\overrightarrow{\boldsymbol{P}}_{FJ}^{(\alpha)}\right) &\simeq \int d\overrightarrow{\boldsymbol{\Phi}}_{FJ}^{(\alpha)}\, C^{(\alpha)}\left(\overrightarrow{\boldsymbol{P}}_{FJ}^{(\alpha)}\right) \mathcal{O}\left(\overrightarrow{\boldsymbol{P}}_{FJ}^{(\alpha)}\right) \\ &= \int d\boldsymbol{\Phi}_F\, B(\boldsymbol{P}_F) \times \int d\Phi_{\text{rad}}^{(\alpha)}\, \frac{C^{(\alpha)}\left(\overrightarrow{\boldsymbol{P}}_{FJ}^{(\alpha)}\right)}{B(\boldsymbol{P}_F)}\, \mathcal{O}\left(\overrightarrow{\boldsymbol{P}}_{FJ}^{(\alpha)}\right) \end{aligned} \tag{2.74}$$

for a given singular region α. A concrete example for (2.74) is

$$\int d\Phi_{\text{rad}}^{(\alpha)} \frac{C^{(\alpha)}\left(\vec{\boldsymbol{P}}_{FJ}^{(\alpha)}\right)}{B(\boldsymbol{P}_F)} = \int dt^{(\alpha)} \int dz^{(\alpha)} \, \frac{1}{2k_1k_2} \frac{\alpha_s}{2\pi} P_{ab\,b}^{(0)}\left(z^{(\alpha)}\right) , \tag{2.75}$$

taking the collinear limit and averaging over the helicities for an $ab(k) \to a(k_1)b(k_2)$ splitting, where $P_{ab\,b}^{(0)}$ are the Altarelli-Parisi splitting functions from (2.71). In order to construct the complete PS in successive collinear limits, it is possible to simply iterate (2.74), multiplying more and more emission factors. However, this approach would result in a violation of unitarity, as each integral contributes positively to the total cross section. This issue can be resolved by introducing the *Sudakov form factor*, which provides the approximate virtual corrections that cancel the real corrections computed above and allows the removal of all real emissions below a certain scale $t_c \sim \Lambda_{\text{QCD}}$. It is of the form

The Sudakov form factor

$$\Pi_F^{(\alpha)}(t_{i+1}, t_i) \equiv \exp\left[- \int_{t_{i+1}}^{t_i} d\Phi_{\text{rad}}^{(\alpha)} \frac{C_{FJ}^{(\alpha)}\left(\vec{\boldsymbol{P}}_{FJ}^{(\alpha)}\right)}{B_F(\boldsymbol{P}_F)} \right] , \tag{2.76}$$

for a splitting associated with the singular region α. The total Sudakov form factor is given by the product $\Pi_F(t_{i+1}, t_i) = \prod_\alpha \Pi_F^{(\alpha)}(t_{i+1}, t_i)$ and represents the probability for no parton branching to occur in the evolution from t_i to t_{i+1}. We can now formulate the PS evolution in terms of a generating functional $\mathbf{PS}_F(t, \boldsymbol{P}_F)$, which allows the expectation value of an observable $\mathcal{O}$ to be computed as

$$\langle \mathcal{O} \rangle_{\text{PS}} = \int d\boldsymbol{\Phi}_F \, B_F(\boldsymbol{P}_F) \, \mathbf{PS}_F(t_0, \boldsymbol{P}_F) \, . \tag{2.77}$$

The starting scale $t_0 \simeq Q^2$ of the PS is on the order of the hard scattering scale Q. The generating functional is defined recursively via

Recursive definition of the PS generating functional

$$\begin{aligned} \mathbf{PS}_F(t_i, \boldsymbol{P}_F) = & \underbrace{\Pi_F\left(t_c, t_i\right) \mathcal{O}\left(\boldsymbol{\Phi}_F\right)}_{\text{virtual + unresolved}} \\ & + \underbrace{\sum_\alpha \int_{t_c}^{t_i} d\Phi_{\text{rad}}^{(\alpha)} \, \frac{C_{FJ}^{(\alpha)}\left(\vec{\boldsymbol{P}}_{FJ}^{(\alpha)}\right)}{B_F(\boldsymbol{P}_F)} \Pi_F(t^{(\alpha)}, t_i) \times \mathbf{PS}_{FJ}\left(t^{(\alpha)}, \vec{\boldsymbol{P}}_{FJ}^{(\alpha)}\right)}_{\text{resolved}} . \end{aligned} \tag{2.78}$$

Expressed in words, it means that there are two possible outcomes in the evolution from t_i to lower scales: The first, represented by the first term in (2.78), is that there is no emission from t_i all the way to $t_c \sim \Lambda_{\text{QCD}}$, where the shower terminates and hadronization begins. This encompasses the virtual and unresolved contributions necessary to restore unitarity. The second, represented by the second term in (2.78), posits that another emission occurs at $t_c < t < t_i$, with no emissions in between. Then, the evolution must be repeated with $t_{i+1} = t$ as the initial scale. In this manner, emission by emission, the PS is built up from Q all the way to Λ_{QCD}.

2.2.1 *Resummation*

This subchapter draws upon [38], which offers a more comprehensive presentation of the subject.

Thus far, we have frequently expanded observables as a perturbative series in the coupling constant (see e.g. (2.8)). However, in full generality, the expansion is more complicated, as contributions with an increasing number of loops are accompanied by an increasing number of powers of logarithms. The virtual NLO contribution to $pp \to \tau^+\tau^-$ in (2.23), for example, included two powers of L_μ. In general, an observable $d\sigma$ can be expanded as

Large logarithms

$$d\sigma = \mathcal{O}(1) + \mathcal{O}(\alpha_s)\left(L^2 + L + 1\right) + \mathcal{O}(\alpha_s^2)\left(L^4 + L^3 + L^2 + L + 1\right) + \dots , \quad (2.79)$$

where $L = \log(r)$ are logarithms. The leading logarithmic contributions at each order, i.e. those with the highest exponent (the *Sudakov* logarithms), correspond to the case where all emissions are simultaneously soft and collinear to their parent particles. The form of r is contingent upon the quantity $d\sigma$ under consideration. For $d\sigma(pp \to ZJ^l)/dp_{T,Z}$, for example, r is of the form $m_Z/p_{T,Z}$. If the spectrum is considered at small $p_{T,Z}$, r and L both grow large, which may spoil the convergence of the series in α_s. In such instances, it is necessary to perform an all-order summation of the large logarithms, *resummation* in short. This corresponds to transforming $d\sigma$ into the form

Resummed differential distributions

$$d\sigma_{\text{res}} = D(\alpha_s)\exp\left[Lg_1(\alpha_s L) + g_2(\alpha_s L) + \alpha_s g_3(\alpha_s L) + \dots\right] + R_f(\alpha_s)\,, \quad (2.80)$$

where $D(\alpha_s)$ and $R_f(\alpha_s)$ are free of logarithms. In a manner analogous to the theoretical accuracy specified for the perturbative series expansion in terms of the powers of the coupling constant involved (i.e. LO, NLO, etc.), the theoretical accuracy of resummed results is reported in terms of the powers of the logarithms. Including g_1 in (2.80) corresponds to the leading logarithmic (LL) approximation, g_2 to the next-to-leading logarithmic (NLL) approximation, and so on.

LL accuracy of PS generators

With (2.74) accurately describing the parton emission in the limit where it is both soft and collinear, the Sudakov form factor of PSs corresponds to the LL resummation of the corresponding observables. Consequently, PSs not only contribute the additional splittings in the evolution from Q to Λ_{QCD}, but also enhance the convergence of the perturbative series by resumming the LL contributions in the expansion (2.79).

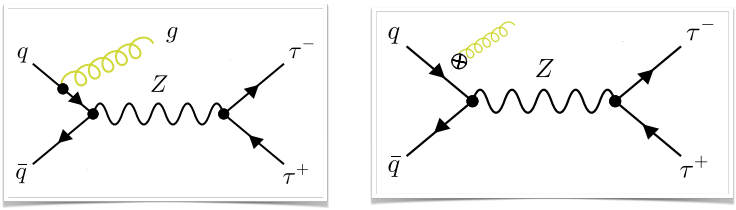

(a) Full NLO diagram (b) LO+PS approximation

Figure 2.9: Schematic depiction of the overcounting of real emissions in a naive NLO+PS combination for $pp \to \tau^+\tau^-$. The full NLO real diagram in (a) includes the emission of an additional gluon, while the LO+PS contribution in (b) contains similar emissions in their approximated limits. If a phase space overlap between the two contributions exists, the gluon emission probability is overcounted.

2.3 Going to NLO+PS: The POWHEG method

In Chapters 2.1 and 2.2 we have discussed the theoretical framework underlying the description of hard parton scatterings at fixed order, including the incorporation of QCD corrections. Furthermore, we have demonstrated the potential of PS generators in modelling the branchings of partonic final-state particles into high-multiplicity jets. Ideally, the two prescriptions should work hand-in-hand. This is not straightforward to achieve, however, as a naive combination of NLO fixed-order results with the PS leads to an overcounting of real emission contributions. This is illustrated schematically in Figure 2.9, once more using the DY $pp \to \tau^+\tau^-$ process as an example. While the full NLO real matrix element (Figure 2.9a) includes the emission of additional partons, such emissions are also approximated by the PS applied to the LO matrix element (Figure 2.9b). A naive NLO+PS implementation thus results in an overcounting (or undercounting) of soft-collinear parton emissions.

Overcounting of soft-collinear emissions

In order to improve on this, let us first recall the LO+PS expression from (2.77). Up to one parton emission, the expectation value of an observable $\mathcal{O}$ is given by

$$\begin{aligned}\langle \mathcal{O} \rangle_{\text{LO+PS}} = \int d\mathbf{\Phi}_F \, B(\boldsymbol{P}_F) \Bigg[&\Pi_F \left(t_c, t_0\right) \mathcal{O}\left(\mathbf{\Phi}_F\right) \\ &+ \sum_\alpha \int_{t_c}^{t_0} d\Phi_{\text{rad}}^{(\alpha)} \frac{C^{(\alpha)}\left(\vec{\boldsymbol{P}}_{FJ}^{(\alpha)}\right)}{B(\boldsymbol{P}_F)} \Pi_F\left(t_c, t^{(\alpha)}\right) \mathcal{O}\left(\vec{\mathbf{\Phi}}_{FJ}^{(\alpha)}\right) \Bigg] .\end{aligned} \tag{2.81}$$

The POWHEG method (short for positive weight hardest emission generator) allows for the extension of (2.81) to the NLO+PS accuracy. To this end, two important concepts are introduced: the POWHEG $\bar{B}$ function and the POWHEG Sudakov form factor Δ_{pwg}. For the former, we reorganize the terms in the NLO subtraction scheme formula from (2.55). Instead of integrating over $d\mathbf{\Phi}_{FJ}$ and using $\bar{M}$ from (2.46) to connect to the underlying n-body configuration, we may begin with an n-body configuration and use the inverse $\vec{M}$ from (2.72) to reach the corresponding singular $(n+1)$-body configurations. For this we decompose

$$R(\boldsymbol{P}_{FJ}) = \sum_\alpha R^{(\alpha)}(\boldsymbol{P}_{FJ}) , \quad G_{\circledast}(\boldsymbol{P}_{F,\circledast}) = \sum_{\alpha_{\circledast}} G_{\circledast}^{(\alpha_{\circledast})}(\boldsymbol{P}_{F,\circledast}) , \tag{2.82}$$

It should be noted that R may also contain non-singular pieces R_f that are not associated with any α. By definition, these can be integrated over in four dimensions directly. We will therefore not consider these contributions further.

The $\bar{B}$ function

into the pieces associated with a given singular region α. We now define $\bar{B}$ as

$$\boxed{\begin{aligned}\bar{B}(\boldsymbol{P}_F) \equiv\ & B(\boldsymbol{P}_F) + V(\boldsymbol{P}_F) \\ & + \sum_\alpha \int d\Phi_{\text{rad}}^{(\alpha)} \left(R^{(\alpha)}\left(\vec{\boldsymbol{P}}_{FJ}^{(\alpha)}\right) - C^{(\alpha)}\left(\vec{\boldsymbol{P}}_{FJ}^{(\alpha)}\right)\right) \\ & + \sum_{\alpha_\oplus} \int \frac{dz}{z} G_\oplus^{(\alpha_\oplus)}\left(\{\boldsymbol{P}_F, z\}\right) + \sum_{\alpha_\ominus} \int \frac{dz}{z} G_\ominus^{(\alpha_\ominus)}\left(\{\boldsymbol{P}_F, z\}\right) .\end{aligned}} \tag{2.83}$$

The POWHEG Sudakov form factor Δ_{pwg}

The Sudakov form factor Δ_{pwg} is defined as

$$\boxed{\Delta_{\text{pwg}}(\boldsymbol{P}_F, p_{T,\text{pwg}}) \equiv \exp\left[- \sum_\alpha \int d\Phi_{\text{rad}}^{(\alpha)} \frac{R^{(\alpha)}\left(\vec{\boldsymbol{P}}_{FJ}^{(\alpha)}\right) \theta\left(q_{T,\text{rad}}^{(\alpha)} - p_{T,\text{pwg}}\right)}{B(\boldsymbol{P}_F)} \right] ,} \tag{2.84}$$

where $q_{T,\text{rad}}$ is a function of the $(n+1)$-body kinematics $\vec{\boldsymbol{\Phi}}_{FJ}$ and is related to the transverse momentum of the radiated parton. As for the PS, the Sudakov form factor Δ_{pwg} can be interpreted as the probability that no parton is radiated with a transverse momentum greater than $p_{T,\text{pwg}}$. In the POWHEG method, the expectation value for an IR-safe observable $\mathcal{O}$, including up to one additional parton emission,

The POWHEG master formula

then reads

$$\boxed{\begin{aligned}\langle \mathcal{O} \rangle_{\text{NLO}} = \int d\boldsymbol{\Phi}_F \bar{B}(\boldsymbol{P}_F) \Bigg[& \Delta_{\text{pwg}}(\boldsymbol{P}_F, p_{T,\text{pwg}}) \mathcal{O}(\boldsymbol{\Phi}_F) \\ & + \sum_\alpha \int_{p_{T,\text{pwg}}} d\Phi_{\text{rad}}^{(\alpha)} \frac{R^{(\alpha)}\left(\vec{\boldsymbol{P}}_{FJ}^{(\alpha)}\right)}{B(\boldsymbol{P}_F)} \Delta_{\text{pwg}}\left(\boldsymbol{P}_F, q_{T,\text{rad}}^{(\alpha)}\right) \mathcal{O}\left(\vec{\boldsymbol{\Phi}}_{FJ}^{(\alpha)}\right) \Bigg] .\end{aligned}} \tag{2.85}$$

A shorthand notation has been introduced, with the lower integration limit $p_{T,\text{pwg}}$ referring to the theta function in (2.84). Note the similarity with (2.81), but also that (2.85) includes the full information on the real matrix element R. Indeed, the POWHEG method models the hardest emission above $p_{T,\text{pwg}}$ at full NLO accuracy in the all-order emission probability of (2.85). Subsequent radiations below the scale of the hard emission $q_{T,\text{rad}}$ are supplied by the PS, using $q_{T,\text{rad}}$ as the starting scale. This necessitates that the PS is p_T-ordered, i.e. that the hard emission scale $q_{T,\text{rad}}$ is compatible with the evolution variable t. If this is the case, the overcounting from Figure 2.9 is avoided: POWHEG uses the full NLO matrix elements to simulate the hardest emission, the PS is used exclusively for the subsequent emissions below. Note that the expression with the all-order Sudakov form factor of the POWHEG method is equivalent to the usual NLO prescription given in (2.55) at $\mathcal{O}(\alpha_s)$.

Although Pythia is p_T-ordered, its definition of relative transverse momentum differs from the one of POWHEG. Consequently, a shower veto should be employed (see [39] and the example main31 of Pythia).

Finally, we note that POWHEG is not the only method that allows for a consistent matching of fixed-order NLO matrix elements with PS generators. The same feat is achieved by the MC@NLO method [40], which avoids overcounting by subtracting from the exact NLO cross section its approximation. This generally results in more negatively weighted events than with the POWHEG method, since the exact NLO expression minus the PS subtraction terms need not be positive.

3

GOING BEYOND THE SM

Host: *The Higgs particle was celebrated world-wide back then. As explanation for mass itself. It seemed like we actually explained something really fundamental.*
John Ellis: *Yeah, we did.*
Host: *But all is not well, John!*

— Panel discussion *The future of particle physics* [41]

This section introduces three significant BSM scenarios that, if realized in nature, would result in discernible signals at the LHC. These scenarios are based on two main approaches to BSM physics: the first, the effective field theory (EFT) approach, is to assume that the SM is the correct theory up to energy scales much higher than those currently accessible at the LHC. Then, the SM Lagrangian is equivalent to the lowest-dimensional terms in a tower of higher-dimensional terms that result from the complete UV model. These higher-dimensional terms induce small indirect signals in SM precision observables that can be investigated at the LHC. The EFT approach is agnostic regarding the specific UV model, thereby providing an ideal framework for interpreting and comparing SM precision measurements in a BSM context. In Chapter 3.1, we introduce the SMEFT as an example of the EFT approach. This will be the main theory discussed in part (I).

The EFT approach

The second approach is to assume that there is BSM physics at or below the TeV scale and to construct complete UV models. These can either involve extended symmetries of the SM or an enlargement of its particle content. In Chapter 3.2, we discuss the 4321 model as an example of the former. It extends the gauge group of the SM in a flavor non-universal way, serving as an example both for an extension of the SM symmetries and an exotic bottom-philic scenario where the BSM sector is mainly coupled to the third fermion family. In Chapter 3.3, we introduce the 2HDM as an example for models with an enlargement of the SM particle spectrum. The extended scalar sector of the 2HDM can further be linked to DM via mixing with a pseudoscalar DM mediator, which results in the 2HDM+a. Both the 4321 and the 2HDM+a will be discussed in further detail in part (II).

Complete UV models

3.1 The SM Effective Field Theory

This chapter draws upon [42], which presents a comprehensive and lucid review of the SMEFT.

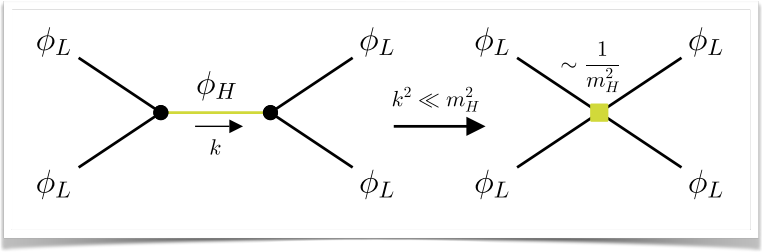

Figure 3.1: For momenta $k^2 \sim m_L \ll m_H$, the heavy field ϕ_H is no longer a dynamical degree of freedom. Interactions where ϕ_H is exchanged turn into local contact interactions involving only the light fields ϕ_L.

3.1.1 *The Philosophy of EFTs (top-down)*

The SMEFT applies the ideas of quantum EFTs to high-scale BSM extensions of the SM. In general, EFTs are employed when the masses m_L, m_H of two fields ϕ_L, ϕ_H differ significantly, we will assume $m_L \ll m_H$. At energies $Q \sim m_L$ (Q being the characteristic energy of a given process), the fields ϕ_H are too heavy to be produced resonantly and therefore cease to constitute dynamical degrees of freedom. The propagators of the heavy fields are replaced by

Contraction of heavy-field propagators

$$\frac{1}{k^2 - m_H^2} \simeq -\frac{1}{m_H^2} + \mathcal{O}\left(\frac{k^2}{m_H^2}\right), \tag{3.1}$$

in the case $k^2 \sim Q^2 \sim m_L^2 \ll m_H^2$. Consequently, interactions where the heavy field ϕ_H is exchanged are transformed into local higher-dimensional contact interactions among the light fields ϕ_L. This is illustrated schematically in Figure 3.1.

The contraction of the heavy field propagators can be formulated rigorously using the path integral formalism. Starting from the generating functional for the full theory

$$Z[J_L] = \int \mathcal{D}\phi_H \mathcal{D}\phi_L \exp\left[\int dx^4 \left(\mathcal{L}(\phi_L, \phi_H) + \phi_L J_L\right)\right] \tag{3.2}$$

(we only couple the sources J_L to the light fields, as we are only interested in Green's functions involving the ϕ_L), we *integrate out* the heavy fields ϕ_H. This results in

$$Z[J_L] = \int \mathcal{D}\phi_L \exp\left[\int dx^4 \left(\mathcal{L}_{\text{EFT}}(\phi_L) + \phi_L J_L\right)\right], \tag{3.3}$$

where $\mathcal{L}_{\text{EFT}}$ contains a renormalizeable part and a tower of higher-dimensional operators

$$\mathcal{L}_{\text{EFT}} = \mathcal{L}_{d\leq 4} + \sum_{d=5}^{\infty} \frac{1}{m_H^{d-4}} \sum_{i=1}^{n_d} C_i^{(d)} \mathcal{O}_i^{(d)}. \tag{3.4}$$

Tower of higher-dimensional EFT operators

In this context, d specifies the mass dimension, the Lagrangian $\mathcal{L}_{d\leq 4}$ contains the renormalizable terms, the $\mathcal{O}_i^{(d)}$ are higher-dimensional local operators involving the light fields ϕ_L, the $C_i^{(d)}$ are prefactors (referred to as *Wilson coefficients*), and n_d counts the number of independent operators at a given mass dimension d. In principle, in order to calculate Green's functions for the light fields ϕ_L, all terms in (3.4)

have to be included. This results in a non-renormalizable theory, as evidenced by the necessity of an infinite tower of higher-dimensional counterterms to render the theory finite. For example, two insertions of the dimension-five operators require a counterterm of dimension six to cancel the divergences, while two insertions of dimension-six operators require a counterterm of dimension eight, and so on. However, when considering processes occurring at a given energy scale Q, the operators $\mathcal{O}_i^d$ pick up a factor Q^{d-4}, meaning that their contributions scale as $(Q/m_H)^{d-4}$. As long as $Q \ll m_H$, we can truncate the series in (3.4) at a certain $d_{\max}$. In phenomenological SMEFT applications, this is typically $d_{\max} = 6$. This approach allows the theory to be renormalized systematically, with contributions beyond $d_{\max}$ being neclected.

Renormalizability of the truncated SMEFT series

3.1.2 *The Philosophy of EFTs (bottom-up)*

Thus far, we have taken a *top-down* perspective on EFTs. If the full UV field theory is known, one can construct a corresponding low-energy EFT by integrating out the heavy modes ϕ_H. However, EFTs can also be applied from the *bottom up*. It is possible to assume that the SM is extended by a more complete BSM theory at energy scales much higher than those currently attainable in experiments, without knowing the exact details of this UV theory. In such a scenario, after integrating out the heavy modes, the effective Lagrangian $\mathcal{L}_{\text{SMEFT}}$ is necessarily of the form (3.4) with $\mathcal{L}_{d\leq 4} = \mathcal{L}_{\text{SM}}$. Here, the $\mathcal{O}_i^{(d)}$ are composed of the SM fields ϕ_{SM} and conserve the symmetries of the SM. In concrete terms,

The SMEFT Lagrangian

$$\mathcal{L}_{\text{SMEFT}} = \mathcal{L}_{\text{SM}} + \sum_{i=1}^{n_5} \frac{C_i^{(5)}\mathcal{O}_i^{(5)}}{\Lambda} + \sum_{i=1}^{n_6} \frac{C_i^{(6)}\mathcal{O}_i^{(6)}}{\Lambda^2} + \mathcal{O}\left(\frac{1}{\Lambda^3}\right), \tag{3.5}$$

where we have denoted the scale of the first layer of BSM physics by Λ. The $\mathcal{O}_i^{(d)}$ include all local higher-dimensional operators that are permitted by symmetry considerations. The symmetries of the SM include Lorentz invariance, the SM gauge symmetry, and potentially the global lepton and baryon number symmetries. The latter two may be fundamental symmetries of the BSM theory, instead of just arising accidentally at lower energies.

The task of writing down a basis of operators $\mathcal{O}_i^{(d)}$ of a given mass dimension d that are allowed by the SM symmetries is non-trivial. There are many redundancies among different operators, in the sense that they induce exactly the same contributions to all physical observables. In order to arrive at a minimal set of operators, it is necessary to eliminate such redundancies. This is done using the following techniques:

The elimination of redundant operators

- **Integration by parts (IBP) identities:** Assuming that all fields vanish at infinity, the IBP identity can be applied to relate different operators. For example, the operators $(D_\mu H)^\dagger (D^\mu H)$ and $-H^\dagger D^2 H$ are equivalent.

  IBP relations

- **Field redefinitions (and equations of motion):** One can show that field redefinitions of the form

  Field redefinition relations

$$\phi \to \tilde{\phi}(\phi) = \phi + \epsilon F(\phi), \tag{3.6}$$

applied to the action $S[\phi] \to S[\tilde{\phi}(\phi)]$, leave the S-matrix invariant and therefore do not change physical observables. Here, $F(\phi)$ is an analytic function (and may in general not just depend on ϕ, but other SM fields as well) multiplied by a small expansion parameter $\epsilon \ll 1$. In the context of the SMEFT, the expansion parameter is typically a power of (Q/Λ). A special case of field redefinitions is $\phi \to \tilde{\phi} = \phi + \epsilon\delta\phi$, resulting in

$$\begin{aligned} S[\phi] \to S[\tilde{\phi}] &= S[\tilde{\phi}]|_{\tilde{\phi}=\phi} + \epsilon \left.\frac{\delta S[\tilde{\phi}]}{\delta\tilde{\phi}}\right|_{\tilde{\phi}=\phi} + \mathcal{O}(\epsilon^2) \\ &= S[\phi] + \epsilon \int d^4x\, E[\phi]\delta\phi + \mathcal{O}(\epsilon^2)\,, \end{aligned} \tag{3.7}$$

Equations of motion relations

where $E[\phi] = (\delta\mathcal{L}[\tilde{\phi}]/\delta\tilde{\phi})|_{\tilde{\phi}=\phi}$ are the equations of motion for the field ϕ. Consequently, to leading order in ϵ, one may use the equations of motion of the SM to relate effective operators giving the same contribution to the S-matrix. The SM equations of motion are listed in [43, (2.8)-(2.12)].

Fierz indentities

- **Fierz identities:** The Fierz identities follow from completeness relations. For the Lorentz group, they read

$$\begin{aligned} (P_A)_{ij} \otimes (P_A)_{kl} &= \frac{1}{2}(P_A)_{il} \otimes (P_A)_{kj} + \frac{1}{8}(\sigma^{\mu\nu}P_A)_{il} \otimes (\sigma_{\mu\nu}P_A)_{kj}\,, \\ (P_A)_{ij} \otimes (P_B)_{kl} &= \frac{1}{2}(\gamma^\mu P_B)_{il} \otimes (\gamma_\mu P_A)_{kj}\,, \\ (\gamma^\mu P_A)_{ij} \otimes (\gamma_\mu P_A)_{kl} &= -(\gamma^\mu P_A)_{il} \otimes (\gamma_\mu P_A)_{kj}\,, \\ (\gamma^\mu P_A)_{ij} \otimes (\gamma_\mu P_B)_{kl} &= 2(P_B)_{il} \otimes (P_A)_{kj}\,, \\ (\sigma^{\mu\nu}P_A)_{ij} \otimes (\sigma_{\mu\nu}P_A)_{kl} &= 6(P_A)_{il} \otimes (P_A)_{kj} - \frac{1}{2}(\sigma^{\mu\nu}P_A)_{il} \otimes (\sigma_{\mu\nu}P_A)_{kj}\,, \\ (\sigma^{\mu\nu}P_A)_{ij} \otimes (\sigma_{\mu\nu}P_B)_{kl} &= 0\,, \end{aligned} \tag{3.8}$$

where $A, B \in \{L, R\}$ with $A \neq B$, and $\sigma^{\mu\nu} = \frac{i}{2}[\gamma^\mu, \gamma^\nu]$. In (3.8), we have not included minus signs that arise from the anticommutation of fermion fields. These must be included in the case of Fierz relations among SMEFT operators. Furthermore, (3.8) only holds in four spacetime dimensions. When expressions are evaluated in general d dimensions, as is the case in dimensional regularization discussed below (2.12), the equations in (3.8) no longer hold. The application of these identities leads to the introduction of *evanescent operators*, which are operators that scale as $(d-4)$ and vanish in four spacetime dimensions. However, they can still induce non-vanishing contributions. We will discuss them in more detail in Subchapters 3.1.3 and 4.1.2. An analogous Fierz identity also exists for $SU(N)$ groups

Evanescent operators

$$(T^a)_{ij} \otimes (T^a)_{kl} = \frac{1}{2}\left(\mathbb{1}_{il} \otimes \mathbb{1}_{kj} - \frac{1}{N}\mathbb{1}_{ij} \otimes \mathbb{1}_{kl}\right)\,, \tag{3.9}$$

where the T^a are the generators of the fundamental representation.

- **Dirac structure reduction:** In four spacetime dimensions, the structures that appear in (3.8) serve as a basis for the Dirac algebra. More complex structures can be reduced to simpler forms by means of the identities [44]

Dirac structure reduction

$$\begin{aligned}
\gamma^\mu\gamma^\nu P_A \otimes \gamma_\mu\gamma_\nu P_A &= (4-2\epsilon) P_A \otimes P_A - \sigma^{\mu\nu} P_A \otimes \sigma_{\mu\nu} P_A \,, \\
\gamma^\mu\gamma^\nu P_A \otimes \gamma_\mu\gamma_\nu P_B &= 4(1+a_{\text{ev}}\epsilon) P_A \otimes P_B + E^{(2)}_{AB} \,, \\
\gamma^\mu\gamma^\nu\gamma^\rho P_A \otimes \gamma_\mu\gamma_\nu\gamma_\rho P_A &= 4(4+b_{\text{ev}}\epsilon)\gamma^\mu P_A \otimes \gamma_\mu P_A + E^{(3)}_{AA} \,, \\
\gamma^\mu\gamma^\nu\gamma^\rho P_A \otimes \gamma_\mu\gamma_\nu\gamma_\rho P_B &= 4(1+c_{\text{ev}}\epsilon)\gamma^\mu P_A \otimes \gamma_\mu P_B + E^{(3)}_{AB} \,, \\
\gamma^\mu\gamma^\nu\gamma^\rho\gamma^\lambda P_A \otimes \gamma_\mu\gamma_\nu\gamma_\rho\gamma_\lambda P_A &= 32(2+d_{\text{ev}}\epsilon) P_A \otimes P_A \\
&\quad - 8(2+e_{\text{ev}}\epsilon)\sigma^{\mu\nu} P_A \otimes \sigma_{\mu\nu} P_A + E^{(4)}_{AA} \,, \\
\gamma^\mu\gamma^\nu\gamma^\rho\gamma^\lambda P_A \otimes \gamma_\mu\gamma_\nu\gamma_\rho\gamma_\lambda P_B &= 16(1+f_{\text{ev}}\epsilon) P_A \otimes P_B + E^{(4)}_{AB} \,,
\end{aligned} \tag{3.10}$$

where once more $A, B \in \{L, R\}$ with $A \neq B$. In (3.10), we have added terms in light gray that vanish identically in four spacetime dimensions. In d dimensions, however, the reduction of Dirac structures is more complex. In fact, the d-dimensional Dirac algebra is no longer closed, and a basis of four-quark operators contains an infinite number of elements. These can be written as antisymmetric products of gamma matrices [45], specifically

$$\gamma^{[\mu_1}\gamma^{\mu_2}\dots\gamma^{\mu_n]} \otimes \gamma_{[\mu_1}\gamma_{\mu_2}\dots\gamma_{\mu_n]} \,, \tag{3.11}$$

for all $n \in \mathbb{N}$. Nevertheless, we may still use (3.10) in loop calculations, provided we consistently include the terms in green. The operators E are evanescent and vanish in four spacetime dimensions. When the Dirac structures on the left-hand side (l.h.s) of (3.10) are replaced by those on the r.h.s, it is necessary to consider the contributions from the corresponding E. For practical purposes, they can be defined as

Evanescent operators arising in Dirac structure reductions

$$\begin{aligned}
E^{(2)}_{AB} &\equiv \gamma^\mu\gamma^\nu P_A \otimes \gamma_\mu\gamma_\nu P_B - 4(1+a_{\text{ev}}\epsilon) P_A \otimes P_B \,, \\
&\dots \\
E^{(4)}_{AB} &\equiv \gamma^\mu\gamma^\nu\gamma^\rho\gamma^\lambda P_A \otimes \gamma_\mu\gamma_\nu\gamma_\rho\gamma_\lambda P_B - 16(1+f_{\text{ev}}\epsilon) P_A \otimes P_B \,.
\end{aligned} \tag{3.12}$$

There is some freedom in defining the $\mathcal{O}(\epsilon)$ terms, and different definitions exist in the literature. We chose to introduce general coefficients $a_{\text{ev}}, \dots, f_{\text{ev}}$ in (3.10), fixing them corresponds to a scheme choice. Consequently, whenever results including evanescent contributions are reported, it is necessary to specify the $a_{\text{ev}}, \dots, f_{\text{ev}}$. It is only when the Wilson coefficients are combined with the matrix elements induced by the SMEFT operators in a consistent manner that the scheme dependence will drop out. A more detailed discussion of the inclusion of evanescent operators in Dirac structure reductions will be presented in Subchapter 4.1.2.

Bosonic operators			
X^3		H^6 and H^4D^2	
$\mathcal{O}_G$	$f^{abc}\, G^{a,\nu}_{\mu} G^{b,\rho}_{\nu} G^{c,\mu}_{\rho}$	$\mathcal{O}_H$	$(H^\dagger H)^3$
$\mathcal{O}_{\tilde{G}}$	$f^{abc}\, \tilde{G}^{a,\nu}_{\mu} G^{b,\rho}_{\nu} G^{c,\mu}_{\rho}$	$\mathcal{O}_{H\Box}$	$(H^\dagger H)\Box(H^\dagger H)$
$\mathcal{O}_W$	$\epsilon^{IJK}\, W^{I,\nu}_{\mu} W^{J,\rho}_{\nu} W^{K,\mu}_{\rho}$	$\mathcal{O}_{HD}$	$(H^\dagger D_\mu H)^*(H^\dagger D^\mu H)$
$\mathcal{O}_{\tilde{W}}$	$\epsilon^{IJK}\, \tilde{W}^{I,\nu}_{\mu} W^{J,\rho}_{\nu} W^{K,\mu}_{\rho}$		
X^2H^2			
$\mathcal{O}_{HG}$	$(H^\dagger H) G^a_{\mu\nu} G^{a,\mu\nu}$	$\mathcal{O}_{HB}$	$(H^\dagger H) B_{\mu\nu} B^{\mu\nu}$
$\mathcal{O}_{H\tilde{G}}$	$(H^\dagger H) \tilde{G}^a_{\mu\nu} G^{a,\mu\nu}$	$\mathcal{O}_{H\tilde{B}}$	$(H^\dagger H) \tilde{B}_{\mu\nu} B^{\mu\nu}$
$\mathcal{O}_{HW}$	$(H^\dagger H) W^I_{\mu\nu} W^{I,\mu\nu}$	$\mathcal{O}_{HWB}$	$(H^\dagger \tau^I H) W^I_{\mu\nu} B^{\mu\nu}$
$\mathcal{O}_{H\tilde{W}}$	$(H^\dagger H) \tilde{W}^I_{\mu\nu} W^{I,\mu\nu}$	$\mathcal{O}_{H\tilde{W}B}$	$(H^\dagger \tau^I H) \tilde{W}^I_{\mu\nu} B^{\mu\nu}$

Table 3.1: Bosonic dimension-six operators $\mathcal{O}_i^{(6)}$ in the Warsaw SMEFT basis. See main text for further details.

3.1.3 *The Warsaw Basis*

The SM symmetry considerations and the aforementioned techniques have been employed to eliminate redundancies among different operators, thereby enabling the construction of bases for the SMEFT operators. At dimension five, a single operator (and its hermitian conjugate) exists, which is of the form

The Weinberg operator

$$\mathcal{O}^{(5)}_{\text{Weinberg}} = \epsilon^{ij}\epsilon^{kl}\, H_j H_l \left(\bar{\ell}^{c,i}_L \ell^k_L\right) . \tag{3.13}$$

Here, ϵ^{ij} represents the two-dimensional fully antisymmetric tensor with $\epsilon^{12} = 1$. This operator violates the lepton number symmetry, and, after EW symmetry breaking, contributes a Majorana mass term for the left-handed neutrinos

$$\mathcal{O}^{(5)}_{\text{Weinberg}} \supset \frac{v^2}{2} \left(\bar{\nu}^c_L \nu_L\right) . \tag{3.14}$$

The Warsaw basis

X generically denotes a gauge boson field, H the Higgs doublet, D a covariant derivative and ψ a fermion field.

We follow the conventions of [46], where τ^I are the Pauli matrices.

At dimension six, there are 59 independent operators that conserve baryon and lepton number. If one includes the full flavor structure for the fermions, this number is increased to 2499 operators. They were first classified in [46], the corresponding minimal set of dimension-6 SMEFT operators is known as the *Warsaw basis*. Table 3.1 presents the Warsaw operators of types X^3, H^6, H^4D^2, and X^2H^2, which exclusively involve bosonic fields. Here, f^{abc} and ϵ^{IJK} are the structure constants of $SU(3)$ and $SU(2)$, respectively, with

$$[T^a, T^b] = i f^{abc} T^c \quad \text{and} \quad \left[\frac{\tau^I}{2}, \frac{\tau^J}{2}\right] = i\epsilon^{IJK}\frac{\tau^K}{2} , \tag{3.15}$$

Two-fermion operators			
$\psi^2 XH$			
$\mathcal{O}_{eW}$	$(\bar{\ell}_L^i \sigma^{\mu\nu} e_R^j)\tau^I H\, W^I_{\mu\nu}$	$\mathcal{O}_{uB}$	$(\bar{q}_L^i \sigma^{\mu\nu} u_R^j)\tilde{H}\, B_{\mu\nu}$
$\mathcal{O}_{eB}$	$(\bar{\ell}_L^i \sigma^{\mu\nu} e_R^j) H\, B_{\mu\nu}$	$\mathcal{O}_{dG}$	$(\bar{q}_L^i \sigma^{\mu\nu} T^a d_R^j) H\, g^a_{\mu\nu}$
$\mathcal{O}_{uG}$	$(\bar{q}_L^i \sigma^{\mu\nu} T^a u_R^j)\tilde{H}\, g^a_{\mu\nu}$	$\mathcal{O}_{dW}$	$(\bar{q}_L^i \sigma^{\mu\nu} d_R^j)\tau^I H\, W^I_{\mu\nu}$
$\mathcal{O}_{uW}$	$(\bar{q}_L^i \sigma^{\mu\nu} u_R^j)\tau^I \tilde{H}\, W^I_{\mu\nu}$	$\mathcal{O}_{dB}$	$(\bar{q}_L^i \sigma^{\mu\nu} d_R^j) H\, B_{\mu\nu}$
$\psi^2 H^2 D$			
$\mathcal{O}^{(1)}_{H\ell}$	$(H^\dagger i \overleftrightarrow{D}_\mu H)(\bar{\ell}_L^i \gamma^\mu \ell_L^j)$	$\mathcal{O}^{(3)}_{Hq}$	$(H^\dagger i \overleftrightarrow{D}^I_\mu H)(\bar{q}_L^i \tau^I \gamma^\mu q_L^j)$
$\mathcal{O}^{(3)}_{H\ell}$	$(H^\dagger i \overleftrightarrow{D}^I_\mu H)(\bar{\ell}_L^i \tau^I \gamma^\mu \ell_L^j)$	$\mathcal{O}_{Hu}$	$(H^\dagger i \overleftrightarrow{D}_\mu H)(\bar{u}_R^i \gamma^\mu u_R^j)$
$\mathcal{O}_{He}$	$(H^\dagger i \overleftrightarrow{D}_\mu H)(\bar{e}_R^i \gamma^\mu e_R^j)$	$\mathcal{O}_{Hd}$	$(H^\dagger i \overleftrightarrow{D}_\mu H)(\bar{d}_R^i \gamma^\mu d_R^j)$
$\mathcal{O}^{(1)}_{Hq}$	$(H^\dagger i \overleftrightarrow{D}_\mu H)(\bar{q}_L^i \gamma^\mu q_L^j)$	$\mathcal{O}_{Hud}$	$i(\widetilde{H}^\dagger D_\mu H)(\bar{u}_R^i \gamma^\mu d_R^j)$
$\psi^2 H^3$			
$\mathcal{O}_{eH}$	$(H^\dagger H)(\bar{\ell}_L^i e_R^j H)$		
$\mathcal{O}_{uH}$	$(H^\dagger H)(\bar{q}_L^i u_R^j \widetilde{H})$		
$\mathcal{O}_{dH}$	$(H^\dagger H)(\bar{q}_L^i d_R^j H)$		

Table 3.2: Two-fermion dimension-six operators $\mathcal{O}_i^{(6)}$ in the Warsaw SMEFT basis. The indices $i, j \in \{1, 2, 3\}$ denote the fermion generations. See main text for further details.

Four-fermion operators			
$(\bar{L}L)(\bar{L}L)$		$(\bar{L}R)(\bar{R}L)$ and $(\bar{L}R)(\bar{L}R)$	
$\mathcal{O}_{\ell\ell}$	$(\bar{\ell}^i_L\gamma_\mu\ell^j_L)(\bar{\ell}^k_L\gamma^\mu\ell^l_L)$	$\mathcal{O}_{\ell edq}$	$(\bar{\ell}^i_{L,m}e^j_R)(\bar{d}^k_R q^l_{L,m})$
$\mathcal{O}^{(1)}_{qq}$	$(\bar{q}^i_L\gamma_\mu q^j_L)(\bar{q}^k_L\gamma^\mu q^l_L)$	$\mathcal{O}^{(1)}_{quqd}$	$(\bar{q}^i_{L,m}u^j_R)\epsilon^{mn}(\bar{q}^k_{L,n}d^l_R)$
$\mathcal{O}^{(3)}_{qq}$	$(\bar{q}^i_L\gamma_\mu\tau^I q^j_L)(\bar{q}^k_L\gamma^\mu\tau^I q^l_L)$	$\mathcal{O}^{(8)}_{quqd}$	$(\bar{q}^i_{L,m}T^a u^j_R)\epsilon^{mn}(\bar{q}^k_{L,n}T^a d^l_R)$
$\mathcal{O}^{(1)}_{\ell q}$	$(\bar{\ell}^i_L\gamma_\mu\ell^j_L)(\bar{q}^k_L\gamma^\mu q^l_L)$	$\mathcal{O}^{(1)}_{\ell equ}$	$(\bar{\ell}^i_{L,m}e^j_R)\epsilon^{mn}(\bar{q}^k_{L,n}u^l_R)$
$\mathcal{O}^{(3)}_{\ell q}$	$(\bar{\ell}^i_L\gamma_\mu\tau^I\ell^j_L)(\bar{q}^k_L\gamma^\mu\tau^I q^l_L)$	$\mathcal{O}^{(3)}_{\ell equ}$	$(\bar{\ell}^i_{L,m}\sigma_{\mu\nu}e^j_R)\epsilon^{mn}(\bar{q}^k_{L,n}\sigma^{\mu\nu}u^l_R)$
$(\bar{R}R)(\bar{R}R)$			
$\mathcal{O}_{ee}$	$(\bar{e}^i_R\gamma_\mu e^j_R)(\bar{e}^k_R\gamma^\mu e^l_R)$	$\mathcal{O}_{ed}$	$(\bar{e}^i_R\gamma_\mu e^j_R)(\bar{d}^k_R\gamma^\mu d^l_R)$
$\mathcal{O}_{uu}$	$(\bar{u}^i_R\gamma_\mu u^j_R)(\bar{u}^k_R\gamma^\mu u^l_R)$	$\mathcal{O}^{(1)}_{ud}$	$(\bar{u}^i_R\gamma_\mu u^j_R)(\bar{d}^k_R\gamma^\mu d^l_R)$
$\mathcal{O}_{dd}$	$(\bar{d}^i_R\gamma_\mu d^j_R)(\bar{d}^k_R\gamma^\mu d^l_R)$	$\mathcal{O}^{(8)}_{ud}$	$(\bar{u}^i_R\gamma_\mu T^a u^j_R)(\bar{d}^k_R\gamma^\mu T^a d^l_R)$
$\mathcal{O}_{eu}$	$(\bar{e}^i_R\gamma_\mu e^j_R)(\bar{u}^k_R\gamma^\mu u^l_R)$		
$(\bar{L}L)(\bar{R}R)$			
$\mathcal{O}_{\ell e}$	$(\bar{\ell}^i_L\gamma_\mu\ell^j_L)(\bar{e}^k_R\gamma^\mu e^l_R)$	$\mathcal{O}^{(1)}_{qu}$	$(\bar{q}^i_L\gamma_\mu q^j_L)(\bar{u}^k_R\gamma^\mu u^l_R)$
$\mathcal{O}_{\ell u}$	$(\bar{\ell}^i_L\gamma_\mu\ell^j_L)(\bar{u}^k_R\gamma^\mu u^l_R)$	$\mathcal{O}^{(8)}_{qu}$	$(\bar{q}^i_L\gamma_\mu T^a q^j_L)(\bar{u}^k_R\gamma^\mu T^a u^l_R)$
$\mathcal{O}_{\ell d}$	$(\bar{\ell}^i_L\gamma_\mu\ell^j_L)(\bar{d}^k_R\gamma^\mu d^l_R)$	$\mathcal{O}^{(1)}_{qd}$	$(\bar{q}^i_L\gamma_\mu q^j_L)(\bar{d}^k_R\gamma^\mu d^l_R)$
$\mathcal{O}_{qe}$	$(\bar{q}^i_L\gamma_\mu q^j_L)(\bar{e}^k_R\gamma^\mu e^l_R)$	$\mathcal{O}^{(8)}_{qd}$	$(\bar{q}^i_L\gamma_\mu T^a q^j_L)(\bar{d}^k_R\gamma^\mu T^a d^l_R)$

Table 3.3: Four-fermion dimension-six operators $\mathcal{O}^{(6)}_i$ in the Warsaw SMEFT basis. The indices $i,j,k,l \in \{1,2,3\}$ denote the fermion generations, $m,n \in \{1,2\}$ are the $SU(2)_L$ indices. See main text for further details.

where T^a and $\tau^I/2$ are the corresponding Lie algebra generators. Furthermore, the field strengths are given by

$$G^a_{\mu\nu} = \partial_{[\mu} G^a_{\nu]} - g_s f^{abc} G^b_\mu G^c_\nu \,, \qquad \tilde{G}_{\mu\nu} = \frac{1}{2}\epsilon_{\mu\nu\rho\sigma} G^{\rho\sigma} \,, \tag{3.16}$$

where $\partial_{[\mu} G^a_{\nu]} = \partial_\mu G^a_\nu - \partial_\nu G^a_\mu$ and $\epsilon_{\mu\nu\rho\sigma}$ is the four-dimensional fully-antisymmetric tensor with $\epsilon_{0123} = +1$. Analogous definitions hold for $W^I_{\mu\nu}$, $B_{\mu\nu}$ with the corresponding couplings constants g_2, g_1. The Higgs doublet H will be introduced in detail around (3.100), the D'Alembert operator of $\mathcal{O}_{H\Box}$ is defined as $\Box \equiv \partial_\mu \partial^\mu$.

Table 3.2 lists the operators of types $\psi^2 XH$, $\psi^2 H^2 D$, and $\psi^2 H^2$, which involve two fermion fields. Here, $\sigma^{\mu\nu} = \frac{i}{2}[\gamma^\mu, \gamma^\nu]$ is the usual Dirac tensor and the convention for the covariant derivatives is exemplified by [46]

$$\begin{aligned} \left(D_\mu q_L\right)_{c_1,m} = \Big(& \delta_{c_1 c_2}\delta_{mn}(\partial_\mu + i g_1 Y_q B_\mu) \\ & + i g_2 \delta_{c_1 c_2} \frac{\tau^I_{mn}}{2} W^I_\mu + i g_s \delta_{mn} T^a_{c_1 c_2} G^a_\mu \Big) q_{L,c_2,n} \,. \end{aligned} \tag{3.17}$$

Furthermore, $H^\dagger i \overleftrightarrow{D}_\mu H = i H^\dagger \left(D_\mu - \overleftarrow{D}_\mu\right) H$, $\tilde{H}_m = \epsilon_{mn} H^*_n$ with ϵ_{mn} the two-dimensional fully-antisymmetric tensor and $q_L, \ell_L, u_R, d_R, e_R$ are the usual SM fermion fields. Finally, the four-fermion operators ψ^4 are listed in Table 3.3, and grouped according to the possible helicity combinations $(\bar{L}L)(\bar{L}L)$, $(\bar{L}R)(\bar{R}L)$, $(\bar{L}R)(\bar{L}R)$, $(\bar{R}R)(\bar{R}R)$ and $(\bar{L}L)(\bar{R}R)$.

Example: The Top Basis It should be noted that the Warsaw basis [46] represents but one of a number of dimension-six SMEFT bases that have been proposed in the literature. In [47], the LHC Top Working Group defined a SMEFT basis that is specifically tailored to the interpretation of top-quark measurements at the LHC. For instance, they replace the four-fermion operators

$$\begin{aligned} \left[\mathcal{O}^{(1)}_{qq}\right]_{3333} &= (\bar{q}^3_L \gamma_\mu q^3_L)(\bar{q}^3_L \gamma^\mu q^3_L) \,, \\ \left[\mathcal{O}^{(3)}_{qq}\right]_{3333} &= (\bar{q}^3_L \gamma_\mu \tau^I q^3_L)(\bar{q}^3_L \gamma^\mu \tau^I q^3_L) \end{aligned} \tag{3.18}$$

of the Warsaw basis by

$$\begin{aligned} \left[\mathcal{O}^{(1)}_{QQ}\right] &= \frac{1}{2}(\bar{q}^3_L \gamma_\mu q^3_L)(\bar{q}^3_L \gamma^\mu q^3_L) \,, \\ \left[\mathcal{O}^{(8)}_{QQ}\right] &= \frac{1}{2}(\bar{q}^3_L \gamma_\mu T^a q^3_L)(\bar{q}^3_L \gamma^\mu T^a q^3_L) \,, \end{aligned} \tag{3.19}$$

in order to separate operators that do or do not interfere with SM QCD amplitudes (e.g. $b\bar{b} \to t\bar{t}$). Bases with (3.18) or (3.19) are equivalent in four dimensions, since (we will henceforth omit the flavor indices)

$$\begin{aligned} \mathcal{O}^{(1)}_{qq} &= (\bar{q}^3_L \gamma_\mu q^3_L)^2 = \left(\bar{t}_L \gamma_\mu t_L + \bar{b}_L \gamma_\mu b_L\right)^2 \,, \\ \mathcal{O}^{(3)}_{qq} &= (\bar{q}^3_L \gamma_\mu \tau^I q^3_L)^2 = (\bar{t}_L \gamma_\mu b_L + \bar{b}_L \gamma_\mu t_L)^2 \\ &\quad + (-i\bar{t}_L \gamma_\mu b_L + i\bar{b}_L \gamma_\mu t_L)^2 + (\bar{t}_L \gamma_\mu t_L - \bar{b}_L \gamma_\mu b_L)^2 \\ &= 4(\bar{t}_L \gamma_\mu b_L)(\bar{b}_L \gamma^\mu t_L) + (\bar{t}_L \gamma_\mu t_L - \bar{b}_L \gamma_\mu b_L)^2 \,, \end{aligned} \tag{3.20}$$

and therefore

$$
\begin{aligned}
\mathcal{O}_{QQ}^{(1)} &= \boxed{\frac{1}{2}\mathcal{O}_{qq}^{(1)}}\,, \\
\mathcal{O}_{QQ}^{(8)} &= \frac{1}{2}\left(\bar{q}_L^3\gamma_\mu T^a q_L^3\right)\left(\bar{q}_L^3\gamma^\mu T^a q_L^3\right) \\
&\overset{(3.9)}{=} \frac{1}{4}\left(\left(\bar{q}_{L,c_1}^3\gamma_\mu q_{L,c_2}^3\right)\left(\bar{q}_{L,c_2}^3\gamma^\mu q_{L,c_1}^3\right) - \frac{1}{3}\left(\bar{q}_L^3\gamma_\mu q_L^3\right)^2\right) \\
&\overset{(3.8)}{=} \frac{1}{4}\left(\bar{q}_{L,m}^3\gamma_\mu q_{L,n}^3\right)\left(\bar{q}_{L,n}^3\gamma^\mu q_{L,m}^3\right) - \frac{1}{12}\mathcal{O}_{qq}^{(1)} \\
&= \frac{1}{4}\left(\left(\bar{t}_L\gamma_\mu t_L\right)^2 + \left(\bar{b}_L\gamma_\mu b_L\right)^2 + 2\left(\bar{t}_L\gamma_\mu b_L\right)\left(\bar{b}_L\gamma^\mu t_L\right)\right) - \frac{1}{12}\mathcal{O}_{qq}^{(1)} \\
&= \frac{1}{4}\left(\frac{1}{2}\mathcal{O}_{qq}^{(1)} + \frac{1}{2}\mathcal{O}_{qq}^{(3)}\right) - \frac{1}{12}\mathcal{O}_{qq}^{(1)} \\
&= \boxed{\frac{1}{24}\mathcal{O}_{qq}^{(1)} + \frac{1}{8}\mathcal{O}_{qq}^{(3)}}\,,
\end{aligned}
\tag{3.21}
$$

where we have used the Fierz identities (3.8) and (3.9). As the former are only exact in four dimensions, the second equality in (3.21) should be extended by an evanescent operator in d dimensions. We define it as

$$
\boxed{\mathcal{O}_{QQ}^{(8)} \equiv \frac{1}{24}\mathcal{O}_{qq}^{(1)} + \frac{1}{8}\mathcal{O}_{qq}^{(3)} + E_{QQ}\,.}
\tag{3.22}
$$

Note that the relations among the Wilson coefficients are transposed and inverted, i.e.

$$
\begin{aligned}
C_{QQ}^{(1)} &= 2C_{qq}^{(1)} - \frac{2}{3}C_{qq}^{(3)}\,, \\
C_{QQ}^{(8)} &= 8C_{qq}^{(3)}\,,
\end{aligned}
\tag{3.23}
$$

in order to obtain $C_{\text{Warsaw}}^{\intercal}\mathcal{O}_{\text{Warsaw}} = C_{\text{top}}^{\intercal}\mathcal{O}_{\text{top}}$.

3.1.4 *The SMEFT Renormalization Group Running*

The mixing of SMEFT operators under the RG running

As previously stated, the SMEFT is systematically improvable. Higher-order loop diagrams can be calculated and renormalized order-by-order in powers of the EFT expansion parameter Λ. However, certain complexities arise in such calculations, which will be discussed in subsequent chapters. One noteworthy aspect of the SMEFT is the operator mixing under the RG running. To illustrate it, let us consider the effective $b\bar{t}W$ vertex.

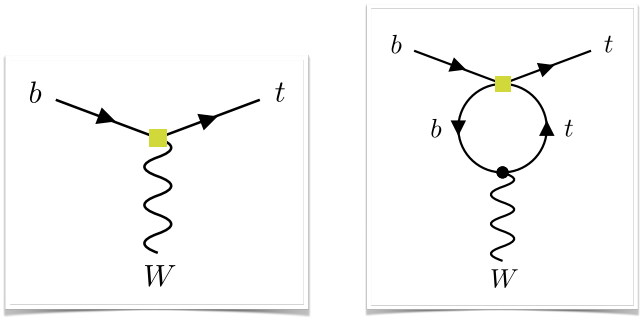

(a) $\mathcal{O}_{Hq}^{(3)}$ (tree-level) (b) $\mathcal{O}_{qq}^{(1)}, \mathcal{O}_{qq}^{(3)}$ (one-loop)

Figure 3.2: Contributions from various SMEFT operators to the $b\bar{t}W$ vertex.

Example: The W Penguin The Warsaw operator $[\mathcal{O}_{Hq,0}^{(3)}]_{33}$ (we will henceforth omit the flavor indices, all fermion fields are of the third family) contributes to $b\bar{t}W$ via the tree-level amplitude

$$\frac{g_2}{\sqrt{2}}\frac{v^2}{\Lambda^2}C_{Hq,0}^{(3)}\left[\bar{u}_t \not{\epsilon}_W P_L u_b\right] , \tag{3.24}$$

where u_t, u_b represent the fermion spinors, ϵ_W denotes the polarization vector of the W boson and $v \simeq 246\,\text{GeV}$ is the vacuum expectation value (VEV) of the SM Higgs field. The subscript 0 in $C_{Hq,0}^{(3)}$ is indicative of the fact that this is the unrenormalized Wilson coefficient. The corresponding Feynman diagram is shown in Figure 3.2a. At the one-loop level, the four-quark operators $C_{qq,0}^{(1)}$ and $C_{qq,0}^{(3)}$ induce the same current contribution via the Penguin diagram depicted in Figure 3.2b. This contribution is of the form

$$\frac{g_2}{\sqrt{2}}\frac{\mathcal{N}m_t^2}{8\pi^2\Lambda^2}\left(\frac{\mu_R^2}{m_t^2}\right)^{\epsilon}\left(\frac{C_{qq,0}^{(1)}+5C_{qq,0}^{(3)}}{\epsilon}-\frac{C_{qq,0}^{(1)}-7C_{qq,0}^{(3)}}{2}\right)\left[\bar{u}_t \not{\epsilon}_W P_L u_b\right] . \tag{3.25}$$

Before embarking on the discussion of the renormalization of (3.25), let us revisit the evanescent operator introduced in (3.22). If one were to apply the Wilson coefficient relations (3.23) directly to (3.25), the resulting expression would be

$$\frac{g_2}{\sqrt{2}}\frac{\mathcal{N}m_t^2}{48\pi^2\Lambda^2}\left(\frac{\mu_R^2}{m_t^2}\right)^{\epsilon}\left(\frac{3C_{QQ}^{(1)}+4C_{QQ}^{(8)}}{\epsilon}-\frac{3C_{QQ}^{(1)}+(9-5)C_{QQ}^{(8)}}{2}\right)\left[\bar{u}_t \not{\epsilon}_W P_L u_b\right] \tag{3.26}$$

without the term in light gray (i.e. with a factor -5 in front of $C_{QQ}^{(8)}$ in the constant part) for the one-loop SMEFT amplitude in the LHC Top Working Group basis. It is incorrect. The color factors of the $C_{QQ}^{(1)}$ and $C_{QQ}^{(8)}$ contributions are

$$\mathbb{1}_{c_1c_2} \quad \text{and} \quad \sum_c T_{c_1c}^a T_{cc_2}^a = C_F\,\mathbb{1}_{c_1c_2} , \tag{3.27}$$

respectively, which is why the ratio between the two contributions has to be C_F. In (3.26), without the green term, the factor is $-5/3$ in the constant

part. The discrepancy can be attributed to the fact that (3.23) only hold in four dimensions. In general d dimensions, the evanescent operator E_{QQ} from (3.22) must be included. When multiplied by the $1/\epsilon$ pole from the loop, this operator contributes a finite rational term in (3.25). Indeed, the inclusion of the evanescent contribution adds the green term 9 to (3.25) and the correct result with the correct color factor is recovered.
We now turn to the renormalization of (3.25). Upon examination of (3.25), we observe that the poles proportional to $C^{(1)}_{qq,0}$ and $C^{(3)}_{qq,0}$ exhibit the same structure as the tree-level contribution proportional to $C^{(3)}_{Hq,0}$ in (3.24). In order to be able to absorb these poles, it is necessary to introduce renormalization factors of the form

$$C_{i,0} = \sum_j \tilde{Z}_{ij} C_j \quad \text{and} \quad \mathcal{O}_{i,0} = \sum_j Z_{ij} \mathcal{O}_j \,, \tag{3.28}$$

with $\tilde{Z}^{\intercal}_{ij} = Z^{-1}_{ij}$ and where the sum goes over all dimension-six operators in the Warsaw basis. We get

$$C^{(3)}_{Hq,0} = \sum_j \tilde{Z}_{\substack{(3)\\Hq}\,j} C_j \supset \tilde{Z}_{\substack{(3)(1)\\Hqqq}} C^{(1)}_{qq} + \tilde{Z}_{\substack{(3)(3)\\Hqqq}} C^{(3)}_{qq} \,. \tag{3.29}$$

Inserting (3.29) into (3.24) and comparing the resulting expression with (3.25), we find that

$$\tilde{Z}_{\substack{(3)(1)\\Hqqq}} = -\frac{1}{8\pi^2}\frac{m_t^2}{v^2}\frac{\mathcal{N}}{\epsilon} \quad \text{and} \quad \tilde{Z}_{\substack{(3)(3)\\Hqqq}} = -5\,\frac{1}{8\pi^2}\frac{m_t^2}{v^2}\frac{\mathcal{N}}{\epsilon} \tag{3.30}$$

are needed in the $\overline{\text{MS}}$ scheme to get rid of the poles.
For completeness, let us add that $C^{(1)}_{qq,0}, C^{(3)}_{qq,0}$ also induce poles proportional to

$$\left[\bar{u}_t \left(k_W^2 \not{\epsilon}_W - (k_W \cdot \epsilon_W) \not{k}_W\right) P_L u_b\right] \tag{3.31}$$

via the Penguin diagram shown in Figure 3.2b. At the tree level, the corresponding operator is of the form [43]

$$\left(\mathcal{O}^{(3)}_{DW}\right)_{ij} \equiv \left[D_\mu, W_{\mu\nu}\right]^I \bar{q}^i_L \gamma^\nu \tau^I q^j_L \,, \tag{3.32}$$

with $\left[D_\nu, W_{\nu\mu}\right]^I$ the covariant derivative in the adjoint representation. In order to cancel these poles, renormalization factors of the form

$$\tilde{Z}_{\substack{(3)\,(3)\\DWqq}} = 5\,\tilde{Z}_{\substack{(3)\,(1)\\DWqq}} = \frac{g_2^2}{96\pi^2}\frac{\mathcal{N}}{\epsilon} \tag{3.33}$$

are necessary. It should be noted that the operator (3.32) is not part of the Warsaw basis, as it can be removed by a field redefinition (see (3.7)). Indeed, using the SM equation of motion

$$\left[D_\mu, W_{\mu\nu}\right]^I = \frac{g_2}{2}\left(\bar{q}^i_L \gamma_\nu \tau^I q^i_L + \ell^i_L \gamma_\nu \tau^I \ell^i_L + H^\dagger i D^I_\nu H\right) \,, \tag{3.34}$$

the operator in (3.32) can be decomposed into a linear combination of $\mathcal{O}^{(3)}_{qq}, \mathcal{O}^{(3)}_{\ell q}$ and $\mathcal{O}^{(3)}_{Hq}$. Consequently, in the Warsaw basis, the renormalization factors in (3.33) are replaced by

$$\begin{aligned} \tilde{Z}^{(3)\,(1)}_{qq\;qq} &= \tilde{Z}^{(3)\,(1)}_{\ell q\;qq} = \tilde{Z}^{(3)\,(1)}_{Hq\,qq} = \frac{g_2^2}{96\pi^2}\frac{\mathcal{N}}{\epsilon}\,, \\ \tilde{Z}^{(3)\,(3)}_{qq\;qq} &= \tilde{Z}^{(3)\,(3)}_{\ell q\;qq} = \tilde{Z}^{(3)\,(3)}_{Hq\,qq} = \frac{5g_2^2}{96\pi^2}\frac{\mathcal{N}}{\epsilon}\,. \end{aligned} \tag{3.35}$$

We will now examine the RG running of the SMEFT Wilson coefficients. In analogy to the $\beta(\alpha_s)$ function in (2.28), we define

$$\boxed{\tilde{\gamma}_{ij}(g) \equiv \tilde{Z}^{-1}_{ik}\frac{d\tilde{Z}_{kj}}{d\ln\mu_R}} \quad \text{and} \quad \boxed{\gamma_{ij}(g) \equiv Z^{-1}_{ik}\frac{dZ_{kj}}{d\ln\mu_R}}\,, \tag{3.36}$$

where g denotes a generic coupling (e.g. g_1, g_2, g_s, etc.) of the SM and $\tilde{Z}_{ij}, Z_{ij}$ are the renormalization factors introduced in (3.28). The matrix γ_{ij} is designated as the anomalous dimension matrix (ADM) of the SMEFT. In analogy to (2.30), writing $Z_{ij} = \delta_{ij} + \sum_{n=1}^{\infty} S_\epsilon^n/\epsilon^n\, Z_{ij,n}$ (and equivalently with the tilde), the $\overline{\text{MS}}$ ADM can be determined straightforwardly via

The ADM of the SMEFT

$$\gamma_{ij} = -2g^2\frac{\partial Z_{ij,1}(g)}{\partial g^2}\,. \tag{3.37}$$

Using (3.28) and the fact that the bare Wilson coefficients are independent of μ_R, we find

The SMEFT RG running

$$\boxed{\frac{dC_i}{d\ln\mu_R}} = -\tilde{Z}^{-1}_{ik}\frac{d\tilde{Z}_{kj}}{d\ln\mu_R}C_j = \boxed{-\tilde{\gamma}_{ij}C_j} = -Z_{ki}\frac{dZ^{-1}_{jk}}{d\ln\mu_R}C_j = \boxed{\gamma_{ji}C_j}\,, \tag{3.38}$$

showing that the renormalization group running is controlled by $\gamma_{ji} = -\tilde{\gamma}_{ij}$. In analogy to (2.32), the solution to (3.38) is

$$\boxed{C_i(\mu_R) = U_{ij}(\mu_R, m_Z)\,C_j(m_Z)\,,} \tag{3.39}$$

with the evolution matrix U_{ij} given by

$$\boxed{U_{ij}(\mu_R, m_Z) = \exp\left[\int_{g(m_Z)}^{g(\mu_R)} dg'\,\frac{\gamma_{ji}(g')}{\beta(g')}\right]\,.} \tag{3.40}$$

As the Z_{ij} contain non-diagonal terms, so does γ_{ij}. Consequently, the evolution matrix U_{ij} *mixes* Wilson coefficients of different operators into each other. A Wilson coefficient that vanishes at the scale m_Z may be non-zero at a different μ_R, with potentially important phenomenological consequences. The complete one-loop ADM of the dimension-six SMEFT operators in the Warsaw basis has been calculated in [43, 48, 49], the running is solved numerically in [50–56].

EXAMPLE: THE *W* PENGUIN Recalling equation (3.30) and $m_t = y_t\, v/\sqrt{2}$ with y_t the Yukawa coupling of the top quark, we find

$$\tilde{Z}^{(3)(1)}_{Hqqq} = \frac{1}{5}\tilde{Z}^{(3)(3)}_{Hqqq} = -\frac{\mathcal{N}}{16\pi^2}\frac{y_t^2}{\epsilon}\,, \tag{3.41}$$

which using (3.37), (3.38) gives

$$\boxed{\frac{dC^{(3)}_{Hq}}{d\ln\mu_R}} = -\sum_j \tilde{\gamma}^{(3)}_{Hq\,j} C_j \supset \boxed{-\frac{y_t^2}{8\pi^2}\left(C^{(1)}_{qq} + 5\,C^{(3)}_{qq}\right)}\,. \tag{3.42}$$

This result, in accordance with [48, (A.28)], demonstrates that the renormalization group running with the Yukawa coupling y_t leads to a mixing of $C^{(1)}_{qq}$ and $C^{(3)}_{qq}$ into $C^{(3)}_{Hq}$. Similarly, in the Warsaw basis, the running with g_2 from the other contributions mentioned earlier is given by

$$\boxed{\frac{dC^{(3)}_{\ell q}}{d\ln\mu_R} = \frac{dC^{(3)}_{Hq}}{d\ln\mu_R} = \frac{g_2^2}{48\pi^2}\left(C^{(1)}_{qq} + 5\,C^{(3)}_{qq}\right)}\,, \tag{3.43}$$

consistent with [49]. There are additional contributions to the $C^{(3)}_{qq}$ running proportional to g_2 that are not covered by the $\tilde{Z}$ in (3.35). The complete running ends up being [49]

$$\frac{dC^{(3)}_{qq}}{d\ln\mu_R} = \frac{g_2^2}{48\pi^2}\left(11C^{(1)}_{qq} - 8C^{(3)}_{qq}\right)\,. \tag{3.44}$$

3.2 The $SU(4)^{[3]} \times SU(3)^{[12]} \times SU(2)_L \times U(1)_X$ (4321) Model

In order to introduce the 4321 gauge unification, we begin with the Yukawa sector of the SM. The Yukawa interactions between the SM Higgs doublet and the SM fermions are given by

$$\boxed{\mathcal{L}_{\text{Yukawa}} = -\left((Y_u)_{ij}\,\bar{q}^i_L \tilde{H} u^j_R + (Y_d)_{ij}\,\bar{q}^i_L H d^j_R + (Y_e)_{ij}\,\bar{\ell}^i_L H e^j_R + \text{h.c.}\right),} \tag{3.45}$$

where the Yukawa couplings $Y_{u,d,e}$ are complex 3×3 matrices in flavor space. *A priori*, one would expect the Yukawa couplings to have entries that are all on the order $\mathcal{O}(1)$. However, experimental data shows that their flavor structure is highly non-generic. This can be demonstrated by employing the singular value decomposition $Y_f = (U^L_f)^\dagger \lambda_f U^R_f$, where U^L_f and U^R_f are unitary matrices and λ_f is diagonal. Neglecting all values smaller than 0.01, the λ_f take the form [57]

The flavor puzzle

$$\lambda_u \approx \text{diag}(0,0,y_t)\,, \qquad \lambda_d \approx \text{diag}(0,0,y_b)\,, \qquad \lambda_e \approx \text{diag}(0,0,y_\tau)\,, \tag{3.46}$$

with

$$y_t = \frac{\sqrt{2}\,m_t}{v} \approx 0.96\,, \qquad y_b = \frac{\sqrt{2}\,m_b}{v} \approx 0.02\,, \qquad y_\tau = \frac{\sqrt{2}\,m_\tau}{v} \approx 0.01\,. \tag{3.47}$$

This indicates that, to a good approximation, there is a

The approximate $U(2)^5$ flavor symmetry of the SM

$$U(2)^5 = U(2)_q \times U(2)_u \times U(2)_d \times U(2)_\ell \times U(2)_e \tag{3.48}$$

flavor symmetry underlying the SM, which distinguishes the fermions of the third generation from those of the lighter two. In other words, the lighter fermion flavors can be rotated (via the $U(2)$ transformations) without changing the SM Lagrangian to a good approximation. This structure does not have an explanation in the SM, which is known as the *flavor puzzle*.

The flavor puzzle has inspired a great deal of theoretical work attempting to address it with BSM physics. In particular, the idea of embedding the SM into a larger gauge group that is flavor non-universal, meaning that it couples differently to the different fermion generations, has gained traction. Such flavor non-universal gauge models can have multiple layers of new physics at different energy scales, which induce the structure of the Yukawa couplings that is observed experimentally. However, in order to avoid exacerbating the Higgs naturalness problem, the initial layer of BSM physics that distinguishes the third generation from the light families typically occurs at the TeV scale. In [58], the authors demonstrated that the generic model building assumptions

The inescapable link between Higgs and flavor

- **Flavor non-universality:** The flavor structure of the SM Yukawas emerges as an accidental symmetry resulting from the embedding of the SM into a flavor non-universal gauge group in the UV.
- **Semi-simple embedding in the UV:** The TeV scale model is ultimately incorporated into an anomaly-free semi-simple gauge theory, which provides an explanation for the quantization of hypercharge.

- **Fundamental and (quasi)-natural Higgs at the TeV scale:** The Higgs boson is a fundamental scalar field up to scales well above the TeV. Consequently, the Higgs mass corrections should not be too large in order to avoid exacerbating the Higgs hierarchy problem.
- **Avoiding proton decay and $\mu \to e$ at low scales:** In order to comply with experimental data, the BSM model should not induce excessive proton decay or $\mu \to e$ transitions.

lead to a very constrained set of viable BSM scenarios. All of these scenarios share a common feature: an $SU(4)^{[3]}$ gauge group that only couples to the third fermion generation (as indicated by the superscript $[3]$). Such models feature a quark-lepton unification in the third family, where the third-generation fermions are collected in $SU(4)^{[3]}$ multiplets of the form

Non-universal $SU(4)$, quark-lepton unification and the U_1 VLQ

$$\psi_L^3 = \begin{pmatrix} q_{L,c_1}^3 \\ \ell_L^3 \end{pmatrix}, \qquad \psi_R^3 = \begin{pmatrix} d_{R,c_1}^3 \\ e_R^3 \end{pmatrix}, \tag{3.49}$$

with $c_1 \in \{1,2,3\}$ specifying the color of the quarks. As usually, the interactions between the $SU(4)^{[3]}$ gauge bosons H_μ^α with $\alpha \in \{1,\dots,15\}$ and the fermions ψ follow

$$-ig_4 H_\mu^\alpha \boldsymbol{T}^\alpha \psi\,, \tag{3.50}$$

where g_4 is the $SU(4)^{[3]}$ coupling strength and $\boldsymbol{T}^\alpha$ are the $SU(4)$ generators

$$\begin{aligned}
\boldsymbol{T}^a &= \begin{pmatrix} T^a & 0_{3\times 1} \\ 0_{1\times 3} & 0 \end{pmatrix}, \\
\boldsymbol{T}^9 &= \frac{1}{2}\begin{pmatrix} 0&0&0&1\\0&0&0&0\\0&0&0&0\\1&0&0&0 \end{pmatrix}, \qquad \boldsymbol{T}^{10} = \frac{1}{2}\begin{pmatrix} 0&0&0&-i\\0&0&0&0\\0&0&0&0\\i&0&0&0 \end{pmatrix}, \quad \boldsymbol{T}^{11} = \frac{1}{2}\begin{pmatrix} 0&0&0&0\\0&0&0&1\\0&0&0&0\\0&1&0&0 \end{pmatrix}, \\
\boldsymbol{T}^{12} &= \frac{1}{2}\begin{pmatrix} 0&0&0&0\\0&0&0&-i\\0&0&0&0\\0&i&0&0 \end{pmatrix}, \qquad \boldsymbol{T}^{13} = \frac{1}{2}\begin{pmatrix} 0&0&0&0\\0&0&0&0\\0&0&0&1\\0&0&1&0 \end{pmatrix}, \quad \boldsymbol{T}^{14} = \frac{1}{2}\begin{pmatrix} 0&0&0&0\\0&0&0&0\\0&0&0&-i\\0&0&i&0 \end{pmatrix}, \\
\boldsymbol{T}^{15} &= \frac{1}{2\sqrt{6}}\,\mathrm{diag}\,(1,1,1,-3)\,,
\end{aligned} \tag{3.51}$$

with T^a for $a \in \{1,\dots,8\}$ the usual $SU(3)$ generators. The generators $\boldsymbol{T}^9$-$\boldsymbol{T}^{14}$ induce tree-level interactions between quarks and leptons. Writing

$$U_\mu^{1,2,3} \equiv \frac{1}{\sqrt{2}}\left(H_\mu^{9,11,13} - iH_\mu^{10,12,14}\right), \tag{3.52}$$

the corresponding Lagrangian becomes

$$\boxed{\mathcal{L}_f \supset \frac{g_4}{\sqrt{2}}\left[\bar{q}_{L,c_1}^3 \gamma^\mu \ell_L^3 + \bar{d}_{R,c_1}^3 \gamma^\mu e_R^3\right] U_\mu^{c_1}\,.} \tag{3.53}$$

The field $U_\mu^{c_1}$ is the singlet VLQ U_1. It attracted attention in the context of the flavor anomalies in $b \to s\ell^+\ell^-$ and $b \to c\tau^-\bar{\nu}$ transitions, since the singlet VLQ was able to explain both deviations from the SM predictions jointly. However, the recent publication of the $b \to s\ell^+\ell^-$ lepton flavor universality (LFU) ratios R_K, R_{K^*} by LHCb at the end of 2022 [59], in agreement with the SM, has severely restricted the possibility of having LFU-violating BSM physics in the b sector [60]. Consequently, the bottom-up motivation for the singlet VLQ has been largely lost. Nevertheless, singlet VLQ models remain motivated by top-down considerations such as the interplay between the flavor puzzle and the hierarchy problem, which point towards non-universal $SU(4)^{[3]}$ unifications. This is in line with our previous discussion.

3.2.1 *The $SU(4)^{[3]} \times SU(3)^{[12]}$ sector of the 4321*

In order to construct a phenomenologically viable model based on $SU(4)^{[3]}$, let us examine the generators $\boldsymbol{T}^1$-$\boldsymbol{T}^8$ and $\boldsymbol{T}^{15}$, which exist in addition to the six generators $\boldsymbol{T}^9$-$\boldsymbol{T}^{14}$ associated with the VLQ interactions. The generators $\boldsymbol{T}^1$-$\boldsymbol{T}^8$ are part of the subgroup $SU(3)^{[3]} \subset SU(4)^{[3]}$, and induce QCD-like interactions among the third-family quarks. In a model based on a single $SU(4)^{[3]}$ gauge group, one identifies $g_4 = g_s$ to obtain the usual QCD interactions of the SM. Consequently, the VLQ interactions are also proportional to g_s and such a model is stringently constrained by experimental data. Therefore, as a next-to-minimal setup involving $SU(4)^{[3]}$, let us consider

$$SU(4)^{[3]} \times SU(3)^{[12]} \,. \tag{3.54}$$

The gauge bosons C_μ^a with $a \in \{1, \ldots, 8\}$ of the $SU(3)^{[12]}$ group only couple to first- and second-generation quarks (as indicated by the superscript [12]). The group (3.54) is broken spontaneously to the SM gauge group $SU(3)_c$ and additional subgroups via two scalar fields Ω_1, Ω_3 that acquire VEVs v_1, v_3. The scalar fields take the form

The 4321 scalar sector

$$\Omega_3 = \begin{pmatrix} \frac{v_3}{\sqrt{2}}\mathbb{1}_{3\times3} + \frac{1}{\sqrt{6}}S_3\,\mathbb{1}_{3\times3} + 2O^aT^a \\ T_3^{c_1} \end{pmatrix} , \qquad \Omega_1 = \begin{pmatrix} T_1^{c_1 *} \\ \frac{v_1}{\sqrt{2}} + S_1 \end{pmatrix} , \tag{3.55}$$

where O^a is an octet, $T_1^{c_1}, T_3^{c_1}$ are triplets and S_1, S_3 singlets under $SU(3)_c$. The usual kinetic terms for the scalar fields,

$$\mathcal{L}_{\text{kin}} \supset \left(D_\mu\Omega_1\right)^\dagger D^\mu\Omega_1 + \text{Tr}\left[\left(D_\mu\Omega_3\right)^\dagger D^\mu\Omega_3\right] , \tag{3.56}$$

with

$$\begin{aligned} D_\mu\Omega_3 &= \partial_\mu\Omega_3 + ig_4H_\mu^\alpha\boldsymbol{T}^{\alpha *}\Omega_3 - ig_3C_\mu^a\Omega_3\left(T^a\right)^\intercal , \\ D_\mu\Omega_1 &= \partial_\mu\Omega_1 + ig_4H_\mu^\alpha\boldsymbol{T}^{\alpha *}\Omega_1 , \end{aligned} \tag{3.57}$$

then lead to the mass eigenstates

$$\begin{aligned} U_\mu^{1,2,3} &= \frac{1}{\sqrt{2}}\left(H_\mu^{9,11,13} - iH_\mu^{10,12,14}\right), & M_U^2 &= \frac{g_4^2}{4}\left(v_1^2+v_3^2\right), \\ G_\mu'^a &= \frac{g_4 H_\mu^a - g_3 C_\mu^a}{\sqrt{g_4^2+g_3^2}}, & M_{G'}^2 &= \frac{v_3^2}{2}\left(g_4^2+g_3^2\right), \\ G_\mu^a &= \frac{g_3 H_\mu^a + g_4 C_\mu^a}{\sqrt{g_4^2+g_3^2}}, & m_G^2 &= 0. \end{aligned} \tag{3.58}$$

Here, g_3 represents the coupling strength of $SU(3)^{[12]}$. It should be noted that in addition to the VLQ U_1 and the usual $SU(3)_c$ gluon G_μ^a, the particle spectrum also contains a massive gluon (coloron) $G_\mu'^a$. This is the result of the two groups $SU(3)^{[3]} \subset SU(4)^{[3]}$ and $SU(3)^{[12]}$ mixing to yield both $G_\mu'^a, G_\mu^a$ in (3.58). The interactions of these particles with the quarks of the third generation read

The coloron G'

$$\boxed{\mathcal{L}_f \supset \underbrace{\frac{g_4^2}{\sqrt{g_4^2+g_3^2}}}_{\sqrt{g_4^2-g_s^2}} \left[\bar{q}^3\gamma^\mu T^a q^3\right] G_\mu'^a + \underbrace{\frac{g_4 g_3}{\sqrt{g_4^2+g_3^2}}}_{g_s} \left[\bar{q}^3\gamma^\mu T^a q^3\right] G_\mu^a,} \tag{3.59}$$

for $q = q_L, u_R, d_R$. Equating the interaction strength of the gluon with g_s, the interaction strength of the coloron becomes equal to $\sqrt{g_4^2 - g_s^2}$. This has significant implications. Whenever a diagram features a gluon exchange proportional to g_s^2, there is a corresponding diagram with a coloron exchange proportional to $g_4^2 - g_s^2$. Consequently, the contributions proportional to g_s^2 cancel among the two, up to the difference in mass $M_{G'} \neq m_G = 0$.

It is worth briefly mentioning the EW part of the 4321 model at this point. We have listed 22 bosonic degrees of freedom in (3.58), whereas $SU(4)^{[3]}$ comes with 15 generators and $SU(3)^{[12]}$ with additional 8, giving a total of 23. Indeed, the spectrum of $SU(4)^{[3]}$ also contains the degree of freedom

$$-ig_4 H_\mu^{15} \boldsymbol{T}^{15}\psi, \tag{3.60}$$

which induces interactions among the quarks and the leptons separately, as can be seen from $\boldsymbol{T}^{15}$ in (3.58). In the full 4321, the gauge group (3.54) is accompanied by the flavor-universal

$$SU(2)_L \times U(1)_X. \tag{3.61}$$

The group $SU(2)_L$ is identical to that of the SM, whereas after spontaneous symmetry breaking, $U(1)_X$ combines with the $U(1)^{[3]} \subset SU(4)^{[3]}$ from the 15$^{\text{th}}$ generator to yield the usual $U(1)_Y$ and an additional heavy Z_μ' . As the effects of the Z_μ' will not be significant below, we have chosen not to discuss it in detail here.

The Z'

3.2.2 *Goldstone boson and ghost interactions*

Finally, when higher-order calculations of the $\mathcal{O}(\alpha_s)$ sector of the 4321 model are performed in Feynman gauge, it is necessary to include the contributions from the

Goldstone bosons and the ghosts. The scalar sector of the 4321 is notable for the inclusion of scalar fields that are charged under QCD. Let us derive the Feynman rules of these fields that will be relevant below. In addition to the mass terms for the gauge bosons, (3.56) also contains the interaction terms between the gauge bosons and the Goldstone bosons. We have

$$\begin{aligned}
\mathrm{Tr}\left[\left(D_\mu \Omega_3\right)^\dagger D^\mu \Omega_3\right] \supset\ & \mathrm{Tr}\left[\Omega_3^\dagger \left(-i g_4 H_\mu^A \boldsymbol{T}^{A*}\right)\left(i g_4 H^{a,\mu} \boldsymbol{T}^{a*}\right)\Omega_3\right] \\
& + \mathrm{Tr}\left[\Omega_3^\dagger \left(-i g_4 H_\mu^A \boldsymbol{T}^{A*}\right)\left(-i g_3 C^{a,\mu}\right)\Omega_3 \left(T^a\right)^\intercal\right] + \text{h.c.} \\
=\ & g_4^2 \frac{v_3}{\sqrt{2}} \mathrm{Tr}\left[T_3^{c_1\dagger} \frac{1}{\sqrt{2}} U_\mu^{c_2} T^{a*}_{c_2 c_1}\right] H^{a,\mu} \\
& - 2 g_3 g_4 \frac{v_3}{\sqrt{2}} \mathrm{Tr}\left[T_3^{c_1\dagger} \frac{1}{\sqrt{2}} U_\mu^{c_2} T^{a*}_{c_2 c_1}\right] C^{a,\mu} + \text{h.c.} \\
=\ & \frac{g_4 v_3}{2}\left[T_3^\dagger T^a U_\mu\right]\left(g_4 H^{a,\mu} - 2 g_3 C^{a,\mu}\right) + \text{h.c.}\,,
\end{aligned} \tag{3.62}$$

where we split $\alpha \in \{1,\ldots,15\}$ into $a = \{1,\ldots,8\}$ and $A = \{9,\ldots,14\}$, and used

$$H_\mu^A \boldsymbol{T}^{A*} = \frac{1}{\sqrt{2}} \begin{pmatrix} 0_{3\times 3} & U_\mu^{c_1\dagger} \\ U_\mu^{c_1} & 0 \end{pmatrix}, \tag{3.63}$$

as well as $(T^a)^\intercal = T^{a*}$. Similarly,

$$\begin{aligned}
\left(D_\mu \Omega_1\right)^\dagger D^\mu \Omega_1 \supset\ & \Omega_1^\dagger \left(-i g_4 H_\mu^A \boldsymbol{T}^{A*}\right)\left(i g_4 H^{\mu,a} T^{a*}\right)\Omega_1 + \text{h.c.} \\
=\ & \frac{g_4^2 v_1}{\sqrt{2}}\left[\frac{1}{\sqrt{2}} U_\mu^{c_2} T^{a*}_{c_2 c_1} T_1^{c_1\dagger}\right] H^{a,\mu} + \text{h.c.} \\
=\ & \frac{g_4^2 v_1}{2}\left[T_1^\dagger T^a U_\mu\right] H^{a,\mu} + \text{h.c.}\,.
\end{aligned} \tag{3.64}$$

Using (3.58) and the fact that the Goldstone bosons associated with the radial mode of the VLQ are given by

$$\pi_U^{c_1} \equiv \frac{v_1 T_1^{c_1} - v_3 T_3^{c_1}}{\sqrt{v_1^2 + v_3^2}}, \tag{3.65}$$

we arrive at

Goldstone boson interactions

$$\boxed{\begin{aligned}
\mathcal{L}_{\text{kin}} \supset\ & g_s M_U \left[\pi_U^\dagger T^a U_\mu\right] G^{a,\mu} \\
& + \sqrt{g_4^2 - g_s^2}\, \frac{M_U^2 - M_{G'}^2}{M_U}\left[\pi_U^\dagger T^a U_\mu\right] G'^{a,\mu} + \text{h.c.}
\end{aligned}} \tag{3.66}$$

Furthermore, the Goldstone bosons associated with the radial mode of the coloron are given by

$$\pi_{G'^a} = \mathrm{Im}\left\{O^a\right\}. \tag{3.67}$$

One can show that there are no terms of the form $\pi_{G'^a}[U_\mu^\dagger T^a U^\mu]$ in the 4321 Lagrangian. The interactions of the ghosts with the corresponding gauge bosons are given by

$$\mathcal{L}_{\text{ghost}} \supset g_4 f^{\alpha\beta\gamma}\left(\partial_\mu \bar{c}_4^\alpha\right) H^{\beta,\mu} c_4^\gamma + g_3 f^{abc}\left(\partial_\mu \bar{c}_3^a\right) C^{b,\mu} c_3^c, \tag{3.68}$$

where $f^{\alpha\beta\gamma}, f^{abc}$ are the structure constants of $SU(4)^{[3]}, SU(3)^{[12]}$ and c_4, c_3 are the corresponding ghost fields. They are directly related to the trilinear gauge boson vertices

$$\begin{aligned}\mathcal{L}_{\text{kin}} &\supset \frac{1}{4} H^{\alpha}_{\mu\nu} H^{\alpha,\mu\nu} + \frac{1}{4} C^{a}_{\mu\nu} C^{a,\mu\nu} \\ &\supset -g_4 f^{\alpha\beta\gamma} \left(\partial_\mu H^{\alpha}_{\nu}\right) H^{\beta,\mu} H^{\gamma,\nu} - g_3 f^{abc} \left(\partial_\mu C^{a}_{\nu}\right) C^{b,\mu} C^{c,\nu} ,\end{aligned} \tag{3.69}$$

where the field strengths $H^{\alpha}_{\mu\nu}$, $C^{a}_{\mu\nu}$ are defined in analogy to (3.16). The trilinear gauge boson vertices involving the VLQ are given by

Triple gauge boson interactions

$$\boxed{\begin{aligned}\mathcal{L}_{\text{kin}} \supset \quad & i g_s \left[\left(\partial_{[\mu} U^{\dagger}_{\nu]} T^a U^{\nu} \, G^{a,\mu} + \text{h.c.} \right) - \partial_{[\mu} G^{a}_{\nu]} \, U^{\mu\dagger} T^a U^{\nu} \right] \\ & + i \sqrt{g_4^2 - g_s^2} \left[\left(\partial_{[\mu} U^{\dagger}_{\nu]} T^a U^{\nu} \, G'^{a,\mu} + \text{h.c.} \right) - \partial_{[\mu} G'^{a}_{\nu]} \, U^{\mu\dagger} T^a U^{\nu} \right] .\end{aligned}} \tag{3.70}$$

Ghost interactions

Similarly, we obtain

$$\boxed{\begin{aligned}\mathcal{L}_{\text{ghost}} \supset \quad & i g_s \Big[\left(\partial_\mu \bar{c}_U\right) T^a U^{\mu} c_{G^a} - U^{\dagger}_{\mu} T^a \left(\partial^\mu \bar{c}_{U^\dagger}\right) c_{G^a} \\ & \qquad - \left(\partial_\mu \bar{c}_{G^a}\right) c_{U^\dagger} T^a U^{\mu} + \left(\partial_\mu \bar{c}_{G^a}\right) U^{\mu\dagger} T^a c_U \Big] \\ & + i \sqrt{g_4^2 - g_s^2} \Big[\left(\partial_\mu \bar{c}_U\right) T^a U^{\mu} c_{G'^a} - U^{\dagger}_{\mu} T^a \left(\partial^\mu \bar{c}_{U^\dagger}\right) c_{G'^a} \\ & \qquad - \left(\partial_\mu \bar{c}_{G'^a}\right) c_{U^\dagger} T^a U^{\mu} + \left(\partial_\mu \bar{c}_{G'^a}\right) U^{\mu\dagger} T^a c_U \Big] .\end{aligned}} \tag{3.71}$$

3.2.3 *Partial decay width*

DECAY WIDTH $\Gamma(U \to b\tau^+)$ As an application of the above Feynman rules, we calculate the $\mathcal{O}(\alpha_s)$ corrections to the decay width $\Gamma(U \to b\tau^+)$. The corresponding Feynman rules are shown in Figure 3.3. The Born matrix element is

$$\mathcal{M}^{(0)}_{U,b\tau} = g_4^2 \, M_U^2 \, \frac{d-2}{d-1} \tag{3.72}$$

in d dimensions, averaged over colors and the VLQ polarization. The decay width is calculated via

$$d\Gamma(U \to b\tau^+) = \frac{|\mathcal{M}_{U,b\tau}|^2}{2M_U} d\Phi_{b\tau}(k; k_1, k_2) , \tag{3.73}$$

where $d\Phi_{b\tau}(k; k_1, k_2)$ was defined in (2.7). Since (3.72) does not depend on the decay kinematics, we calculate

$$\Phi_{b\tau} \equiv \int d\Phi_{b\tau}(k; k_1, k_2) = \frac{(4\pi)^{2-d} \pi^{\frac{d-1}{2}}}{\Gamma\left(\frac{d-1}{2}\right)} \tag{3.74}$$

in isolation, the LO decay width then reads

$$\boxed{\Gamma^{(0)}(U \to b\tau^+)} = \frac{\left|\mathcal{M}^{(0)}_{U,b\tau}\right|^2}{2M_U} \Phi_{b\tau} = \boxed{\frac{g_4^2 \, M_U}{24\pi}} . \tag{3.75}$$

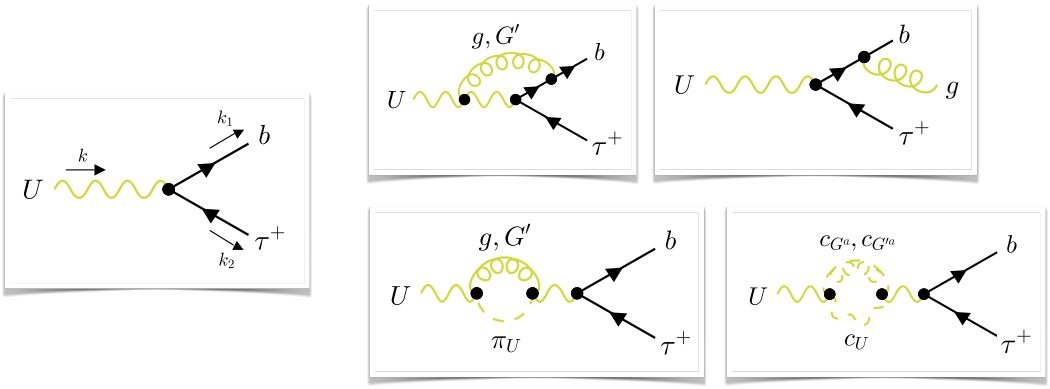

Figure 3.3: A selection of Feynman diagrams contributing to the decay width $U \to b\tau^+$. The diagram on the left shows the Born contributions. The diagrams on the right depict $\mathcal{O}(\alpha_s)$ virtual and real corrections to the same process.

As in $pp \to \tau^+\tau^-$, the virtual NLO corrections manifest as K factors to the LO matrix element. We write

$$\mathcal{M}^{(1)}_{U,b\tau} \equiv \left(K^{(1)}_b + K^{(1)}_U + K^{(1)}_V\right) \mathcal{M}^{(0)}_{U,b\tau}\,, \tag{3.76}$$

where $K^{(1)}_b$ comes from the field strength correction of the b quark, $K^{(1)}_U$ comes from the field strength correction of the VLQ U and $K^{(1)}_V$ comes from the vertex corrections. Examples of the latter two are depicted in Figure 3.3, while the former is shown in Figure 2.4.

We have previously calculated the one-loop field strength correction of quarks from a gluon loop in (2.22). In this context, it is necessary to include the coloron running in the loop as well, which results in the OS scheme expression

$$\boxed{K^{(1)}_b} = \frac{1}{2}\delta Z_b = \frac{C_F\,\alpha_s}{8\pi}\mathcal{N}\left(\frac{1}{\epsilon_{\text{IR}}} + L_\mu + \ln(x_U) - \frac{1}{2}\right)\,, \tag{3.77}$$

where $L_\mu = \ln(\mu_R^2/M_U^2)$ and $x_U = M_U^2/M_{G'}$. It should be noted that as a consequence of the coupling structure in (3.59), the UV poles proportional to g_s are always cancelled between the gluon and coloron contributions. To facilitate the presentation of intermediate results, we will set $x_U = 1$ in the following. Our final result will again contain the full dependence on x_U.

The VLQ OS field strength correction is defined as

$$\delta Z_U(k^2) = \frac{d}{dk^2}\Sigma_U(k^2)\bigg|_{k^2=M_U^2}\,, \tag{3.78}$$

including all diagrams with gluons, colorons, Goldstone bosons and ghosts running in the loop (see Figure 3.3), one finds

$$\boxed{K^{(1)}_U} = \frac{1}{2}\delta Z_U = \frac{\alpha_s}{8\pi}\mathcal{N}\left(-\frac{8}{3}\left(\frac{1}{\epsilon_{\text{IR}}} + L_\mu\right) + \frac{56}{9} - \frac{8}{9}\sqrt{3}\pi\right) \tag{3.79}$$

for $x_U = 1$. This agrees with [61, (14)].

The vertex correction for $x_U = 1$ reads

$$\boxed{K_V^{(1)}} = \frac{\alpha_s C_F}{4\pi}\mathcal{N}\left(-\frac{1}{\epsilon_{\rm IR}^2} - \frac{2+L_\mu}{\epsilon_{\rm IR}} - \sqrt{3}\pi + \frac{7\pi^2-12}{12} - \frac{4L_\mu + L_\mu^2}{2}\right), \quad (3.80)$$

consistent with [61, (15)]. The total virtual NLO correction to the decay width $\Gamma(U \to b\tau^+)$ is finally given by

$$\boxed{\Gamma^{(1)}_{\rm virtual}(U \to b\tau^+)} = 2\,\mathrm{Re}\left\{K_b^{(1)} + K_U^{(1)} + K_V^{(1)}\right\}\frac{\left|\mathcal{M}^{(0)}_{U,b\tau}\right|^2}{2M_U}\Phi_{b\tau}\,. \quad (3.81)$$

For the real contribution, we express the matrix element $\mathcal{M}_{U,b\tau g}$ in terms of the Mandelstam variables s_{12}, s_{13} and s_{23} (see (2.11)), where k_3 denotes the momentum of the radiated gluon (coloron radiation is neglected, which is suppressed by the coloron mass and does not contribute to the cancellation of the IR poles). We then parametrise the three-body phase space $d\Phi_{b\tau g}(k; k_1, k_2, k_3)$ as [62]

$$\int d\Phi_{b\tau g} = \frac{\left(M_U^2\right)^{1-2\epsilon}\Phi_{b\tau}}{(4\pi)^{\frac{d}{2}}\Gamma(1-\epsilon)}\int_0^1 d\lambda_1 d\lambda_2\, \lambda_1^{-\epsilon}(1-\lambda_1)^{-\epsilon}\lambda_2^{-\epsilon}(1-\lambda_2)^{1-2\epsilon}, \quad (3.82)$$

where $d = 4 - 2\epsilon$. Inserting

$$s_{12} = M_U^2(1-\lambda_2)(1-\lambda_1)\,, \quad s_{13} = M_U^2(1-\lambda_2)\lambda_1\,, \quad s_{13} = M_U^2\lambda_2\,, \quad (3.83)$$

and performing the integral over $d\lambda_1 d\lambda_2$, we find

$$\boxed{\Gamma^{(1)}_{\rm real}(U \to b\tau^+)} = \frac{g_4^2}{4\pi}\frac{M_U}{(d-1)}\frac{\alpha_s C_F}{4\pi}\Bigg(\frac{1}{\epsilon_{\rm IR}^2} + \frac{7}{2\epsilon_{\rm IR}} + \frac{2L_\mu}{\epsilon_{\rm IR}} + 7L_\mu + 2L_\mu^2 - \frac{5\pi^2}{6} + \frac{155}{12}\Bigg). \quad (3.84)$$

Finally, combining everything, we obtain

$$\boxed{\Gamma(U \to b\tau^+) = \frac{g_4^2 M_U}{24\pi}\left[1 + \Delta(x_U)\right]}\,, \quad (3.85)$$

with

$$\boxed{\begin{aligned}\Delta(x) = \frac{\alpha_s}{4\pi}\Bigg(&-\frac{4}{9}\left(7x^2 - 27x - 37\right) - \frac{16\pi^2}{9} \\ &- \frac{4}{9}\left(7x^2 - 22x - 9\right)B(x) - \frac{16}{3}\left(2x+1\right)C(x) \\ &+ \frac{2}{9}\left(7x^3 - 36x^2 + 21x + 30\right)\ln x\Bigg),\end{aligned}} \quad (3.86)$$

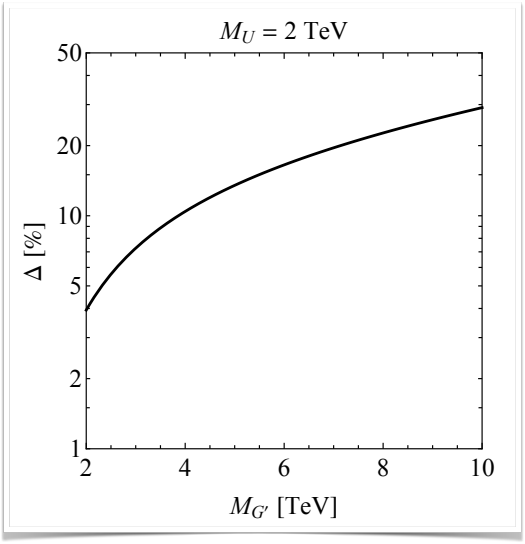

Figure 3.4: Numerical size of the $\mathcal{O}(\alpha_s)$ correction to the partial decay width $U \to b\tau^+$ as a function of the coloron mass $M_{G'}$, fixing the VLQ mass to $M_U = 2\,\text{TeV}$.

and

$$B(x) = \sqrt{(x-4)\,x}\,\ln\left[\frac{x+\sqrt{(x-4)\,x}}{2\sqrt{x}}\right],$$

$$C(x) = -\frac{\pi^2}{6} - \frac{1}{2}\ln^2\left[\frac{\sqrt{(x-4)\,x}-x}{2-x+\sqrt{(x-4)\,x}}\right] + \text{Li}_2\left[\frac{2}{x+\sqrt{(x-4)\,x}}\right] - \text{Li}_2\left[\frac{2}{2-x+\sqrt{(x-4)\,x}}\right]. \tag{3.87}$$

It should be noted that $\Delta(1) = \alpha_s/4\pi\,[76/3 - 32\pi/3\sqrt{3}]$, which is in agreement with [61, (18)]. The numerical size of the NLO QCD correction $\Delta(x_U)$ is shown in Figure 3.4. In the plot the mass of the singlet VLQ is set to $M_U = 2\,\text{TeV}$. It can be observed that the $\mathcal{O}(\alpha_s)$ corrections to the partial decay width $U \to b\tau^+$ grow with increasing coloron mass $M_{G'}$. Notice that the observed enhancement originates from logarithmic non-decoupling contributions of the form $\ln\left(M_{G'}^2/M_U^2\right)$. Further details can be found in [61, 63].

3.3 EXTENDED SCALAR SECTORS AND DARK MATTER (DM)

The EW sector of the SM

In order to introduce extended scalar sectors and their connections to DM, we begin by examining the EW sector of the SM in more detail. It is a gauge theory based on the gauge group

$$SU(2)_L \times U(1)_Y \,, \tag{3.88}$$

accordingly, the EW Lagrangian contains the part

$$\mathcal{L}_{\text{gauge}} = -\frac{1}{4} B^{\mu\nu} B_{\mu\nu} - \frac{1}{4} W^{I,\mu\nu} W^I_{\mu\nu} \,, \tag{3.89}$$

with $W^I_{\mu\nu}, B_{\mu\nu}$ defined in analogy to (3.16). Experimentally, one finds that not the W^I_μ, B_μ are the physical states, but rather the linear combinations

$$W^\pm_\mu = \frac{1}{\sqrt{2}} \left(W^1_\mu \mp i W^2_\mu \right) \,, \qquad Z_\mu = \frac{g_2 W^3_\mu - g_1 B_\mu}{\sqrt{g_1^2 + g_2^2}} \,, \qquad A_\mu = \frac{g_1 W^3_\mu + g_2 B_\mu}{\sqrt{g_1^2 + g_2^2}} \,. \tag{3.90}$$

Gauge boson masses

They come with non-zero masses [64]

$$m_W = 80.377(12)\ \text{GeV} \,, \qquad m_Z = 91.1876(21)\ \text{GeV} \,, \qquad m_\gamma = 0 \,. \tag{3.91}$$

This presents a theoretical problem, as the introduction of mass terms of the form

$$m_W^2 W^+_\mu W^{-,\mu} \tag{3.92}$$

violates gauge invariance, which can be seen by inserting the gauge transformation of the fields $W^\pm$. Similarly, mass terms for the fermions of the form

$$m_\psi \left(\bar{\psi}_L \psi_R + \bar{\psi}_R \psi_L \right) \tag{3.93}$$

also violate gauge invariance. This follows from the fact that ψ_L, ψ_R are not in the same representation under $SU(2)_L \times U(1)_Y$. What are the consequences of including such mass terms in the Lagrangian despite the violation of gauge invariance? Would this lead to tangible problems in the calculation of physical predictions?

3.3.1 *Unitarity violation without the Higgs*

We test it by giving the $V = W^\pm, Z$ fields a mass without concern for the underlying mechanism that provides it. The gauge boson at rest has momentum $k^\mu = (m_V, 0, 0, 0)$, where m_V is its mass. There are three polarization vectors

$$\epsilon^\mu_1 = (0,1,0,0) \,, \qquad \epsilon^\mu_2 = (0,0,1,0) \,, \qquad \epsilon^\mu_3 = (0,0,0,1) \tag{3.94}$$

that satisfy $\epsilon_i \cdot k = 0$. A boost along the z-axis transforms the gauge boson's momentum to $k^\mu = (E_k, 0, 0, k)$. This results in the third polarization vector becoming

The longitudinal polarization modes of massive gauge bosons

$$\epsilon^\mu_L(k) \equiv \epsilon^\mu_3(k) = \left(\frac{k}{m_V}, 0, 0, \frac{E_k}{m_V} \right) \,. \tag{3.95}$$

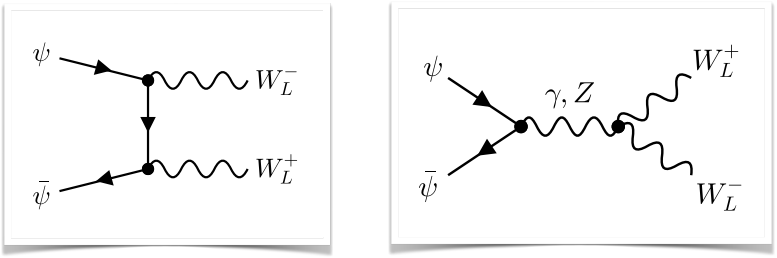

Figure 3.5: Feynman diagrams for the processes contributing to $\psi\bar{\psi} \to W_L^+ W_L^-$.

It corresponds to the longitudinal polarization of the massive gauge boson. The gauge boson propagator becomes

$$\frac{-i}{k^2 - m_V^2}\left(g^{\mu\nu} - \frac{k^\mu k^\nu}{m_V^2}\right). \tag{3.96}$$

We will now consider the production of a gauge boson pair via the fusion of fermions $\psi\bar{\psi} \to W^+W^-$, which could occur at a lepton or hadron collider. The corresponding Feynman diagrams are shown in Figure 3.5. In particular, we will focus on the production of longitudinal $W^\pm$ modes

$$\psi(k_\oplus)\bar{\psi}(k_\ominus) \to W_L^+(k_1) W_L^-(k_2)\,. \tag{3.97}$$

Since for large momenta ϵ_L^μ behaves as $\epsilon_L^\mu(k_i) \simeq k_i^\mu / m_W$, the corresponding contribution may violate unitarity in the limit $k_i \to \infty$. In the case of massless fermion fields ψ, this is not the case, as the gauge symmetry ensures that the contributions violating unitary cancel in the total sum. However, if $m_\psi \neq 0$, additional unitarity-violating contributions arise. Naively, one might expect these to originate from the longitudinal mode of the Z propagator in the right Feynman diagram of Figure 3.5. These contributions vanish, however, which is to be expected given the Higgs mechanism and the Feynman rules for the Goldstone bosons in Feynman gauge. There are no $\varphi^0 W^+ W^-$ or $\varphi^0\varphi^+\varphi^-$ vertices. Nevertheless, we do obtain contributions proportional to m_ψ from both diagrams in Figure 3.5. In the limit $s \to \infty$ and by inserting $\epsilon_L^\mu(k_i) \simeq k_i^\mu / m_W$, the leading contributions from the longitudinal W modes are of the form

An explicit calculation for $\psi\bar{\psi} \to W_L^+ W_L^-$ with massless fermions is given in [65, Chapter 21.2].

Violation of unitarity at high energies

$$\boxed{i m_\psi \frac{g_2^2}{4 m_W^2} \bar{v}_\psi(k_\ominus) u_\psi(k_\oplus) \sim m_\psi \sqrt{s}\,.} \tag{3.98}$$

One can show that such contributions lead to a violation of unitarity at $\sqrt{s} \sim 1$ TeV [12].

3.3.2 *Adding one Higgs doublet*

In order to address this issue, we introduce a complex scalar doublet field, designated as $H = (\phi_1 + i\phi_2, \phi_3 + i\phi_4)$, in the representation $(\mathbf{2}, 1)$ of the $SU(2)_L \times U(1)_Y$ group. This field is endowed with a potential of the form

The Higgs mechanism

$$V(H) = -\mu^2 H^\dagger H + \lambda\,(H^\dagger H)^2\,, \tag{3.99}$$

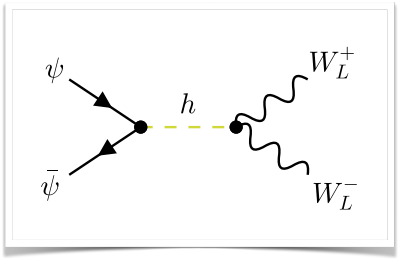

Figure 3.6: Additional process contributing to $\psi\bar{\psi} \to W_L^+ W_L^-$ via the s channel exchange of a Higgs h.

where $\mu^2 > 0$. The potential is minimized by the VEV

$$\langle H \rangle = \begin{pmatrix} 0 \\ \frac{v}{\sqrt{2}} \end{pmatrix} , \tag{3.100}$$

with $v = \sqrt{\mu^2/(2\lambda)}$. We reparameterize H by expanding its modes around the VEV

$$H = \begin{pmatrix} \varphi^+ \\ \frac{1}{\sqrt{2}} \left(v + h + \varphi^0 \right) \end{pmatrix} , \tag{3.101}$$

and find that the terms $\left(D_\mu H\right)^\dagger \left(D^\mu H\right)$ with

$$D_\mu H = \left(\partial_\mu + i g_2 \frac{\sigma^I}{2} W_\mu^I + i g_1 B_\mu \right) H \tag{3.102}$$

generate the correct mass terms for the vector bosons, while the Yukawa terms of the form (3.45) generate the masses for the fermions. How does this address the issue of unitarity violation in the UV?

In addition to the diagrams in Figure 3.5, there is now a contribution from the Higgs boson h running in the s-channel, depicted in Figure 3.6. It gives a leading contribution of the form

Cancellation of the unitarity-violating contributions by the Higgs

$$\boxed{-i \frac{y_\psi g_2}{2 m_W} \bar{v}_\psi(k_\ominus) u_\psi(k_\oplus) ,} \tag{3.103}$$

which, using $y_\psi = \sqrt{2} m_\psi / v = g_2 m_\psi / 2 m_W$, exactly cancels the unitary-violating contribution from (3.98). The SM with EW symmetry breaking based on one Higgs doublet is a consistent theory.

3.3.3 *Experimental evidence for the Higgs mechanism*

Experimental evidence for the Higgs mechanism

What experimental evidence supports the Higgs mechanism as outlined above? In 2012, the LHC collaborations identified a particle that closely resembles the massive radial mode predicted by the Higgs mechanism. Its has a mass of [64]

$$m_h = 125.25(17) \text{ GeV} , \tag{3.104}$$

is a scalar, and has the predicted decay modes with signal strengths

$$\begin{aligned} \mu_{WW} &= 1.00(8)\,, & \mu_{ZZ} &= 1.02(8)\,, & \mu_{\gamma\gamma} &= 1.10(7)\,, \\ \mu_{bb} &= 0.99(12)\,, & \mu_{\tau\tau} &= 0.91(9)\,, & \mu_{\mu\mu} &= 1.21(35)\,. \end{aligned} \tag{3.105}$$

Its decays to invisible final states, i.e. in association with E_T^{miss}, have been constrained to $\text{BR}(h \to \text{invisible}) < 9\%$. The decays to undetected final states have been constrained to $\text{BR}(h \to \text{undetected}) < 19\%$ [66]. In addition, we can define the parameter ρ_0, which is sensitive to new sources of $SU(2)_L \times U(1)_Y$ breaking. This parameter is given by [64, Review 10]

The ρ parameter

$$\boxed{\rho_0 = \frac{m_W^2}{m_Z^2\, c_w^2\, \rho}\,,} \tag{3.106}$$

where $c_w^2 = g_2^2/(g_1^2 + g_2^2)$ is the cosine of the weak mixing angle and $\rho = 1 + \rho_t$ accounts for higher-order corrections proportional to the top mass. From a global fit to experimental data, one finds [64, Review 10]

$$\rho_0 = 1.00038(20)\,, \tag{3.107}$$

which is consistent with the SM expectation $\rho_0 = 1$. In the event that additional scalar particles contribute to the breaking of the $SU(2)_L \times U(1)_Y$ gauge symmetry, the ρ_0 parameter becomes [64, Review 10]

$$\boxed{\rho_0 = \frac{\sum_{i=1}^{n} \left(I_i\,(I_i+1) - \frac{1}{4}Y_i^2\right) v_i^2}{\sum_{i=1}^{n} \frac{1}{2} Y_i^2 v_i^2}\,.} \tag{3.108}$$

This formula indicates that additional Higgs particles in representations corresponding to $(I_i, Y_i) = \left(\frac{1}{2}, \pm 1\right)$ or $(0,0)$ may be added to the SM without affecting the value of ρ_0. Other scalars with small VEVs or scalars transforming in larger $SU(2)_L$ representations may be added to the SM content as well. However, such models necessarily have to be large and complex. Consequently, the simplest model serving as a benchmark for extensions of the SM scalar sector are therefore models with two Higgs doublets.

3.3.4 *Adding a second Higgs doublet*

In this subchapter, we will consider 2HDMs with two Higgs fields H_1 and H_2 of hypercharge $Y = 1$. The most general scalar potential for H_1 and H_2 can have $\mathcal{CP}$-conserving and $\mathcal{CP}$-violating minima. In order to simplify the analysis, we will make the following assumptions: (1) $\mathcal{CP}$ is conserved in the Higgs sector, and (2) discrete symmetries eliminate all quartic terms odd in either of the doublets from the potential. In this case, the most general scalar potential is given by [67, 68]

The scalar potential of the 2HDM

$$\begin{aligned} V(H_1, H_2) = {} & m_{11}^2\, H_1^\dagger H_1 + m_{22}^2\, H_2^\dagger H_2 - m_{12}^2 \left(H_1^\dagger H_2 + H_2^\dagger H_1\right) + \frac{\lambda_1}{2}\left(H_1^\dagger H_1\right)^2 \\ & + \frac{\lambda_2}{2}\left(H_2^\dagger H_2\right)^2 + \lambda_3\, H_1^\dagger H_1 H_2^\dagger H_2 + \lambda_4\, H_1^\dagger H_2 H_2^\dagger H_1 \\ & + \frac{\lambda_5}{2}\left[\left(H_1^\dagger H_2\right)^2 + \left(H_2^\dagger H_1\right)^2\right]\,, \end{aligned} \tag{3.109}$$

where all parameters are real. As in the case of the SM, we expand both Higgs doublets around their VEVs v_i for $i = 1, 2$. We obtain

$$H_i = \begin{pmatrix} \varphi_i^+ \\ \frac{1}{\sqrt{2}}\left(v_i + h_i + i\varphi_i^0\right) \end{pmatrix}, \tag{3.110}$$

having a total of 8 real degrees of freedom in the fields H_1 and H_2. Considering the mass matrices resulting from the scalar potential [67],

The mass eigenstates

$$\begin{aligned} &\left(m_{12}^2 - \frac{\lambda_4+\lambda_5}{4}v^2\sin 2\beta\right)\begin{pmatrix}\varphi_1^- & \varphi_2^-\end{pmatrix}\begin{pmatrix}\tan\beta & -1 \\ -1 & 1/\tan\beta\end{pmatrix}\begin{pmatrix}\varphi_1^+ \\ \varphi_2^+\end{pmatrix}, \\ &\left(m_{12}^2 - \frac{\lambda_5}{2}v^2\sin 2\beta\right)\begin{pmatrix}\varphi_1^0 & \varphi_2^0\end{pmatrix}\begin{pmatrix}\tan\beta & -1 \\ -1 & 1/\tan\beta\end{pmatrix}\begin{pmatrix}\varphi_1^0 \\ \varphi_2^0\end{pmatrix}, \\ &-\begin{pmatrix}h_1 & h_2\end{pmatrix}\begin{pmatrix} m_{12}^2\tan\beta + \lambda_1 v^2\cos^2\beta & -m_{12}^2 + \frac{\lambda_{345}}{2}v^2\sin 2\beta \\ -m_{12}^2 + \frac{\lambda_{345}}{2}v^2\sin 2\beta & m_{12}^2/\tan\beta + \lambda_2 v^2\sin^2\beta \end{pmatrix}\begin{pmatrix}h_1 \\ h_2\end{pmatrix}, \end{aligned} \tag{3.111}$$

where $\tan\beta = v_2/v_1$, $v^2 = v_1^2 + v_2^2$ and $\lambda_{345} = \lambda_3 + \lambda_4 + \lambda_5$, it can be observed that the first two matrices have a vanishing determinant. This is to be expected from Goldestone's theorem, given that three degrees of freedom are required to give the $W^\pm$ and Z bosons their masses. The states corresponding to the zero eigenvalues are the Goldstone bosons that provide the longitudinal modes of the gauge bosons. The remaining mass eigenstates can be found by diagonalizing the first two mass matrices by a rotation with angle β and the last mass matrix by a rotation with angle α ($\alpha \neq \beta$ in general). This results in the physical mass eigenstates [67]

$$\boxed{\begin{aligned} H^\pm &= -\varphi_1^\pm\sin\beta + \varphi_2^\pm\cos\beta\,, \quad A = -\varphi_1^0\sin\beta + \varphi_2^0\cos\beta\,, \\ h &= -h_1\sin\alpha + h_2\cos\alpha\,, \qquad H = h_1\cos\alpha + h_2\sin\alpha\,, \end{aligned}} \tag{3.112}$$

which generically all have non-vanishing masses M_{H^+}, M_A, M_H, m_h. It is implicitly assumed that h is the lighter of the two scalar states, i.e. $m_h \leq M_H$. It should be noted that if the initial Higgs doublets were rotated by $\tilde{H}_1 = H_1\cos\beta + H_2\sin\beta$ and $\tilde{H}_2 = -H_1\sin\beta + H_2\cos\beta$, only $\tilde{H}_1$ would come with a non-zero VEV, while the VEV of $\tilde{H}_2$ would vanish. Accordingly, the scalar state obtained via [67]

The alignment limit

$$\boxed{h_{\text{SM}} = h_1\cos\beta + h_2\sin\beta = h\sin(\alpha-\beta) - H\cos(\alpha-\beta)} \tag{3.113}$$

has the exact properties of the SM Higgs. It follows that for $\cos(\alpha-\beta) = 0$, we have $h = h_{\text{SM}}$, i.e. the lightest scalar mode of the 2HDM exhibits the exact properties of the SM Higgs. This is referred to as the *alignment limit*.

In order to couple the Higgs doublets to the SM fermions, we write down Yukawa interactions analogous to (3.45)

$$\begin{aligned} \mathcal{L}_{\text{Yukawa}} = -\sum_{k=1,2}\Big(&(Y_u^k)_{ij}\,\bar{q}_L^i\tilde{H}_k u_R^j + (Y_d^k)_{ij}\,\bar{q}_L^i H_k d_R^j \\ &+ (Y_e^k)_{ij}\,\bar{\ell}_L^i H_k e_R^j + \text{h.c.}\Big)\,. \end{aligned} \tag{3.114}$$

The presence of two Higgs doublets introduces a new complexity. While in the case of a single Higgs doublet the Yukawa interactions are diagonal in flavor space with respect to the fermion mass basis, this is generically no longer the case in the 2HDM. When both Higgs doublets couple to the same fermion flavor, diagonalizing the mass matrices in general no longer coincides with diagonalizing the Yukawa interaction matrices. This results in flavor-changing Higgs interactions (i.e. flavor-changing neutral currents). Since the experimental bounds on such processes are strong, one generally assumes a *natural flavor conservation hypothesis*, which states that only one of the two Higgs doublets couples to a given fermion flavor. This can be achieved, for instance, by imposing a $\mathbb{Z}_2$ symmetry under which the two doublets are charged differently. This also eliminates the quartic terms odd in either of the doublets from the potential in (3.109). The possibilities for the Yukawa assignments are then [69]

Yukawa assignments under the flavor conservation hypothesis

$$\begin{aligned} &Y_u^1 = Y_d^1 = Y_e^1 = 0\,, \quad \text{(type I)}\,, && Y_u^1 = Y_d^2 = Y_e^2 = 0\,, \quad \text{(type II)}\,, \\ &Y_u^1 = Y_d^1 = Y_e^2 = 0\,, \quad \text{(type III)}\,, && Y_u^1 = Y_d^2 = Y_e^1 = 0\,, \quad \text{(type IV)}\,. \end{aligned} \tag{3.115}$$

For the type II 2HDM in the alignment limit, the phenomenologically relevant Yukawa interactions are [69]

$$\begin{aligned} \mathcal{L}_{\text{Yukawa}} \supset &- \frac{y_t}{\sqrt{2}}\,\bar{t}\left(h - \cot\beta\, H + i\cot\beta\, A\gamma^5\right) t \\ &- \sum_{\psi=b,\tau} \frac{y_\psi}{\sqrt{2}}\bar{\psi}\left(h + \tan\beta\, H + i\tan\beta\, A\gamma^5\right)\psi \\ &+ \left(\frac{y_t}{\sqrt{2}} V_{tb}\cot\beta\, H^+ \bar{t}_R b_L + \frac{y_b}{\sqrt{2}} V_{tb}\tan\beta\, H^+ \bar{t}_L b_R + \text{h.c.}\right), \end{aligned} \tag{3.116}$$

with y_t, y_b, y_τ the Yukawa couplings of (3.46). In above expression, the element V_{tb} of the Cabibbo-Kobayashi-Maskawa (CKM) matrix appeared. It is given by

$$V_{tb} \equiv [U_u^L]^*_{i3}\,[U_d^L]_{i3}\,, \tag{3.117}$$

where U_u^L, U_d^L are the unitary 3×3 matrices introduced in the singular value decomposition of the Yukawa couplings Y_f below (3.45). It quantifies the shift between the fermion *mass* eigenstates, for which the Yukawa couplings take the diagonal form λ_f, and the *flavor* eigenstates, for which all gauge interactions are flavor-independent.

3.3.5 *The 2HDM with a pseudoscalar DM mediator*

There is compelling evidence for the existence of additional matter within our galaxies. This matter interacts gravitationally but is not composed of ordinary baryonic matter. It constitutes approximately 25% of the energy density in the Universe and is referred to as DM. While the true nature of DM remains unknown, numerous experiments are currently searching for corresponding signals. These experiments can be broadly categorized into three classes: *accelerator experiments* attempting to create DM in collisions, *indirect detection experiments* searching for the

annihilation products of DM, and *direct detection experiments* searching for direct interactions of DM with baryonic matter.

Direct detection experiments look for low-energy interactions between DM and a detector body made up of baryonic matter. Such interactions can be described in a model-independent way by using an EFT. Assuming that the DM particle χ is a Dirac fermion, the possible effective interaction vertices at zero momentum transfer are [70]

Effective DM interactions

$$\begin{aligned}&\lambda_{N,e}\left[\bar{\chi}\chi\right]\left[\bar{\psi}_N\psi_N\right]+\lambda_{N,o}\left[\bar{\chi}\gamma^\mu\chi\right]\left[\bar{\psi}_N\gamma_\mu\psi_N\right]\\&+\xi_{N,e}\left[\bar{\chi}\gamma^\mu\gamma^5\chi\right]\left[\bar{\psi}_N\gamma_\mu\gamma^5\psi_N\right]-\frac{\xi_{N,e}}{2}\left[\bar{\chi}\sigma^{\mu\nu}\chi\right]\left[\bar{\psi}_N\sigma_{\mu\nu}\psi_N\right],\end{aligned}\tag{3.118}$$

where ψ_N is the nucleon spinor. One can show that $\lambda_{N,e}, \lambda_{N,o}$ lead to interactions that do not depend on the nucleon spin, i.e. are spin-independent (SI), while the interactions induced by $\xi_{N,e}, \xi_{N,o}$ are spin-dependent (SD). In the SI case, the contributions from the individual nucleons add up, resulting in a DM-nucleus interaction cross section of [70]

SI DM-nucleus interactions

$$\sigma^{\mathrm{SI}}=\frac{4\mu_\chi^2}{\pi}\left(\lambda_p Z+\lambda_n\left(A-Z\right)\right)^2,\tag{3.119}$$

where $\mu_\chi = M_\chi m_A / \left(M_\chi + m_A\right)$ with m_A the nucleus mass and Z (A) is the nucleus charge (total number of nucleons). It is noteworthy that there is a strong enhancement $\sigma^{\mathrm{SI}} \sim A^2$ for $\lambda_p \approx \lambda_n$ in the case of heavy nuclei. For SD interactions, the differing spins of the various nucleons result in cancellations among the various interaction amplitudes, thereby reducing the overall cross section for the DM-nucleus interaction. Consequently, the constraints derived from direct detection experiments on $\lambda_{N,e}, \lambda_{N,o}$ are considerably stronger than those on $\xi_{N,e}, \xi_{N,o}$.

SD DM-nucleus interactions

In contrast, accelerator experiments, including the LHC, search for DM particles produced directly in high-energy collisions. An intriguing class of DM models that can be probed at colliders is that of mediator models featuring a mediator particle charged under both the SM and dark quantum numbers. In particle collisions, the mediator particle is produced and then subsequently decays to a pair of DM particles. In order to describe such scenarios, it is not sufficient to employ EFTs of the form (3.118), since the DM mediator must be treated as a dynamical degree of freedom to describe its production at the LHC. It is therefore desirable to establish suitable benchmarks for the DM mediator that capture the main signatures to be expected at colliders. Given that models inducing effective interactions proportional to $\lambda_{N,o}, \lambda_{N,e}$ at low energies are already subject to stringent constraints from direct detection searches, it is reasonable to consider mediator benchmarks that do not generate these at the tree level. Such models include mediators with pseudo-scalar or axial-vector interactions.

DM mediator scenarios

Coupling a pseudoscalar DM mediator to an extended scalar sector

Consequently, we introduce a new pseudoscalar P coupled to DM via

$$\boxed{\mathcal{L}_\chi = -iy_\chi P\bar{\chi}\gamma^5\chi\,.}\tag{3.120}$$

We can further couple P to the extended scalar sector of the 2HDM (and thus, the SM) by adding the terms

$$\boxed{\frac{1}{2}M_P^2 P^2 + P\left(ib_P H_1^\dagger H_2 + \text{h.c.}\right) + P^2\left(\lambda_{P1}\, H_1^\dagger H_1 + \lambda_{P2}\, H_2^\dagger H_2\right)} \tag{3.121}$$

to the scalar potential in (3.109). This does not alter the mass eigenstates $H^\pm, h, H$, but in the pseudoscalar sector the mass eigenstate A now mixes with the state P. The resulting mass matrix can be diagonalized by a rotation with angle θ, giving two mass eigenstates

$$\begin{pmatrix} A' \\ a \end{pmatrix} = \begin{pmatrix} \cos\theta & \sin\theta \\ -\sin\theta & \cos\theta \end{pmatrix} \begin{pmatrix} A \\ P \end{pmatrix}, \tag{3.122}$$

where we assume $M_a < M_{A'}$ without loss of generality. From this point forward, we will refer to A' simply by A, dropping the dash. The resulting model is known as 2HDM+a. The Yukawa assignments of the type II 2HDM+a in the alignment limit are [69]

Yukawa assignments in the 2HDM+a

$$\begin{aligned} \mathcal{L}_{\text{Yukawa}} \supset & -\frac{y_t}{\sqrt{2}}\bar{t}\left(h - \cot\beta\, H + i\cot\beta\,\left(\cos\theta\, A - \sin\theta\, a\right)\gamma^5\right) t \\ & - \sum_{\psi=b,\tau} \frac{y_\psi}{\sqrt{2}}\bar{\psi}\left(h + \tan\beta\, H + i\tan\beta\,\left(\cos\theta\, A - \sin\theta\, a\right)\gamma^5\right)\psi \\ & + \frac{y_t}{\sqrt{2}} V_{tb}\cot\beta\, H^+ \bar{t}_R b_L + \frac{y_b}{\sqrt{2}} V_{tb}\tan\beta\, H^+ \bar{t}_L b_R + \text{h.c.} \\ & - i y_\chi\left(\sin\theta\, A + \cos\theta\, a\right)\bar{\chi}\gamma^5\chi\,. \end{aligned} \tag{3.123}$$

Further phenomenologically relevant trilinear interaction terms arise from the scalar potentials (3.121) and (3.109). The corresponding couplings in the alignment limit are of the form [69]

Trilinear Higgs interactions

$$\begin{aligned} g_{haa} &= \frac{1}{m_h v}\Big[\quad \left(m_h^2 - 2M_H^2 + 4M_{H^\pm}^2 - 2M_a^2 - 2\lambda_3 v^2\right)\sin^2\theta \\ &\qquad - 2\left(\lambda_{P1}\cos^2\beta + \lambda_{P2}\sin^2\beta\right) v^2\cos^2\theta\Big]\,, \\ g_{Haa} &= \frac{1}{M_H v}\Big[\quad \cot(2\beta)\left(2m_h^2 - 4M_H^2 + 4M_{H^\pm}^2 - 2\lambda_3 v^2\right)\sin^2\theta \\ &\qquad + \sin(2\beta)\left(\lambda_{P1} - \lambda_{P2}\right) v^2\cos^2\theta\Big]\,, \\ g_{Aah} &= \frac{1}{M_A v}\Big[\quad m_h^2 - 2M_H^2 - M_A^2 + 4M_{H^\pm}^2 - M_a^2 - 2\lambda_3 v^2 \\ &\qquad + 2\left(\lambda_{P1}\cos^2\beta + \lambda_{P2}\sin^2\beta\right) v^2\Big]\sin\theta\cos\theta\,. \end{aligned} \tag{3.124}$$

Note that ahh is $\mathcal{CP}$-violating and Hhh vanishes in the alignment limit. Furthermore, there are trilinear vertices involving gauge bosons. Phenomenologically, the most relevant are HaZ and H^+aW^-, which are given in [69, (4.8), (4.12)]. Note that aW^+W^- and aZZ are $\mathcal{CP}$-violating, while ahZ, HW^+W^-, HZZ and H^+hW^- all vanish in the alignment limit.

This concludes our introduction of the 2HDM+a model. We have demonstrated why the Higgs doublet must be introduced in the SM in order to avoid the violation of unitarity at large energies, that additional Higgs doublets may be added without causing tension with experimental data, and how such an extended scalar sector may be connected to DM.

Part (I)

PRECISION

Precision matters.

— Mookie Betts (baseball player)

4

PRECISE THEORETICAL PREDICTIONS FOR THE LHC

Be precise.
A lack of precision is dangerous
when the margin of error is small.

— Donald Rumsfeld
(former US Secretary of Defense)

In Section 2, we presented the fundamental concepts underlying the calculation of NLO+PS accurate predictions for the LHC. By now, NLO+PS has become standard in particle physics phenomenology, certainly for SM processes, but also for many BSM scenarios. Even automated NLO+PS tools are available that, in principle, allow to simulate arbitrary BSM models. With the HL-LHC on the horizon, however, and its ability to measure SM observables with percent-level uncertainties, NLO+PS is no longer sufficient to match the precision on the theoretical side. Consequently, the community has progressed towards NNLO or even next-to-next-to-next-to-leading order (N^3LO) accurate theoretical predictions. This section will highlight important concepts of precision phenomenology, with a particular focus on calculations in the SMEFT. It is beyond the scope of this section to provide a comprehensive review of the field. Indeed, many of the topics would warrant a separate thesis in their own right. Nevertheless, we aim to provide an overview of aspects of precision calculations that will be relevant to the project presented in Section 5.

In essence, there are two main components that render beyond-NLO calculations more complex: The first is the increase in the number of loops, which correspond to complicated integrals that have to be solved. The second is the increase in the number of final-state particles, which leads to more scales (more degrees of freedom) being present in the corresponding amplitude expressions. In Chapter 4.1, we will discuss how to deal with the former, including the renormalization of the SMEFT contributions at the two-loop level. The efficient calculation of diagrams with more final-state particles will be the topic of Chapter 4.2. Finally, as in the NLO case, the virtual and real corrections must be combined in order to cancel all IR poles, and the full NNLO predictions must be consistently matched to the PS generators in order for the latter to provide subsequent emissions without overcounting. This is accomplished by the `POWHEG` $\texttt{MiNNLO}_{\text{PS}}$ method, which will be introduced in Chapter 4.3.

4.1 Multiloop Diagrams (Virtual Corrections)

4.1.1 *Solving Loop Integrals*

This chapter draws upon the introduction to IBP relations presented in [71].

Solving the integrals that arise in multiloop Feynman diagrams is frequently a major bottleneck in precision calculations. While the evaluation of integrals remains a challenging undertaking, there are now a number of techniques available that decompose the problem into more manageable components. A few of these techniques will be introduced below, including the tensor reduction, the integration by parts (IBP) relations, and the expansion in external momenta.

Note that due to momentum conservation, a diagram with $(E+1)$ external legs generally has E linearly independent momenta.

Let us define a generic two-loop integral. The integral is defined by two integration momenta q_1, q_2, and E linearly independent external momenta labelled $k_1, \ldots, k_E$. We combine the two writing $p_i = q_1, q_2, k_1, \ldots, k_E$ with $i \in [0, M]$ and $M = 2 + E$. As previously defined, the Mandelstam invariants are $s_{ij} = q_i \cdot q_j$ for $i \leq j$. This implies that

$$N = 3 + 2E \tag{4.1}$$

of them, namely those with $i \leq 2$, contain integration variables. The remaining s_{ij} are products of external momenta $k_i \cdot k_j$. Furthermore, the diagram must contain $I = 4 + E$ internal lines that are associated with the propagators D_a for $a = [1, I]$. In general, $N - I = E - 1$ can be greater than zero, indicating that there are more scalar products s_{ij} containing integration variables than there are denominators. In this case, we extend the denominators by additional *irreducible numerators* $D_{I+1}, \ldots, D_N$, which allow us to write

Irreducible numerators

$$D_a = \sum_{i=1}^{2} \sum_{j=1}^{M} \alpha_a^{ij} s_{ij} + \beta_a \,, \tag{4.2}$$

where α_a^{ij}, β_a are numbers, such that $D_1, \ldots, D_N$ are linearly independent. Consequently, one can solve for s_{ij}, giving

$$s_{ij} = \sum_{a=1}^{N} \alpha_{ij}^{a} \left(D_a - \beta_a \right) \,. \tag{4.3}$$

Two-loop integrals (tensor)

A generic two-loop integral is then of the form

$$\boxed{\mathcal{I}\left[f(q_1, q_2); n_1, \ldots, n_N\right] \equiv (\mu_R^2)^{2\epsilon} \int \frac{d^d q_1}{(2\pi)^d} \frac{d^d q_2}{(2\pi)^d} \frac{f(q_1, q_2)}{D_1^{n_1} \ldots D_N^{n_N}} \,,} \tag{4.4}$$

with $(n_1, \ldots, n_N) \in \mathbb{Z}^N$. In general, the numerator $f(q_1, q_2)$ may involve products of integration variables, such as $q_1 \cdot q_2$, or tensor structures with open Lorentz indices, such as $q_1^\mu q_2^\nu$. Fortunately, these integrals can always be reduced to a sum of scalar integrals with $f(q_1, q_2) = 1$.

Tensor Reduction The tensor structure of integrals with open Lorentz indices can be inferred from Lorentz symmetry arguments. The first few are

Tensor reduction

$$\begin{aligned}
\mathcal{I}\left[q_\bullet^\mu; n_1, \ldots, n_N\right] &= C_i^\bullet\, k_i^\mu\,, \\
\mathcal{I}\left[q_\bullet^\mu q_\bullet^\nu; n_1, \ldots, n_N\right] &= C_{00}^\bullet g^{\mu\nu} + C_{ij}^\bullet\, k_i^\mu k_j^\nu\,, \\
\mathcal{I}\left[q_\bullet^\mu q_\bullet^\nu q_\bullet^\rho; n_1, \ldots, n_N\right] &= C_{00i}^\bullet g^{\{\mu\nu} k_i^{\rho\}} + C_{ijk}^\bullet\, k_i^{\{\mu} k_j^\nu k_k^{\rho\}}\,, \\
\mathcal{I}\left[q_\bullet^\mu q_\bullet^\nu q_\bullet^\rho q_\bullet^\sigma; n_1, \ldots, n_N\right] &= C_{0000}^\bullet g^{\{\mu\nu} g^{\rho\sigma\}} + C_{00ij}^\bullet\, g^{\{\mu\nu} k_i^\rho k_j^{\sigma\}} + C_{ijkl}^\bullet\, k_i^{\{\mu} k_j^\nu k_k^\rho k_l^{\sigma\}}\,.
\end{aligned} \tag{4.5}$$

In above equation, $q_\bullet$ is used to represent an integration momentum q_1, q_2. The coefficients $C^\bullet$ are composed of loop integrals that do not contain open Lorentz indices in the numerator. It should be noted that these coefficients are dependent on the specific combination of integration momenta q_1, q_2 on the l.h.s, indicated by the superscript $\bullet$. The coefficients $C^\bullet$ can be determined by contracting both sides of (4.5) with external loop momenta or the metric tensor, resulting in a linear set of equations.

Upon solving these equations, only integrals with scalar products of the integration variables in the numerators remain. These can be further decomposed into scalar integrals with $f(q_1, q_2) = 1$. To demonstrate this, let us consider an integral of the form $\mathcal{I}\left[s_{ij}; n_1, \ldots, n_N\right]$. By means of (4.3), it can be transformed to

$$\sum_{a=1}^{N} \alpha_{ij}^a \mathcal{I}\left[1; n_1, \ldots, n_a - 1, \ldots, n_N\right] - \sum_{a=1}^{N} \alpha_{ij}^a \beta_a \mathcal{I}\left[1; n_1, \ldots, n_N\right]\,, \tag{4.6}$$

which only involves scalar integrals. The recursive application of this strategy to integrals involving multiple scalar products in the numerator equally results in a sum of scalar integrals.

IBP Relations Thus far, we have achieved to reduce all two-loop integrals to a sum of scalar integrals of the form

Two-loop integrals (scalar)

$$\boxed{\mathcal{I}\left[n_1, \ldots, n_N\right] \equiv (\mu_R^2)^{2\epsilon} \int \frac{d^d q_1}{(2\pi)^d} \frac{d^d q_2}{(2\pi)^d} \frac{1}{D_1^{n_1} \ldots D_N^{n_N}}\,,} \tag{4.7}$$

with $(n_1, \ldots, n_N) \in \mathbb{Z}^N$. Fortunately, such integrals can be decomposed further into a linear combination of so-called *master integrals* by applying symmetry relations. The most well-known of these are IBP identities. They result from the invariance of Feynman integrals under infinitesimal transformations of the form

$$q_i \to q_i + \delta\alpha\, p_j\,, \tag{4.8}$$

once more using the notation introduced at the beginning of this subchapter. Such infinitesimal transformations form a Lie algebra

$$(\mu_R^2)^{2\epsilon} \int \frac{d^d q_1}{(2\pi)^d} \frac{d^d q_2}{(2\pi)^2}\, O_{ij} \frac{1}{D_1^{n_1} \ldots D_N^{n_N}} = 0 \tag{4.9}$$

with $O_{ij} = \frac{\partial}{\partial q_i} \cdot q_j$, where $i \leq 2$ and $j \geq i$. The corresponding Lie bracket is

$$\left[O_{ij}, O_{i'j'}\right] = \delta_{ij'} O_{i'j} - \delta_{i'j} O_{ij'}\,. \tag{4.10}$$

IBP relations Rewriting the O_{ij} in terms of the propagators D_a, one finds

$$\boxed{\begin{aligned} O_{ij} &= d\,\delta_{ij} + \sum_{a=1}^{N}\sum_{b=1}^{N}\sum_{m=1}^{M} \alpha_a^{mi}\alpha_{mj}^{b}(1+\delta_{mi})(D_b-\beta_b)\frac{\partial}{\partial D_a} && (j\leq 2)\,, \\ O_{ij} &= \sum_{a=1}^{N}\left[\sum_{m=1}^{2}\sum_{b=1}^{N} \alpha_a^{mi}\alpha_{mj}^{b}(1+\delta_{mi})(D_b-\beta_b) + \sum_{m=3}^{M}\alpha_a^{mi}s_{mj}\right]\frac{\partial}{\partial D_a} && (j>2)\,. \end{aligned}} \tag{4.11}$$

It should be noted that multiplying D_b to the scalar integral will result in a lowering of the corresponding index n_b, while the action of $\partial/\partial D_a$ will result in an increase of n_a by one (or, in the case when $n_a = 0$, the integral will be set to zero). Therefore, the operators O_{ij} relate integrals with different $(n_1,\ldots,n_N)$ by virtue of (4.9). If these relations are used in a clever manner, it is possible to relate complicated integrals to a sum of less complicated ones. Applying this recursively results in a small subset of master integrals that must be calculated. This can either be done analytically or with numerical techniques. To illustrate the power of IBP relations, we present an example.

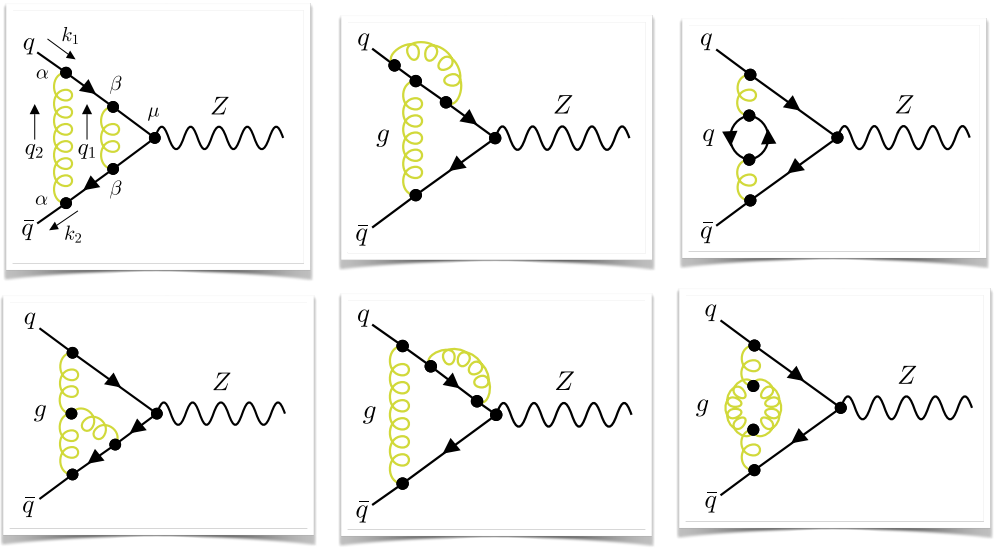

Figure 4.1: Feynman diagrams for the two-loop K-factor to the partonic scattering process $q\bar{q} \to \tau^+\tau^-$ with a Z boson exchange.

EXAMPLE: DY As in the one-loop case (see (2.18)), the two-loop contribution to the $q\bar{q} \to Z$ vertex can be expressed as the tree-level matrix element multiplied by a K-factor

$$\left(\frac{\alpha_s}{4\pi}\right)^2 \mathcal{M}^{(2)}_{q\bar{q},\tau\tau} = K^{(2)}\mathcal{M}^{(0)}_{q\bar{q},\tau\tau}\,. \tag{4.12}$$

Examples of Feynman diagrams that contribute to the bare $K_0^{(2)}$ are shown in Figure 4.1. Let us examine the first diagram in greater detail. Its contribution to $K_0^{(2)}$ can be determined from

$$\mathcal{M}^{(2)*}_{0,q\bar{q},\tau\tau}\mathcal{M}^{(0)}_{q\bar{q},\tau\tau}\,, \tag{4.13}$$

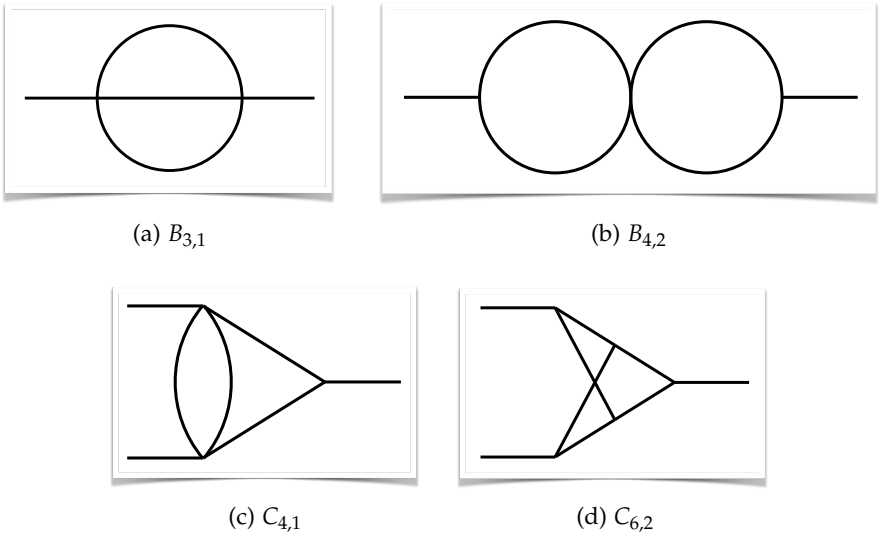

(a) $B_{3,1}$ (b) $B_{4,2}$

(c) $C_{4,1}$ (d) $C_{6,2}$

Figure 4.2: Scalar two-loop integrals.

to which we get a contribution from the vector coupling of the Z (we avoid the discussion of the treatment of γ_5 in d dimensions here, see [24, Sec. 4.4] for further information) proportional to

$$\int \frac{d^d q_1 d^d q_2}{(2\pi)^{2d}} \frac{\mathrm{Tr}\left[\not{k}_2 \gamma^\alpha (\not{k}_2+\not{q}_2)\gamma^\beta (\not{k}_2+\not{q}_{12})\gamma^\mu (\not{k}_1+\not{q}_{12})\gamma_\beta (\not{k}_2+\not{q}_2)\gamma_\alpha \not{k}_1 \gamma_\mu\right]}{(k_2+q_2)^2 (k_2+q_{12})^2 (k_1+q_{12})^2 (k_1+q_2)^2 q_1^2 q_2^2} \tag{4.14}$$

in the unpolarized case, with $q_{12} = q_1 + q_2$ for brevity. In (4.14), we have used *Casimir's trick* for massless fermions and further stripped off all couplings and the color factor

$$T^a T^b T^b T^a = C_F^2 \, \mathbb{1} \,. \tag{4.15}$$

After simplifying the Dirac algebra, the numerator of (4.14) decomposes into a sum of scalar products of the integration momenta q_1, q_2 and external momenta k_1, k_2. As denominators, we choose

$$\begin{aligned} &D_1 = (k_2+q_2)^2 \,, \quad && D_2 = (k_2+q_{12})^2 \,, \quad && D_3 = (k_1+q_{12})^2 \\ &D_4 = (k_1+q_2)^2 \,, \quad && D_5 = q_1^2 \,, && D_6 = q_2^2 \,, \end{aligned} \tag{4.16}$$

which we extend by the irreducible numerator

$$D_7 = (q_1+q_2)^2 \,. \tag{4.17}$$

Without the trace in the numerator, (4.14) is of the form $\mathcal{I}[1,1,1,1,1,1,0]$. With the trace, and employing the strategy outlined in (4.6), (4.14) can be expressed as a sum over integrals of lower sectors (including less denominators), such as $\mathcal{I}[0,1,1,1,1,1,0]$ or $\mathcal{I}[0,1,-1,1,1,1,0]$. After the IBP reduction, the master integrals that remain are

$$\begin{aligned} &B_{3,1} \equiv \mathcal{I}[0,1,0,1,0,1,0] \,, \quad && B_{4,2} \equiv \mathcal{I}[1,1,1,1,0,0,0] \,, \\ &C_{4,1} \equiv \mathcal{I}[0,1,1,0,1,1,0] \,. \end{aligned} \tag{4.18}$$

They are depicted diagrammatically in Figure 4.4, along with the integral $C_{6,2}$ that appears in other Feynman diagrams of Figure 4.1. The aforementioned master integrals are sufficiently simple to be calculated analytically, given that all internal lines are massless. They are [23]

$$\begin{aligned}
B_{3,1}(s) &= \frac{-\mathcal{N}^2}{(16\pi^2)^2}\left(-\frac{\mu_R^2}{s}\right)^{2\epsilon} s\left(-\frac{1}{4\epsilon}-\frac{13}{8}\right), \\
B_{4,2}(s) &= \frac{-\mathcal{N}^2}{(16\pi^2)^2}\left(-\frac{\mu_R^2}{s}\right)^{2\epsilon}\left(\frac{1}{\epsilon^2}+\frac{4}{\epsilon}+12\right), \\
C_{4,1}(0,0,s) &= \frac{-\mathcal{N}^2}{(16\pi^2)^2}\left(-\frac{\mu_R^2}{s}\right)^{2\epsilon}\left(\frac{1}{2\epsilon^2}+\frac{5}{2\epsilon}+\left(\zeta_2+\frac{19}{2}\right)\right), \\
C_{6,2}(0,0,s) &= \frac{-\mathcal{N}^2}{(16\pi^2)^2}\left(-\frac{\mu_R^2}{s}\right)^{2\epsilon}\frac{1}{s^2}\left(\frac{1}{\epsilon^4}-\frac{5\zeta_2}{\epsilon^2}-\frac{27\zeta_3}{\epsilon}-23\zeta_2^2\right),
\end{aligned} \tag{4.19}$$

where ζ_2, ζ_3 are values of the Riemann zeta function and where we followed the conventions of (2.13). The total unrenormalized $K_0^{(2)}$ in terms of these master integrals is given in [23, (2.25)], which we have recalculated explicitly using *FeynCalc* [72–75] and *LiteRed* [76], finding perfect agreement. The renormalization of $K^{(2)}$ is achieved via [23]

$$K^{(2)} \equiv K_0^{(2)} - \frac{\beta_0}{\epsilon} K_0^{(1)}, \tag{4.20}$$

where $K_0^{(1)}$ is the bare one-loop K factor defined in (2.18) and β_0 is the usual renormalization group factor of QCD given in (2.26). Overall, one finds

$$\begin{aligned}
K^{(2)} = &\left(\frac{\alpha_s}{4\pi}\right)^2\left(-\frac{\mu_R^2}{s}\right)^{2\epsilon}\mathcal{N}^2 \\
&\times\Bigg[\quad C_F^2\left(\frac{2}{\epsilon^4}+\frac{6}{\epsilon^3}+\frac{41}{2\epsilon^2}+\frac{6\zeta_2-20\zeta_3+\frac{221}{4}}{\epsilon}-\frac{68\zeta_2^2}{5}\right. \\
&\qquad\left.+29\zeta_2-54\zeta_3+\frac{1151}{8}\right) \\
&+C_F C_A\left(-\frac{11}{6\epsilon^3}+\frac{\zeta_2-\frac{83}{9}}{\epsilon^2}+\frac{-\frac{11\zeta_2}{3}+13\zeta_3-\frac{4129}{108}}{\epsilon}\right. \\
&\qquad\left.+\frac{49\zeta_2^2}{5}-\frac{202\zeta_2}{9}+\frac{152\zeta_3}{3}-\frac{89173}{648}\right) \\
&+C_F n_f\left(\frac{1}{3\epsilon^3}+\frac{14}{9\epsilon^2}+\frac{\frac{2\zeta_2}{3}+\frac{353}{54}}{\epsilon}+\frac{28\zeta_2}{9}-\frac{8\zeta_3}{3}+\frac{7541}{324}\right)\Bigg],
\end{aligned} \tag{4.21}$$

which agrees with [77, (17)] up to the different normalization with $\mathcal{N}$ instead of S_ϵ (see (2.15)).

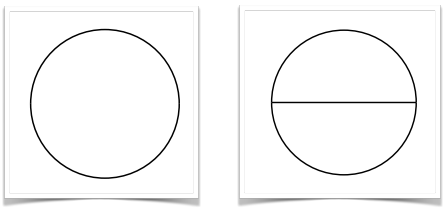

(a) $A_{1,1}$ (b) $A_{3,1}$

Figure 4.3: Scalar one- and two-loop bubble integrals.

Before concluding this subchapter, it is worth briefly mentioning one additional technique for calculating loop integrals. It is particularly useful in the context of EFT matching calculations, where the external momenta are assumed to be small compared to the scales of the UV theory.

Expansion in external momenta

Expansion in External Momenta The calculation of scalar multiloop integrals can be approximated by expanding them in the external momenta. The expansion of an arbitrary scalar two-point function with external momentum k and internal masses $\{m_i\}$ is given by [78]

Two-point integrals

$$B(k^2, \{m_i\}) = \sum_{n=0}^{\infty} b_n (k^2)^n \,, \tag{4.22}$$

with

$$b_n = \frac{1}{4^n\, n!} \frac{\Gamma\left(\frac{d}{2}\right)}{\Gamma\left(\frac{d}{2}+n\right)} \left(\Box_k^n B(k^2, \{m_i\})\right)\big|_{k=0} \,. \tag{4.23}$$

The operator $\Box_k \equiv \partial^2 / \left(\partial k_\mu \partial k^\mu\right)$ and d are the number of space-time dimensions. It should be noted that the integrals on the r.h.s of (4.23) only involve bubble integrals that can be reduced to a small number of master integrals via partial fraction decomposition and IBP relations. Similarly, the expansion of an arbitrary scalar three-point function with external momenta k_1, k_2 and internal masses $\{m_i\}$ is given by [79]

Three-point integrals

$$C(k_1, k_2, \{m_i\}) = \sum_{L=0}^{\infty} \sum_{l+m+n=L} c_{lmn}\, (k_1^2)^l (k_2^2)^m (k_1 k_2)^n \,, \tag{4.24}$$

with

$$c_{lmn} = \left(D_{lmn}\, C(k_1, k_2, \{m_i\})\right)\big|_{k_1=k_2=0} \,, \tag{4.25}$$

and

$$\begin{aligned} D_{00n} &= \sum_{i=1}^{\left[\frac{n}{2}\right]+1} \frac{(-4)^{1-i}\, \Gamma\left(\frac{d}{2}+n-i\right) \Gamma(d-1)}{2\,\Gamma(i)\Gamma(n-2i+3)\Gamma(n+d-2)\Gamma\left(n+\frac{d}{2}\right)} \left(\Box_{12}\right)^{n-2i+2} \left(\Box_{11}\Box_{22}\right)^{i-1} \,, \\ D_{l0n} &= \frac{\Gamma\left(\frac{d}{2}+n\right)}{\Gamma(l+1)\Gamma\left(\frac{d}{2}+l+n\right)} \left(\frac{\Box_{11}}{4}\right)^l D_{00n} \,. \end{aligned} \tag{4.26}$$

The operators $\Box_{ij}$ are defined as $\partial^2/(\partial k_{i,\mu}\partial k_j^\mu)$. We finally list one- and two-loop bubble integrals that are relevant in the SMEFT example presented below [80, 81]

$$\begin{aligned} A_{1,1}(\{M\}) &= \frac{i\mathcal{N}}{16\pi}\left(\frac{\mu_R^2}{M^2}\right)^\epsilon M^2\,\frac{\csc(\pi\epsilon)}{1-\epsilon}\,, \\ A_{3,1}(\{M_1,M_2,0\}) &= \frac{-\mathcal{N}^2}{(16\pi^2)^2}\left(\frac{\mu_R^2}{M_1^2}\right)^{2\epsilon} M_1^2 \\ &\times\Bigg[\frac{(1+x_2)}{2\epsilon^2}+\frac{3x_2-2x_2\ln(x_2)+3}{2\epsilon}+\frac{1}{6}\Big(-6(x_2-1)\mathrm{Li}_2(1-x_2) \\ &\quad +(21+\pi^2)(1+x_2)+3x_2(\ln(x_2)-6)\ln(x_2)\Big)+\mathcal{O}(\epsilon)\Bigg]\,, \end{aligned} \tag{4.27}$$

where $x_2 = M_2^2/M_1^2$, csc denotes the cosecant and where we followed the conventions of (2.13). The integral $A_{3,1}(\{M_1,0,0\})$ may be obtained from above expression in the limit $x_2 \to 0$.

4.1.2 *Multiloop Calculations in the SMEFT*

The mixing of SMEFT operators under the RG running (discussed in Subchapter 3.1.4) makes the renormalization of multiloop SMEFT amplitudes more complex than the usual QCD renormalization. To illustrate this, we present a specific example and subsequently provide a general recipe for the renormalization of two-loop SMEFT amplitudes.

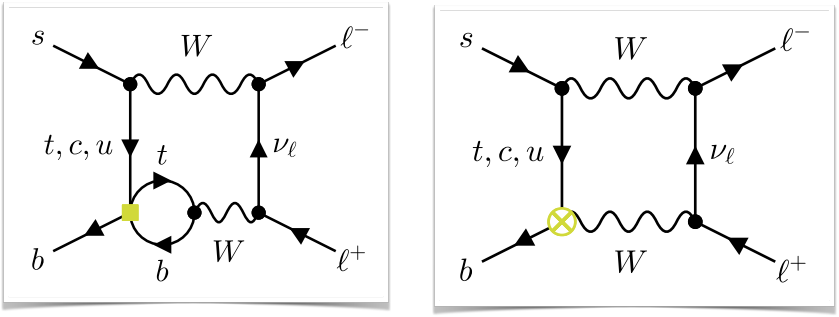

(a) Two-Loop Diagram (b) One-Loop Counterterm Diagram

Figure 4.4: The two-loop contribution of $\mathcal{O}_{qq}^{(1)}, \mathcal{O}_{qq}^{(3)}$ to the $bs\ell^+\ell^-$ box parameter B, together with the appropriate one-loop counterterm contribution.

EXAMPLE: SMEFT CONTRIBUTION TO THE B PARAMETER The B parameter is defined as the coefficient of the $bs\ell^+\ell^-$ box contribution in the broken phase

$$\mathcal{L}_{\text{EFT}} \supset -4V_{tb}^*V_{ts}\frac{G_F}{\sqrt{2}}\frac{\alpha}{2\pi s_w^2}B(x_t)\left(\bar{b}\gamma^\mu P_L s\right)\left(\bar{\ell}\gamma_\mu P_L \ell\right)\,, \tag{4.28}$$

where $\ell = e, \mu, \tau$ represents an arbitrary charged lepton, V_{tb}, V_{ts} are elements of the CKM matrix, and $x_t = m_t^2/m_W^2$. It receives a two-loop contribution from the dimension-six SMEFT operators $[\mathcal{O}_{qq}^{(1)}]_{3333}, [\mathcal{O}_{qq}^{(3)}]_{3333}$, the corresponding diagram is depicted in Figure 4.4a.
We work in the down basis, whereby the flavor and mass eigenstates are aligned in the down sector, while they are rotated by the corresponding elements of the CKM matrix in the up sector. Although $[\mathcal{O}_{qq}^{(1)}]_{3333}, [\mathcal{O}_{qq}^{(3)}]_{3333}$ (henceforth, we will omit the flavor indices) only involve third-family quarks in the *flavor* basis (see (3.20)), in the *mass* basis they also involve left-handed charm and up quarks. Consequently, the corresponding contributions must be included, as indicated in Figure 4.4a. Indeed, the contributions with the top, charm, and up quark scale as $V_{tb}^* V_{ts}$, $V_{cb}^* V_{cs}$ and $V_{ub}^* V_{us}$, respectively. In the limit of vanishing quark masses, the contribution from the first cancels against the latter two, as can be seen from the unitarity of the CKM matrix

$$V^\dagger V = \mathbb{1} \;\; \rightarrow \;\; \sum_{q=t,c,u} V_{qb}^* V_{qs} = 0 \;\; \rightarrow \;\; V_{tb}^* V_{ts} = -\left(V_{cb}^* V_{cs} + V_{ub}^* V_{us}\right) . \tag{4.29}$$

This cancellation is known as the Glashow-Iliopoulos-Maiani (GIM) mechanism. In the case of a non-vanishing top mass, however, the cancellation is not exact, and terms proportional to m_t remain. It should be noted that the contributions with the other top line in Figure 4.4a replaced by charm or up are subleading ($|V_{tb}|^2 \gg |V_{cb}|^2, |V_{ub}|^2$), and therefore neglected. The two-loop diagram in Figure 4.4a can be computed using the methods outlined in Subchapter 4.1.1, setting all external momenta to zero. The bare result has poles of the form

$$\Delta B_0(x_t) \supset -\frac{\mathcal{N}}{\epsilon} \frac{\alpha v^2 |V_{tb}|^2}{32\pi s_w^2} \frac{x_t \left(x_t - \ln(x_t) - 1\right)}{(x_t - 1)^2} \left(C_{qq}^{(1)} + 5 C_{qq}^{(3)}\right) . \tag{4.30}$$

They are non-rational, as evidenced by their dependence on $\ln(x_t)$. The cancellation of these singularities is once more related to the non-diagonal renormalization constants $C_{i,0} = \sum_j \tilde{Z}_{ij} C_j$, which were introduced in (3.28). The operators $\mathcal{O}_{Hq}^{(3)}$ and $\mathcal{O}_{DW}^{(3)}$ (defined in Table 3.2 and (3.32), respectively) contribute to $\Delta B_0(x_t)$ at the one-loop level via the diagram shown in Figure 4.4b. In the renormalization procedure, the bare Wilson coefficients $C_{Hq,0}^{(3)}, C_{DW,0}^{(3)}$ are replaced by

$$\begin{aligned} C_{Hq,0}^{(3)} &= \sum_j \tilde{Z}_{\substack{(3)\\Hq}\,j} C_j \;\supset\; \tilde{Z}_{\substack{(3)\,(1)\\Hqqq}} C_{qq}^{(1)} + \tilde{Z}_{\substack{(3)\,(3)\\Hqqq}} C_{qq}^{(3)} , \\ C_{DW,0}^{(3)} &= \sum_j \tilde{Z}_{\substack{(3)\\DW}\,j} C_j \;\supset\; \tilde{Z}_{\substack{(3)\;\;(1)\\DWqq}} C_{qq}^{(1)} + \tilde{Z}_{\substack{(3)\;\;(3)\\DWqq}} C_{qq}^{(3)} , \end{aligned} \tag{4.31}$$

with the corresponding one-loop renormalization factors $\tilde{Z}$ calculated in (3.30) and (3.33). This results in counterterms proportional to $C_{qq}^{(1)}, C_{qq}^{(3)}$. As previously demonstrated in (3.42) and below, the aforementioned counterterms are related to the one-loop ADM of the SMEFT.

Including the counterterm diagrams shown in Figure 4.4b, the contributions to the renormalized ΔB become finite and of the form

$$\Delta B(x_t) = -\frac{\alpha\,|V_{tb}|^2}{384\pi\, s_w^2}\frac{v^2}{\Lambda^2}\left(\xi_{qq}^{(1)}(x_t)\,C_{qq}^{(1)} + \xi_{qq}^{(3)}(x_t)\,C_{qq}^{(3)}\right), \tag{4.32}$$

where

$$\begin{aligned}\xi_{qq}^{(1)}(x_t) &= 2x_t^2\left(\pi^2(2x_t-1)-12\right) - 24x_t^2\ln(x_t) + 6x_t^2(2x_t-1)\ln^2(x_t)\\ &\quad + 12x_t^2(2x_t-1)\mathrm{Li}_2(1-x_t) + 12f(x_t)\ln(x_{\mu t}),\\ \xi_{qq}^{(3)}(x_t) &= 5\xi_{qq}^{(1)}(x_t) + 72f(x_t),\end{aligned} \tag{4.33}$$

and

$$f(x) \equiv \frac{x^2}{x-1} - \frac{x^2}{(x-1)^2}\ln(x). \tag{4.34}$$

The fact that $\xi_{qq}^{(3)}$ is almost (but not entirely) proportional to $\xi_{qq}^{(1)}$ can again be understood from the perspective of the Top Working Group basis (see (3.19)). In this basis, the contributions from $C_{QQ}^{(1)}$ and $C_{QQ}^{(8)}$ are proportional by virtue of (3.27). This exact proportionality is spoiled in the Warsaw basis due to evanescent contributions from E_{QQ} (see discussion around (3.26)). It should further be noted that all terms in (4.33) vanish for $x_t \to 0$, as required by the GIM mechanism. In the derivation of (4.33) we have used

$$\gamma^\mu\gamma^\nu\gamma^\rho P_L \otimes \gamma_\mu\gamma_\nu\gamma_\rho P_L = 4(4+b_{\mathrm{ev}}\epsilon)\gamma^\mu P_L \otimes \gamma_\mu P_L + E_{LL}^{(3)} \tag{4.35}$$

from (3.10). The definition of the evanescent (i.e., the choice of b_{ev}) is not relevant in this case, as the final result does not depend on it. Similarly, the replacement in (4.35) is not necessary to obtain the poles in (4.30), and thus no evanescent counterterms need to be included.

Recipe for renormalizing two-loop amplitudes in the SMEFT

We are now in a position to present the general recipe for renormalizing two-loop SMEFT amplitudes in $\overline{\mathrm{MS}}$, which has been adapted from [24]:

- Calculate the full (bare) two-loop amplitude $\mathcal{A}_0$ with contributions from the SMEFT operators $\{\mathcal{O}_i\}$ ($\{\mathcal{O}_{qq}^{(1)}, \mathcal{O}_{qq}^{(3)}\}$ in the example above). If needed, reduce the Dirac structures using (3.10) with an explicit choice of $a_{\mathrm{ev}}, \ldots, f_{\mathrm{ev}}$. The result is of the form

  Bare two-loop integral

  $$\mathcal{A}_0 = \sum_i \left(\frac{\mu_R^2}{Q^2}\right)^{2\epsilon}\left[\frac{\xi_i^{(-2)}}{\epsilon^2} + \frac{\xi_i^{(-1)}}{\epsilon} + \xi_i^{(0)} + \mathcal{O}(\epsilon)\right] C_i, \tag{4.36}$$

  where Q is the typical scale of the process.

- ***Subdivergences*** Take the divergent one-particle-irreducible subdiagrams of the full two-loop diagrams (the $b\bar{t}W$ vertex above), and determine the operators $\{\mathcal{O}_j\}$ ($\{\mathcal{O}_{Hq}^{(3)}, \mathcal{O}_{DW}^{(3)}\}$ above) that receive poles from $\{\mathcal{O}_i\}$. It should be noted that operators of a given dimension only mix into operators of the same or lower dimension. Consequently, only operators $\mathcal{O}_j$ of dimension equal or lower to

the dimension of the $\mathcal{O}_i$ have to be considered. Should the need arise, reduce the $\{\mathcal{O}_j\}$ by means of (3.10). The coefficients $a_{\text{ev}}, \ldots, f_{\text{ev}}$ are irrelevant in this step. Determine the $\overline{\text{MS}}$ renormalization constants $\tilde{Z}_{ji} \sim \mathcal{O}(\epsilon^{-1})$ needed to cancel the poles proportional to the Wilson coefficients C_i.

- Insert the $\{\mathcal{O}_j\}$ into the remaining one-loop subdiagram of the full two-loop diagram (in the example above, this was the one-loop diagram shown in Figure 4.4b). If needed, reduce the resulting Dirac structures with (3.10), using the same coefficients $a_{\text{ev}}, \ldots, f_{\text{ev}}$ as before. Replace the Wilson coefficients C_j by $\tilde{Z}_{ji}C_i$. The result is of the form

Insertion of subdivergences into the remaining diagram

$$\begin{aligned}\mathcal{A}_C &= \sum_{i,j}\left(\frac{\mu_R^2}{Q^2}\right)^{\epsilon}\left[\frac{\tilde{\xi}_{C,j}^{(-1)}}{\epsilon}+\tilde{\xi}_{C,j}^{(0)}+\tilde{\xi}_{C,j}^{(1)}\,\epsilon+\mathcal{O}(\epsilon^2)\right]\tilde{Z}_{ji}C_i \\ &\equiv \sum_{i}\left(\frac{\mu_R^2}{Q^2}\right)^{\epsilon}\left[\frac{\xi_{C,i}^{(-2)}}{\epsilon^2}+\frac{\xi_{C,i}^{(-1)}}{\epsilon}+\xi_{C,i}^{(0)}+\mathcal{O}(\epsilon)\right]C_i\,.\end{aligned} \tag{4.37}$$

- If (3.10) has been used in the reduction of the $\{\mathcal{O}_j\}$ above, insert the corresponding evanescent operators $\{E_j\}$ (defined via (3.12)) into the remaining one-loop subdiagram. Reduce the resulting Dirac structures with (3.10), and insert $\tilde{Z}_{ji}C_i$. The result is of the form

Evanescent counterterms

$$\begin{aligned}\mathcal{A}_E &= \sum_{i,j}\left(\frac{\mu_R^2}{Q^2}\right)^{\epsilon}\left[\tilde{\xi}_{E,j}^{(0)}+\tilde{\xi}_{E,j}^{(1)}\,\epsilon+\mathcal{O}(\epsilon^2)\right]\tilde{Z}_{ji}C_i \\ &\equiv \sum_{i}\left(\frac{\mu_R^2}{Q^2}\right)^{\epsilon}\left[\frac{\xi_{E,i}^{(-1)}}{\epsilon}+\xi_{E,i}^{(0)}+\mathcal{O}(\epsilon)\right]C_i\,.\end{aligned} \tag{4.38}$$

The total result finally reads

$$\boxed{\begin{aligned}\mathcal{A} &\equiv \mathcal{A}_0+\mathcal{A}_C+\frac{1}{2}\mathcal{A}_E \\ &= \sum_i\left(\frac{\xi_i^{(-2)}+\xi_{C,i}^{(-2)}}{\epsilon^2}+\frac{\xi_i^{(-1)}+\xi_{C,i}^{(-1)}+\frac{1}{2}\xi_{E,i}^{(-1)}}{\epsilon}+\frac{\xi_i^{(0)}+\xi_{C,i}^{(0)}+\frac{1}{2}\xi_{E,i}^{(0)}}{\epsilon}\right)C_i\,.\end{aligned}} \tag{4.39}$$

One finds that the coefficients of the double poles satisfy

$$\boxed{\xi_{C,i}^{(-2)}=-2\xi_i^{(-2)}\,,} \tag{4.40}$$

i.e. they do not cancel exactly. The cancellation is only complete after the inclusion of diagrams with two counterterm insertions. Since the latter are exclusively $\mathcal{O}(\epsilon^{-2})$, they may be omitted in the determination of the $\mathcal{O}(\epsilon^{-1})$ and $\mathcal{O}(\epsilon^0)$ pieces of the total result. The single poles of $\mathcal{A}$ should only contain rational coefficients. It is important to note that due to the differing exponents of (μ_R^2/Q^2) in (4.36) and (4.37), as well as because of (4.40), terms of the form $\log(\mu_R^2/Q^2)/\epsilon$ cancel out in (4.39). The remaining rational poles are related to the two-loop ADM of the SMEFT. The additional terms $\xi_{E,i}^{(-1)}$ serve to remove the mixing of evanescent operators with physical operators.

4.2 Multiemission Diagrams (Real Corrections)

4.2.1 *The Spinor-Helicity Formalism*

The spinor-helicity formalism offers a concise representation of matrix elements with a large number of final-state particles. We will use it below, and thus provide a brief introduction here. The starting point is the realization that the positive and negative energy solutions of the massless Dirac equation are identical up to normalization conventions. Indeed, one can choose the spinors $u_\pm(k) \equiv P_\pm u(k) \equiv \frac{1}{2}\,(1 \pm \gamma_5)\,u(k)$ and $v_\mp(k) \equiv P_\mp v(k) \equiv \frac{1}{2}\,(1 \mp \gamma_5)\,v(k)$ to be equal to each other. We introduce [82]

Spinor-helicity brackets

$$\begin{aligned} |i\rangle &= u_+(k_i) = v_-(k_i)\,, \qquad \langle i| = \overline{u}_-(k_i) = \overline{v}_+(k_i)\,, \\ |i] &= u_-(k_i) = v_+(k_i)\,, \qquad [i| = \overline{u}_+(k_i) = \overline{v}_-(k_i)\,. \end{aligned} \tag{4.41}$$

The usual bilinears are given by

$$\langle i\,j\rangle = \overline{u}_-(k_i)u_+(k_j)\,, \quad [i\,j] = \overline{u}_+(k_i)u_-(k_j)\,, \quad \langle i|\gamma^\mu|j] = \overline{u}_-(k_i)\gamma^\mu u_-(k_j)\,, \tag{4.42}$$

for scalar and vector currents. Furthermore, the identities

$$\begin{aligned} \langle i\,j\rangle &= -\langle j\,i\rangle\,, & [i\,j] &= -[j\,i]\,, \\ |i\rangle[i| &= P_+ \not{k}_i\,, & |i]\langle i| &= P_- \not{k}_i\,, \\ \langle i\,j\rangle[j\,i] &= \left(k_i + k_j\right)^2\,, & \langle i|\gamma^\mu|j] &= [j|\gamma^\mu|i\rangle\,, \\ \langle i|\gamma^\mu|i] &= 2k_i^\mu\,, & [i|\gamma^\mu|j\rangle[k|\gamma_\mu|l\rangle &= 2[i\,k]\langle l\,j\rangle\,, \\ \langle i\,j\rangle\langle k\,l\rangle &= \langle i\,k\rangle\langle j\,l\rangle + \langle i\,l\rangle\langle k\,j\rangle\,, \end{aligned} \tag{4.43}$$

Polarization vectors

hold, which may be used to simplify calculations. The polarization vectors $\epsilon_\mu^\pm$ of massless gauge bosons can also be expressed in terms of the bracket notation

$$\epsilon_\mu^+(k_i,q) = \frac{\langle q|\gamma_\mu|k_i]}{\sqrt{2}\,\langle q\,k_i\rangle}\,, \qquad \epsilon_\mu^-(k_i,q) = -\frac{\langle k_i|\gamma_\mu|q]}{\sqrt{2}\,[q\,k_i]}\,. \tag{4.44}$$

In this context, k_i prepresents the gauge boson momentum, while q is an auxiliary massless vector, commonly referred to as the *reference momentum*. The choice of q corresponds to a gauge fixing. One can choose a different q for each gluon momentum k in an amplitude. However, one should not change it within the calculation of a gauge-invariant quantity. The identities

$$\begin{aligned} \left(\epsilon_\mu^+\right)^* &= \epsilon_\mu^-\,, \\ \epsilon^+ \cdot \left(\epsilon^+\right)^* &= -1\,, \qquad \epsilon^+ \cdot \left(\epsilon^-\right)^* = 0\,, \end{aligned} \tag{4.45}$$

and

$$\begin{aligned} \epsilon^\pm(k_i,q)\cdot k_i &= 0\,, & \epsilon^\pm(k_i,q)\cdot q &= 0\,, \\ \epsilon^+(k_i,q)\cdot\epsilon^+(k_j,q) &= 0\,, & \epsilon^-(k_i,q)\cdot\epsilon^-(k_j,q) &= 0\,, \\ \epsilon^+(k_i,k_j)\cdot\epsilon^-(k_j,q) &= 0\,, & \epsilon^+(k_i,q)\cdot\epsilon^-(k_j,k_i) &= 0\,, \\ \not{\epsilon}^+(k_i,k_j)|j\rangle &= 0\,, & \not{\epsilon}^-(k_i,k_j)|j] &= 0\,, \\ [j|\not{\epsilon}^+(k_i,k_j) &= 0\,, & \langle j|\not{\epsilon}^-(k_i,k_j) &= 0\,, \end{aligned} \tag{4.46}$$

usually lead to substantial simplifications if the q are chosen apropriately. The relevant formulas for the numerical implementation of the spinor-helicity brackets can be found in [82, Sec. 2.2].

	F	FJ	FJJ	$FJ^{l\geq 3}$
POWHEG (F)	NLO	LO	LL	LL
POWHEG (FJ)	–	NLO	LO	LL
MiNLO′	NLO	NLO	LO	LL
MiNNLOPS	NNLO	NLO	LO	LL

Table 4.1: Formal accuracies achieved by the POWHEG, MiNLO′ and MiNNLOPS methods for different final states involving a color singlet F and a variable number of additional partonic emissions J. LL accuracy in this context means that the corresponding contributions are only generated by the PS system.

4.3 Going to NNLO+PS: The POWHEG MiNLO′ and MiNNLOPS Methods

In Chapter 2.3, we have described the POWHEG method, which allows for the calculation of NLO+PS accurate predictions for inclusive F observables that are agnostic about additional parton emissions J. However, if one imposes cuts on J, the accuracy of the prediction reduces to LO. This is because only the LO matrix elements $\mathcal{R}(\boldsymbol{P}_{FJ})$ for FJ production are included in (2.85). The formal accuracies of the various POWHEG methods for different FJ^l final states are summarized in Table 4.1. An approach to improve the precision of the FJ prediction is to apply the POWHEG procedure to the final state FJ directly, with $B(\boldsymbol{P}_{FJ})$ as the Born and $R(\boldsymbol{P}_{FJJ})$ as the real contribution. This approach is effective for observables exclusive in the hardest emission, but it is evident that the NLO prediction for FJ diverges when integrated over all emissions J. This is because it lacks the virtual contributions $V(\boldsymbol{P}_F)$ that cancel the IR divergences of $B(\boldsymbol{P}_{FJ})$. It is therefore of interest to ask whether it is possible to combine NLO+PS accurate predictions for F and FJ in a consistent manner, such that the NLO accuracy is retained in both classes of observables. This *merging* problem was solved by the POWHEG MiNLO′ method, an extension of the POWHEG MiNLO method, which achieves NLO accuracy for F and FJ simultaneously in the case where F is a massless color singlet system. It was later extended to the POWHEG MiNNLOPS method, which achieves full NNLO+PS accuracy for colorless F.

Merging NLO+PS generators for F and FJ

We will start our discussion with an examination of the POWHEG MiNLO method, and subsequently detail its extension to MiNLO′ and MiNNLOPS. MiNLO [83], an acronym for *multi-scale improved NLO*, was conceived as an NLO extension of the Catani-Krauss-Kuhn-Webber (CKKW) [84] merging procedure. The CKKW procedure allows for the consistent combination of fixed-order LO matrix elements with PS systems, thereby resumming large logarithms that arise from kinematic configurations involving disparate scales.

The MiNLO method

In order to formulate the MiNLO method, let us consider an event produced by the Born or virtual (real) contributions in an NLO simulation where l $(l+1)$ partons are emitted in association with a color singlet state F. We further assume that m powers of α_s are associated with the production of F. We proceed in the following way:

In the case of gluon-gluon fusion (ggF) Higgs production $pp \to h$, for example, the production of $F = h$ is associated with two powers of α_s.

- First, we recursively cluster the colored partons in the event using a k_t clustering algorithm. To each vertex $i \in [1, l]$ of the branching history, we assign a

scale q_i ($q_1 < \cdots < q_l$), which is equal to the relative transverse momentum at which the branching occurred. In the case of $(l+1)$ partons, we assign q_0 to the first clustering. We set Q to the invariant mass of F and Q_0 to q_1, where Q_0 is the scale below which all radiation is interpreted as inclusive.

- l powers of α_s are evaluated at the scales $\mu_1, \ldots, \mu_l$ with $\mu_i = K_R\, q_i$, where K_R is the usual renormalization scale variation factor – equal to 1 for the central value and varied between 0.5 and 2 to study scale variation uncertainties. We will describe later how to set the scale of the additional factor of α_s present in the virtual and real contributions. The scales of all m remaining powers of α_s are set to $K_R\, Q$.

This choice of μ_R allows for the cancellation between the μ-dependence in $\prod_{i=1}^{l} \alpha_s(\mu_l) \cdot \alpha_s(\mu_Q)^m$ multiplied to the Born matrix element with the μ-dependence in the logarithm $\ln \frac{\mu_R^2}{Q^2}$ of the virtual matrix element.

- The renormalization scale μ_R present in the virtual contributions is set to

$$\mu_R = \left((\mu_Q)^m \times \prod_{i=1}^{l} \mu_i \right)^{\frac{1}{l+m}}, \tag{4.47}$$

the factorization scale is set to $K_F\, q_1$, with K_F being the usual factorization scale variation factor.

- For each internal line between vertices i and j of the branching history, the factor

$$\frac{\Delta_g(Q_0, q_i)}{\Delta_g(Q_0, q_j)} \tag{4.48}$$

with Δ_g the gluon Sudakov form factor

$$\begin{aligned} \Delta_g(Q, q_T) &\equiv \exp\left(-\tilde{S}(q_T)\right) \\ &= \exp\left(-2 \int_{q_T}^{Q} \frac{dq}{q} \left(A(\alpha_s(q)) \ln \frac{Q^2}{q^2} + B(\alpha_s(q)) \right) \right) \end{aligned} \tag{4.49}$$

is multiplied. It may be interpreted as the probability for the corresponding parton to evolve from q_i to q_j without branching. In the case of a real contribution, the factor (4.48) involving q_0 is not considered. The coefficients A, B in (4.49) permit a perturbative expansion

Generally, $[...]^{(n)}$ denotes the n^{th}-order coefficient of $(\alpha_s/2\pi)^n$ in the following discussion.

$$A(\alpha_s) = \sum_{n=1}^{\infty} [A]^{(n)} \left(\frac{\alpha_s}{2\pi} \right)^n, \qquad B(\alpha_s) = \sum_{n=1}^{\infty} [B]^{(n)} \left(\frac{\alpha_s}{2\pi} \right)^n. \tag{4.50}$$

This also allows for an expansion $\Delta_g(Q, q_T) = 1 - \frac{\alpha_s}{2\pi} \left[\tilde{S}(q_T)\right]^{(1)} + \mathcal{O}(\alpha_s^2)$ to first order in α_s.

- Given that multiplying the factor (4.48) to the Born matrix element results in terms that are already accounted for in the NLO matrix elements, it is necessary to subtract the LO contribution from the Sudakov factor. Schematically, a replacement

$$B \to B \times \left(1 + \frac{\alpha_s}{2\pi} \left[\tilde{S}(q_T)\right]^{(1)} \right) \tag{4.51}$$

therefore has to be performed.

The MiNLO′ method

In [85], the authors realized the full potential of the MiNLO method, extending it to MiNLO′. They applied the method outlined above to a POWHEG FJ NLO generator. The corresponding POWHEG formula is given by

The MiNLO′ master formula

$$\begin{aligned}\langle\mathcal{O}\rangle_{\text{NLO}} = \int d\mathbf{\Phi}_{FJ}\bar{B}(\boldsymbol{P}_{FJ})\Bigg[&\Delta_{\text{pwg}}(p_{T,\text{pwg}})\mathcal{O}(\mathbf{\Phi}_{FJ}) \\ &+\sum_{\alpha}\int_{p_{T,\text{pwg}}} d\Phi^{(\alpha)}_{\text{rad}}\frac{R^{(\alpha)}\left(\vec{\boldsymbol{P}}^{(\alpha)}_{FJJ}\right)}{B(\boldsymbol{P}_{FJ})}\Delta_{\text{pwg}}\left(q^{(\alpha)}_{T,\text{rad}}\right)\mathcal{O}\left(\vec{\mathbf{\Phi}}^{(\alpha)}_{FJJ}\right)\Bigg],\end{aligned} \tag{4.52}$$

in complete analogy to (2.85). Implementing the MiNLO procedure, however, the $\bar{B}$ function has to be modified to

The $\bar{B}$ function in MiNLO′

$$\begin{aligned}\bar{B}(\boldsymbol{P}_{FJ}) \equiv \alpha_s^m(Q)\,\alpha_s(q_1)\,\exp(-\tilde{S}(q_1))\Bigg[&B(\boldsymbol{P}_{FJ})\left(1+\frac{\alpha_s(q_1)}{2\pi}[\tilde{S}(q_1)]^{(1)}\right) \\ &+V(\boldsymbol{P}_{FJ})+\sum_{\alpha}\int d\Phi^{(\alpha)}_{\text{rad}}R^{(\alpha)}\left(\vec{\boldsymbol{P}}^{(\alpha)}_{FJJ}\right)\Bigg].\end{aligned} \tag{4.53}$$

In above formula, we have omitted the subtraction counterterms for the sake of clarity, and have also stripped $(m+1)$ powers of α_s from the Born (B), virtual (V), and real (R) matrix elements. The scale of the remaining factor of α_s in V and R is set to $K_R\,q_1$, where q_1 is the transverse momentum of F. This choice of notation is made to facilitate an analogy with MiNLO.

NLO+PS accuracy for F and FJ

Now, the central claim is the following: the FJ POWHEG NLO generator implemented in the above manner retains its accuracy when integrated over the phase space of the emitted parton J, provided that the expansion up to $\mathcal{O}(\alpha_s^2)$ is included in (4.50). Consequently, MiNLO′ solves the aforementioned merging problem, and achieves NLO accuracy for F and FJ simultaneously.

p_T resummation formula

The correctness of the claim can be substantiated by reference to the all-order analytic formula [86]

$$\begin{aligned}\frac{d\sigma}{d\mathbf{\Phi}_F\,dp_T} &= \exp(-\tilde{S}(p_T))D(p_T)+R_f(p_T) \\ &= \exp(-\tilde{S}(p_T))\underbrace{\left[D(p_T)+\frac{R_f(p_T)}{\exp(-\tilde{S}(p_T))}\right]}_{①}\end{aligned} \tag{4.54}$$

for the production of a color singlet state F with transverse momentum p_T in association with additional radiation. The R_f terms are non-singular in the small p_T limit. It is worth noting the similarities between (4.54) and our general resummation formula in (2.80). We further write

$$D(p_T) \equiv -\frac{d\tilde{S}(p_T)}{dp_T}\mathcal{L}(p_T)+\frac{d\mathcal{L}(p_T)}{dp_T}, \tag{4.55}$$

where $\mathcal{L}$ (see [86, (4.31)]) involves the parton luminosities, the Born squared amplitude for the production of the color-singlet F, the hard-virtual corrections up to two loops and the collinear coefficient functions up to second order. The Sudakov form factor $\tilde{S}$ has been defined in (4.49). We now seek to expand ① in (4.54) to the right

order to achieve NLO accuracy in $d\sigma$ integrated over p_T. For this purpose, we notice that all terms in ① contain at most a singularity of the form $1/p_T$ and factors of the order $\alpha_s^a(p_T)\log^b\frac{Q}{p_T}$ with $b \leq 1$. Since

$$\int_{p_{T,\text{pwg}}}^{Q} \frac{dp_T}{p_T}\alpha_s^a(p_T)\log^b\left(\frac{Q}{p_T}\right)\exp[-\tilde{S}(p_T)] \sim \mathcal{O}\left(\alpha_s^{a-\frac{b+1}{2}}(Q)\right), \tag{4.56}$$

we have to expand ① up to order $\alpha_s^2(p_T)$ in order to reach NLO accuracy inclusively. Using (4.54) to write

$$\begin{aligned} R_f(p_T) = \quad & \frac{\alpha_s(p_T)}{2\pi}\left[\frac{d\sigma_{FJ}}{d\mathbf{\Phi}_F dp_T}\right]^{(1)} \\ & + \frac{\alpha_s^2(p_T)}{4\pi^2}\left[\frac{d\sigma_{FJ}}{d\mathbf{\Phi}_F dp_T}\right]^{(2)} - \exp[-\tilde{S}(p_T)]D(p_T)\,, \end{aligned} \tag{4.57}$$

plugging this into ① and expanding ① to $\mathcal{O}(\alpha_s^2)$, one obtains

$$\begin{aligned} \frac{d\sigma}{d\mathbf{\Phi}_F dp_T} = \exp(-\tilde{S}(p_T))\Bigg[& \frac{\alpha_s(p_T)}{2\pi}\left[\frac{d\sigma_{FJ}}{d\mathbf{\Phi}_F dp_T}\right]^{(1)}\left(1+\frac{\alpha_s(p_T)}{2\pi}[\tilde{S}(p_T)]^{(1)}\right) \\ & + \frac{\alpha_s^2(p_T)}{4\pi^2}\left[\frac{d\sigma_{FJ}}{d\mathbf{\Phi}_F dp_T}\right]^{(2)}\Bigg], \end{aligned} \tag{4.58}$$

which is equivalent to (4.53) for $p_T = q_1$. In conclusion, one can demonstrate that the FJ generator based on the MiNLO′ method achieves full NLO accuracy when integrating over the p_T of J, provided that all terms $[A]^{(1)}, [A]^{(2)}, [B]^{(1)}, [B]^{(2)}$ in $\tilde{S}$ are included.

Conceptually, we are now close to a full NNLO + PS method. In proposing the MiNLO′ method [85], the authors noted that an *a posteriori* reweighting of events generated by MiNLO′ to the differential NNLO cross section

NNLO+PS via reweighting

$$w(\mathbf{\Phi}_F) = \frac{\left(\frac{d\sigma}{d\mathbf{\Phi}_F}\right)_{\text{NNLO}}}{\left(\frac{d\sigma}{d\mathbf{\Phi}_F}\right)_{\text{MiNLO}'}} \tag{4.59}$$

leads to predictions that are NNLO accurate in F and retain the NLO accuracy of MiNLO′ in FJ. This approach yields a complete NNLO+PS method. Nevertheless, while this technique was applied to a few LHC processes, the reweighting proved to be a significant computational burden, prompting the development of an NNLO+PS method that eliminates the need for reweighting. This was accomplished by the POWHEG MiNNLO$_{\text{PS}}$ [86] method.

The MiNNLO$_{\text{PS}}$ method

In the first MiNNLO$_{\text{PS}}$ publication [86], the term in square brackets was $(\alpha_s/2\pi)^2[D(p_T)]^{(3)}$, it was later realized [87] that keeping the higher-order terms $\mathcal{O}(\alpha_s^4)$ in $D(p_T)$ is beneficial.

In order to promote (4.58) to NNLO accuracy, one has to expand ① in (4.54) to $\mathcal{O}(\alpha_s^3)$. This adds

$$\begin{aligned} \frac{d\sigma}{d\mathbf{\Phi}_F dp_T} \supset F^{\text{corr}}(\mathbf{\Phi}_{\text{FJ}})\Bigg[& D(p_T) - \frac{\alpha_s(p_T)}{2\pi}[D(p_T)]^{(1)} \\ & - \left(\frac{\alpha_s(p_T)}{2\pi}\right)^2[D(p_T)]^{(2)}\Bigg] + R_f \text{ terms} \end{aligned} \tag{4.60}$$

to (4.58), where the R_f terms arise from the $\mathcal{O}(\alpha_s^3)$ expansion of $R_f(p_T)/\exp[-\tilde{S}(p_T)]$ and can be ignored as they do not contain a $1/p_T$ factor and therefore only contribute to the total cross section at N^{3}LO. The factor $F^{\text{corr}}(\mathbf{\Phi}_{FJ})$ is needed in the POWHEG MiNNLOPS implementation to determine the appropriate function to spread the NNLO corrections in the FJ phase space (see [86, Sec. 3]). Finally, the POWHEG MiNNLOPS master formula is given by

The MiNNLOPS master formula

$$\begin{aligned}\langle\mathcal{O}\rangle_{\text{NNLO}} = \int d\mathbf{\Phi}_{FJ}\, \bar{B}_{\text{MiNNLOPS}}(\boldsymbol{P}_{FJ}) \Bigg[&\Delta_{\text{pwg}}(p_{T,\text{pwg}})\mathcal{O}(\mathbf{\Phi}_{FJ}) \\ &+ \sum_{\alpha} \int_{p_{T,\text{pwg}}} d\Phi_{\text{rad}}^{(\alpha)} \frac{R^{(\alpha)}\left(\vec{\boldsymbol{P}}_{FJJ}^{(\alpha)}\right)}{B(\boldsymbol{P}_{FJ})} \Delta_{\text{pwg}}\left(q_{T,\text{rad}}^{(\alpha)}\right) \mathcal{O}\left(\vec{\mathbf{\Phi}}_{FJJ}^{(\alpha)}\right) \Bigg],\end{aligned} \tag{4.61}$$

with

$\bar{B}$ in the MiNNLOPS method

$$\begin{aligned}\bar{B}_{\text{MiNNLOPS}}(\boldsymbol{P}_{FJ}) = \exp[-\tilde{S}(q_1)] \Bigg[&\frac{\alpha_s(q_1)}{2\pi} \left[\frac{d\sigma_{FJ}}{d\mathbf{\Phi}_F dq_1}\right]^{(1)} \left(1 + \frac{\alpha_s(q_1)}{2\pi}[\tilde{S}(q_1)]^{(1)}\right) \\ &+ \frac{\alpha_s^2(q_1)}{4\pi^2} \left[\frac{d\sigma_{FJ}}{d\mathbf{\Phi}_F dq_1}\right]^{(2)} + F^{\text{corr}}(\mathbf{\Phi}_{\text{FJ}}) \\ &\times \left(D(q_1) - \frac{\alpha_s(q_1)}{2\pi}[D(q_1)]^{(1)} - \frac{\alpha_s^2(q_1)}{4\pi^2}[D(q_1)]^{(2)}\right)\Bigg].\end{aligned} \tag{4.62}$$

As in (4.53), we denote the transverse momentum of F by q_1. The full expanded expression for (4.62) can be found in [86].

In summary, the POWHEG MiNNLOPS method works as follows:

Summary of the MiNNLOPS method

- FJ is generated at NLO accuracy according to the POWHEG method, inclusive in the radiation of a second light parton J.
- The limit in which the first J becomes unresolved is corrected by supplementing appropriate Sudakov form factors and higher-order terms, following the MiNLO′ method and supplying the additional D terms (see (4.62)). This ensures the NNLO accuracy in F.
- The kinematics of the second radiated J (accounted for inclusively in the first step above) is generated through the POWHEG method, preserving the NLO accuracy of the FJ cross section.
- All subsequent radiation is added by the PS.

While other frameworks for the consistent matching of NNLO predictions to PS generators exist, notably the GENEVA [88, 89] and UNNLOPS [90, 91] methods, the simplicity and flexibility of POWHEG MiNNLOPS method make it stand out.

5

SMEFT EFFECTS IN HIGGSSTRAHLUNGS PRODUCTION AT NNLO+PS

I think we have it.

— Rolf-Dieter Heuer,
announcing the discovery
of the Higgs

5.1 Introduction

In order to showcase how precise predictions for the effects of SMEFT operators in LHC observables are obtained, we will present the relevant sections of our publication [LS1]. We calculated NNLO+PS accurate predictions for the effects of the SMEFT operators modifying the VVh ($V = W, Z$ being the massive SM vector bosons) and $Vf\bar{f}$ (f being the SM fermions) couplings in the Higgsstrahlungs production processes $pp \to Zh \to \ell^+\ell^- h$ and $pp \to Wh \to \ell\nu h$ employing the POWHEG MiNNLO$_{\text{PS}}$ method.

Phenomenological importance of $pp \to Vh$

The Higgsstrahlungs production channel $pp \to Vh$ is particularly relevant regarding the measurement of the SM Higgs boson decay to a pair of bottom quarks ($h \to b\bar{b}$). The latter has the largest branching ratio, expected to be close to 60%, for the SM Higgs at 125 GeV. Even though ggF production $gg \to h$ is the dominant production channel of the Higgs boson at the LHC, with a cross section that is orders of magnitude larger than the one for $pp \to Vh$, the large QCD backgrounds from multi-jet production make a search for $gg \to h \to b\bar{b}$ challenging. Instead, the most sensitive production mode for detecting $h \to b\bar{b}$ decays is $pp \to Vh$, where the leptonic decay of the vector boson enables a clean selection, leading to a significant background reduction. The $h \to b\bar{b}$ decay mode has been observed by both ATLAS and CMS in LHC Run II [92, 93], and these measurements constrain the $h \to b\bar{b}$ signal strength in the Higgsstrahlungs processes $\left(\mu_{Vh}^{b\bar{b}}\right)$ to be SM-like within about 25%. With LHC Run III ongoing and the high-luminosity upgrade (HL-LHC) on the horizon, the precision of the $\mu_{Vh}^{b\bar{b}}$ measurements is expected to improve significantly, resulting in an ultimate projected HL-LHC accuracy of 15% (5%) in the case of the Wh (Zh) production channel [94, 95].

Higgs characterization program

Besides providing a probe of the dominant decay mode of the Higgs boson, precision Vh measurements also play an important role in the Higgs characterization program which is commonly performed in the framework of the SMEFT [46, 96, 97]. In fact, radiative corrections in the SMEFT to both Vh production [98–103] and the $h \to f\bar{f}$ decays [104–108] have been calculated. The existing studies for Vh production have mostly focused on the subset of higher-dimensional interactions that modify the couplings of the Higgs to two vector bosons achieving NLO [98–100, 109, 110]

and NNLO [111] accuracy in QCD, respectively, while in the case of $h \to b\bar{b}$ both NLO QCD and NLO EW corrections to the total decay width have been calculated for the full set of relevant dimension-six SMEFT operators [104–106]. In the publications [101–103] special attention has finally been paid to the class of SMEFT operators that lead to interactions between a Higgs, W or Z boson, and light quarks.

Implementing SMEFT effects at NNLO+PS accuracy using the MiNNLO$_{PS}$ method

The goal of the project [LS1] is to generalise and to extend the recent SMEFT calculation [108] which has achieved NNLO+PS accuracy for the dimension-six operators that contribute to the subprocesses $pp \to Zh$ and $h \to b\bar{b}$ directly in QCD. This class of operators includes effective Yukawa- and chromomagnetic dipole-type interactions of the bottom quark that modify the $h \to b\bar{b}$ decay but do not play a role in $pp \to Zh$ production. Purely EW effective interactions that alter the couplings of the Higgs to gauge bosons are instead not included in the NNLO+PS MC generator presented in [108]. Since these types of SMEFT contributions can lead to phenomenologically relevant effects in the Higgsstrahlungs processes [98–100, 109–111], we include these type of interactions in the current article, extending the NLO SMEFT calculations [98–100] to the NNLO level. Likewise, we improve the precision of the calculations of SMEFT corrections to $pp \to Vh$ production that are associated to couplings between a Higgs, W or Z boson, and light quarks [101–103] to NNLO in QCD. The obtained fixed-order SMEFT predictions are implemented into the POWHEG-BOX [21] and consistently matched to a PS using the MiNNLO$_{PS}$ method [86, 87]. In this way, NNLO QCD accuracy is retained for both production and decays, while the matching to the PS ensures a realistic exclusive description of the $pp \to Zh \to \ell^+\ell^- h$ and the $pp \to Wh \to \ell\nu h$ process at the level of hadronic events. These features make our new NNLO+PS generator a precision tool for future LHC Higgs characterization studies in the SMEFT framework.

5.2 SMEFT operators

Throughout this section we neglect all light fermion masses in both the SM and SMEFT corrections to the $pp \to Zh$ and $pp \to Wh$ processes. The Warsaw basis (see Subchapter 3.1.3) contains the following three independent operators

VVh operators

$$\begin{aligned} \mathcal{O}_{HB} &= (H^\dagger H) B_{\mu\nu} B^{\mu\nu}\,, \qquad \mathcal{O}_{HW} = (H^\dagger H) W^a_{\mu\nu} W^{a,\mu\nu}\,, \\ \mathcal{O}_{HWB} &= (H^\dagger \tau^I H) W^I_{\mu\nu} B^{\mu\nu}\,, \end{aligned} \tag{5.1}$$

that modify the couplings between the Higgs and two vector bosons at tree level. In the case of the operators that result in couplings between the Higgs, a W or a Z boson and light quarks, we consider the following four effective interactions

V(h)qq̄ operators

$$\begin{aligned} \mathcal{O}^{(1)}_{Hq} &= (H^\dagger i \overleftrightarrow{D}_\mu H)(\bar{q}_L \gamma^\mu q_L)\,, \qquad \mathcal{O}^{(3)}_{Hq} = (H^\dagger i \overleftrightarrow{D}^I_\mu H)(\bar{q}_L \gamma^\mu \tau^I q_L)\,, \\ \mathcal{O}_{Hd} &= (H^\dagger i \overleftrightarrow{D}_\mu H)(\bar{d}_R \gamma^\mu d_R)\,, \qquad \mathcal{O}_{Hu} = (H^\dagger i \overleftrightarrow{D}_\mu H)(\bar{u}_R \gamma^\mu u_R)\,, \\ \mathcal{O}_{Hud} &= (\widetilde{H}^\dagger i D_\mu H)(\bar{u}_R \gamma^\mu d_R)\,. \end{aligned} \tag{5.2}$$

Illustrative diagrams that contribute to Zh production and involve an insertion of one of the operators in (5.1) or (5.2) are displayed in Figure 5.1. Notice that $\mathcal{O}_{Hud}$

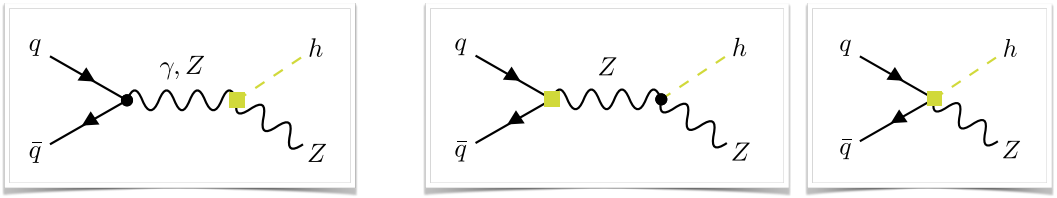

Figure 5.1: Tree-level SMEFT contributions to $q\bar{q} \to Zh$ production. The diagram on the left involves an insertion of one of the operators defined in (5.1), while the two graphs on the right stem from an insertion of one of the operators given in (5.2). The operator insertions are indicated by the light green squares.

only contributes to $pp \to Wh$ production and the dimension-six SMEFT Lagrangian includes the sum of the operator $\mathcal{O}_{Hud}$ and its hermitian conjugate.

Besides the two set of operators (5.1) and (5.2) that alter the $pp \to Vh$ production process, we also consider effective interactions that modify the $Z \to \ell^+\ell^-$ and $W \to \ell\nu$ decays at tree level. In the Warsaw basis there are three such operators, namely

$V(h)\ell\bar{\ell}$ operators

$$\begin{aligned} \mathcal{O}_{H\ell}^{(1)} &= (H^\dagger i \overleftrightarrow{D}_\mu H)(\bar{\ell}_L \gamma^\mu \ell_L)\,, \quad \mathcal{O}_{H\ell}^{(3)} = (H^\dagger i \overleftrightarrow{D}_\mu^I H)(\bar{\ell}_L \gamma^\mu \tau^I \ell_L)\,, \\ \mathcal{O}_{He} &= (H^\dagger i \overleftrightarrow{D}_\mu H)(\bar{e}_R \gamma^\mu e_R)\,. \end{aligned} \tag{5.3}$$

Notice that in writing (5.2) and (5.3) we have assumed that the full SMEFT Lagrangian respects an approximate $U(3)^5$ flavor symmetry which allows us to drop all flavor indices.

The final type of SMEFT corrections that change the Higgsstrahlungs processes indirectly is provided by the Wilson coefficients of the operators that shift the Higgs kinetic term and/or the EW SM input parameters. In order to fully describe these shifts the following three additional operators are needed at tree level:

Further operators

$$\begin{aligned} \mathcal{O}_{H\Box} &= (H^\dagger H)\Box(H^\dagger H)\,, \quad \mathcal{O}_{HD} = (H^\dagger D_\mu H)^*(H^\dagger D^\mu H)\,, \\ \mathcal{O}_{\ell\ell} &= (\bar{\ell}_L \gamma_\mu \ell_L)(\bar{\ell}_L \gamma^\mu \ell_L)\,. \end{aligned} \tag{5.4}$$

5.3 Calculation of Matrix Elements: $q\bar{q} \to Vh$

5.3.1 *SM calculation*

A core input of the NNLO QCD calculation are the squared matrix elements up to $\mathcal{O}(\alpha_s^2)$ in the SMEFT. To better explain how the calculation of these squared matrix elements is performed, we first revisit the structure of the NNLO computation in the SM, which we have repeated, and also implemented into the `POWHEG` framework. Before doing so, we note that we will generically refer to the process $pp \to Vh$ (and its corresponding subprocesses) in both the text and corresponding figures in what follows, but it should be understood that $V = W, Z$ refers to a final-state lepton pair, and that the calculation does include spin-correlation effects in the gauge-boson decays.

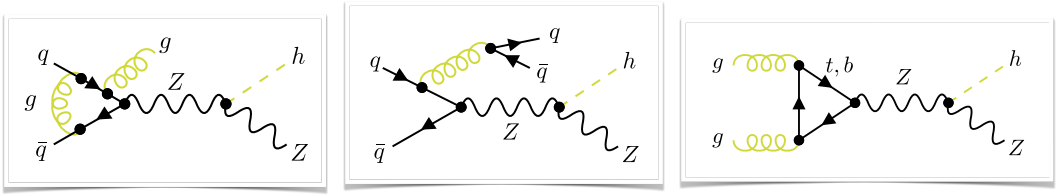

Figure 5.2: Examples of higher-order QCD corrections to $pp \to Zh$ production within the SM. The diagram on the left features additional virtual and real gluon lines (B-type), the diagram in the middle involves a second quark line (C- and D-type) and the diagram on the right is a ggF contribution (A-type). Consult the main text for further details.

A-, B-, C- and D-type amplitudes

In the NNLO calculation of $pp \to Vh$, the contributing partonic channels can be classified according to the number of external quark lines (A $= 0$, B $= 1$, C $=$ D $= 2$), external gluons, and also by the number of loops at the squared amplitude level – see also [112]. Starting with the B-type corrections (i.e. those with a single external quark line), the required squared matrix elements are called `B0g0V, B1g0V, B0g1V, B1g1V, B2g0V, B0g2V`, where the number before `g` refers to the number of additional external gluons relative to the LO contribution for that type, and the number after the `g` refers to the number of loops at the squared level. For example, the left most diagram in Figure 5.2 contains one additional gluon (relative to the Born-level contribution in the quark-antiquark fusion or ggF channel) and is a one-loop graph, and would therefore contribute to `B1g1V` through interference with the corresponding tree-level amplitude. In the case of the SM, the analytic expressions for the corresponding spinor-helicity amplitudes can be found in [112–115]. To obtain the desired squared matrix elements, the spinor-helicity amplitudes can be squared and then summed over all contributing helicities numerically – an explicit example of this procedure is given below. The C-type corrections feature two external quarks lines, or in other words a double real emission contribution with two final-state quarks, and arise from the interference of diagrams such as that represented in the center of Figure 5.2. The D-type corrections account for the additional structures that can appear when same-flavor quarks are considered. These squared matrix elements are called `C0g0V` and `D0g0V` and within the SM the analytic expressions for the corresponding spinor-helicity amplitudes are provided in the work [112]. Finally, the ggF contributions shown on the right in Figure 5.2 constitute the third type of correction which are considered (A-type). They are referred to as `A0g2V` and the corresponding SM spinor-helicity amplitudes are given in [116]. Notice that due to charge conservation the third type of corrections only contributes to the $pp \to Zh$ but not the $pp \to Wh$ process. We add that the corrections called $V_{I,II}$ and $R_{I,II}$ that are related to top-quark loops and involve one external quark line [117] are neglected in our SM calculation. Since in total the numerical effect of these contributions amounts to only around 1% [108, 117, 118], ignoring the $V_{I,II}$ and $R_{I,II}$ terms seems justified at present.

The corresponding calculation including the impact of SMEFT operators (which will be discussed in the following subchapter) can also be performed using spinor-helicity techniques. That calculation requires new helicity amplitudes which can (in

Example of **B1g0Z**

part) be obtained from knowledge of the SM amplitudes. For clarity of explanation, it will be useful to first consider an explicit example in the SM. To do that we consider the case of `B1g0Z` which involves a single external quark line and one external gluon at tree level. A corresponding SM Feynman diagram is displayed on the left-hand side in Figure 5.3. Note that we consider the leptons (quarks) to be outgoing (incoming). The corresponding spinor-helicity amplitude with left-handed fermion chiralities and a physical gluon with a negative helicity reads

***B1g0Z* spinor-helicity amplitude in the SM**

$$\mathcal{A}_{\texttt{B1g0Z}}\left(1_q^-, 2_g^-, 3_{\bar{q}}^+; 4_\ell^-, 5_{\bar{\ell}}^+\right) = \frac{\langle 34\rangle}{\langle 12\rangle\langle 23\rangle}\Big(\langle 13\rangle\,[51] + \langle 23\rangle\,[52]\Big)\,, \tag{5.5}$$

where $\langle ij\rangle$ and $[ij]$ denote the usual spinor products – see Chapter 4.2. Notice that the semicolon in the expression on the l.h.s of (5.5) separates the particles with incoming and outgoing convention, respectively. The amplitudes for the remaining helicity combinations can be obtained via the following parity and charge conjugation relations

$$\begin{aligned}
\mathcal{A}_{\texttt{B1g0Z}}\left(1_q^-, 2_g^+, 3_{\bar{q}}^+; 4_\ell^-, 5_{\bar{\ell}}^+\right) &= -\mathcal{A}_{\texttt{B1g0Z}}\left(3_q^-, 2_g^-, 1_{\bar{q}}^+; 5_\ell^-, 4_{\bar{\ell}}^+\right)^*\,,\\
\mathcal{A}_{\texttt{B1g0Z}}\left(1_q^-, 2_g^{h_g}, 3_{\bar{q}}^+; 4_\ell^+, 5_{\bar{\ell}}^-\right) &= \mathcal{A}_{\texttt{B1g0Z}}\left(1_q^-, 2_g^{h_g}, 3_{\bar{q}}^+; 5_\ell^-, 4_{\bar{\ell}}^+\right)\,,\\
\mathcal{A}_{\texttt{B1g0Z}}\left(1_q^+, 2_g^{h_g}, 3_{\bar{q}}^-; 4_\ell^-, 5_{\bar{\ell}}^+\right) &= -\mathcal{A}_{\texttt{B1g0Z}}\left(3_q^-, 2_g^{h_g}, 1_{\bar{q}}^+; 4_\ell^-, 5_{\bar{\ell}}^+\right)\,,\\
\mathcal{A}_{\texttt{B1g0Z}}\left(1_q^+, 2_g^{h_g}, 3_{\bar{q}}^-; 4_\ell^+, 5_{\bar{\ell}}^-\right) &= -\mathcal{A}_{\texttt{B1g0Z}}\left(3_q^-, 2_g^{h_g}, 1_{\bar{q}}^+; 5_\ell^-, 4_{\bar{\ell}}^+\right)\,.
\end{aligned} \tag{5.6}$$

The resulting spin-averaged matrix element `B1g0Z` takes the form

$$\texttt{B1g0Z} = \frac{8\pi\alpha_s C_F}{C_A}\sum_{h_q,h_g,h_\ell}\left|\frac{g_{Zq}^{h_q} g_{Z\ell}^{h_\ell} g_{hZZ}}{D_Z(s_{123})\,D_Z(s_{45})}\,\mathcal{A}_{\texttt{B1g0Z}}\left(1_q^{h_q}, 2_g^{h_g}, 3_{\bar{q}}^{-h_q}; 4_\ell^{h_\ell}, 5_{\bar{\ell}}^{-h_\ell}\right)\right|^2\,, \tag{5.7}$$

where

$$s_{ij} = \left(k_i + k_j\right)^2\,, \qquad s_{ijk} = s_{ij} + s_{jk} + s_{ki}\,, \tag{5.8}$$

are the usual Mandelstam invariants with k_i the four-momentum of particle i. We have furthermore introduced

$$D_Z(s) = s - m_Z^2 + i m_Z \Gamma_z\,, \tag{5.9}$$

with Γ_Z denoting the total decay width of the Z boson. The symbols $g_{Zf}^{h_f}$ and g_{hZZ} represent the $Zf\bar{f}$ and hZZ coupling strengths, respectively. The explicit expressions for these quantities are given in Appendix A.

To compute the SMEFT contributions that involve modified couplings between the Higgs and two vector bosons, it is important to notice that by using the spinor identity

$$\langle i\,j\rangle[k\,l] = \frac{1}{2}\langle j|\gamma^\mu|k]\langle i|\gamma_\mu|l]\,, \tag{5.10}$$

the result (5.5) can be rewritten as

$$\mathcal{A}_{\texttt{B1g0Z}}\left(1_q^-, 2_g^-, 3_{\bar{q}}^+; 4_\ell^-, 5_{\bar{\ell}}^+\right) = \langle 4|\gamma_\mu|5]\,\mathcal{A}^\mu_{qgq}(1_q^-, 2_g^-, 3_{\bar{q}}^+)\,. \tag{5.11}$$

Spinor-helicity amplitude for the $q\bar{q}g$ subprocess

Here the spinor-helicity amplitude corresponding to the $q\bar{q}g$ subprocess with the indicated helicities is given by

$$\mathcal{A}^{\mu}_{qgq}(1^{-}_{q}, 2^{-}_{g}, 3^{+}_{\bar{q}}) = \frac{\langle 1\,3\rangle\langle 3|\gamma^{\mu}|1] + \langle 2\,3\rangle\langle 3|\gamma^{\mu}|2]}{2\langle 1\,2\rangle\langle 2\,3\rangle}\,. \tag{5.12}$$

5.3.2 *SMEFT calculation*

The technically most involved part of the SMEFT calculation results from insertions of the three operators introduced in (5.1) since $\mathcal{O}_{HB}$, $\mathcal{O}_{HW}$ and $\mathcal{O}_{HWB}$ generate modified hVV vertices with helicity structures different from the one present in the SM, i.e. the spinor chain $\langle 4|\gamma_{\mu}|5]$ in (5.11). These modifications can be included at the level of (5.5) by means of generalised currents that describe the splitting of the initial vector boson V_1 into the outgoing vector boson V_2 and the Higgs boson h [98]. If the initial-state quarks and final-state leptons are left-handed the relevant generalised neutral currents are given by

New helicity structures arising in the SMEFT

$$\begin{aligned}
\mathcal{A}^{\mu}_{hZZ}(k_{123}, 4^{-}_{\ell}, 5^{+}_{\bar{\ell}}) = \frac{g^{-}_{Zq}\, g^{-}_{Z\ell}}{D_Z(s_{123})\, D_Z(s_{45})} \Bigg[& \langle 4|\gamma^{\mu}|5] \left(g_{hZZ} + \delta g^{(3)}_{hZZ}\right) \\
& + \langle 4|\gamma^{\mu}|5] \left(\delta g^{(2)}_{hZZ}\,(s_{123} + s_{45})\right) - \delta g^{(2)}_{hZZ}\, k^{\mu}_{123} \langle 4|\not{k}_{123}|5] \\
& - \frac{\delta g^{(1)}_{hZZ}}{2} \left(\langle 4|\gamma^{\mu}\not{k}_{123}|4\rangle [4\,5] + \langle 4\,5\rangle [5|\not{k}_{123}\gamma^{\mu}|5]\right) \Bigg]\,, \\
\mathcal{A}^{\mu}_{h\gamma Z}(k_{123}, 4^{-}_{\ell}, 5^{+}_{\bar{\ell}}) = \frac{g^{-}_{\gamma q}\, g^{-}_{Z\ell}}{s_{123}\, D_Z(s_{45})} \Bigg[& - \frac{\delta g^{(1)}_{h\gamma Z}}{2} \Big(\langle 4|\gamma^{\mu}|5]\langle 4|\not{k}_{123}|4] \\
& + \langle 4|\gamma^{\mu}|5]\langle 5|\not{k}_{123}|5] - 2\left(k^{\mu}_{4} + k^{\mu}_{5}\right)\langle 4|\not{k}_{123}|5]\Big) \\
& + \delta g^{(2)}_{h\gamma Z} \left(\langle 4|\gamma^{\mu}|5]\, s_{123} - k^{\mu}_{123}\,\langle 4|\not{k}_{123}|5]\right) \Bigg]\,,
\end{aligned} \tag{5.13}$$

where the structures $\mathcal{A}^{\mu}_{hZZ}$ and $\mathcal{A}^{\mu}_{h\gamma Z}$ encode the modified hZZ and $h\gamma Z$ vertices, respectively, and k_{123} denotes the four-momentum of the incoming vector boson. The symbols $g^{h_q}_{\gamma q}$ are the $\gamma q\bar{q}$ coupling strengths while $\delta g^{(1)}_{hZZ}$, $\delta g^{(2)}_{hZZ}$, $\delta g^{(3)}_{hZZ}$, $\delta g^{(1)}_{h\gamma Z}$ and $\delta g^{(2)}_{h\gamma Z}$ are anomalous couplings that describe the interactions between the Higgs boson and the relevant vector bosons as indicated by the subscript. The explicit expressions for all the couplings appearing in (5.13) can be found in Appendix A. We stress that although the anomalous couplings $\delta g^{(2)}_{hZZ}$ and $\delta g^{(2)}_{h\gamma Z}$ do not receive corrections from the Wilson coefficients C_{HB}, C_{HW}, and C_{HWB} our `POWHEG-BOX` implementation contains the full generalised neutral currents (5.13). The presented MC code can therefore be used to extend the Higgsstrahlungs computations in the anomalous-coupling framework [109–111] to the NNLO+PS level.

By looking at (5.11) and (5.13) it is now readily seen that in order to obtain the spin-averaged squared matrix element `B1g0Z` that contains the contributions from

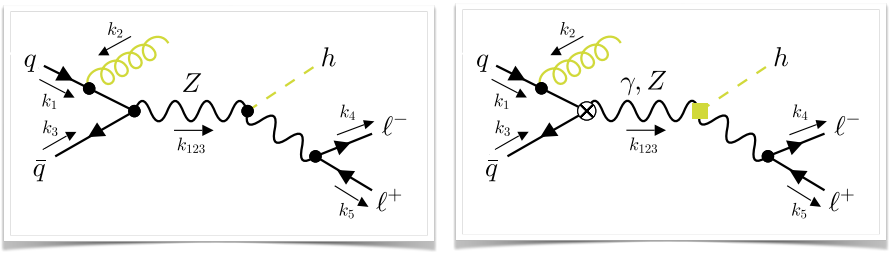

Figure 5.3: Example graphs that contribute to the `B1g0Z` matrix elements. The diagram on the left shows a SM contribution. On the right we instead depict a SMEFT correction that receives contributions from the generalised hZZ and $h\gamma Z$ currents introduced in (5.13). The four-momentum flow is indicated by the black arrows and labels. See the main text for additional explanations.

the SM as well as the Wilson coefficients C_{HB}, C_{HW}, and C_{HWB} one just has to replace the coupling and propagator dressed helicity amplitude appearing in the modulus of (5.7) by the following spinor contraction

Full SMEFT amplitude for ***B1g0Z***

$$\mathcal{A}_{qgq,\mu}\left(1_q^{h_q}, 2_g^{h_g}, 3_{\bar{q}}^{-h_q}\right)\left[\mathcal{A}^{\mu}_{hZZ}(k_{123}, 4_\ell^{h_\ell}, 5_{\bar{\ell}}^{-h_\ell}) + \mathcal{A}^{\mu}_{h\gamma Z}(k_{123}, 4_\ell^{h_\ell}, 5_{\bar{\ell}}^{-h_\ell})\right] . \tag{5.14}$$

A schematic depiction of (5.14) is given on the right in Figure 5.3. Notice that all helicity configurations of $\mathcal{A}^{\mu}_{qgq}$ can be obtained from (5.11) and (5.12) using the relations (5.6) while in the case of $\mathcal{A}^{\mu}_{hZZ}$ and $\mathcal{A}^{\mu}_{h\gamma Z}$ one just has to perform the replacements $g^{-}_{Vf} \to g^{h_f}_{Vf}$ for $f = q, \ell$ and $V = Z, \gamma$.

Insertions of the operators (5.2) and (5.3) lead to the Feynman diagrams shown on the right-hand side in Figure 5.1 at tree level. In order to capture this contribution in the case of the squared matrix element `B1g0Z`, one simply has to add the term

Contributions with quartic $Vhf\bar{f}$ vertices

$$\left(\frac{\delta g^{(1)h_q}_{hZq}\, g^{h_\ell}_{Z\ell}}{D_Z(s_{45})} + \frac{g^{h_q}_{Zq}\, \delta g^{(1)h_\ell}_{hZ\ell}}{D_Z(s_{123})}\right) \mathcal{A}_{\texttt{B1g0Z}}\left(1_q^{h_q}, 2_g^{h_g}, 3_{\bar{q}}^{-h_q}; 4_\ell^{h_\ell}, 5_{\bar{\ell}}^{-h_\ell}\right) , \tag{5.15}$$

to the corresponding dressed SM amplitude appearing within the modulus of (5.7). The analytic expressions for the couplings $\delta g^{(1)h_f}_{hZf}$ are given in Appendix A. In (5.15), the first term in the brackets describes the contribution from $\mathcal{O}^{(1)}_{Hq}$, $\mathcal{O}^{(3)}_{Hq}$, $\mathcal{O}_{Hd}$, and $\mathcal{O}_{Hu}$, while the second term is induced by $\mathcal{O}^{(1)}_{H\ell}$, $\mathcal{O}^{(3)}_{H\ell}$ and $\mathcal{O}_{He}$. Notice that compared to the corresponding SM contribution in (5.7), the SMEFT correction proportional to $\delta g^{(1)h_q}_{hZq}$ in (5.15) is missing the Z-boson propagator depending on s_{123}. This feature explains the high-energy growth [101–103] of the SMEFT $pp \to Vh$ amplitudes involving the Wilson coefficients $C^{(1)}_{Hq}$, $C^{(3)}_{Hq}$, C_{Hd}, and C_{Hu}.

The last type of SMEFT corrections to the matrix element `B1g0Z` is associated to the tree-level shifts of the SM parameters and couplings. EW input scheme corrections from C_{HD}, C_{HWB}, $C^{(3)}_{H\ell}$, and $C_{\ell\ell}$ lead to the shifts δg_1, δg_2, and δv of the $U(1)_Y$, $SU(2)_L$ gauge coupling, and the Higgs VEV, respectively, that in turn induce the shifts $\delta g^{(0)}_{hZZ}$ and $\delta g^{(0)h_f}_{Zf}$ in the respective couplings of the Z boson. The expressions for these shifts are listed in Appendix A. In practice, the input scheme corrections

Input scheme corrections

Direct shifts in the $Zf\bar{f}$ couplings

can be accounted for by applying the replacements $g_{hZZ} \to g_{hZZ} + \delta g^{(0)}_{hZZ}$ and $g^{h_f}_{Zf} \to g^{h_f}_{Zf} + \delta g^{(0)\,h_f}_{Zf}$ to (5.7). Similarly, the Wilson coefficients $C^{(1)}_{Hq}$, $C^{(3)}_{Hq}$, C_{Hd}, C_{Hu}, $C^{(1)}_{H\ell}$, $C^{(3)}_{H\ell}$, and C_{He} lead to direct shifts in the $Zf\bar{f}$ couplings that we include through the shifts $g^{h_f}_{Zf} \to g^{h_f}_{Zf} + \delta g^{(1)\,h_f}_{Zf}$ in (5.7). The expressions for the latter shifts are again given in Appendix A.

While we have used the spinor-helicity amplitudes $\mathcal{A}_{\texttt{B1g0Z}}$ in this chapter as examples to illustrate the general approach that we have employed in our SMEFT calculation of $pp \to Vh$ at NNLO in QCD, it is important to realize that the computation of all other spinor-helicity amplitudes and squared matrix elements proceeds in an analogous manner. In the case of the SMEFT corrections arising from the choice of EW input scheme as well as those associated to insertions of the operators (5.2) and (5.3), this is clear in view of the factorization properties of these contributions (cf. (5.15)). Likewise, since the spinor-helicity structure of the partonic part of a given SMEFT amplitude remains the same as in the SM, it can simply be extracted from the SM expressions and contracted with the part of the SMEFT amplitude that does change. It follows that an explicit calculation of the full partonic structures for the higher-order corrections to $pp \to Vh$ in the SMEFT can always be avoided, because the relevant amplitudes can be obtained from those in the SM by applying relations à la (5.11) and (5.14) which involves only spinor algebra. Still the calculation of all spinor contractions needed to achieve NNLO accuracy for the $pp \to Vh$ processes in the SMEFT is a non-trivial task and the final expressions for the spinor-helicity amplitudes turn out to be too lengthy to be reported here. All algebraic manipulations of spinor products needed in the context of this work have been performed with the aid of the `Mathematica` package `S@M` [119].

5.4 Calculation of Matrix Elements: $g\bar{g} \to Vh$

Our calculation of $gg \to Zh$ production is based on the spinor-helicity amplitudes for the SM derived in [116] and implemented into `MCFM` [120]. In unitary gauge, the expression for the triangle contributions with positive gluon helicities and left-handed fermion chiralities reads

Spinor-helicity amplitude for `A0g2Z`$\triangle$ in the SM

$$\mathcal{A}^{q}_{\texttt{A0g2Z}\triangle}\left(1^{+}_{g},2^{+}_{g},3^{-}_{\ell},4^{+}_{\bar{\ell}}\right) = -\frac{2\,[21]\left([41]\,\langle 13\rangle + [42]\,\langle 23\rangle\right)}{\langle 12\rangle}\left(1-\frac{s_{12}}{m_Z^2}\right) \times m_q^2\, C_{3,1}(s_{12},0,0,m_q,m_q,m_q)\,. \tag{5.16}$$

Notice that we have followed the convention of [116] and written the amplitude for all momenta outgoing. In (5.16), the two terms in the last factor in the first line stem from the transversal and longitudinal part of the Z-boson propagator in unitary gauge, respectively, q is the quark running in the loop with mass m_q and $C_{3,1}$ is the scalar triangle integral defined as in (2.13), but with masses for the propagators [121, 122]. The corresponding SM Feynman diagram is displayed on the right-hand side in Figure 5.2. Similarly, we have implemented the box amplitudes

$$\mathcal{A}^{q}_{\texttt{A0g2Z}\square}\left(1^{+}_{g},2^{+}_{g},3^{-}_{\ell},4^{+}_{\bar{\ell}}\right)\,, \qquad \mathcal{A}^{q}_{\texttt{A0g2Z}\square}\left(1^{-}_{g},2^{+}_{g},3^{-}_{\ell},4^{+}_{\bar{\ell}}\right)\,, \tag{5.17}$$

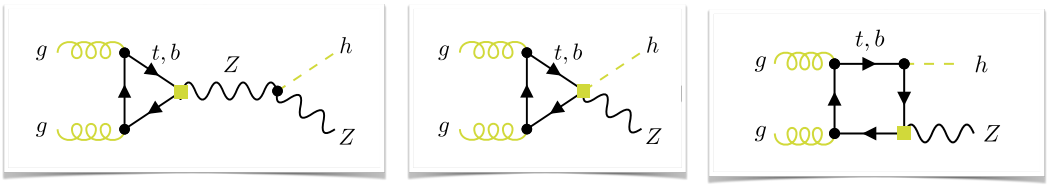

Figure 5.4: Examples of contributions to $gg \to Zh$ production within the SMEFT. All graphs involve an insertion of one of the operators given in (5.2) as indicated by the light green squares. Further details can be found in the main text.

which are too lengthy to be reported here but may be inspected in our squared matrix element library. The remaining non-zero helicity combinations may be obtained via parity and charge conjugation relations. In the case of the triangle contributions, these relations take the form

$$\begin{aligned} \mathcal{A}^q_{\texttt{A0g2Z}\triangle}\left(1^-_g, 2^-_g, 3^\mp_\ell, 4^\pm_{\bar{\ell}}\right) &= -\overline{\mathcal{A}^q_{\texttt{A0g2Z}\triangle}\left(1^+_g, 2^+_g, 4^\mp_\ell, 3^\pm_{\bar{\ell}}\right)}\,, \\ \mathcal{A}^q_{\texttt{A0g2Z}\triangle}\left(1^\pm_g, 2^\pm_g, 3^+_\ell, 4^-_{\bar{\ell}}\right) &= \mathcal{A}^q_{\texttt{A0g2Z}\triangle}\left(1^\pm_g, 2^\pm_g, 4^-_\ell, 3^+_{\bar{\ell}}\right)\,, \end{aligned} \tag{5.18}$$

where the overline means that the brackets should be exchanged, i.e. $[\ldots] \leftrightarrow \langle\ldots\rangle$. Analogous relations hold for the box contributions including the cases where the gluons have opposite helicities which are only present for $\mathcal{A}^q_{\texttt{A0g2Z}\square}$.

Including the triangle and box contributions, the resulting spin-averaged matrix element takes the form

$$\texttt{A0g2Z} = \frac{\alpha_s^2}{8\pi^2\,(C_A^2-1)^2} \sum_{h_g,h_\ell=\pm} \left| \sum_{q=t,b} \left(\mathcal{A}^q_\triangle + \sum_{s=\pm} \frac{m_q^2}{m_z^2}\, \mathcal{A}^{q,s}_\square \right) \right|^2\,, \tag{5.19}$$

with

$$\mathcal{A}^q_\triangle = \frac{(g^-_{Zq} - g^+_{Zq})\, g^{h_\ell}_{Z\ell}\, g_{hZZ}}{D_Z(s_{12})\, D_Z(s_{34})}\, \mathcal{A}^q_{\texttt{A0g2Z}\triangle}\left(1^{h_g}_g, 2^{h_g}_g, 3^{h_\ell}_\ell, 4^{-h_\ell}_{\bar{\ell}}\right)\,, \tag{5.20}$$

$$\mathcal{A}^{q,\pm}_\square = \frac{(g^-_{Zq} - g^+_{Zq})\, g^{h_\ell}_{Z\ell}\, g_{hZZ}}{D_Z(s_{34})}\, \mathcal{A}^q_{\texttt{A0g2Z}\square}\left(1^{h_g}_g, 2^{\pm h_g}_g, 3^{h_\ell}_\ell, 4^{-h_\ell}_{\bar{\ell}}\right)\,. \tag{5.21}$$

Here $D_Z(s)$ has been defined in (5.9) while the expressions for the couplings $g^\pm_{Zf}$ and g_{hZZ} can be found in (A.2). The coupling g_{hZZ} appearing in (5.21) requires some explanation. In fact, the box contributions do not involve a hZZ vertex but instead the Higgs boson couples directly to the quarks. However, since

$$g_{hZZ}\,\frac{m_q^2}{m_Z^2} = \frac{v\,(g_1^2+g_2^2)}{2}\,\frac{m_q^2}{m_Z^2} = \frac{2m_Z^2}{v}\,\frac{m_q^2}{m_Z^2} = \frac{2m_q^2}{v}\,, \tag{5.22}$$

with a factor m_q/v coming from the $hq\bar{q}$ vertex and another m_q stemming from the mass insertion in the box diagram the expected mass dependence for $\mathcal{A}^q_{\texttt{A0g2Z}\square}$ is recovered.

Furry theorem

It is important to realize that as a result of the generalised Furry theorem the vector-current coupling of the Z boson, which is proportional to the combination $(g^-_{Zq} + g^+_{Zq})$ of couplings, does not contribute to the spin-averaged matrix element `A0g2Z` as given in (5.19). However, the axial-current part contributes, as signalled by the factor $(g^-_{Zq} - g^+_{Zq})$ in both (5.20) and (5.21), and this contribution is directly connected to the $U(1)_A \times SU(3)_c$ gauge anomaly. In fact, a regulator and a loop routing scheme must be introduced to properly define the amplitude $\mathcal{A}^q_{\texttt{A0g2Z}\triangle}$, rendering its expression scheme-dependent – for a detailed explanation of this point see for example [15]. Within the SM, the axial parts of the top- and bottom-quark couplings obey

Anomaly cancellation in the SM

$$(g^-_{Zt} - g^+_{Zt}) = -(g^-_{Zb} - g^+_{Zb})\,, \tag{5.23}$$

and as a result all gauge anomalies are cancelled. It follows that the sum over q that appears in (5.19) evaluates to

$$\sum_{q=t,b} (g^-_{Zq} - g^+_{Zq})\,\mathcal{A}^q_{\texttt{A0g2Z}\triangle} = (g^-_{Zt} - g^+_{Zt})\,\left(\mathcal{A}^t_{\texttt{A0g2Z}\triangle} - \mathcal{A}^b_{\texttt{A0g2Z}\triangle}\right)\,, \tag{5.24}$$

and in consequence any scheme-dependent constant shift in the amplitude $\mathcal{A}^q_{\texttt{A0g2Z}\triangle}$ drops out in the combination $\left(\mathcal{A}^t_{\texttt{A0g2Z}\triangle} - \mathcal{A}^b_{\texttt{A0g2Z}\triangle}\right)$. Notice that in the degenerate or zero mass case the sum (5.24) vanishes identically. Since we treat the light-quark generations as massless, down-, up-, strange-, and charm-quark loops hence do not need to be included in the spin-averaged matrix element (5.19).

The amplitudes including the SMEFT contributions to (5.19) were computed with the procedure outlined in Subchapter 5.3.2. Since the SM amplitudes were derived in unitary gauge, only SMEFT contributions to vertices involving the Z boson have to be considered. We have checked explicitly that in Feynman gauge, the SMEFT effects in the Goldstone diagrams are equivalent to the effects in the longitudinal part of the amplitude in unitary gauge. In addition to the contributions with an effective $Zq\bar{q}$ or $Z\ell^+\ell^-$ vertex represented by the diagram on the left in Figure 5.4, there are also contributions with $hZq\bar{q}$ or $hZ\ell^+\ell^-$ vertices. A corresponding graph is depicted on the right in Figure 5.4. In these cases only the transversal part of (5.16) contributes – the longitudinal part vanishes because the Z boson couples directly to the leptons that are treated as massless – and therefore in addition to dropping the factor $D_Z(s_{12})$ in (5.20), one also has to discard the longitudinal part in (5.16) by removing the factor $(1 - s_{12}/m_Z^2)$. This leads to the following contribution

Contributions with quartic $Vhf\bar{f}$ vertices

$$\left[\frac{\left(\delta g^{(1)-}_{hZq} - \delta g^{(1)+}_{hZq}\right) g^{h_\ell}_{Z\ell}}{D_Z(s_{34})} + \frac{\left(g^-_{Zq} - g^+_{Zq}\right)\delta g^{(1)\,h_\ell}_{hZ\ell}}{D_Z(s_{12})}\right]\,\frac{\mathcal{A}^q_{\texttt{A0g2Z}\triangle}\left(1^{h_g}_g, 2^{h_g}_g, 3^{h_\ell}_\ell, 4^{-h_\ell}_{\bar{\ell}}\right)}{1 - \frac{s_{12}}{m_Z^2}}\,, \tag{5.25}$$

from SMEFT diagrams with a $hZq\bar{q}$ or $hZ\ell^+\ell^-$ vertex. This contribution can be included by simply adding the expression (5.25) to the sum over q in (5.19).

The triangle contributions with a $Zq\bar{q}$ or a $hZq\bar{q}$ vertex depicted in Figure 5.4 deserve further discussion. In fact, in their sum these contributions cancel exactly [123],

which is an interesting feature of the SMEFT. To explicitly see this cancellation we rewrite the SMEFT $Zq\bar{q}$ contribution to (5.20) in the following way

$$\begin{aligned}\mathcal{A}^{q}_{\triangle} &\propto \frac{\left(\delta g^{(1)-}_{Zq} - \delta g^{(1)+}_{Zq}\right) g^{h_\ell}_{Z\ell}\, g_{hZZ}}{D_Z(s_{12}) D_Z(s_{34})} = \frac{\frac{v}{2}\left(\delta g^{(1)-}_{hZq} - \delta g^{(1)+}_{hZq}\right) g^{h_\ell}_{Z\ell}\, \frac{2m_Z^2}{v}}{\left(s_{12} - m_Z^2\right) D_Z(s_{34})} \\ &= -\frac{\left(\delta g^{(1)-}_{hZq} - \delta g^{(1)+}_{hZq}\right) g^{h_\ell}_{Z\ell}}{D_Z(s_{34})} \frac{1}{1 - \frac{s_{12}}{m_Z^2}}\,.\end{aligned} \tag{5.26}$$

Here we have used (5.9), (A.2), and (A.5) in the first step. Notice that the final result in (5.26) is up to an overall sign and the amplitude $\mathcal{A}^{q}_{\texttt{A0g2Z}\triangle}$ equal to the first term in (5.25), which proves the cancellation. For simplicity, we have treated m_Z^2 as real here, however, the discussion does not change if one replaces it by its complex counterpart $m_Z^2 - i m_Z \Gamma_Z$ in both $D_Z(s_{12})$ and g_{hZZ}. The only contributions that remain for the operators in (5.2) are therefore the box contributions shown in the middle of Figure 5.4. Note that for the operators in (5.1) both the triangle and box diagrams are non-vanishing.

Anomaly cancellation in the SMEFT

Notice that the cancellation of the triangle contributions in $pp \to Zh$ production guarantees that both relevant and irrelevant anomalous contributions depending on the Wilson coefficients of the operators (5.2) automatically annul. In fact, it can be shown [124–128] that the cancellation of relevant anomalous contributions is a general feature of the SMEFT, while the cancellation of irrelevant terms can always be achieved by adding an appropriate local counterterm, i.e. a Wess-Zumino term [129], to the SMEFT Lagrangian. As a result, the condition for the cancellation of relevant gauge anomalies in the SMEFT is the same as in the SM and only dependent on the gauge quantum numbers of the fermionic sector, as one would naively expect from an effective field theory point of view. The observed cancellation between the triangle contribution with a $Zq\bar{q}$ and a $hZq\bar{q}$ vertex hence implies that one does not need to introduce a Wess-Zumino term to obtain a scheme-independent expression for the $gg \to Zh$ amplitudes in the SMEFT.

We finally note that the amplitude for the generalised neutral current proportional to $\delta g^{(1)}_{hZZ}$ as given in (5.13) vanishes in `A0g2Z`. Also $\delta g^{(1)}_{h\gamma Z}$ and $\delta g^{(2)}_{h\gamma Z}$ have no effect, since the photon couples vectorially to the quark loop. Only $\delta g^{(3)}_{hZZ}$ as given in (A.4) and the corresponding SMEFT operators contribute to $gg \to Zh$ production. This contribution is however not anomalous and hence needs no special treatment. Let us finally mention that we have used `OpenLoops 2` [130] as well as the implementation `SMEFT@NLO` [45] together with `MadGraph5_aMC@NLO` [131] to cross check the results presented in this section.

5.5 POWHEG Implementation

5.5.1 *Squared matrix element `Fortran` library*

Squared matrix element `Fortran` library

We provide all squared matrix elements discussed in the previous sections in a self-contained `Fortran` library [132]. Our library includes the spinor-helicity amplitudes for the dimension-four SM and dimension-six SMEFT contributions as well as the

definitions for the couplings and the propagators depending on the EW input scheme, which are combined and evaluated numerically in the squared matrix elements up to the desired SMEFT power counting order. Details on the library can be found in [LS1, Sec. 3.3].

5.5.2 *NNLO+PS implementation in* `POWHEG`

In the following, we briefly describe how we implemented the fixed-order NNLO SMEFT calculations of $pp \to Zh \to \ell^+\ell^- h$ and $pp \to Wh \to \ell\nu h$ in the `POWHEG` framework. We first recall that within the SM, calculations of the $pp \to Vh$ processes have recently reached NNLO+PS accuracy [118, 133–135]. In fact, here we follow the approach presented in [118].

$q\bar{q}F$ generator using `POWHEG` `MiNNLO`$_{\text{PS}}$

In the case of Higgsstrahlung from $q\bar{q}F$, we use the `MiNNLO`$_{\text{PS}}$ method to match our fixed-order NNLO matrix elements to the PS. As described in Chapter 4.3, the starting point of `MiNNLO`$_{\text{PS}}$ is the calculation of the $q\bar{q} \to Vh$ channel in association with one light QCD parton at NLO according to the `POWHEG` method [18, 136], inclusive in the radiation of a second light QCD parton. The computation of the relevant matrix elements has been outlined in Section 5.3 and relies on the SM spinor-helicity amplitudes calculated in [112–115]. In a second step, an appropriate Sudakov form factor and higher-order corrections are applied such that the calculation remains finite in the unresolved limit of the light partons and NNLO accurate for inclusive $q\bar{q} \to Vh$ production. In the third step, the kinematics of the second radiated parton (accounted for inclusively in the first step) is generated following the `POWHEG` method to preserve the NLO accuracy of the Vh plus jet cross section, including subsequent radiation through `Pythia 8.2` [33]. We stress that since all emissions are ordered in transverse momentum (p_T) and the used Sudakov form factor matches the LLs generated by `Pythia 8.2`, the `MiNNLO`$_{\text{PS}}$ approach maintains the LL accuracy of the PS. While our `MiNNLO`$_{\text{PS}}$ generator for $q\bar{q} \to Vh$ production uses the infrastructure of the NNLO+PS SM Higgsstrahlungs generator [118], the parts of the code that calculate the matrix elements are entirely new and independent. To validate our implementation of the SM computation we have performed extensive numerical checks against [118]. The individual spinor-helicity amplitudes were furthermore compared to a private implementation of the results presented in [112] (which entered the calculation [137]), and results for the squared amplitudes were numerically validated with `OpenLoops 2` [130].

ggF generator using `POWHEG`

The ggF one-loop contributions to Higgsstrahlung, i.e. the $gg \to Zh$ process, can instead be computed independently at LO+PS and simply added to the $q\bar{q}F$ results. We have written a corresponding generator using the `POWHEG` framework. We have validated our implementation of the corresponding SM spinor-helicity amplitudes numerically against `OpenLoops 2` at the level of the squared matrix element.

Besides the direct SMEFT contributions described in Chapter 5.3, the $pp \to Vh$ processes also receive corrections from the propagators of the Z and W bosons, because SMEFT operators generically modify the masses and the total decay widths of all unstable particles. Our `POWHEG-BOX` implementation contains the complete tree-level shifts of the relevant masses and total decay widths that are induced by the Wilson coefficients of the operators (5.1) to (5.4) for the α, the α_μ as well as the

LEP scheme. For instance, in the case of the total decay width of the Z and W boson in the LEP scheme, we find the relevant shifts

Decay width corrections

$$\delta\Gamma_Z \simeq -\frac{v^2}{\Lambda^2}\Big[1.99C_{HWB} - 1.14C_{Hq}^{(1)} - 3.89C_{Hq}^{(3)} + 0.46C_{Hd} - 0.62C_{Hu} + 0.46C_{H\ell}^{(1)} + 4.98C_{H\ell}^{(3)} + 0.46C_{He} + 1.63C_{HD} - 3.25C_{\ell\ell}\Big]\,\text{GeV}\,, \quad (5.27)$$

$$\delta\Gamma_W \simeq -\frac{v^2}{\Lambda^2}\Big[4.77C_{HWB} - 2.67C_{Hq}^{(3)} + 5.31C_{H\ell}^{(3)} + 2.16C_{HD} - 3.32C_{\ell\ell}\Big]\,\text{GeV}\,.$$

These results agree with those presented in the literature (see for instance [138]). We stress that we do not perform an expansion in the SMEFT corrections to the propagators of the Z and W boson. In consequence, the dependence on the Wilson coefficients of our numerical results is generally non-linear. The resulting non-linear effects are however always very small.

5.6 Phenomenological analysis

In the following, we present NNLO+PS accurate results for $pp \to Zh \to \ell^+\ell^- h$ with a stable Higgs boson including the SMEFT effects discussed in Chapter 5.3. All SM input parameters are taken from the most recent Particle Data Group (PDG) review [64]. We use the values $\alpha = 1/127.951$, $G_F = 1.1663788 \cdot 10^{-5}\,\text{GeV}^{-2}$, $m_Z = 91.1876\,\text{GeV}$, $\Gamma_Z^{\text{SM}} = 2.4952\,\text{GeV}$, $m_h = 125.09\,\text{GeV}$ and $\Gamma_h^{\text{SM}} = 4.1\,\text{MeV}$. The values of the weak mixing angle, the $U(1)_Y$ and $SU(2)_L$ gauge coupling and the Higgs VEV are calculated in the LEP scheme $\{\alpha, G_F, m_Z\}$. The `NNPDF31_nnlo_as_01180` PDFs [139] are employed in our MC simulations and events are showered with `PYTHIA 8.2` [33] utilising the Monash tune [140]. To target the $Z \to \ell^+\ell^-$ decay, we select events with two charged leptons (electrons or muons). The leptons are defined at the dressed level, meaning the lepton four-momentum is combined with the four-momenta of nearby prompt photons arising in the shower using a dressing-cone size of $\Delta R_{\ell\gamma} < 0.1$. The leptons are required to have $p_{T,\ell} > 15\,\text{GeV}$ and a pseudorapidity of $|\eta_\ell| < 2.5$. The invariant mass of the dilepton pair is restricted to $m_{\ell^+\ell^-} \in [75, 105]\,\text{GeV}$. These restrictions are close to those imposed by the existing ATLAS and CMS studies of [92, 93, 141–143] and we will simply refer to them as *fiducial cuts* in what follows.

In order to showcase the sensitivity of $pp \to Zh$ to contributions of the SMEFT dimension-six operators listed in Section 5.2, we worked out benchmark scenarios for the values of their Wilson coefficients that are still allowed by current experimental constraints. The details of this discussion can be found in [LS1, Sec. 4], it considers the PDG average for the W mass, the Z boson coupling measurements from LEP and SLD, as well as $h \to WW$, $h \to ZZ$, $h \to \gamma\gamma$ and $h \to \gamma Z$ measurements at the LHC. The benchmarks are

SMEFT Wilson coefficient benchmarks

$$C_{HB} = 0.015\,, \qquad C_{HW} = -0.05\,, \qquad C_{HWB} = 0\,, \quad (5.28)$$

for the operators modifying the VVh vertex, and

$$C_{Hq}^{(3)} = 0.05\,, \qquad C_{Hq}^{(1)} = C_{Hd} = C_{Hu} = 0\,, \quad (5.29)$$

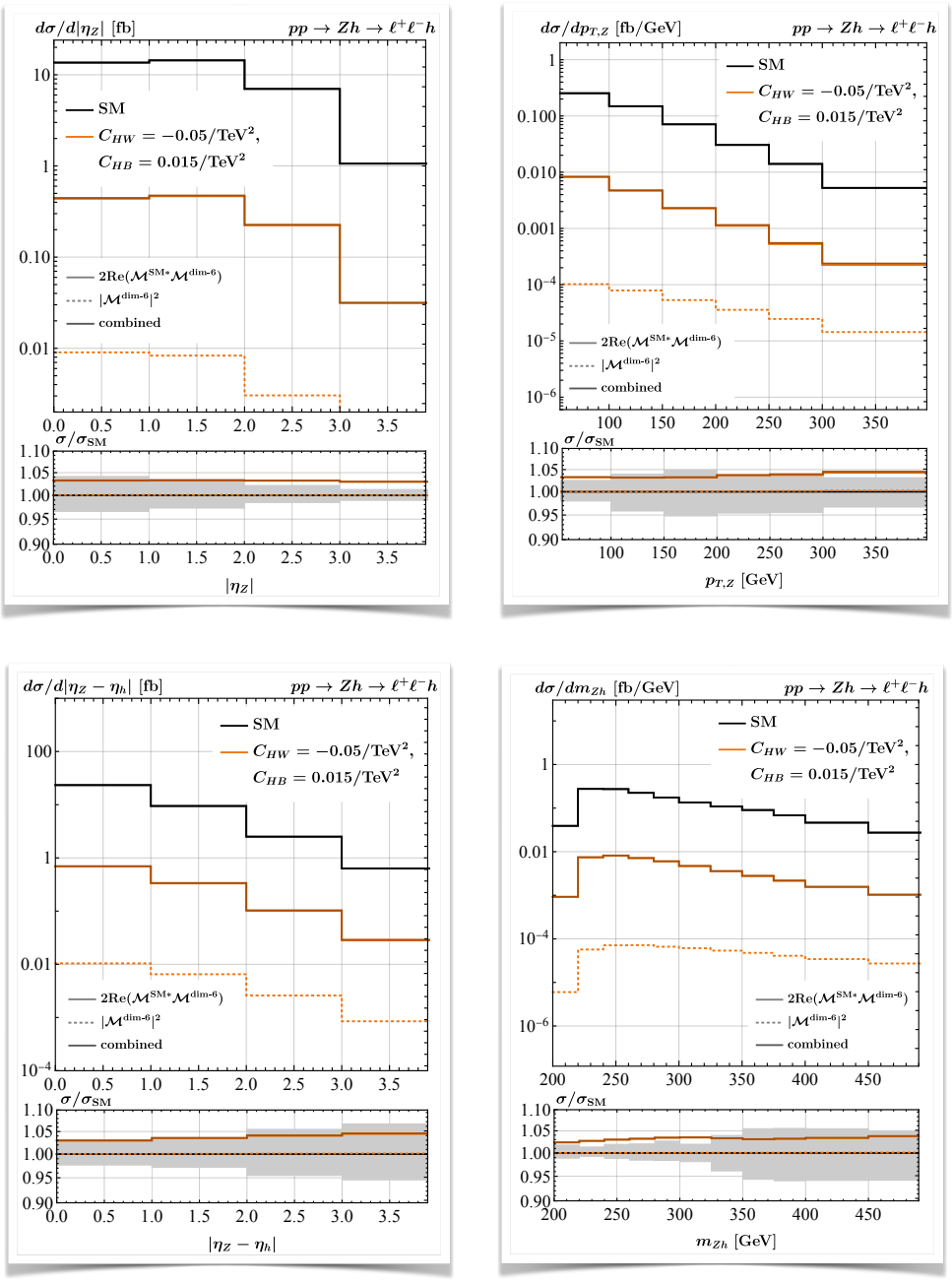

Figure 5.5: NNLO+PS predictions for $pp \to Zh \to \ell^+\ell^- h$ production in the SMEFT benchmark scenario (5.28) assuming a common operator suppression scale of $\Lambda = 1\,\text{TeV}$. The four panels show the fiducial cross section differential in $|\eta_Z|$ (upper left), $p_{T,Z}$ (upper right), $|\eta_Z - \eta_h|$ (lower left) and m_{Zh} (lower right) for proton-proton collisions at 13 TeV. The SM predictions are indicated by the solid black lines while the solid (dotted) orange curves represent the SMEFT contribution linear (quadratic) in the Wilson coefficients. The solid dark orange lines correspond to the sums of the linear and quadratic SMEFT contributions. The lower panels depict the ratios between the BSM and the SM distributions with the gray band representing the SM scale uncertainties. See main text for further details.

$$C_{Hd} = -0.1\,, \qquad C_{Hq}^{(1)} = C_{Hq}^{(3)} = C_{Hu} = 0\,, \tag{5.30}$$

$$C_{Hu} = 0.1\,, \qquad C_{Hq}^{(1)} = C_{Hq}^{(3)} = C_{Hd} = 0\,, \tag{5.31}$$

$$C_{Hq}^{(1)} = 0.05\,, \qquad C_{Hq}^{(3)} = C_{Hd} = C_{Hu} = 0\,, \tag{5.32}$$

for the operators modifying the $Vf\bar{f}$ vertices. Wilson coefficients that are not listed in above benchmarks are set to zero, the SMEFT scale Λ is assumed to be 1 TeV.

C_{HB}, C_{HW}, C_{HWB}

The four panels in Figure 5.5 display our NNLO+PS predictions for the process $pp \to Zh \to \ell^+\ell^- h$ in the SMEFT benchmark scenario (5.28) assuming LHC collisions with a center-of-mass energy of $\sqrt{s} = 13\,\text{TeV}$. The fiducial cross sections differential in the Z-boson pseudorapidity $|\eta_Z|$ (upper left) and transverse momentum $p_{T,Z}$ (upper right) as well as the pseudorapidity difference $|\eta_Z - \eta_h|$ (lower left) and the invariant mass m_{Zh} (lower right) of the Zh system are shown. The central renormalization scale μ_R and factorization scale μ_F are set according to the MiNNLO$_{\text{PS}}$ procedure [86, 87] (see Section 4.3) and the gray bands in the lower panels represent the corresponding perturbative uncertainties in the SM. These uncertainties have been obtained from seven-point scale variations enforcing the constraint $1/2 \leq \mu_R/\mu_F \leq 2$. Within the SM they do not exceed 5% for what concerns the considered distributions, and relative scale uncertainties of very similar size are also found in the case of the SMEFT spectra. The SM predictions are indicated by the solid black lines while the solid (dotted) orange curves represent the SMEFT contributions that are linear (quadratic) in the Wilson coefficients. Notice that the linear (quadratic) SMEFT contributions arise from the interference of the SMEFT and SM amplitudes (self-interference of the SMEFT amplitudes). The solid dark orange lines finally correspond to the sums of the linear and quadratic SMEFT contributions. We observe that in the case of the $|\eta_Z|$ distribution the SMEFT effects related to C_{HB} and C_{HW} to first approximation simply shift the spectra by a constant amount. In the cases of the $p_{T,Z}$, the $|\eta_Z - \eta_h|$ and the m_{Zh} spectra the relative sizes of the SMEFT corrections instead grow with increasing $p_{T,Z}$, $|\eta_Z - \eta_h|$ and m_{Zh}, respectively. It is also evident from all panels that the quadratic SMEFT contributions are negligibly small compared to the linear terms. Numerically, we find that the benchmark scenario (5.28) leads to relative corrections of around +2% to +5% in the studied distributions – the fiducial cross section is enhanced by +3.5% compared to the SM.

Notice that while the predicted deviations are sometimes larger than the corresponding SM scale uncertainties, they are typically smaller than the ultimate projected HL-LHC accuracy in Zh production channel that amounts to 5% [94, 95]. From this numerical exercise one can conclude that future constraints on the Wilson coefficients C_{HB}, C_{HW} and C_{HWB} from Vh production are unlikely to be as stringent as the limits that future determinations of the Higgs signal strengths in $h \to \gamma\gamma$ and $h \to \gamma Z$ will allow to set.

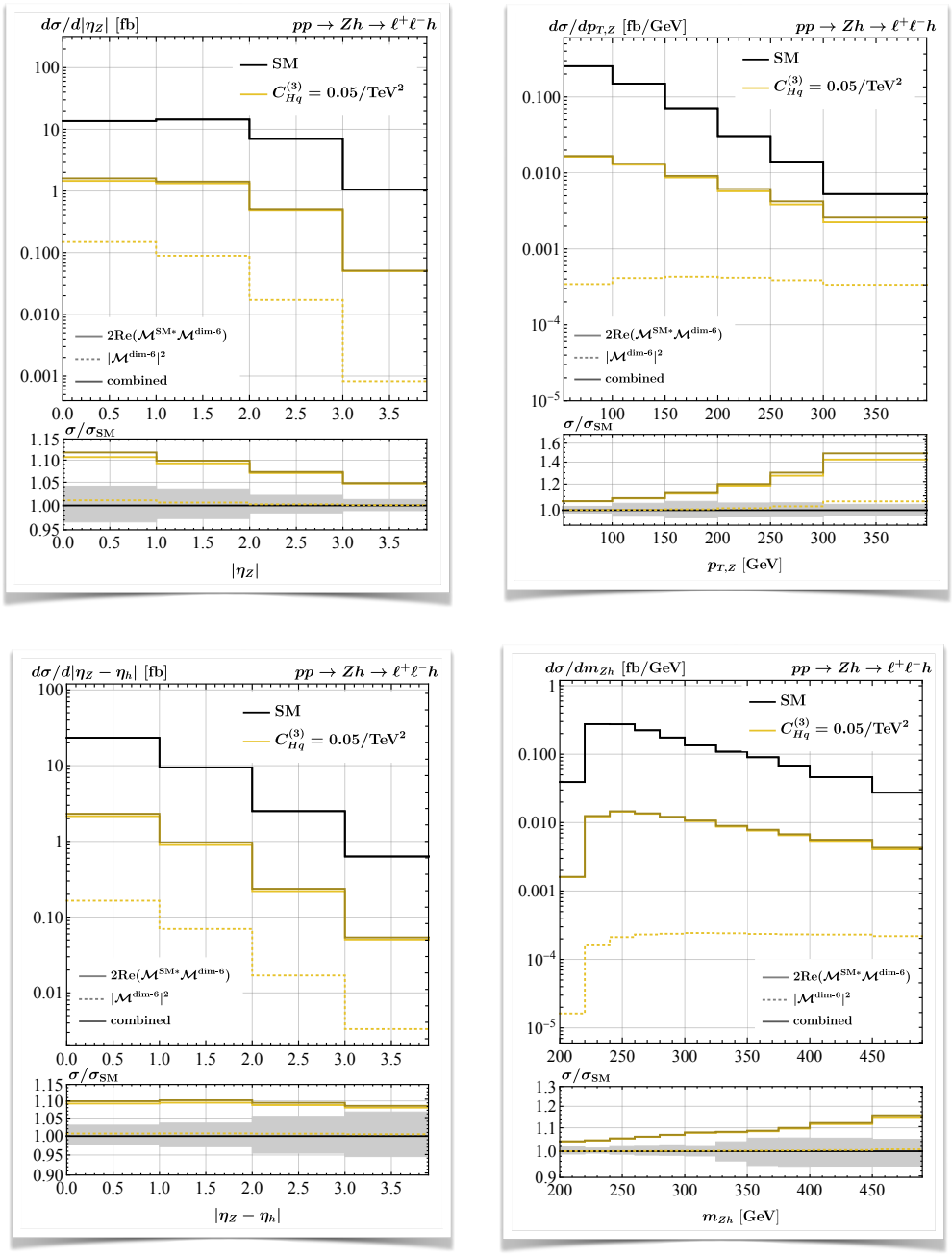

Figure 5.6: As Figure 5.5 but for benchmark scenario (5.29) with $\Lambda = 1\,\text{TeV}$. The yellow lines correspond to the BSM results.

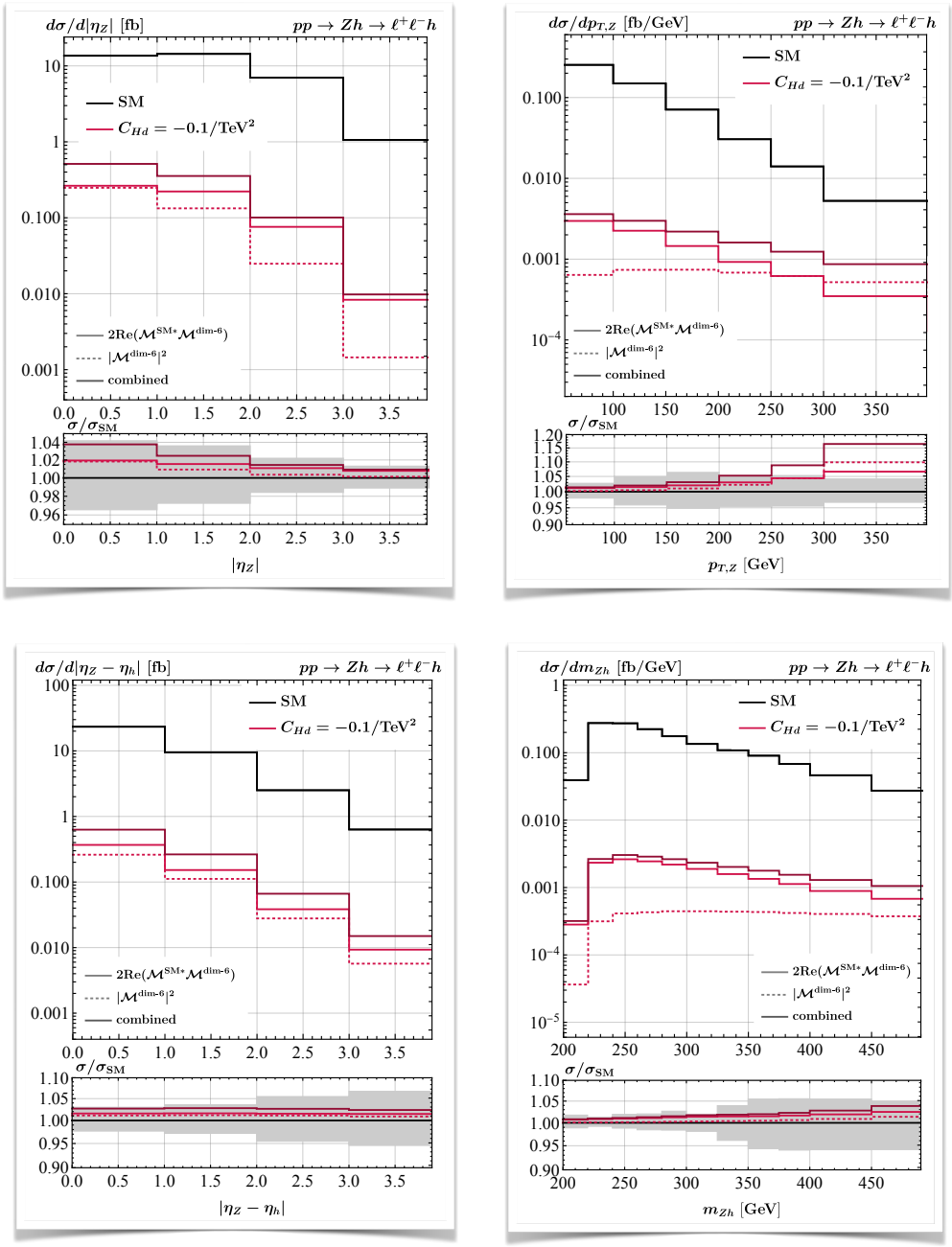

Figure 5.7: As Figure 5.5 but for benchmark scenario (5.30) assuming $\Lambda = 1\,\text{TeV}$. The red curves represent the BSM results.

$C_{Hq}^{(3)}$, C_{Hd}, C_{Hu}, $C_{Hq}^{(1)}$

Figures 5.6 to 5.8 contain our NNLO+PS predictions for $pp \to Zh \to \ell^+\ell^- h$ production in the SMEFT benchmark scenarios (5.29) to (5.31). In all cases we have employed an operator suppression scale of $\Lambda = 1\,\text{TeV}$. The results depicted in the first three figures show very similar features. In all cases the relative SMEFT corrections are rather flat in the $|\eta_Z|$ and $|\eta_Z - \eta_h|$ distributions, while in the case of the $p_{T,Z}$ and m_{Zh} spectra they get larger with increasing $p_{T,Z}$ and m_{Zh}. The observed high-energy growth is expected from (5.15) and in all three cases most pronounced in the $p_{T,Z}$ distribution. One also sees that the linear SMEFT effects are largest in the benchmark scenario with $C_{Hq}^{(3)} = 0.05$ where they can exceed $+50\%$ compared to the SM for $p_{T,Z} > 300\,\text{GeV}$. The respective effects in the benchmark scenario with $C_{Hd} = -0.1$ ($C_{Hu} = 0.1$) just correspond to around $+7\%$ ($+20\%$). The observed hierarchy of SMEFT effects can be traced back to the approximate pattern $g_{Zd}^- \simeq -g_{Zu}^- \simeq -6g_{Zd}^+ \simeq 3g_{Zu}^+$ of left- and right-handed Z-boson couplings within the SM and the feature $\delta g_{Zd}^{(1)-} \propto -C_{Hq}^{(3)}$ and $\delta g_{Zu}^{(1)-} \propto C_{Hq}^{(3)}$ – see (A.6). Notice also that the size of the quadratic SMEFT corrections is relatively small in the case of (5.29) while these effects are comparable to or even larger than the linear terms for the benchmark scenarios specified in (5.30) and (5.31). In the case of the SMEFT benchmark scenario (5.32) the pattern of SMEFT deviations turns out to be more complicated. This is illustrated in the four panels of Figure 5.9. One observes that the linear SMEFT effects are typically small and even change sign in some distributions as indicated by the transitions from solid to dashed lines. To understand these features it is important to realize that $g_{Zd}^- \simeq -g_{Zu}^-$, $\delta g_{Zd}^{(1)-} \propto -C_{Hq}^{(1)}$ and $\delta g_{Zu}^{(1)-} \propto -C_{Hq}^{(1)}$ and to keep in mind that the down-quark luminosity in a proton is smaller than the up-quark luminosity at large x while the two luminosities are of similar size at small x. For the choice $C_{Hq}^{(1)} = 0.05$, the down- and up-quark contributions thus tend to cancel leading to a numerical suppression of the full linear SMEFT effects compared to naive expectation. It is also evident from the shown results that the quadratic SMEFT corrections are as large in magnitude as the linear terms. In fact, in the case of the $p_{T,Z}$ and m_{Zh} spectra the two types of SMEFT effects have opposite relative signs resulting in very small combined BSM contributions not exceeding the level of $+2\%$ in the case of the $p_{T,Z}$ distribution. Notice finally that due to the energy growth most of the sensitivity to the SMEFT effects considered in Figures 5.6 to 5.9 comes from the high-energy tails of kinematic distributions such as the $p_{T,Z}$ and m_{Zh} spectra. In such a case the Higgs-boson decay products are significantly boosted, giving rise to very specific kinematic features and providing additional handles to distinguish signal from background events. The articles [101–103] have exploited this feature to obtain stringent constraints on the dimension-six operators (5.2) using future hypothetical hadron collider measurements of Vh production. The MiNNLO$_{\text{PS}}$ generator presented in this work would allow to improve the accuracy of these studies from the NLO+PS to the NNLO+PS level. A comparison between the NLO+PS of [100] and our NNLO+PS predictions detailing the size of the NNLO corrections can be found in Appendix B.

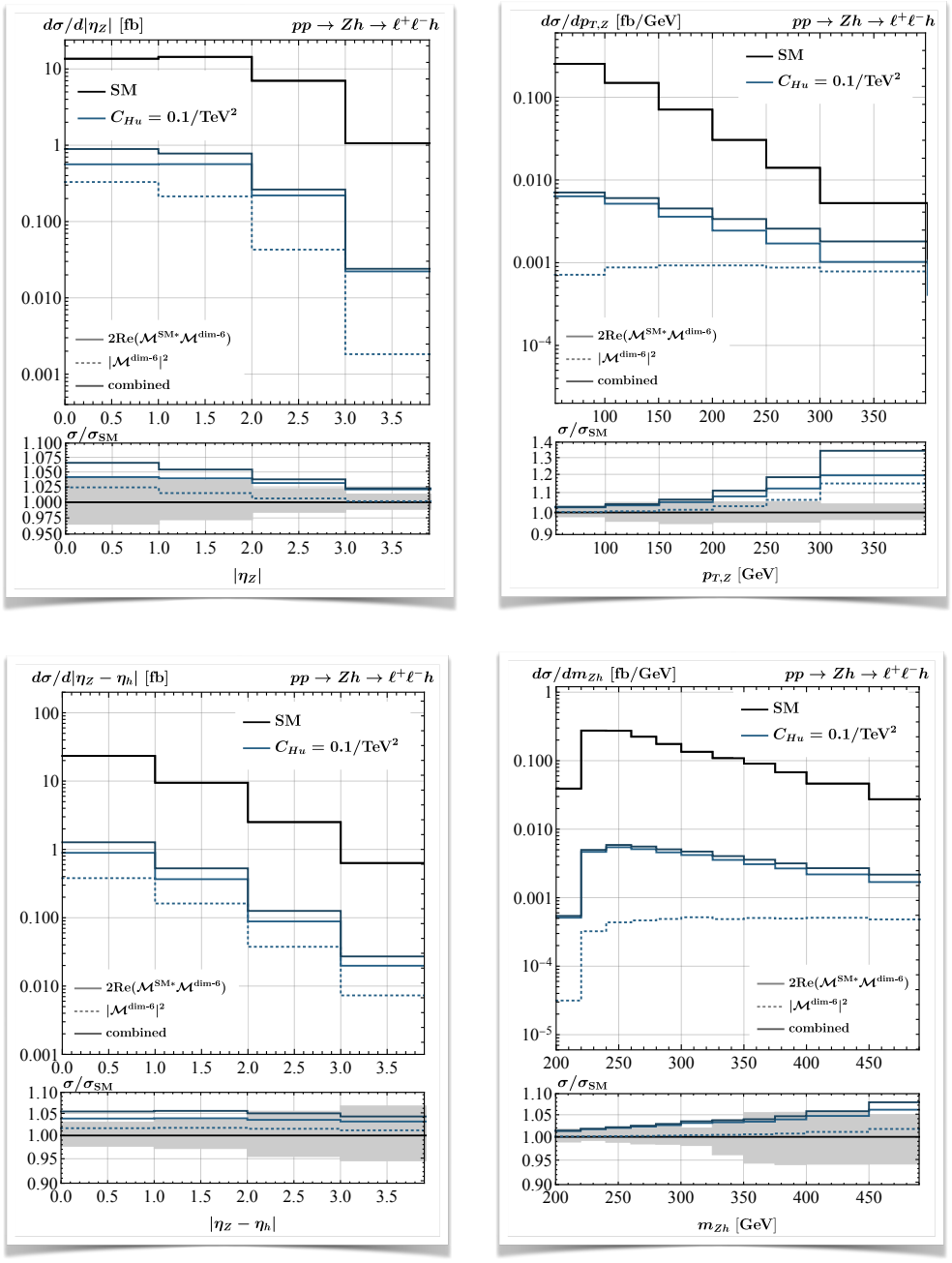

Figure 5.8: As Figure 5.5 but for benchmark scenario (5.31) with $\Lambda = 1\,\text{TeV}$. The blue lines are the BSM results.

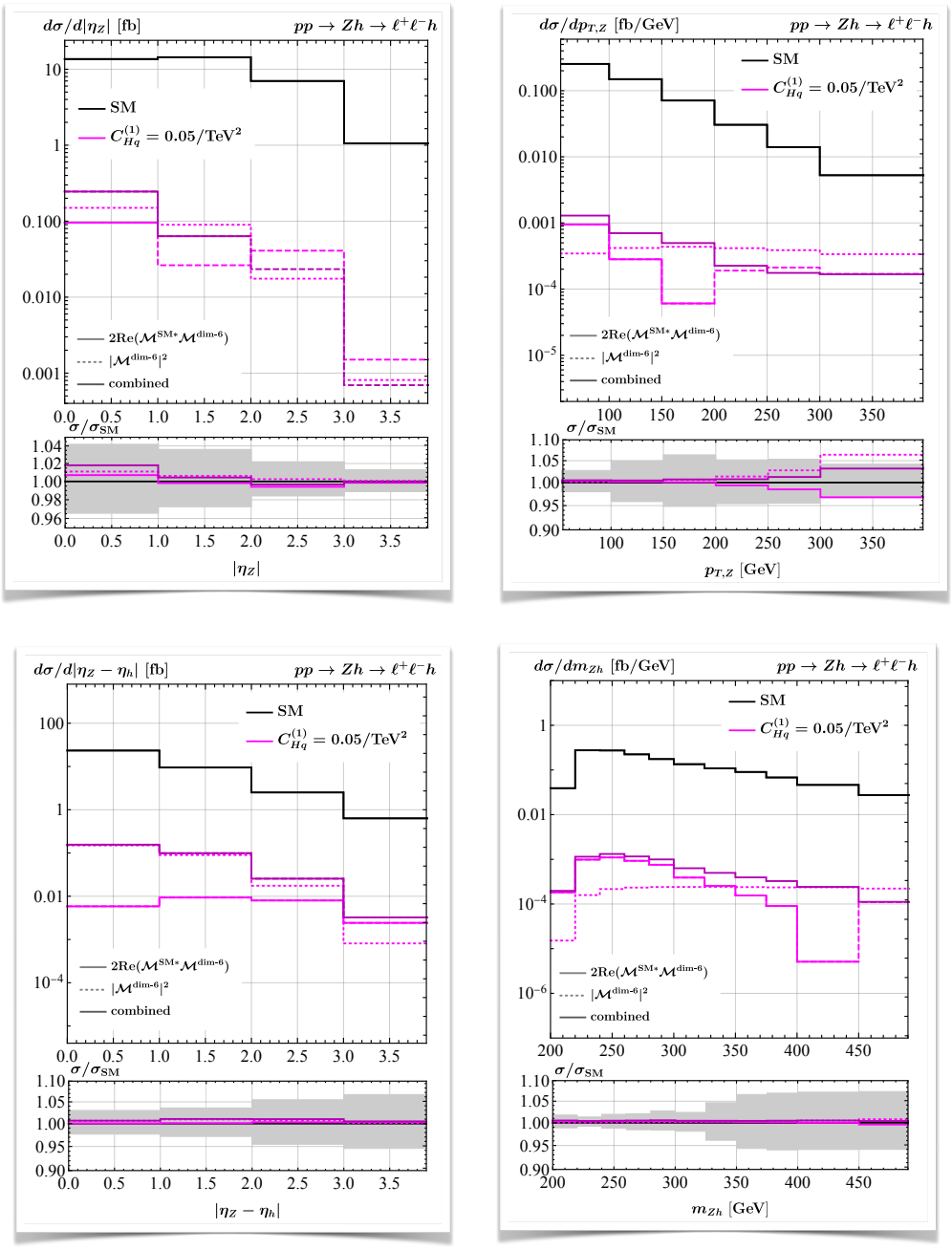

Figure 5.9: As Figure 5.5 but for benchmark scenario (5.32) assuming $\Lambda = 1\,\text{TeV}$. The SMEFT predictions are colored in magenta. In the case of the linear SMEFT contributions the solid (dashed) lines correspond to positive (negative) corrections to the relevant distribution.

5.7 Summary

We have presented novel SMEFT predictions for Higgsstrahlung in hadronic collisions. Specifically, we have calculated the NNLO QCD corrections for the complete sets of dimension-six operators that describe the interactions between the Higgs and two vector bosons and the couplings of the Higgs, a W or a Z boson, and light fermions. These fixed-order predictions have been consistently matched to a PS using the MiNNLO$_{\text{PS}}$ method and the matching has been implemented into the POWHEG-BOX. Our new MC implementation allows for a realistic exclusive description of Vh production at the level of hadronic events including SMEFT effects. This feature makes it an essential tool for future Higgs characterization studies by the ATLAS and CMS collaborations, and we therefore make the relevant code available for download on the official POWHEG-BOX web page [144]. Notice that together with the MC code presented in [108], one can now simulate the $pp \to Zh \to \ell^+\ell^- b\bar{b}$ and $pp \to Wh \to \ell\nu b\bar{b}$ processes at NNLO+PS including a total number of 17 dimension-six SMEFT operators.

We have performed an NNLO+PS study of the impact of SMEFT contributions on several kinematic distributions in $pp \to Zh \to \ell^+\ell^- h$ production for a stable Higgs boson considering the simple benchmark scenarios identified earlier. While in our POWHEG implementation the user can choose between the α, α_μ, and LEP schemes, for concreteness our discussion was based on the LEP scheme which uses $\{\alpha, G_F, m_Z\}$ as EW input parameters. Another feature of our MC code worth highlighting is that it is able to compute separately both the SMEFT corrections that are linear and quadratic in the Wilson coefficients. Our numerical analysis showed that once the stringent constraints from m_W, $h \to \gamma\gamma$ and $h \to \gamma Z$ are imposed the numerical impact of C_{HB}, C_{HW} and C_{HWB} on the kinematic distributions in $pp \to Zh \to \ell^+\ell^- h$ are rather limited, amounting to relative deviations of no more than 5%. Future limits on the Wilson coefficients of the effective interaction in (5.1) from Vh production are therefore unlikely to be competitive with the limits that future determinations of the Higgs signal strengths in $h \to \gamma\gamma$ and $h \to \gamma Z$ will allow to set. This will in particular be the case if the latter measurements turn out to be SM-like. The situation turns out to be more promising in the case of the operators (5.2) that induce couplings of the Higgs, a W or a Z boson and light quarks. The sensitivity of $pp \to Zh \to \ell^+\ell^- h$ to the Wilson coefficients $C_{Hq}^{(1)}$, $C_{Hq}^{(3)}$, C_{Hd}, and C_{Hu} arises from the energy growth of the respective amplitudes which results in enhanced high-energy tails of kinematic distributions such as the $p_{T,Z}$ and m_{Zh} spectra. Numerically, we found that these enhancements can reach 50% in the $p_{T,Z}$ spectrum in the region where the Higgs-boson decay products are significantly boosted. As shown in the papers [101–103], future hypothetical HL-LHC measurements of Vh production can therefore provide constraints on the Wilson coefficients $C_{Hq}^{(1)}$, $C_{Hq}^{(3)}$, C_{Hd}, and C_{Hu} that are competitive with the bounds obtained from projected global SMEFT fits. Utilising the MiNNLO$_{\text{PS}}$ generator presented in this work would allow to improve the accuracy of the studies [101–103] from the NLO+PS to the NNLO+PS level.

Notice that in our phenomenological analysis we have focused on the 0-jet categories of the stage 1.2 simplified template cross sections (STXS) framework [145–147] for the Vh production processes. However, it is important to realize that our POWHEG

implementation of the Higgsstrahlungs processes also allows to simulate the different 1-jet STXS categories with NLO+PS accuracy. This represents an important improvement compared to the MC code presented in [100] or the `SMEFT@NLO` package [45] which are only LO+PS accurate for 1-jet observables in Vh production. Finally, the presented squared matrix element library contains all spinor-helicity amplitudes that are needed to obtain NNLO+PS predictions for DY production taking into account the effects of the dimension-six operators (5.2) and (5.3). Modifying the code such that one can calculate the SMEFT effects in diboson production at NNLO+PS due to operators that induce anomalous triple gauge couplings is also relatively straightforward.

Part (II)

NOVEL SIGNATURES

"What makes the desert beautiful",
the little prince said, "is that it hides a well somewhere..." [...]
Whether it's a house or the stars of the desert,
what makes them beautiful is invisible!

— Antoine de Saint-Exupéry

6

VECTOR LEPTOQUARK EFFECTS IN DRELL-YAN AT NLO+PS

Walter Innes suggested that,
if a particle named "Upsilon" turned out to be a mirage,
they could simply call it an "Oops-Leon".

— On the discovery of the Υ ($b\bar{b}$) particle [148],
providing the first strong evidence for
the third fermion family

6.1 Introduction

In this section, we present aspects of our publication [LS3] that are particularly relevant in the context of predicting novel signatures at the LHC. We derived NLO+PS accurate predictions for VLQ effects in $pp \to \tau^+\tau^-$, including the additional structure from the full 4321 gauge completion entering in loops. As previously stated in Chapter 3.2, VLQs are expected to mainly couple to the third fermion family, assuming they are related to the flavor puzzle of the SM. It is therefore desirable to combine both $pp \to \tau^+\tau^-$ and $pp \to \tau^+\tau^- b$ final states in a consistent MC code, given that signatures with and without jets tagged as b-jets are studied in LHC analyses. Although the b-tag category is subject to lower statistics, it benefits from a much better signal-to-background ratio between the VLQ and SM contributions. As such, VLQs provide an excellent benchmark for a *bottom-philic* scenario, i.e. a model that is mainly coupled to the third fermion family. These evade searches involving light quarks and therefore constitute a more exotic signature at the LHC.

Several different search strategies for third-generation LQs have so far been considered at the LHC. While the ATLAS and CMS collaborations have initially focused on strong LQ pair production in gluon-gluon fusion or quark-antiquark annihilation, recently also single LQ production in gluon-quark fusion and t-channel LQ exchange in DY dilepton production have been exploited to constrain the LQ-quark-lepton couplings. See [166–170] for the latest experimental results of these kinds. Resonant LQ signatures arising from quark-lepton annihilation at the LHC [171–174] have also been studied and found to provide complementary information compared to the other third-generation LQ search strategies [175].

The t-channel LQ exchange in DY

Further detailed investigations of other non-resonant phenomena in DY production related to the semi-leptonic B-decay anomalies can be found in the articles [149–165].

In the context of the singlet VLQ model, LHC searches for non-resonant di-tau final states have been shown to be particularly important [169, 176–181]. Given the relevance of the $pp \to \tau^+\tau^-$ process, the main goal of this article is to improve the theoretical description of DY dilepton production in models with a singlet VLQ by calculating the relevant NLO corrections in QCD. These fixed-order predictions are

NLO+PS implementation based on the POWHEG method

then consistently matched to a PS utilising the POWHEG method [18, 136] as implemented in the POWHEG-BOX [21]. This allows for a realistic exclusive description of DY dilepton processes in singlet VLQ models at the level of hadronic events. Similar calculations have been performed in the case of scalar LQs in [182, LS4] and the research presented in the following constitutes a non-trivial extension of [LS4]. The added complications that arise here are related to the fact that unambiguous NLO QCD calculations are only possible in the case of a massive VLQ if the corresponding field is embedded into a consistent UV-complete model. An inescapable consequence of such an embedding is the presence of additional states, like for example colorons, which carry non-zero $SU(3)_c$ charges and have masses close to that of the VLQ [178, 183]. As stressed in the second part of the trilogy [61, 63, 184], a proper treatment of all $\mathcal{O}(\alpha_s)$ corrections is therefore necessary to determine the full NLO QCD contributions. Calculations such as [185] that only include the corrections associated to virtual and real QCD emissions can lead to inaccurate results in realistic third-generation VLQ models. In order to obtain the proper $\mathcal{O}(\alpha_s)$ corrections to DY dilepton production in VLQ models, our NLO+PS POWHEG-BOX implementation therefore contains the contributions from virtual and real gluons as well as coloron loops. The obtained analytic expressions furthermore serve as an independent cross check of the computations presented in the publication [61].

In our phenomenological analysis, we discuss the numerical impact of the NLO QCD corrections on the kinematic distributions that enter the existing ATLAS and CMS searches for non-resonant phenomena in di-tau final states. Since it is known that the requirement of additional final-state jets containing the decay of a B hadron (i.e., jets tagged as b-jets) helps to improve the LHC sensitivity of third-generation LQ searches [153, 157, 166, 169, 170, 186–191], we pay special attention to this feature in our study. Based on our DY di-tau analyses we are able to derive improved limits on the parameter space of third-generation singlet VLQ models using the results [169] that utilise the full LHC Run II integrated luminosity of 138 fb^{-1} obtained for proton-proton collisions at $\sqrt{s} = 13\,\text{TeV}$.

6.2 THEORETICAL FRAMEWORK

Effective VLQ–fermion interactions

As we have seen in Chapter 3.2, a singlet VLQ may be added to the SM Lagrangian with the effective fermion interactions

$$\mathcal{L}_f \supset \frac{g_4}{\sqrt{2}} \left[\beta_L^{ij}\, \bar{q}_L^{i,c_1}\, \gamma^\mu\, \ell_L^j + \beta_R^{ij}\, \bar{d}_R^{i,c_1}\, \gamma^\mu\, e_R^j \right] U_\mu^{c_1} + \text{h.c.} \tag{6.1}$$

In our POWHEG-BOX implementation of the simplified Lagrangian (6.1), the relevant third-generation LQ-quark-lepton couplings are treated as real.

In Chapter 3.2, we considered $\beta_R^{ij} = \beta_L^{ij} = \delta_{i3}\delta_{j3}$ based on the $SU(4)^{[3]}$ unification, but from a general bottom-up point of view the fermion–VLQ interactions may come with arbitrary β_L, β_R. In the context of the anomalies in $b \to s\ell^+\ell^-$ and $b \to c\tau^-\bar{\nu}$, the LQ-quark-lepton couplings $\beta_L^{33}, \beta_R^{33}, \beta_L^{23}, \beta_L^{32}, \beta_L^{22}$ were usually chosen to be non-zero and to follow the pattern $|\beta_L^{33}| \simeq |\beta_R^{33}| \gtrsim |\beta_L^{23}| \gg |\beta_L^{32}| \simeq |\beta_L^{22}|$, while the remaining couplings were omitted.

The simplified interactions described by (6.1) do not provide a consistent UV completion for the singlet VLQ field which renders higher-order perturbative calculations

based on (6.1) in general ambiguous. As we have seen, a well-motivated class of UV-complete theories that incorporates a singlet VLQ are non-universal $SU(4)^{[3]}$ theories. The minimal gauge group that leads to the effective interactions of the form (6.1) and that is phenomenologically viable is

The need for a UV completion

The 4321 gauge group

$$SU(4)^{[3]} \times SU(3)^{[12]} \times SU(2)_L \times U(1)_X \,, \tag{6.2}$$

the 4321. Below, we restrict ourselves to the $SU(4)^{[3]} \times SU(3)^{[12]}$ sector of (6.2) which includes the LQ interactions and $\mathcal{O}(\alpha_s)$ corrections thereof (see Chapter 3.2 for an overview), while neglecting contributions that involve the $SU(2)_L \times U(1)_X$ subgroup. This means in particular that we do not consider contributions to DY dilepton production that arise from the color singlet state Z' that also appears in the spectrum of the 4321 model after spontaneous symmetry breaking [183, 192–196]. This omission is firstly motivated because the Z' does not contribute to the $\mathcal{O}(\alpha_s)$ corrections we are interested in. Secondly, while the color singlet does contribute to DY dilepton production, the tree-level s-channel exchange of a Z' leads to a narrow resonance in the dilepton invariant mass spectrum of $pp \to \tau^+\tau^-$. In contrast, the leading contribution to DY dilepton production due to (6.1) corresponds to a non-resonant signal associated to t-channel exchange of the singlet VLQ. Since experimentally resonant DY dilepton signatures can in principle be disentangled from non-resonant ones, treating the Z' and the U contributions also separately in a theoretical analysis seems justified.

Contributions from the Z'

6.3 Calculation in a nutshell

Representative Feynman diagrams leading to DY di-tau production in the presence of (3.59), (6.1) are displayed in Figures 6.1 and 6.2. The first figure shows the tree-level process involving t-channel singlet VLQ exchange (left) and the corresponding real gluon corrections (middle and right). Notice that all depicted contributions are initiated by bottom-quark ($b\bar{b}$) fusion. We include real contributions with both non-resonant (middle) and resonant (right) intermediate U states, the latter case corresponding to single-LQ production with a subsequent decay of the singlet VLQ to a pair of a bottom quark and an anti-tau, i.e. $gb \to U\tau^-$ followed by $U \to b\tau^+$. These resonant diagrams also contribute at $\mathcal{O}(\alpha_s)$ and are particularly important for invariant di-tau masses ($m_{\tau\tau}$) close to the singlet VLQ mass M_U. At the same time, we neglect $\mathcal{O}(\alpha_s)$ corrections associated to real coloron emissions. This is theoretically justified because these contributions are, unlike the real gluon emissions, IR finite by themselves. Furthermore, the stringent bounds on the coloron mass from LHC searches for dijet and ditop production [181] that impose $M_{G'} \gtrsim 3\,\text{TeV}$ are expected to render the resonant G' contribution to the $b\bar{b} \to \tau^+\tau^-$ process insignificant for all practical purposes.

LO and NLO real contributions

We work in the five-flavour scheme, where charm- and bottom-quarks are considered as partons in the proton and as such have a corresponding PDF.

In Figure 6.2, we display an assortment of the virtual $\mathcal{O}(\alpha_s)$ contributions that are included in our calculation. The three factorizable corrections shown on the left exhibit UV divergences, which only cancel if both the gluon and coloron contributions are included. This shows that the coloron contributions are intimately tied to the gluon corrections in the 4321 model. Notice that besides the interaction terms between the SM fermions and the colored gauge bosons (3.59) also factorizable

NLO virtual contributions

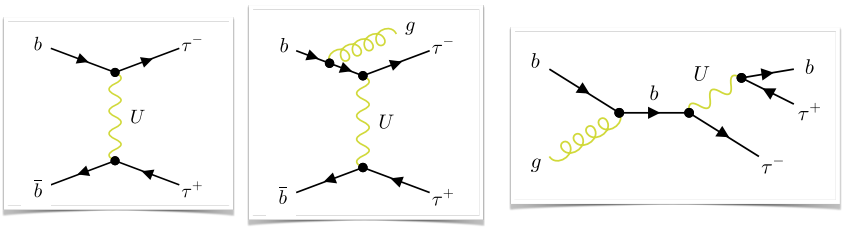

Figure 6.1: Examples of singlet VLQ contributions to the DY di-tau spectrum initiated by bottom-quark fusion. The left Feynman diagram describes the tree-level process involving t-channel singlet VLQ exchange (U), while the middle (right) graph represents the real gluon (g) corrections with non-resonant (resonant) intermediate U. See main text for further details.

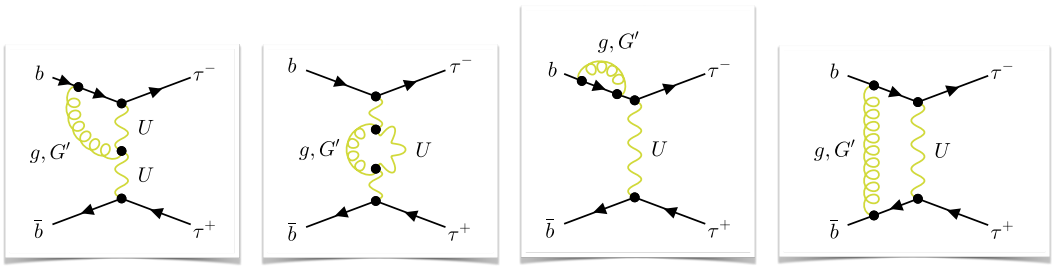

Figure 6.2: Virtual $\mathcal{O}(\alpha_s)$ corrections to the singlet VLQ contribution in DY di-tau production, with a gluon (g) or a coloron (G') running in the loop. The three graphs on the left show the factorizable contributions. They arise from LQ-quark-lepton vertex corrections as well as from LQ and quark wave function corrections. The diagram on the far right depicts a non-factorizable contribution due to a box diagram. For additional explanations consult the main text.

diagrams with vertices involving only colored gauge bosons and graphs with Goldstone bosons and ghosts need to be considered if the computation is performed in the Feynman or any other renormalisable or R_ξ gauge (see Subchapter 3.2.2 for details). Last but not least, the process $b\bar{b} \to \tau^+\tau^-$ receives finite contributions from the non-factorizable box diagram shown on the very right in Figure 6.2.

Besides QCD corrections to the $b\bar{b} \to \tau^+\tau^-$ process, we also study the potential size of interference effects between the SM background and the singlet VLQ signal. We treat these effects at the LO in perturbation theory, which means that our `POWHEG-BOX` implementation of DY dilepton production contains the squared matrix elements built from the SM corrections involving Z-boson or photon exchange in the s-channel and the t-channel singlet VLQ exchange contribution (cf. the left diagram in Figure 6.1).

Our newest `POWHEG-BOX` implementation also contains all interference contributions at NLO+PS accuracy [197].

In the calculation of the squared matrix elements, we use conventional dimensional regularization for both UV and IR singularities. For the generation and computation of the squared matrix elements, we rely on the `Mathematica` packages `FeynRules` [198], `FeynArts` [199], `FormCalc` [122] and `Package-X` [200], while making use of `LoopTools` [121] for the numerical evaluation of the Passarino-Veltman integrals that appear in the one-loop contributions. Hereafter, we work in the OS

scheme. To deal with the soft and collinear singularities of the real corrections to the t-channel singlet VLQ exchange contribution, cf. the middle diagram in Figure 6.1, and to cancel the IR poles of the one-loop virtual corrections, cf. the first and the third diagram in Figure 6.2, we exploit the FKS subtraction [27, 28]. Specifically, we use the `POWHEG-BOX` to automatically build the soft and collinear counterterms and remnants, also checking the behaviour of the real squared matrix elements in the soft and collinear limits against their soft and collinear approximations. Notice that the real NLO QCD contributions that describe resonant single production of a U and its subsequent decay, cf. the right diagram in Figure 6.1, are IR finite and hence do not require an IR subtraction. Our MC code therefore allows to achieve NLO+PS accuracy for DY dilepton production in singlet VLQ models. The presented generator is in particular able to generate events with one additional QCD parton from the matrix element calculation without the need to introduce a spurious merging or matching scale. Two-jet events are instead exclusively generated by the PS in our MC setup.

6.4 Numerical applications

We have presented the calculation of the $\Gamma(U \to b\tau^+)$ partial decay width of the singlet VLQ at $\mathcal{O}(\alpha_s)$ accuracy in Subchapter 3.2.3. The same calculation for the limit $x_U = M_U^2/M_{G'}^2 = 1$ has been published previously in [61]. Notice that in the more generic case of the LQ-quark-lepton interactions (6.1), the total decay width of the LQ includes the processes $U \to b\tau^+$ and $U \to t\bar{\nu}_\tau$, and can be obtained from (3.85) by the simple replacement

$$g_4^2 \to g_4^2 \left[\left(2 - 3x_t/2 + x_t^3/2\right) \left|\beta_L^{33}\right|^2 + \left|\beta_R^{33}\right|^2 \right] /2 \,. \tag{6.3}$$

*NLO **partial decay width***
We neglect the impact of radial modes. In the case of the partial decay widths this has been shown in [61] to be an excellent approximation for $M_U, M_{G'} \ll M_R$ with M_R denoting the common mass of the radial modes.

Here $x_t = m_t^2/M_U^2$ and we have included the corrections due to the non-negligible top-quark mass $m_t \simeq 163\,\text{GeV}$ that arise from the tree-level phase space and the squared matrix element at LO. Top-quark mass terms that arise at $\mathcal{O}(\alpha_s)$ and that would lead to a flavour-dependent correction $\Delta(x_U)$ are instead neglected. We believe this simplification to be an excellent approximation for LQ and coloron masses in the TeV range. Before moving on, let us finally add that the finite, renormalization scale independent corrections (3.85) also appear as universal $\mathcal{O}(\alpha_s)$ contributions to all low-energy observables that involve a LQ-quark-lepton vertex resulting from (6.1). These corrections can be simply included by using, instead of the tree-level coupling g_4, the QCD corrected on-shell coupling $g_4\,(1 + \Delta(x_U)/2)$ in the low-energy predictions [61]. We have displayed the numerical size of the NLO QCD correction $\Delta(x_U)$, as defined in (3.85), in Figure 3.4. There, we found a large x_U-dependence of $\Delta(x_U)$. To gauge the ambiguities in our numerical analysis that are related to the choice of the masses of the heavy colored vector states of the 4321 model, we will employ two benchmarks, namely $M_{G'} = M_U$ and $M_{G'} = 2.5 M_U$. While the former choice is motivated by simplicity, the second option reflects the fact that the existing LHC bounds on the mass of the coloron are more stringent than those on the singlet VLQ by at least a factor of two [167, 181].

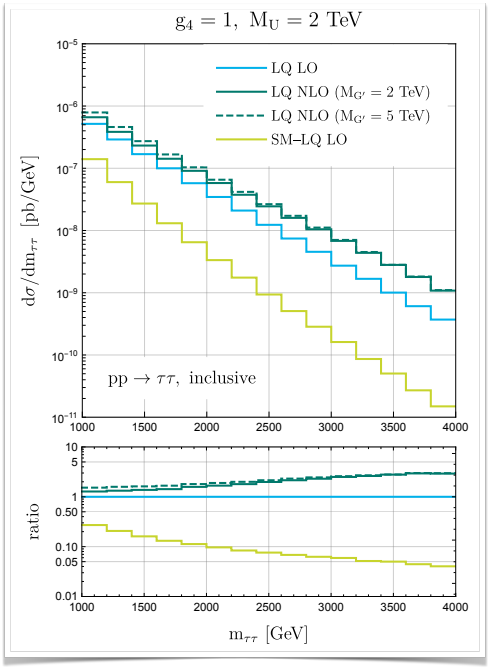

Figure 6.3: Inclusive $pp \to \tau^+\tau^-$ production cross sections as a function of $m_{\tau\tau}$ for the parameter choices $g_4 = 1$ and $M_U = 2\,\text{TeV}$. The blue and dark green correspond to the LQ distributions at the LO (LQ LO) and the NLO (LQ NLO) in QCD, respectively, while the light green histograms illustrate the magnitude of the interference effects between the SM background and the LQ signal (SM-LQ LO). In the case of the solid (dashed) dark green line the coloron mass is set to $M_{G'} = 2\,\text{TeV}$ ($M_{G'} = 5\,\text{TeV}$). The lower panel depicts the ratios between the different LQ contributions and the relevant LQ LO distribution.

Inclusive $m_{\tau\tau}$ spectrum

The simplest observable that one can study in DY di-tau production is the invariant mass $m_{\tau\tau}$ of the di-tau system. In Figure 6.3, we present our results for the LQ corrections to the corresponding spectrum in inclusive $pp \to \tau^+\tau^-$ production, employing `NNPDF40_nlo_as_01180` PDFs [201]. The blue and dark green lines resemble the LQ distributions at the LO (LQ LO) and the NLO (LQ NLO) in QCD, respectively, while the light green curve illustrates the size of the interference effects between the SM background and the LQ signature (SM-LQ LO). In the case of the solid (dashed) dark green line the coloron mass is set to $M_{G'} = 2\,\text{TeV}$ ($M_{G'} = 5\,\text{TeV}$). From the lower panel of the plot it is evident that the NLO QCD effects play an important role in obtaining precise predictions as they amount to around 40% (150%) at $m_{\tau\tau} = 1.5\,\text{TeV}$ ($m_{\tau\tau} = 3\,\text{TeV}$) compared to the tree-level LQ prediction. Notice that at NLO in QCD the DY di-tau production spectra resulting from LQ exchange depend on the mass $M_{G'}$ of the coloron. For the two choices of $M_{G'}$ shown in the figure, we find relative differences of the order of 10% between the two distributions. The observed effects are therefore similar in size to the $M_{G'}$ dependence of the $\mathcal{O}(\alpha_s)$ corrections to the partial decay width of the $U \to b\tau^+$ channel (cf. Figure 3.4). The interference effects between the SM DY background and the LQ signal turn out to be destructive in the shown $m_{\tau\tau}$ range, amounting to approximately 15% (5%) for $m_{\tau\tau} = 1.5\,\text{TeV}$ ($m_{\tau\tau} = 3\,\text{TeV}$).

The SM-LQ LO results shown in Figures 6.3, 6.4 and 6.5 represent the magnitudes of the corresponding predictions for the interference effects between the SM background and the LQ signal.

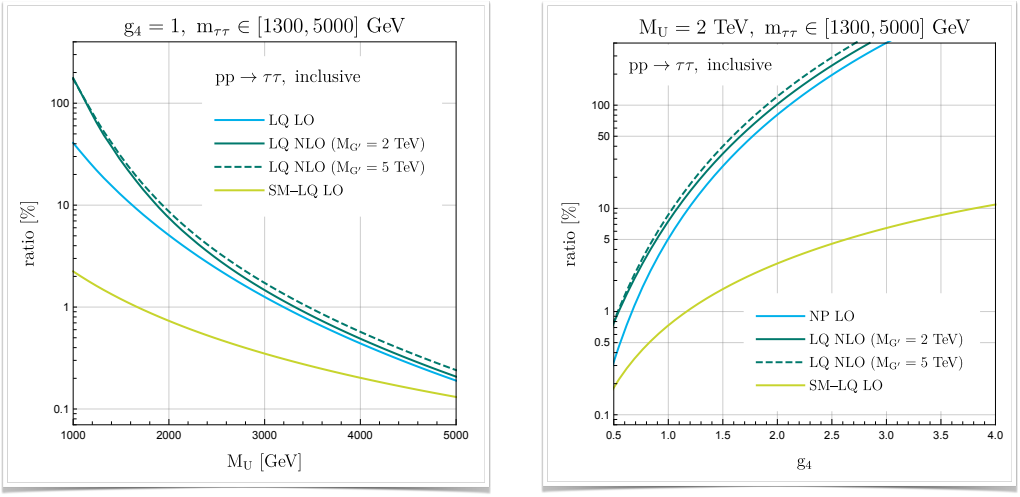

Figure 6.4: Ratios between the individual LQ corrections and the inclusive DY SM background calculated at the NLO in QCD. The shown results correspond to the fiducial region defined by $p_{T,\tau} > 30\,\text{GeV}$, $|\eta_\tau| < 2.5$ and $m_{\tau\tau} \in [1300, 5000]\,\text{GeV}$. The left (right) plot depicts the results as a function of M_U (g_4) for fixed $g_4 = 1$ ($M_U = 2\,\text{TeV}$). The color coding and meaning of the different curves resembles those in Figure 6.3. Additional details can be found in the main text.

Dependence on M_U

In Figure 6.4, we furthermore display the ratios between the individual LQ contributions and the DY di-tau SM background. The normalization is calculated at the NLO in QCD and we select events with two opposite-sign same-flavour tau leptons that are both required to have a transverse momentum of $p_{T,\tau} > 30\,\text{GeV}$ and a pseudorapidity of $|\eta_\tau| < 2.5$. The invariant masses of the di-tau pairs must fall into the range $m_{\tau\tau} \in [1300, 5000]\,\text{GeV}$. Detector efficiency corrections are not taken into account. The left panel displays our results as a function of M_U fixing the overall coupling strength that appears in (6.1) to $g_4 = 1$. From this figure it is clearly visible that the relative size of the NLO QCD corrections decreases for increasing singlet VLQ mass. Numerically, we find relative effects of around 330%, 50% and 15% for $M_U = 1\,\text{TeV}$, $M_U = 2\,\text{TeV}$ and $M_U = 3\,\text{TeV}$, respectively. This feature can be traced to the fact that the NLO QCD corrections related to s-channel single-LQ production followed by the decay of the LQ, cf. the right Feynman diagram in Figure 6.1, decouple faster than the real and virtual corrections to the t-channel Born-level LQ contribution, cf. the middle graph in Figure 6.1 and the gluon-exchange diagrams in Figure 6.2. One also observes that the interference effects represent only subleading corrections in the mass window $m_{\tau\tau} \in [1300, 5000]\,\text{GeV}$, amounting to an effect of at most -2% relative to the SM background for the considered M_U values.

Dependence on g_4

On the r.h.s in Figure 6.4, we finally depict our ratio predictions as a function of g_4, setting the mass of the singlet VLQ to $M_U = 2\,\text{TeV}$. It is evident from the plot that the relative size of the NLO QCD corrections decreases for increasing overall coupling strength. In the case of $M_{G'} = 2\,\text{TeV}$, the higher-order QCD effects amount, compared to the tree-level LQ result, to around 140%, 50%, and 30% for $g_4 = 0.5$, $g_4 = 1$ and $g_4 = 2$. For $M_{G'} = 5\,\text{TeV}$ the corresponding numbers read 150%, 70%, and 50%. This behaviour can be understood by realizing that the squared amplitude of the t-channel Born-level LQ contribution scales as $|g_4|^4$, while the resonant single-

LQ production rate is proportional to $|g_4|^2$. One again sees that the interference contributions are numerically subleading even for large couplings g_4 where they just reach the level of -10%.

6.5 PHENOMENOLOGICAL ANALYSIS

Full phenomenological analysis of b-veto and b-tag categories

LHC searches for signatures involving tau pairs in the final state like those performed in the publications [166, 169, 170] are known [176–181] to provide strong constraints on LQ models. To illustrate the role that additional b-jets play in analyses of this kind, we will consider as an example the recent CMS search [169] for $\tau\tau$ final states with both taus decaying to hadrons (τ_h). These τ_h candidates are distinguished from jets originating from the hadronization of light-flavoured quarks or gluons, and from electrons or muons by employing the τ-tagger described in the article [202]. The used working points have an efficiency of approximately 50%, 70% and 70% for identification in the case of jets, electrons and muons, respectively. The corresponding rejection factors are about 230, 20, and 770. Both τ_h candidates are required to have $p_{T,\tau} > 40\,\text{GeV}$ and $|\eta_\tau| < 2.1$, and their pseudorapidity-azimuth separation must be greater than $\Delta R_{\tau\tau} = 0.3$. Jets are clustered using the anti-k_t algorithm with radius $R = 0.4$, as implemented in `FastJet` [203]. Light-flavoured quark or gluon jets need to fulfil $p_{T,j} > 30\,\text{GeV}$ and $|\eta_j| < 4.7$, while b-jets with $p_{T,b} > 20\,\text{GeV}$ and $|\eta_b| < 2.5$ are selected. In order to identify b-jets, we employ the CMS b-tagging efficiencies stated in [204, 205]. The used b-tagging working point yields a b-tagging efficiency of around 80% and a rejection in the ballpark of 100 for jets arising from light-flavoured quarks or gluons. Our analysis is implemented into `MadAnalysis 5` [206] and employs `Delphes 3` [207] as a fast detector simulator. `Pythia 8` [33] is used to shower the events. Effects from hadronization, underlying event modelling or QED effects in the PS are not included in our MC simulations. Applying our MC chain to the SM NLO DY prediction obtained with the `POWHEG-BOX`, we are able reproduce the SM DY background as given in [169] to within around 30%. This comparison represents a non-trivial cross check of our di-tau analysis.

Total transverse mass m_T^{tot}

In order to separate the LQ signal from the SM background, the distributions of the total transverse mass defined as [208]

$$m_T^{\text{tot}} = \sqrt{m_T^2(\vec{p}_T^{\,\tau_1}, \vec{p}_T^{\,\tau_2}) + m_T^2(\vec{p}_T^{\,\tau_1}, \vec{p}_T^{\,\text{miss}}) + m_T^2(\vec{p}_T^{\,\tau_2}, \vec{p}_T^{\,\text{miss}})}\,, \tag{6.4}$$

are considered. Here τ_1 (τ_2) refers to the first (second) hadronic τ candidate and $\vec{p}_T^{\,\tau_1}$, $\vec{p}_T^{\,\tau_2}$ and $\vec{p}_T^{\,\text{miss}}$ are the vectors with magnitude p_{T,τ_1}, p_{T,τ_2} and E_T^{miss}. The missing transverse energy constructed from the transverse momenta of all the neutrinos in the event is denoted by E_T^{miss}. The transverse mass of two transverse momenta $p_{T,i}$ and $p_{T,j}$ entering (6.4) is given by

$$m_T(\vec{p}_T^{\,i}, \vec{p}_T^{\,j}) = \sqrt{2\,p_{T,i}\,p_{T,j}\,(1 - \cos\Delta\phi)}\,, \tag{6.5}$$

where $\Delta\phi$ is the azimuthal angular difference between the vectors $\vec{p}_T^{\,i}$ and $\vec{p}_T^{\,j}$.

In Figure 6.5, we compare the m_T^{tot} distributions as defined in (6.4) within the SM and the 4321 model (6.1) for the parameter choices $g_4 = 1$ and $M_U = 2\,\text{TeV}$. The left (right) panel displays the results for the no b-tag (b-tag) category. The black

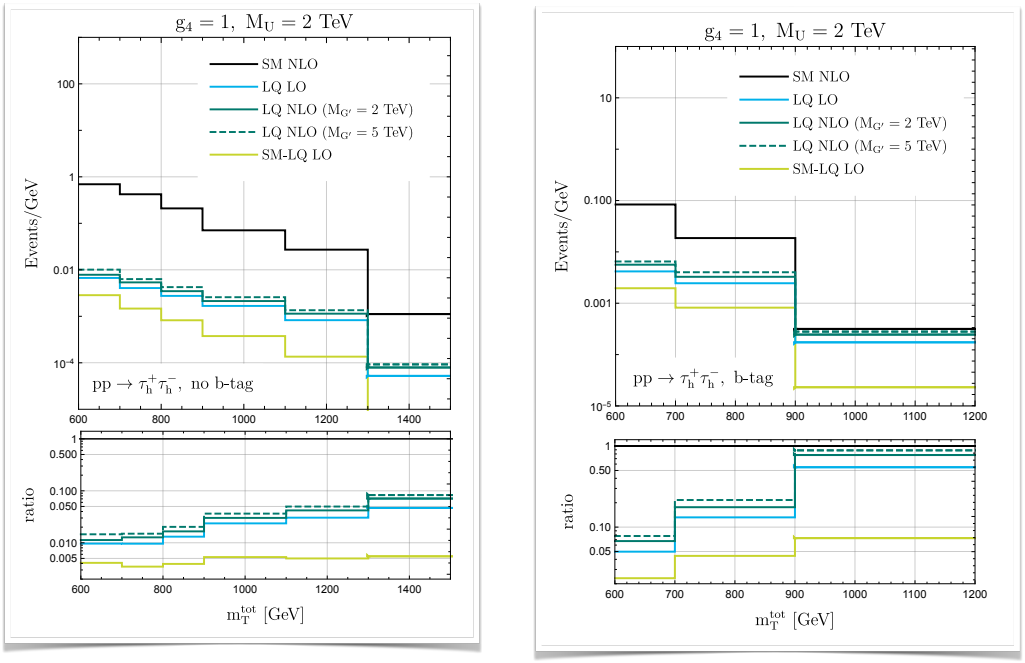

Figure 6.5: Distributions of m_T^{tot} in the no b-tag (left panel) and the b-tag (right panel) category in the final state containing two hadronic tau leptons. The black curves correspond to the SM expectations of the DY background provided by CMS in [169]. This search is based on 138 fb^{-1} of integrated luminosity collected in pp collisions at $\sqrt{s} = 13$ TeV. The blue and dark green curves instead represent the LQ LO and LQ NLO predictions assuming $g_4 = 1$ and $M_U = 2$ TeV. In the case of the solid (dashed) dark green lines the coloron mass is set to $M_{G'} = 2$ TeV ($M_{G'} = 5$ TeV). The light green histograms illustrate the size of the interference effects between the LQ signal and the SM background called SM-LQ LO. The definition of the signal regions (SRs) and other experimental details can be found in the main text.

curves represent the SM expectations of the DY background taken from [169], while the blue and dark green histograms are the LQ LO and LQ NLO predictions obtained using our POWHEG-BOX code. The solid (dashed) dark green LQ NLO results assume $M_{G'} = 2$ TeV ($M_{G'} = 5$ TeV). All predictions correspond to 138 fb^{-1} of pp data collected at $\sqrt{s} = 13$ TeV. From the lower left panel one sees that in the no b-tag category the NLO LQ contribution amounts to a relative correction of less than 10% compared to the SM DY background for $m_T^{\text{tot}} > 1300$ GeV. For what concerns the b-tag category, one instead observes from the lower right panel that in the highest m_T^{tot} bin with $m_T^{\text{tot}} > 900$ GeV the NLO LQ signal constitutes around 85% of the SM DY background. This feature clearly shows that for third-generation VLQs the sensitivity of DY searches notably improves by demanding an additional b-jet in the final state. It is furthermore important to realize that the NLO QCD effects enhance the LO LQ predictions in the no b-tag (b-tag) category by approximately 35% (30%) in the highest m_T^{tot} bin, making higher-order QCD effects phenomenologically relevant. On the other hand, the dependence of the NLO LQ distributions on $M_{G'}$ is weak. This renders the constraints derived below model-independent in the sense that one can set a limit on g_4 as a function of M_U essentially without

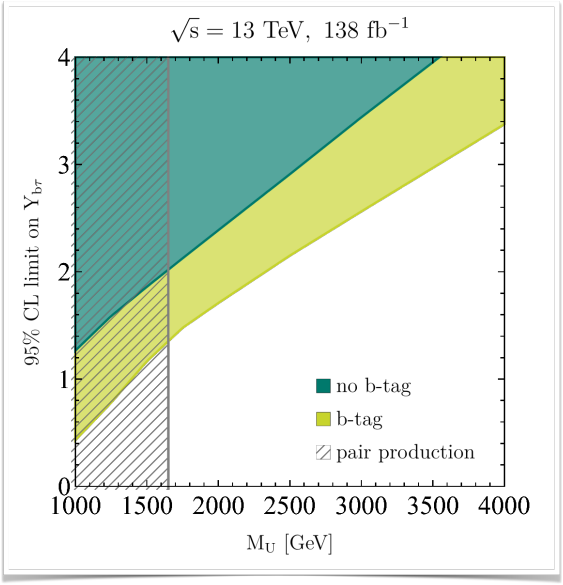

Figure 6.6: Comparison of the 95% CL constraints on the $M_U - g_4$ plane that arise from the latest LHC Run II hadronic di-tau analysis [169]. The dark (light) green exclusion corresponds to the no b-tag (b-tag) category of the latter search, while the hatched gray parameter space is excluded by strong pair production of third-generation LQs [209]. Consult the main text for additional explanations.

making a reference to the choice of the coloron mass as long as $M_{G'} = \mathcal{O}(M_U)$. One finally sees that the considered SM-LQ LO interference effects amount to a few permille in the case of the no b-tag category, while they can exceed the level of 5% if one requires the presence of a b-tag in the events. In contrast to what has been suggested in the recent work [169], interference effects therefore play only a minor role in the SRs that are relevant for non-resonant DY searches for third-generation singlet VLQs at the LHC.

Exclusion limits

Based on the di-tau search strategies detailed above, we now derive NLO+PS accurate 95% CL limits on the $M_U - g_4$ plane. Since we have seen that the choice of coloron mass has only a minor impact on the m_T^{tot} spectrum, we employ $M_{G'} = M_U$ for simplicity when determining the exclusion bounds. Figure 6.6 shows our 95% CL limits on the $M_U - g_4$ parameter space that follow from the two b-jet categories considered in the CMS search [169] for two hadronic tau leptons. The dark and light green exclusion corresponds to the no b-tag and the b-tag category of this analysis, respectively, while the parameter space excluded by strong pair production of third-generation LQs [168] is indicated by the hatched gray vertical band. This search excludes $M_U < 1650\,\text{GeV}$ at 95% CL. The significance of the individual b-jet categories of the search [169] is calculated as a ratio of Poisson likelihoods modified to incorporate systematic uncertainties on the background as Gaussian constraints [210]. Our statistical analysis includes the six (three) highest m_T^{tot} bins in the case of the no b-tag (b-tag) category. One first observes that the bound on g_4 that follows from the search with a b-tag is more stringent than the one that derives from a strategy that requires no b-jet. We add that the difference between the no b-tag and b-tag constraints is rather pronounced in the case of the CMS analysis [169], because this search

observes a resonant-like excess with a significance of around 3σ at $m_T^{\text{tot}} \simeq 1.2\,\text{TeV}$ in the no b-tag sample. Consequently, the resulting no b-tag limits on the LQ parameter space are weaker than expected. Notice finally that for $M_U \lesssim 1.7\,\text{TeV}$ the exclusions contour starts to deviate from its linear behaviour. This is a consequence of the contribution associated to single-LQ production with subsequent decay of the LQ, cf. the right diagram in Figure 6.1, scaling as $|g_4|^2$ compared to the $|g_4|^4$ dependence of the squared amplitude of the t-channel Born-level LQ contribution.

6.6 Summary

Our main goal was to refine the theoretical description of DY dilepton production in VLQ models. To this purpose, we have calculated the NLO QCD corrections to the $pp \to \tau^+\tau^-$ process. The actual computation involves the evaluation of the real and virtual corrections to the t-channel Born-level contribution and the calculation of resonant single-LQ production followed by the decay of the LQ. One complication compared to the computation of $\mathcal{O}(\alpha_s)$ corrections to DY dilepton production in scalar LQ models [182, LS4] arises from the fact that realistic VLQ models such as the 4321 model contain additional states that carry non-zero $SU(3)_c$ charges (see Chapter 3.2). In fact, in the case at hand, both gluon and coloron exchange has to be considered in order to determine the full NLO QCD contributions to DY dilepton production. Our $\mathcal{O}(\alpha_s)$ computation furthermore serves as an independent cross check of the calculation of the singlet VLQ decay width in the 4321 model presented in [61]. Besides QCD corrections, we have also studied the size of interference effects between the DY SM background and the LQ signature, finding that these effects are in general small in the SRs of the existing LHC DY dilepton searches.

The calculated fixed-order predictions have been implemented into a dedicated MC code, which consistently matches them to a PS employing the `POWHEG` method. As a result, a realistic exclusive description of DY dilepton processes in the singlet VLQ model at the level of hadronic events can be obtained without the introduction of an unphysical merging or matching scale. Our MC generator should prove useful for everyone interested in comparing accurate theory predictions to LHC data, and we therefore make the relevant code to simulate NLO+PS events for the $pp \to \tau^+\tau^-$ process in the singlet VLQ model of the form (6.1) available for download [197].

In our phenomenological analysis, we have studied the case of $pp \to \tau^+\tau^-$ production that arises from the LQ-quark-lepton couplings (6.1) supplemented by the Goldstone boson, pure gauge and ghost contributions in (3.66), (3.69) and (3.70), respectively. Since the $pp \to \tau^+\tau^-$ signatures result from bottom-quark fusion, initial-state radiation will always lead to an enhanced b-jet activity in the events. Devising search strategies with different b-jet categories is therefore expected to help improve the LHC sensitivity [153, 157, 166, 169, 170, 186–191]. To illustrate this point, we have performed a recast of the search [169] that employs $138\,\text{fb}^{-1}$ of pp data collected at $\sqrt{s} = 13\,\text{TeV}$. This analysis studies two disjoint SRs, and we found that the search strategy that requires the presence of an additional b-tagged jet outperforms the search strategy that vetos b-jets. This provides an illustrative example for a case where a dedicated search for a more exotic signal outperforms the search based on a more generic final state.

Further constraints on the parameter space of third-generation VLQs that arise from the LHC Run II analyses [166, 170] may be found in our [LS3, Appendix B].

Utilising [169] together with our POWHEG-BOX implementation we have finally derived NLO+PS accurate constraints on the masses and couplings of the 4321 model. Again, the *b*-tag search targeting bottom-philic BSM scenarios clearly outperforms the more generic *b*-veto search. Our POWHEG-BOX generator provides an improved signal modelling compared to the matched MLM [211] LO MadGraph5_aMCNLO [131] samples used in [169]. Similar statements also apply to the signal generations used in the analyses [166, 170]. This makes our MC implementation an essential tool for ATLAS and CMS searches for singlet VLQs in di-tau final states at future LHC runs.

7

LLPS FROM EXTENDED SCALAR SECTORS

The master accomplishes more and more by doing less and less
until finally he accomplishes everything by doing nothing.

— Laozi (philosopher),
to be reinterpreted in the context of
$\sin\theta \to 0$ in the 2HDM+a

7.1 Introduction

This section presents aspects of our publication [LS2] with a focus on the exotic long-lived signatures that can arise in the 2HDM+a model. We demonstrate that as $\sin\theta$ (see Subchapter 3.3.5) becomes small, the pseudoscalar Higgs boson a can become long-lived. Consequently, rather than searching for SM particles and missing transverse momentum (E_T^{miss}) signatures from the $a \to \chi\bar{\chi}$ decay, it becomes advantageous to probe for a via LLP searches at the LHC. As such, the LLP phenomenology of the 2HDM+a provides an illustrative example of how dedicated searches for exotic signatures can extend the reach of the LHC.

The 2HDM+a

The 2HDM+a [69, 212–214], introduced in Subchapter 3.3.5, has by now established itself as a pillar of the LHC DM search programme [215–236]. It includes a DM candidate in the form of a Dirac fermion, which is a singlet under the SM gauge group, four 2HDM spin-0 states and an additional $\mathcal{CP}$-odd mediator that is meant to provide the dominant portal between the dark and the visible sector. Since in models with pseudoscalar mediators the DM direct detection constraints are weaker compared to models with scalar mediators (see Subchapter 3.3.5), the former models are more attractive from an astrophysical point of view, since they often allow to reproduce the observed DM relic abundance in a wider parameter space and with less tuning. These features admit a host of E_T^{miss} and non-E_T^{miss} signatures in the 2HDM+a model at colliders which can and have been consistently compared and combined. See for instance [230, 232, 237] for such combinations.

LLPs

BSM scenarios in which the hidden and the visible sectors are connected through a Higgs portal are also being actively probed for at colliders. One rather generic feature in such BSM models is the appearance of new electrically neutral LLPs that give rise to displaced vertex signatures in the LHC detectors – see for example [238–240] for detailed reviews of theoretical and experimental aspects of LLPs at the LHC. The main goal of this section is to point out that besides interesting prompt E_T^{miss} and non-E_T^{miss} signatures, the 2HDM+a model can also have an attractive LLP phenomenology. In fact, in the 2HDM+a model the role of the LLP is played

by the additional pseudoscalar a, which depending on its mass can be pair produced efficiently in the decays of both the 125 GeV Higgs and the non-SM $\mathcal{CP}$-even Higgs, i.e. $h \to aa$ and $H \to aa$. To illustrate the different facets of the LLP phenomenology in the 2HDM+a model, we identify two suitable parameter benchmarks. For these benchmark scenarios we determine the bounds on the mixing angle θ of the two $\mathcal{CP}$-odd weak spin-0 eigenstates as a function of the mass of the LLP that are set by the existing LHC searches for displaced Higgs decays [241–257]. It turns out that depending on the precise mass spectrum of the spin-0 states, mixing angles θ from around a few 10^{-8} to about 10^{-5} can be excluded with LHC Run II data. To the best of our knowledge, mixing angles θ in this range cannot be tested by any other means, which highlights the special role that LLPs searches play in constraining the parameter space of the 2HDM+a model. In fact, as we will further demonstrate, parameter choices that lead to an interesting LLP phenomenology can in general also correctly predict the measured DM relic density. The regions of 2HDM+a parameter space singled out in our article therefore deserve, in our humble opinion, dedicated experimental explorations in future LHC runs.

7.2 2HDM+a model primer

In order to understand under which circumstances the additional pseudoscalar a in the 2HDM+a model can be an LLP, it is useful to recall its partial decay modes. Further details on the structure of the 2HDM+a model can be found for instance in [69, 219]. In the alignment limit, i.e. $\cos(\beta - \alpha) = 0$, and choosing for concreteness the Yukawa sector of the 2HDM+a model to be of type-II, one has at tree level

Partial decay widths to fermions

$$\begin{aligned} \Gamma(a \to \chi\bar{\chi}) &= \frac{y_\chi^2}{8\pi} m_a \sqrt{1 - \frac{4m_\chi^2}{m_a^2}} \cos^2\theta\,, \\ \Gamma(a \to f\bar{f}) &= \frac{N_c^f \eta_f^2 y_f^2}{16\pi} m_a \sqrt{1 - \frac{4m_f^2}{m_a^2}} \sin^2\theta\,. \end{aligned} \tag{7.1}$$

At the one-loop level, the pseudoscalar a can also decay to gauge bosons. The largest partial decay width is the one to gluon pairs. It takes the form

Partial decay width to gluons

$$\Gamma(a \to gg) = \frac{\alpha_s^2}{32\pi^3 v^2} m_a^3 \left| \sum_{q=t,b,c} \eta_q \, f\left(\frac{4m_q^2}{m_a^2}\right) \right|^2 \sin^2\theta\,, \tag{7.2}$$

with

$$f(z) = z \arctan^2\left(\frac{1}{\sqrt{z-1}}\right)\,. \tag{7.3}$$

Here m_a is the mass of the pseudoscalar a, m_χ is the mass of the DM particle, y_χ is the Yukawa coupling of the pseudoscalar a to a pair of DM particles and $\sin\theta$ quantifies the mixing of the two $\mathcal{CP}$-odd weak spin-0 eigenstates. Furthermore, $N_c^q = 3$, $N_c^l = 1$, $\eta_u = \cot\beta$, $\eta_d = \tan\beta$, $\eta_l = \tan\beta$ and $y_f = \sqrt{2} m_f / v$ with m_f the mass of the relevant SM fermion, $v \simeq 246\,\text{GeV}$ the Higgs VEV and α_s the strong coupling constant. From the analytic expressions (7.1) and (7.2), it is evident that the pseudoscalar a can only be long-lived if $\sin\theta$ is sufficiently small, i.e. $\sin\theta \to 0$,

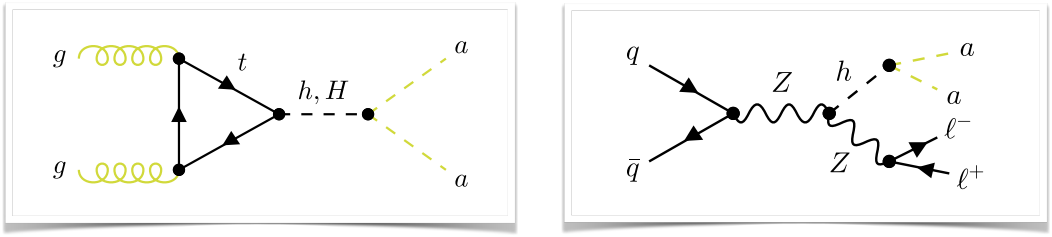

Figure 7.1: Examples of tree-level Feynman diagrams representing $pp \to aa$ production via gluon-gluon fusion (ggF) Higgs production (left) and $pp \to l^+l^-aa$ production in associated Zh production (right) in the 2HDM+a model. The possible decay modes of the pseudoscalar a are not shown. Consult the text for further details.

and decays to DM are strongly suppressed/absent which can be achieved either via decoupling, i.e. $y_\chi \to 0$, or by forbidding the process kinematically, i.e. $m_\chi > m_a/2$.

Given the strong suppression of the couplings of the pseudoscalar a to SM fermions in the limit $\sin\theta \to 0$, the only possibility to produce a long-lived a is via the decay of heavier spin-0 state ϕ into a pair of such pseudoscalars. In the case that the scalar potential is $\mathcal{CP}$ conserving, the ϕ has to be a $\mathcal{CP}$-even state, which implies that in the 2HDM+a model one can have both decays of the 125 GeV Higgs h and the heavy $\mathcal{CP}$-even Higgs H. The corresponding partial decay widths can be written as

Production of the long-lived pseudoscalar a via the decays of heavier Higgs bosons

$$\Gamma\left(\phi \to aa\right) = \frac{g_{\phi aa}^2}{32\pi}\, m_\phi \sqrt{1 - \frac{4m_a^2}{m_\phi^2}}\,, \tag{7.4}$$

with $\phi = h, H$. For $\sin\theta \simeq 0$, the relevant trilinear couplings are given by [69]

$$\begin{aligned} g_{haa} &\simeq -\frac{2v}{m_h}\left(\lambda_{P1}\cos^2\beta + \lambda_{P2}\sin^2\beta\right)\,, \\ g_{Haa} &\simeq \frac{v}{m_H}\sin\left(2\beta\right)\left(\lambda_{P1} - \lambda_{P2}\right)\,, \end{aligned} \tag{7.5}$$

where $m_h \simeq 125\,\text{GeV}$ is the mass of the SM-like Higgs, while $\lambda_{P1}, \lambda_{P2}$ are the quartic couplings that appear in the 2HDM+a scalar potential as $P^2\left(\lambda_{P1} H_1^\dagger H_1 + \lambda_{P2} H_2^\dagger H_2\right)$. Here P denotes the additional pseudoscalar in the weak eigenstate basis, which satisfies $P \simeq a$ for $\sin\theta \simeq 0$.

The trilinear couplings entering (7.5) can be constrained phenomenologically. In the case of g_{haa}, one can require that the partial decay width $\Gamma\left(h \to aa\right)$ does not exceed the total decay width Γ_h of the 125 GeV Higgs as measured directly at the LHC. For $m_a \ll m_h$, this leads to the inequality [232]

$$|g_{haa}| \lesssim \sqrt{\frac{32\pi\Gamma_h}{m_h}} \simeq 0.94\,, \tag{7.6}$$

where in the last step we have employed the latest 95% CL bound of $\Gamma_h < 1.1\,\text{GeV}$ that follows from the LHC measurements of the total SM-like Higgs width [258, 259]. Inserting the first expression of (7.5) into (7.6) then leads to the following relation

$$\left|\lambda_{P1}\cos^2\beta + \lambda_{P2}\sin^2\beta\right| \lesssim 0.24\,. \tag{7.7}$$

In the case of g_{Haa}, one obtains in a similar fashion

$$|g_{Haa}| \lesssim \sqrt{\frac{32\pi\Gamma_H}{m_H}} \simeq 3.2\,, \tag{7.8}$$

where in the final step we have set the ratio between the total decay width and the mass of the heavy Higgs to $\Gamma_H/m_H = 10\%$. This choice is motivated by the observation that for significantly larger ratios different treatments of the H propagator lead to notable changes in the heavy Higgs production cross section, and thus the LLP signal, compared to the case of a Breit-Wigner propagator with fixed width. Combining the second relation in (7.5) with (7.8), it follows that

$$\left|\frac{v}{m_H}\sin(2\beta)\,(\lambda_{P1}-\lambda_{P2})\right| \lesssim 3.2\,. \tag{7.9}$$

The above discussion illustrated that in the limit $\sin\theta \to 0$, an LLP signature can arise in the 2HDM+a model from h or H production followed by the decay of the intermediate Higgs to a pair of pseudoscalars. Representative tree-level graphs showing $pp \to aa$ production in ggF Higgs production (left) and $pp \to l^+l^-aa$ production in associated Higgs production (right) that appear in the 2HDM+a model can be found in Figure 7.1. Notice that in the former case both the 125 GeV Higgs and the heavy $\mathcal{CP}$-even Higgs contribute in the alignment limit. This is not the case for the latter process, as the HZZ vertex vanishes identically in the limit $\cos(\beta-\alpha) \to 0$.

7.3 Parameter benchmarks

Besides the phenomenological bounds (7.7) and (7.9) that constrain the sizes of the quartic couplings λ_{P1} and λ_{P2}, the requirement for the scalar potential to be bounded from below also restricts the quartic couplings, as well as other parameters of the 2HDM+a model. Assuming that $\lambda_{P1}, \lambda_{P2} > 0$ and that $\sin\theta \simeq 0$, one finds two bounded-from-below conditions that take the form [219]

$$\lambda_3 > 2\lambda\,, \qquad \lambda_3 \gtrsim -2\lambda\cot^2(2\beta)\,. \tag{7.10}$$

Here, the parameter λ_3 denotes the usual quartic coupling from the 2HDM scalar potential and $\lambda = m_h^2/(2v^2) \simeq 0.13$ is the cubic SM Higgs self-coupling. In order to fulfil these relations and to avoid the tight constraints from Higgs and EW precision physics, we make the following common parameter choices

General parameter choices

$$\lambda_3 = 0.3\,, \quad \cos(\beta-\alpha) = 0\,, \quad \tan\beta = 1\,, \quad m_H = m_A = m_{H^\pm}\,, \quad y_\chi = 1\,. \tag{7.11}$$

For concreteness, we furthermore employ a Yukawa sector of type-II throughout this work.

The first 2HDM+a benchmark scenario that we will study as an example to illustrate the possible LLP phenomenology in the 2HDM+a model is:

Benchmark I

$$\{\lambda_{P1}, \lambda_{P2}, m_\chi\} = \{2\cdot 10^{-3}, 2\cdot 10^{-3}, 170\,\text{GeV}\}\,, \quad \text{(benchmark I)}\,. \tag{7.12}$$

We furthermore treat $\sin\theta$ and m_a as free parameters but require that $m_a < m_h/2$, so that the LLP can be pair produced in the decay of the 125 GeV Higgs boson. The precise value of the common heavy Higgs mass is irrelevant in such a situation and we simply set it to $m_H = 600\,\text{GeV}$ in benchmark I. Notice that the quartic couplings λ_{P1} and λ_{P2} have been chosen such that the constraint (7.7) is easily fulfilled. In fact, in the limit $m_a \to 0$ the benchmark I parameter choices imply

$$\Gamma_h = 4.15\,\text{MeV}\,, \tag{7.13}$$

a value that is very close to the SM prediction of $\Gamma_h^{\text{SM}} = 4.07\,\text{MeV}$ [260]. The corresponding $h \to aa$ branching ratio is

Partial decay width of the SM Higgs

$$\text{BR}\,(h \to aa) = 1.9\%\,. \tag{7.14}$$

The proper decay length of the pseudoscalar a for masses $m_a \in [20, 60]\,\text{GeV}$ can be approximated by

Decay length (benchmark I)

$$\frac{c\tau_a}{\text{m}} \simeq 4.8 \cdot 10^{-12} \left(\frac{\text{GeV}}{m_a}\right)^{0.9} \frac{1}{\sin^2\theta}\,, \tag{7.15}$$

which means that for

$$\sin\theta \simeq 4.2 \cdot 10^{-7}\,, \tag{7.16}$$

a pseudoscalar of $m_a = 40\,\text{GeV}$ has a proper decay length of around 1 m. The result (7.15) includes higher-order QCD corrections employing the formulas presented in Appendix A of the paper [261] as implemented in [262]. Notice further that for the choices (7.12) and assuming that $\sin\theta \simeq 0$, the additional 2HDM Higgses are all narrow, i.e. $\Gamma_H/m_H \simeq 2\%$, $\Gamma_A/m_A \simeq 4\%$ and $\Gamma_{H^\pm}/m_{H^\pm} \simeq 4\%$, with $\text{BR}\,(H \to t\bar{t}) \simeq 100\%$, $\text{BR}\,(A \to t\bar{t}) \simeq 100\%$ and $\text{BR}\,(H^\pm \to tb) \simeq 100\%$.

In our second 2HDM+a benchmark scenario that leads to an interesting LLP phenomenology, we consider the following parameter choices

Benchmark II

$$\{\lambda_{P1}, \lambda_{P2}, m_\chi\} = \{3, 0, 770\,\text{GeV}\}\,, \quad \text{(benchmark II)}\,. \tag{7.17}$$

The parameters $\sin\theta$, m_H and m_a are instead treated as input with the requirements $m_a > m_h/2$ and $m_a < m_H/2$, so that the LLP can only be pair produced in the decay $H \to aa$ of the heavy $\mathcal{CP}$-even Higgs boson H. Notice that the values λ_{P1} and λ_{P2} in (7.17) satisfy the constraint (7.9). Taking for example $m_H = 600\,\text{GeV}$ and $m_a = 150\,\text{GeV}$, the total decay width of the heavy $\mathcal{CP}$-even Higgs is given by

$$\Gamma_H = 22\,\text{GeV}\,, \tag{7.18}$$

which implies that $\Gamma_H/m_H = 3.7\%$. The corresponding branching ratios are

$$\text{BR}\,(H \to aa) = 35\%\,, \qquad \text{BR}\,(H \to t\bar{t}) = 65\%\,, \tag{7.19}$$

meaning that the decays of the heavy Higgs to two LLPs does not have the largest branching ratio but that di-top decays are more frequent. Notice that given the structure of the trilinear coupling g_{Haa} in (7.5), this feature will be even more pronounced for heavier $\mathcal{CP}$-even Higgs bosons H.

Partial decay width of the heavy Higgs H

Decay length (benchmark II)

In the range $m_a \in [100, 300]\,\text{GeV}$, the proper decay length of the pseudoscalar a is approximately given by

$$\frac{c\tau_a}{\text{m}} \simeq 1.2 \cdot 10^{-10} \left(\frac{\text{GeV}}{m_a}\right)^{1.6} \frac{1}{\sin^2\theta}\,, \tag{7.20}$$

where again the results of [261, 262] have been used. It follows that for

$$\sin\theta \simeq 2.1 \cdot 10^{-7}\,, \tag{7.21}$$

a pseudoscalar of $m_a = 150\,\text{GeV}$ has a proper decay length of about 1m. Notice finally that in the case of (7.12) with $\sin\theta \simeq 0$, one has $\Gamma_A/m_A \simeq 4\%$ and $\Gamma_{H^\pm}/m_{H^\pm} \simeq 4\%$ with $\text{BR}\,(A \to t\bar{t}) \simeq 100\%$ and $\text{BR}\,(H^\pm \to tb) \simeq 100\%$.

7.4 LLP constraints

At the LHC, searches for displaced Higgs boson decays into LLPs have been carried out by the ATLAS, CMS and LHCb collaborations in different final states, covering proper decay lengths from around $10^{-3}\,\text{m}$ to $10^3\,\text{m}$ [241–257]. The LLP mean decay length determines the search strategies and reconstruction techniques that are employed – see for instance Section 5 of the review [230] for comprehensive descriptions of the details of the experimental techniques employed in LHC LLP searches.

Constraints on benchmark I

We first consider the 2HDM+a benchmark I scenario (7.12) with $m_a < m_h/2$. In this case the pseudoscalar a can be pair produced in the decay of the 125 GeV Higgs boson. The dominant decay modes of the pseudoscalar are $\text{BR}\,(a \to c\bar{c}) \simeq 53\%$, $\text{BR}\,(a \to \tau^+\tau^-) \simeq 38\%$, and $\text{BR}\,(a \to gg) \simeq 10\%$ for the case when the mass of a is below the bottom-quark threshold, and $\text{BR}\,(a \to b\bar{b}) \simeq 85\%$, $\text{BR}\,(a \to c\bar{c}) \simeq 4\%$, $\text{BR}\,(a \to \tau^+\tau^-) \simeq 7\%$, and $\text{BR}\,(a \to gg) \simeq 3\%$ when it is above. LLP searches that target pseudoscalar pair production in ggF Higgs or associated Zh production (cf. Figure 7.1) leading to multi-jet or four-bottom final states therefore provide the most stringent constraints. Looking for displaced leptons instead leads to significantly weaker restrictions because of the small leptonic branching ratios.

In Figure 7.2, we show an assortment of LLP constraints in the m_a–$\sin\theta$ plane that apply in the case of (7.12). All limits result from LHC searches that consider this ggF Higgs production. The dotted red exclusion corresponds to the search [244] that considers displaced hadronic jets in the ATLAS calorimeter (CM) and the muon spectrometer (MS) [243], while the dotted blue constraint instead results from the ATLAS search [245] that utilises the inner detector (ID) and the MS. These searches use up to $36\,\text{fb}^{-1}$ and $33\,\text{fb}^{-1}$ of $\sqrt{s} = 13\,\text{TeV}$ data, respectively. The dotted green (purple) lines represent an upgrade of the MS (CM) search strategy to $139\,\text{fb}^{-1}$ of luminosity collected in LHC Run II. The corresponding limits are reported in the ATLAS publication [253] and [254], respectively. The dashed yellow contour is finally the exclusion that derives from the CMS search [248] which employs the muon endcap and $137\,\text{fb}^{-1}$ of $\sqrt{s} = 13\,\text{TeV}$ data. From the figure it is evident that in the 2HDM+a benchmark I scenario the existing LHC searches for displaced Higgs decays to hadronic jets allow to exclude values of $\sin\theta$ between around 10^{-7} and 10^{-5} with the exact bound depending on the mass of the pseudoscalar a. The

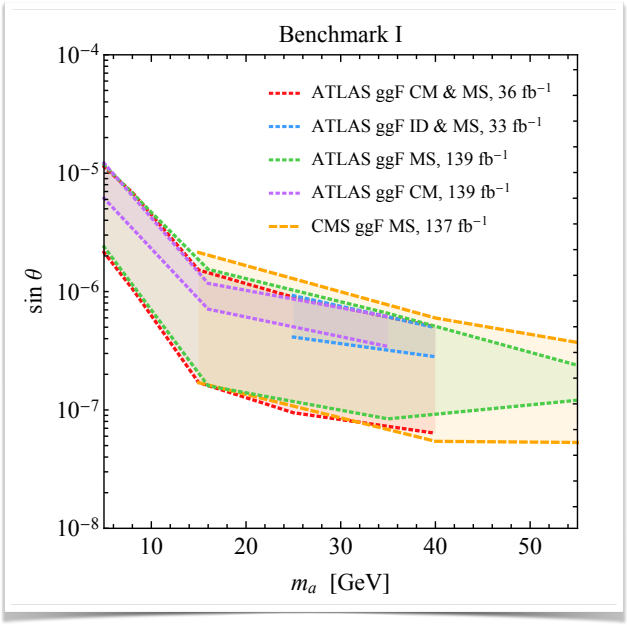

Figure 7.2: 95% CL exclusion regions in the m_a–$\sin\theta$ plane for the 2HDM+a benchmark I scenario (7.12). The dotted red, blue, green and purple lines correspond to the limits following from the ATLAS searches [243, 244], [245], [253] and [254], respectively. The dashed yellow curves instead represent the bound that arises from the CMS search [248]. The parameter space between the lines is disfavoured. See main text for further details.

excluded parameter space corresponds to proper decay lengths $c\tau_a$ in the range from around 59 m to 0.08 m. Notice that given the smallness of the $h \to aa$ branching ratio (cf. (7.14)), our benchmark I scenario easily evades the present bounds on the undetected or invisible branching ratios of the 125 GeV Higgs [66] that amount to 19% and 9%, respectively. In fact, even a possible future HL-LHC upper limit on the invisible branching ratio of the SM-like Higgs of $\text{BR}(h \to \text{invisible}) < 2.5\%$ [263] would not be stringent enough to test (7.12) indirectly. This feature underlines the special role that LLP searches for displaced Higgs decays can play in testing 2HDM+a models with mixing angles θ close to zero.

Constraints on benchmark II

Let us now turn our attention to the benchmark II scenario (7.17). In this case the parameters are chosen such that an LLP signal may arise from the prompt decay of the heavy $\mathcal{CP}$-even Higgs, i.e $H \to aa$, followed by the displaced decays of the pseudoscalars to a pair of SM fermions $a \to f\bar{f}$ or gluons $a \to gg$. Given our choice of Yukawa sector and $\tan\beta$, the a dominantly decays to the heaviest SM fermion, which means that depending on the precise value of its mass either $a \to b\bar{b}$ or $a \to t\bar{t}$ provide the largest rate. To illustrate these two possibilities we consider in benchmark II the mass combination $m_H = 600\,\text{GeV}$ with $m_a \in [50, 275]\,\text{GeV}$ as well as $m_H = 1000\,\text{GeV}$ with $m_a \in [50, 475]\,\text{GeV}$. At a center-of-mass energy of $\sqrt{s} = 13\,\text{TeV}$ the relevant inclusive heavy Higgs production cross sections are $\sigma(pp \to H) \simeq 2.0\,\text{pb}$ and $\sigma(pp \to H) \simeq 0.12\,\text{pb}$ [264], respectively. Notice that in the first case and assuming $m_a = 150\,\text{GeV}$, the heavy Higgs branching ratios (7.19) as well as $\text{BR}(a \to b\bar{b}) \simeq 62\%$, $\text{BR}(a \to c\bar{c}) \simeq 3\%$, $\text{BR}(a \to \tau^+\tau^-) \simeq 7\%$ and

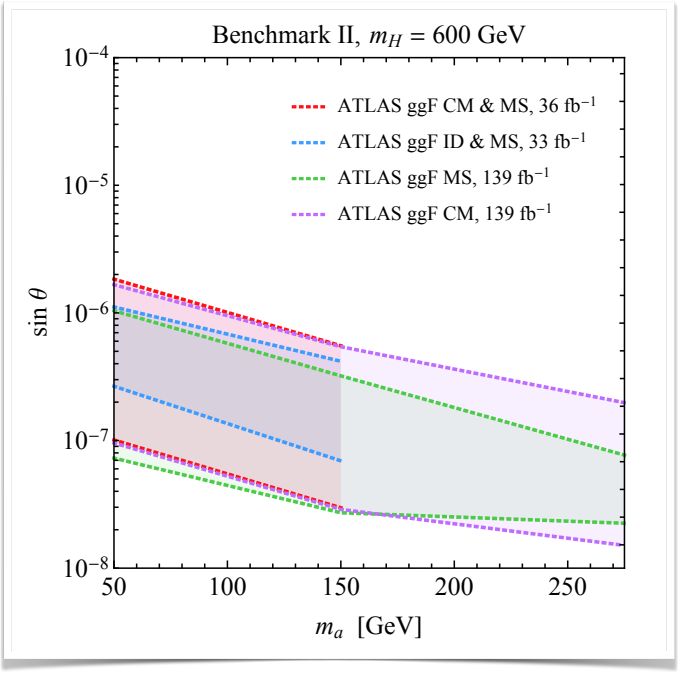

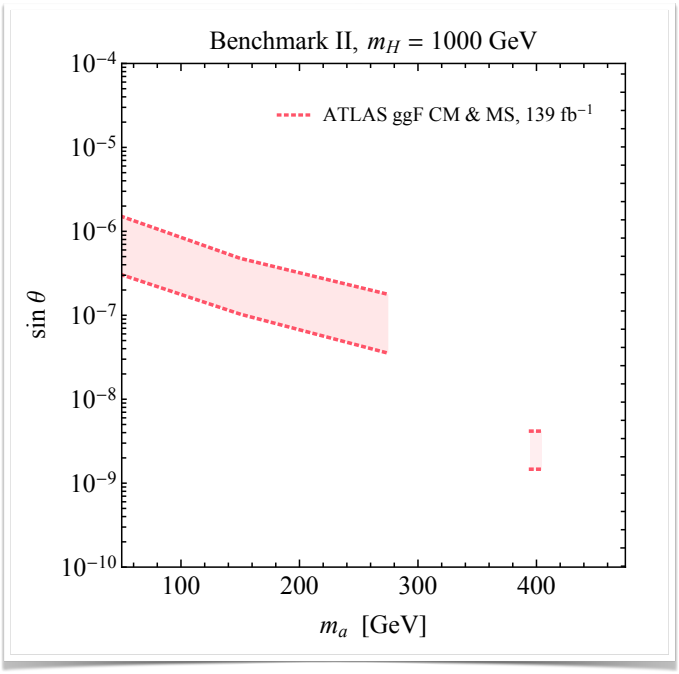

Figure 7.3: As Figure 7.2, but for the two 2HDM+a benchmark II scenarios (7.17). The upper (lower) panel depicts the results for $m_H = 600\,\text{GeV}$ ($m_H = 1000\,\text{GeV}$). The dotted red, blue, green and purple lines in the upper panel correspond to the bounds following from [243, 244], [245], [253] and [254], respectively. The dotted red exclusion in the lower panel instead represents the combination of the ATLAS searches [243, 244, 253, 254]. The shaded parameter regions are disfavoured. Further explanations can be found in the main text.

$\mathrm{BR}(a \to gg) \simeq 28\%$ apply. In the second case, one has instead $\mathrm{BR}(H \to aa) \simeq 9\%$, $\mathrm{BR}(H \to t\bar{t}) \simeq 91\%$ and $\mathrm{BR}(a \to t\bar{t}) \simeq 100\%$ for $m_a = 400\,\mathrm{GeV}$.

In the upper panel of Figure 7.3, we display the relevant 95% CL exclusion regions in the m_a–$\sin\theta$ plane that apply in the case of the 2HDM+a benchmark II scenario with $m_H = 600\,\mathrm{GeV}$. One observes that the ATLAS searches [243–245, 253, 254] allow to exclude $\sin\theta$ values between $2 \cdot 10^{-8}$ and $2 \cdot 10^{-6}$. The corresponding proper decay lengths $c\tau_a$ range from 53 m to 0.04 m. The lower plot in Figure 7.3 shows the limits on $\sin\theta$ that a combination of the four ATLAS searches [243, 244, 253, 254] allow to set in the 2HDM+a benchmark II scenario (7.17), assuming $m_H = 1000\,\mathrm{GeV}$. One observes that the existing LLP searches can exclude mixing angles for the mass points $m_a = 50\,\mathrm{GeV}, 150\,\mathrm{GeV}, 275\,\mathrm{GeV}$, and $400\,\mathrm{GeV}$, while the 2HDM+a realization with $m_a = 475\,\mathrm{GeV}$ remains untested at present. For pseudoscalar masses below the top-quark threshold, $\sin\theta$ values between around $4 \cdot 10^{-8}$ and $2 \cdot 10^{-6}$ are excluded, whereas for $m_a = 400\,\mathrm{GeV}$ mixing parameters in the range of about $4 \cdot 10^{-9}$ and $1 \cdot 10^{-9}$ are disfavoured. The excluded parameter space corresponds to $c\tau_a$ values ranging from around 9.7 m to 0.06 m. Notice that the order of magnitude improvement of the constraint on $\sin\theta$ from the point $m_a = 275\,\mathrm{GeV}$ to $m_a = 400\,\mathrm{GeV}$ is readily understood by recalling that in the former case one has $\Gamma_a \simeq 16\,\mathrm{MeV}\sin^2\theta$, while in the latter case $\Gamma_a \simeq 12\,\mathrm{GeV}\sin^2\theta$ as a result of the open $a \to t\bar{t}$ channel. We add that improving the limits [253, 254] by a factor of four would allow to probe our 2HDM+a benchmark II scenario for $m_H = 1000\,\mathrm{GeV}$ and $m_a = 475\,\mathrm{GeV}$. A final remark concerns the possibility to search for the heavy $\mathcal{CP}$-even Higgs in the processes $pp \to H \to t\bar{t}$ or $pp \to t\bar{t}H \to 4t$. While LHC searches for spin-0 resonances in both di-top [265–267] and four-top production [268–271] have been performed, it turns out that the existing searches do not provide any bound on our 2HDM+a benchmark II model for both $m_H = 600\,\mathrm{GeV}$ and $m_H = 1000\,\mathrm{GeV}$ in the m_a ranges considered in Figure 7.3. This finding again stresses the unique role that LLPs searches can play in the 2HDM+a model in constraining the parameter space.

7.5 Summary

The main lesson that can be learnt from the analytic and numerical results presented in this section is that LHC searches for displaced Higgs decays can provide unique constraints on 2HDM+a model realizations. In fact, LLP signatures appear in the context of the 2HDM+a model in a natural fashion if the mixing angle θ of the two $\mathcal{CP}$-odd weak spin-0 eigenstates is very small and the DM sector is either decoupled or kinematically inaccessible. In order to emphasise this generic finding, we have studied two distinct parameter benchmarks and explored the sensitivity of the existing LHC LLP searches by performing parameter scans in the m_a–$\sin\theta$ plane. The results of these scans can be found in Figures 7.2 and 7.3.

In the benchmark I scenario, we have chosen the 2HDM+a parameters such that the 125 GeV Higgs boson gives rise to an LLP signature through its prompt decay $h \to aa$ followed by the displaced decays of the pseudoscalars to SM fermions, such as $a \to b\bar{b}$ or gluons. One important feature that is nicely illustrated in our benchmark I scan is that the LLP searches for displaced hadronic jets that have been performed at LHC Run II can probe regions of parameter space with mixing angles θ

in the ballpark of 10^{-7} to 10^{-5} that are presently not accessible by any other means. In fact, in our benchmark I scenario the predicted $h \to aa$ branching ratio turns out to be below the target sensitivity that the HL-LHC is expected to reach on undetected or invisible decays of the 125 GeV Higgs boson. 2HDM+a realizations like (7.12) are therefore unlikely to be testable indirectly at the LHC in searches for both prompt $h \to aa \to 4f$ production or through signatures involving a significant amount of E_T^{miss} such as $h \to$ invisible or mono-jet final states.

The benchmark II parameters were instead chosen such that the LLP signal arises from the prompt decay $H \to aa$ of the heavy $\mathcal{CP}$-even Higgs followed by the displaced decays of the pseudoscalars to a pair of SM fermions or gluons. Depending on the precise value of the LLP mass, either the $a \to b\bar{b}$ or the $a \to t\bar{t}$ mode turns out to provide the largest rate. In order to illustrate these two distinct possibilities, we have considered in benchmark II the mass combination $m_H = 600\,\text{GeV}$ with $m_a \in [50, 275]\,\text{GeV}$ as well as $m_H = 1000\,\text{GeV}$ with $m_a \in [50, 475]\,\text{GeV}$. In the former case, we found that the existing LHC searches for displaced heavy Higgs decays provide stringent constraints on θ, excluding values of the mixing angle between $2 \cdot 10^{-8}$ and $2 \cdot 10^{-6}$. The limits on the benchmark II scenario with $m_H = 1000\,\text{GeV}$ turned out to be noticeably weaker than the bounds for $m_H = 600\,\text{GeV}$, due to the order of magnitude smaller inclusive heavy Higgs production cross section. Still, for the three mass values $m_a = 50\,\text{GeV}, 150\,\text{GeV}$ and $275\,\text{GeV}$, θ values between $4 \cdot 10^{-8}$ and $2 \cdot 10^{-6}$ are excluded, whereas for $m_a = 400\,\text{GeV}$ mixing parameters in the range of $4 \cdot 10^{-9}$ and $1 \cdot 10^{-9}$ are disfavoured by the searches for the displaced heavy Higgs decays performed at LHC Run II. We expect that LLP searches at LHC Run III and beyond will provide sensitivity to 2HDM+a models à la (7.17) with heavy $\mathcal{CP}$-even Higgs masses of the order of 1 TeV and pseudoscalar masses m_a above the top-quark threshold. Let us finally note that in future LHC runs, it should also be possible to probe 2HDM+a benchmark II models with a heavy $\mathcal{CP}$-even Higgs that satisfies $m_H > 2m_a$ and $m_H > 2m_t$ through spin-0 resonance searches in di-top and four-top production. A detailed analysis of this issue is however beyond the scope of this work.

It has furthermore been demonstrated that parameter choices that give rise to an interesting LLP phenomenology can simultaneously explain the observed DM abundance without excessive tuning. The corresponding discussion can be found in Appendix C. The results and parameter benchmarks presented in this section should provide a useful starting point for interpretations of future ATLAS, CMS and LHCb searches for displaced Higgs decays to hadronic jets in the context of the 2HDM+a model. We therefore encourage and look forward to experimental explorations in this direction.

CONCLUSIONS

8 CONCLUSIONS

Nature's music is never over;
her silences are pauses, not conclusions.

— Mary Webb (poet)

Where does BSM physics hide at the LHC? *In the tails.* As the LHC collaborations are preparing for the HL-LHC run, scheduled to commence in 2029 and conclude in 2041, the particle physics phenomenology community is focussing on improving their theoretical predictions. This thesis highlighted three studies, originally published in [LS1, LS3, LS2], which contribute to the improvement of the theoretical predictions for BSM signatures. In essence, they can be classified into two ways to approach BSM searches at the LHC:

The first approach, discussed in part (I), entails the search for small deviations in SM precision observables. In this context, precise predictions for the SM backgrounds and BSM signals are required, to surpass the results achieved during previous LHC runs. The formal fixed-order accuracies of these predictions have recently reached the NNLO to N^{3}LO and NLO to NNLO levels, respectively. In Section 2, we presented a review of the fundamental techniques that are employed in this context. An introduction the the SMEFT was given in Section 3, and in Section 4, we outlined the extension of the theoretical techniques to higher orders perturbative, with a particular focus on higher-order SMEFT calculations.

In Section 5, we then presented our calculation of SMEFT effects in the Higgsstrahlung $pp \to Vh$ process at NNLO+PS accuracy, where we employed the recently developed `POWHEG MiNNLO`$_{\text{PS}}$ method. `MiNNLO`$_{\text{PS}}$ allows for the on-the-fly simulation of NNLO QCD corrections, consistently matched to PS generators in order to simulate the subsequent emissions at LL accuracy. Our `MiNNLO`$_{\text{PS}}$ code allows for the simulation of contributions from the operators $\mathcal{O}_{HB}$, $\mathcal{O}_{HW}$, $\mathcal{O}_{HWB}$, which modify the VVh vertex, from the operators $\mathcal{O}_{Hq}^{(1)}$, $\mathcal{O}_{Hq}^{(3)}$, $\mathcal{O}_{Hd}$, $\mathcal{O}_{Hu}$, $\mathcal{O}_{Hud}$, $\mathcal{O}_{H\ell}^{(1)}$, $\mathcal{O}_{H\ell}^{(3)}$, $\mathcal{O}_{He}$, which enter $V(h)f\bar{f}$, and $\mathcal{O}_{H\Box}$, $\mathcal{O}_{HD}$, $\mathcal{O}_{\ell\ell}$, which shift the Higgs kinetic term and/or the EW input parameter relations, both at the linear $\mathcal{O}(\Lambda^{-2})$ and the quadratic $\mathcal{O}(\Lambda^{-4})$ level, and for the α, α_μ and LEP EW input schemes individually. We consider it to be an essential tool for future Higgs characterization studies by the ATLAS and CMS collaborations.

In the matrix element calculation, we encountered interesting theoretical aspects. Firstly, this included repurposing SM spinor-helicity expressions for the higher-order diagrams contributing to $pp \to Vh$. Indeed, as the SMEFT operators entering the VVh vertex modify its helicity structure but leave the helicity structure of the $q\bar{q}Z$ vertex with all its QCD corrections invariant, it is possible isolate the $q\bar{q}Z$ structures in the SM and re-contract them with the new SMEFT VVh vertices to obtain the full

SMEFT amplitudes. Secondly, SMEFT operators entering the $t\bar{t}Z$ or $b\bar{b}Z$ vertices could potentially spoil the cancellation of gauge anomalies in $gg \to Zh$ contributions with a heavy-quark ggZ triangle. We showed that this is not the case. It is known that the SMEFT is anomaly-free, which for the $Z(h)q\bar{q}$ operators manifests as a cancellation between the triangle diagrams involving $Zq\bar{q}$ and $Zhq\bar{q}$ vertices.

In Chapter 5.6, we then conducted a phenomenological analysis based on the Wilson coefficient benchmark choices (5.28)-(5.32) allowed or even preferred by current data, where we investigated the sensitivity of the Higgsstrahlungs process $pp \to Zh\ell^+\ell^-$ to SMEFT effects. Particularly noteworthy are the effects of $\mathcal{O}_{Hq}^{(3)}$, $\mathcal{O}_{Hu}$, $\mathcal{O}_{Hd}$, which are pronounced at high transverse momenta $p_{T,Z}$ of the Z boson, as illustrated in the Figure 5.6. Indeed, the contributions from diagrams with a quartic $Zhq\bar{q}$ vertex begin to dominate over the SM background in the tail of the $p_{T,Z}$ spectrum, as they do not receive the suppression from the first Z propagator. Consequently, $pp \to Zh$ is better suited to search for contributions from $\mathcal{O}_{Hq}^{(3)}$, $\mathcal{O}_{Hu}$, $\mathcal{O}_{Hd}$ than e.g. $pp \to Z$, where only $Zq\bar{q}$ corrections of these operators enter. Improving the statistics of $pp \to Vh$ searches in *the tails* could reveal such BSM effects.

The second approach to maximizing the new physics potential of the HL-LHC is to consider non-standard signatures that clearly stand out from the SM backgrounds in dedicated analyses. This was the main topic of Part (II).

As a first example, we considered VLQs that are predominantly coupled to third-family fermions. They arise in the 4321 gauge unification, which is built upon a non-universal $SU(4)^{[3]}$ group. The latter is a general feature of models addressing the SM flavor puzzle without causing tension with low-energy data or exacerbating the Higgs hierarchy problem, as explained in Section 3. In Section 6, we presented our NLO+PS calculation of VLQ effects in $pp \to \tau^+\tau^-$, which we published for phenomenological applications as a `POWHEG-BOX` generator [197]. We included effects of the G', π_U, $\pi_{G'}$ gauge and Goldstone bosons as well as of the gauge ghosts $c_U, c_{U^\dagger}, c_{G'}$ present in the spectrum of the 4321 model in the Feynman gauge. From a theoretical point of view, this calculation provides an intriguing example of $\mathcal{O}(\alpha_s)$ corrections with contributions from a scalar sector charged under QCD. Practically, our `POWHEG` code consistently combines non-resonant t-channel contributions of VLQs in $pp \to \tau^+\tau^-$ with their single-resonant contributions in $pp \to \tau^+\tau^- b$, rendering it an essential tool for searches conducted by the ATLAS and CMS experiments. Indeed, we are currently assisting the ATLAS collaboration in importing our `POWHEG` code into their event generation system.

In Chapter 6.5, we presented a phenomenological analysis of the VLQ signatures in the $pp \to \tau^+\tau^-$ spectrum. Particularly relevant are the NLO real corrections involving b quark emissions, which lead to $\tau^+\tau^- b$ final states. These can be separated from more generic $\tau^+\tau^-$ final states by requiring an additional b-tagged jet. In the b-tag category, the SM background contribution is significantly suppressed, as the majority of the DY events originate from light initial-state quarks. Conversely, the contributions of the bottom-philic VLQs are predominantly associated with b-quarks, resulting in a weaker suppression than for the SM. This provides a compelling case for VLQ signature searches in *the tails* of $\tau^+\tau^- b$ distributions at the LHC.

As a second example, we considered an extended scalar sector with two Higgs doublets, whose pseudoscalar mode mixes with a pseudoscalar DM mediator. This model is known as the 2HDM+a, and was introduced in Section 3. In Section 7, we demonstrated that the 2HDM+a can exhibit an intriguing LLP phenomenology in the limit $\sin\theta \simeq 0$ of minimal mixing with the extended scalar sector. This scenario is further compatible with current relic density measurements in the standard thermal relic freeze-out scenario, as discussed in Appendix C. Consequently, the LLP limit of the 2HDM+a serves as an important benchmark for LHC exotica searches: Firstly, since the couplings of a to the SM fermions are inherited from the extended Higgs sector, the 2HDM+a provides an LLP with clearly defined decay pattern. Indeed, only a few parameters enter the expressions for the couplings of a to fermions in (3.123), rendering the model highly predictive. Secondly, a light pseudoscalar mediator coupled both to DM and, minimally, to the SM represents a prime example of models on the lifetime or small coupling frontier. While the majority of LHC searches to date have focused on heavy BSM physics leading to high-p_T signals, it is possible that new physics could be light, feebly interacting, and long-lived. At the ATLAS and CMS experiments, such particles traverse macroscopic distances (millimeters to meters) from the primary interaction point, until they decay in the outer layers of the detector. This provides a clean search ground, with a small number of signal events sufficing to claim a discovery, since so few of the SM particles produced in LHC collisions live long enough to mimic a signal.

We have demonstrated the power of ATLAS and CMS LLP searches by reinterpreting their constraints in the context of the 2HDM+a. Specifically, these include searches that look for LLPs decaying to two narrow jets in the CM or MS, with no associated activity in the tracker. The resulting constraints are particularly strong for a light a pair-produced in decays of the SM Higgs (see Figure 7.2), where parts of the 2HDM+a parameter space can be probed that are currently inaccessible by any other means. With the HL-LHC run probing further into *the tails* of lifetime distributions, we may uncover such feebly interacting particles connected to the DM puzzle.

The next few decades of high-energy physics will be defined by the exploration of the Higgs sector. Precise measurements of its couplings, including in particular its trilinear self-interaction, will allow for the testing of the predictions of the SM at unprecedented levels. As such, the HL-LHC program and the potential electron-electron Future Circular Collider (FCC) extension will provide us with exciting new insights into the fabrics of the Higgs. We believe that the final word regarding the elementary scalar sector has not yet been spoken.

Und der ganze Mambo Jambo...

— Bavarian proverb

ACKNOWLEDGMENTS

First of all, I would like to express my gratitude to my supervisor, Ulrich Haisch, for his continuous support, advice and the great discussions we had over the years. All it takes is a "also, ich habe mir das mal angeschaut..." to know that new insights into the fabric of physics are near. You taught me so much. A big thank you also goes to (in alphabetical order) Paolo Gambino, Rhorry Gauld, Marius Wiesemann, and Giulia Zanderighi for their guidance and support in the exploration of new research avenues. I am further grateful to Andreas Weiler for his official supervision, and for the financial support of the Collaborative Research Center SFB1258.

My doctoral journey in Munich would not have been the same without the old guard Amando, Darren, Gabriël, Markus, Silvia, Stefan, William, the in-betweeners Alessandro, Antonela, Aparna, Chen-Yu, Chiara, Christian, Giovanni, Johannes, Manuel, Marco, and the new youngsters Ann-Sophie, Fazila, Florian, Jakob, Joachim, Ronja – and all the others who make the MPP to this remarkable place!

I am further indebted to my childhood friends, Alessandro, Jan, Nico, and Raphael, for keeping me grounded and always welcoming me back in Bern. And last but not least, I wish to express my gratitude to my parents Dieter und Simone, my sister Anne, and my wife Viktoriia for their constant love and support.

Ah geh!

Congratulations on your child! You have to thank my wife.

Hinten hat der Frosch die Locken.

Haha, you idiot. No, for you it's still Dr. Idiot.

No, compañero, no.

Habe die Ehre! Neuss? Noice.

Ig hetti gern es Sirüpli.

Kriege ich Kuschels?

APPENDIX

A

HIGGSSTRAHLUNG: ANALYTIC EXPRESSIONS FOR THE COUPLINGS

In this appendix, we provide the analytic formulas for the parameters and couplings that appear in Sections 5.3 and 5.4. The presented expressions have been implemented into our MC code which allows the user to choose between the α, α_μ, and LEP schemes. We refer the interested reader to the articles [97, 272, 273] for additional technical details on EW input schemes in the SMEFT context.

In order to write the expression in this appendix as compactly as possible we introduce the following abbreviations

$$\begin{aligned} g_\pm &= \sqrt{g_1^2 \pm g_2^2}\,, \qquad \Delta m = \sqrt{m_Z^2 - m_W^2}\,, \\ s_w &= \sqrt{\frac{1}{2}\left[1 - \sqrt{1 - \frac{2\sqrt{2}\pi\alpha}{G_F m_Z^2}}\right]}\,, \quad c_w = \sqrt{1 - s_w^2}\,, \end{aligned} \tag{A.1}$$

where α is the fine-structure constant, G_F is the Fermi constant as extracted from muon decay and m_Z (m_W) is the mass of the Z (W) boson in the OS scheme. The relevant expressions for the $U(1)_Y$ and $SU(2)_L$ gauge couplings g_1 and g_2 and the Higgs VEV v in terms of the EW input parameters are given in Table A.1 for the α, the α_μ and the LEP scheme.

In terms of the parameters g_1, g_2 and v the $Zf\bar{f}$, $\gamma f\bar{f}$ and hZZ coupling strengths take the following form in the SM

$$g_{Zf}^{\pm} = \frac{g_1^2 Y_f^{\pm} - 2g_2^2 T_f^{3\pm}}{2g_+}\,, \qquad g_{\gamma f}^{\pm} = -\frac{g_1 g_2 Q_f^{\pm}}{g_+}\,, \qquad g_{hZZ} = \frac{v g_+^2}{2}\,. \tag{A.2}$$

Notice that these relations are independent of the employed EW input scheme. Here the symbol Y_f represents the weak hypercharge, T_f^3 is the third component of the weak isospin and Q_f denotes the electric charge. The fermions are $f = q, \ell$ with $q = d, u$ and $\ell = e, \nu$, and the helicity states f_+ and f_- are identical to the chirality states f_R and f_L in the massless limit.

The relations among the EW input parameters and g_1, g_2, and v are modified at tree level by the presence of some of the dimension-six SMEFT operators listed in (5.1) to (5.4), leading to so-called input scheme corrections. These can be accounted for via the shifts $x \to x + \delta x$ for $x = g_1, g_2, v$. We summarise the relevant shifts in Table A.2. The input scheme corrections δg_1 δg_2, and δv themselves lead to the

	g_1	g_2	v
α-scheme $\{G_F, m_Z, m_W\}$	$2\sqrt[4]{2}\sqrt{G_F}\Delta m$	$2\sqrt[4]{2}\sqrt{G_F}\, m_W$	$\frac{1}{\sqrt[4]{2}\sqrt{G_F}}$
α_μ-scheme $\{\alpha, m_Z, m_W\}$	$\sqrt{4\pi\alpha}\,\frac{m_Z}{m_W}$	$\sqrt{4\pi\alpha}\,\frac{m_Z}{\Delta m}$	$\frac{m_W \Delta m}{\sqrt{\pi\alpha}\, m_Z}$
LEP-scheme $\{\alpha, G_F, m_Z\}$	$\frac{\sqrt{4\pi\alpha}}{c_w}$	$\frac{\sqrt{4\pi\alpha}}{s_w}$	$\frac{1}{\sqrt[4]{2}\sqrt{G_F}}$

Table A.1: The parameters g_1, g_2, and v expressed in terms of the input parameters for the three EW input schemes implemented in the POWHEG code.

shifts $\delta g_{Zf}^{(0)\pm}$ and $\delta g_{hZZ}^{(0)}$ of the $Zf\bar{f}$ and hZZ couplings, respectively. We find the following scheme-independent results

$$\begin{aligned}\delta g_{Zf}^{(0)\pm} &= \frac{g_1^3 \delta g_1 Y_f^{\pm} - 2 g_2^3 \delta g_2 T_f^{3\pm} - g_1^2 g_2 \delta g_2 \left(Y_f^{\pm} + 4 T_f^{3\pm}\right)}{2\,\sqrt[3/2]{g_+}} \\ &\qquad + \frac{2 g_1 g_2^2 \delta g_1 \left(Y_f^{\pm} + T_f^{3\pm}\right)}{2\,\sqrt[3/2]{g_+}}\,, \\ \delta g_{hZZ}^{(0)} &= v\left(g_1 \delta g_1 + g_2 \delta g_2\right).\end{aligned} \tag{A.3}$$

At the same time, the SMEFT operators listed in (5.1) to (5.4) give direct contributions to the Z-boson couplings to two gauge bosons. We find the following analytic expressions for the non-zero couplings

$$\begin{aligned}\delta g_{hZZ}^{(1)} &= \frac{4v}{g_+^2}\left[g_1^2 C_{HB} + g_2^2 C_{HW} + g_1 g_2 C_{HWB}\right], \\ \delta g_{h\gamma Z}^{(1)} &= \frac{4v}{g_+^2}\left[g_1 g_2 C_{HB} - g_1 g_2 C_{HW} - \frac{g_-^2}{2} C_{HWB}\right], \\ \delta g_{hZZ}^{(3)} &= v^3\left[g_1 g_2 C_{HWB} + \frac{3 g_+^2}{8} C_{H\Box} + \frac{g_+^2}{2} C_{HD}\right].\end{aligned} \tag{A.4}$$

Furthermore, we obtain $\delta g_{hZZ}^{(2)} = \delta g_{h\gamma Z}^{(2)} = 0$, meaning that the corresponding Dirac structures are not generated at the dimension-six level in the SMEFT. The expressions for the $hZf\bar{f}$ couplings can finally be written as

$$\delta g_{hZf}^{(1)\pm} = \frac{2\delta g_{Zf}^{(1)\pm}}{v}\,, \tag{A.5}$$

	$\delta g_1/g_1$	$\delta g_2/g_2$	$\delta v/v$
α-scheme $\{G_F, m_Z, m_W\}$	$-\frac{\frac{m_Z^2 C_{HD}}{4\Delta m^2}+C_{H\ell}^{(3)}-\frac{C_{\ell\ell}}{2}+\frac{m_W C_{HWB}}{\Delta m}}{\sqrt{2}G_F}$	$-\frac{1}{\sqrt{2}G_F}\left(C_{H\ell}^{(3)}-\frac{C_{\ell\ell}}{2}\right)$	$\frac{1}{\sqrt{2}G_F}\left(C_{H\ell}^{(3)}-\frac{C_{\ell\ell}}{2}\right)$
α_μ-scheme $\{\alpha, m_Z, m_W\}$	$-\frac{m_W^2\Delta m^2}{4\pi\alpha m_Z^2}C_{HD}$	$\frac{m_W^3(m_W C_{HD}+4\Delta m C_{HWB})}{4\pi\alpha m_Z^2}$	$-\frac{m_W^3(m_W C_{HD}+4\Delta m C_{HWB})}{4\pi\alpha m_Z^2}$
LEP-scheme $\{\alpha, G_F, m_Z\}$	$\frac{s_w\left[c_w C_{HWB}+\frac{s_w C_{HD}}{4}+s_w\left(C_{H\ell}^{(3)}-\frac{C_{\ell\ell}}{2}\right)\right]}{\sqrt{2}G_F(c_w^2-s_w^2)}$	$-\frac{c_w\left[s_w C_{HWB}+\frac{c_w C_{HD}}{4}+c_w\left(C_{H\ell}^{(3)}-\frac{C_{\ell\ell}}{2}\right)\right]}{\sqrt{2}G_F(c_w^2-s_w^2)}$	$\frac{1}{\sqrt{2}G_F}\left(C_{H\ell}^{(3)}-\frac{C_{\ell\ell}}{2}\right)$

Table A.2: SMEFT input scheme corrections for the three EW input schemes implemented in the MC code.

where

$$\begin{aligned}
\delta g_{Zd}^{(1)-} &= \frac{v^2 g_+}{2}\left(C_{Hq}^{(1)}+C_{Hq}^{(3)}\right), \qquad \delta g_{Zu}^{(1)-} = \frac{v^2 g_+}{2}\left(C_{Hq}^{(1)}-C_{Hq}^{(3)}\right), \\
\delta g_{Ze}^{(1)-} &= \frac{v^2 g_+}{2}\left(C_{H\ell}^{(1)}+C_{H\ell}^{(3)}\right), \qquad \delta g_{Z\nu}^{(1)-} = \frac{v^2 g_+}{2}\left(C_{H\ell}^{(1)}-C_{H\ell}^{(3)}\right), \qquad \text{(A.6)} \\
\delta g_{zd}^{(1)+} &= \frac{v^2 g_+}{2}C_{Hd}, \qquad \delta g_{Zu}^{(1)+} = \frac{v^2 g_+}{2}C_{Hu}, \qquad \delta g_{Ze}^{(1)+} = \frac{v^2 g_+}{2}C_{He},
\end{aligned}$$

are the relevant direct SMEFT corrections to the $Zf\bar{f}$ couplings.

B

HIGGSSTRAHLUNG: SMEFT EFFECTS AT NLO+PS AND NNLO+PS

NLO QCD correction to Vh production in the SMEFT have been calculated by several groups [98–103]. By now these computations can also be performed automatically by means of the combination of `SMEFT@NLO` and `MadGraph5_aMC@NLO`. In what follows, we will use the `POWHEG-BOX` implementation of $pp \to Zh \to \ell^+\ell^- h$ production presented in [100] to obtain the relevant NLO+PS predictions.

In Figure B.1, we compare the SM predictions for the $|\eta_Z|$ (upper left), $p_{T,Z}$ (upper right), $|\eta_Z - \eta_h|$ (lower left) and m_{Zh} (lower right) distribution in $pp \to Zh$ production obtained at NLO+PS and NNLO+PS, respectively. The dashed (solid) lines correspond to the full NLO+PS (NNLO+PS) results, while the dotted curves depict the ggF contributions that start to contribute at NNLO+PS. From the displayed results it is evident that the NNLO corrections modify the NLO spectra in a non-trivial fashion. The relative size of the NNLO corrections amounts to less than 15% in the $|\eta_Z|$ spectrum, while in the case of the $p_{T,Z}$, $|\eta_Z - \eta_h|$ and m_{Zh} distributions the effects can reach up to around 30%. Notice that for the $p_{T,Z}$ spectrum the NNLO corrections are most pronounced in the vicinity of $p_{T,Z} \simeq m_t$, while in the case of $|\eta_Z - \eta_h|$ and m_{Zh} the largest corrections arise in the tail of the distribution for $|\eta_Z - \eta_h| \gtrsim 3$ and $m_{Zh} \gtrsim 350\,\text{GeV}$, respectively. The enhancement of the $p_{T,Z}$ spectrum at $p_{T,Z} \simeq m_t$ is related to the fact that for such transverse momenta the Z boson is able to resolve the top-quark loop in the graph displayed on the right in Figure 5.2. In fact, another feature that is apparent from the solid and dashed lines in the lower panels is that within the SM the ggF NNLO effects are in general significantly larger than the $q\bar{q}F$ NNLO counterparts.

The NLO+PS and NNLO+PS predictions corresponding to the SMEFT benchmark scenario (5.28) and (5.29) are given in Figure B.2 and Figure B.3, respectively. The dashed gray (solid black) histograms correspond to the NLO+PS (NNLO+PS) results in the SM, while the dashed (solid) coloured results are the corresponding SM+SMEFT predictions. One observes that while the NLO+PS and NNLO+PS results for the full predictions involving the squared matrix elements including the sum of both the SM and SMEFT contributions are notably different, the ratios between the SM+SMEFT and SM results turn out to be essentially independent on whether they are calculated at NLO or NNLO. In order to understand this feature one has to recall that in the SM the dominant NNLO corrections to $pp \to Zh \to \ell^+\ell^- h$ production arise from the $gg \to Zh$ channel, while the NNLO corrections associated to the $q\bar{q} \to Zh$ and $qg \to Zh$ channels are small. The opposite is the case in the SMEFT, where effects stemming from the $gg \to Zh$ channel are suppressed compared to the SM as a result of the cancellation of triangle contributions discussed in Section 5.4. We add that the comparisons of SM+SMEFT predictions present in this appendix represent a non-trivial validation of our new NNLO+PS MC code for Higgsstrahlung.

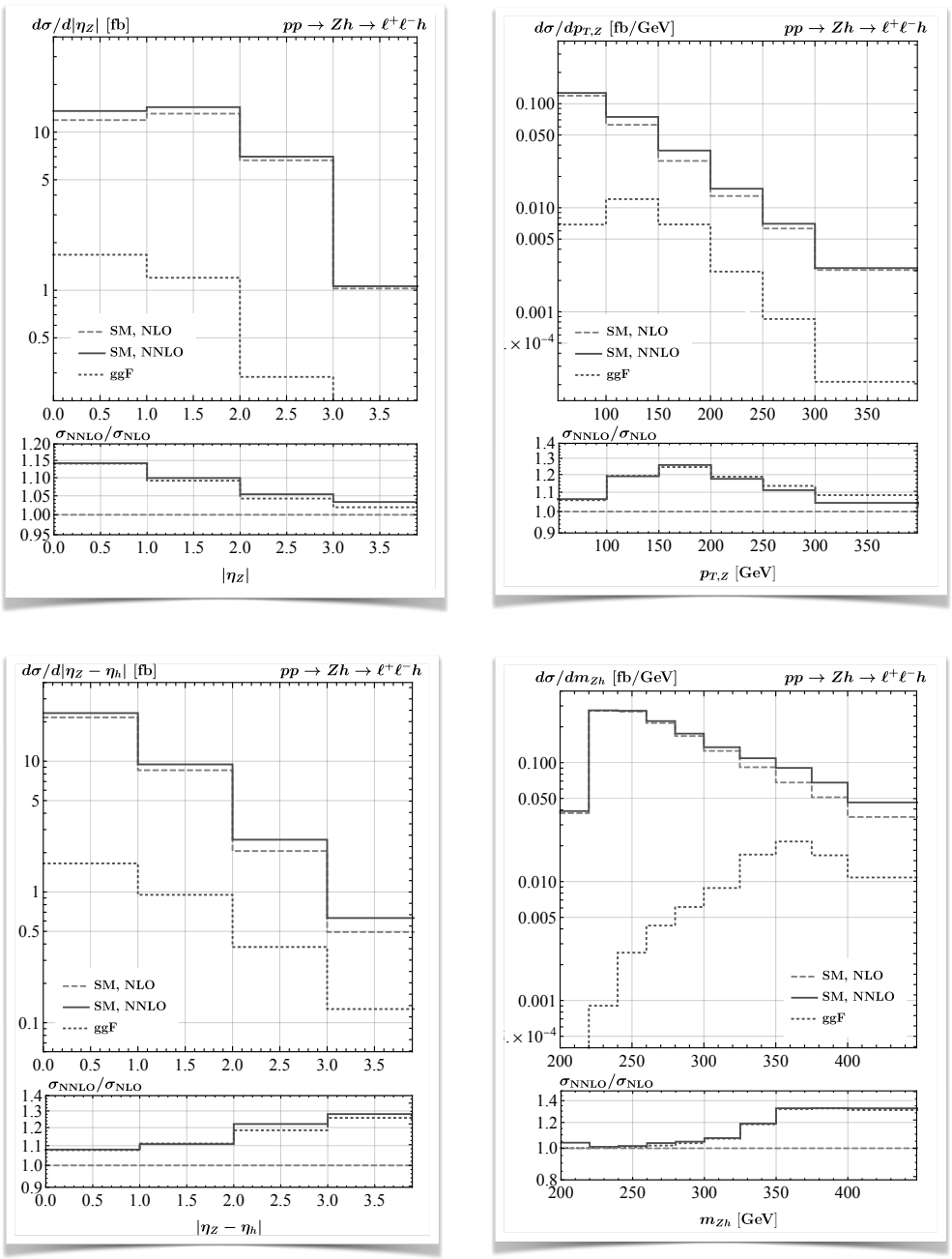

Figure B.1: SM NLO+PS and NNLO+PS results for $pp \to Zh \to \ell^+\ell^- h$ production. The $|\eta_Z|$ (upper left), $p_{T,Z}$ (upper right), $|\eta_Z - \eta_h|$ (lower left) and m_{Zh} (lower right) spectra are shown. The dashed (solid) lines illustrate the NLO+PS (NNLO+PS) results, while the dotted curves are the ggF NNLO+PS corrections. The solid (dotted) lines in the lower panels depict the ratios between the full NNLO+PS (NLO+PS plus ggF NNLO+PS) and the NLO+PS results. See main text for further explanations.

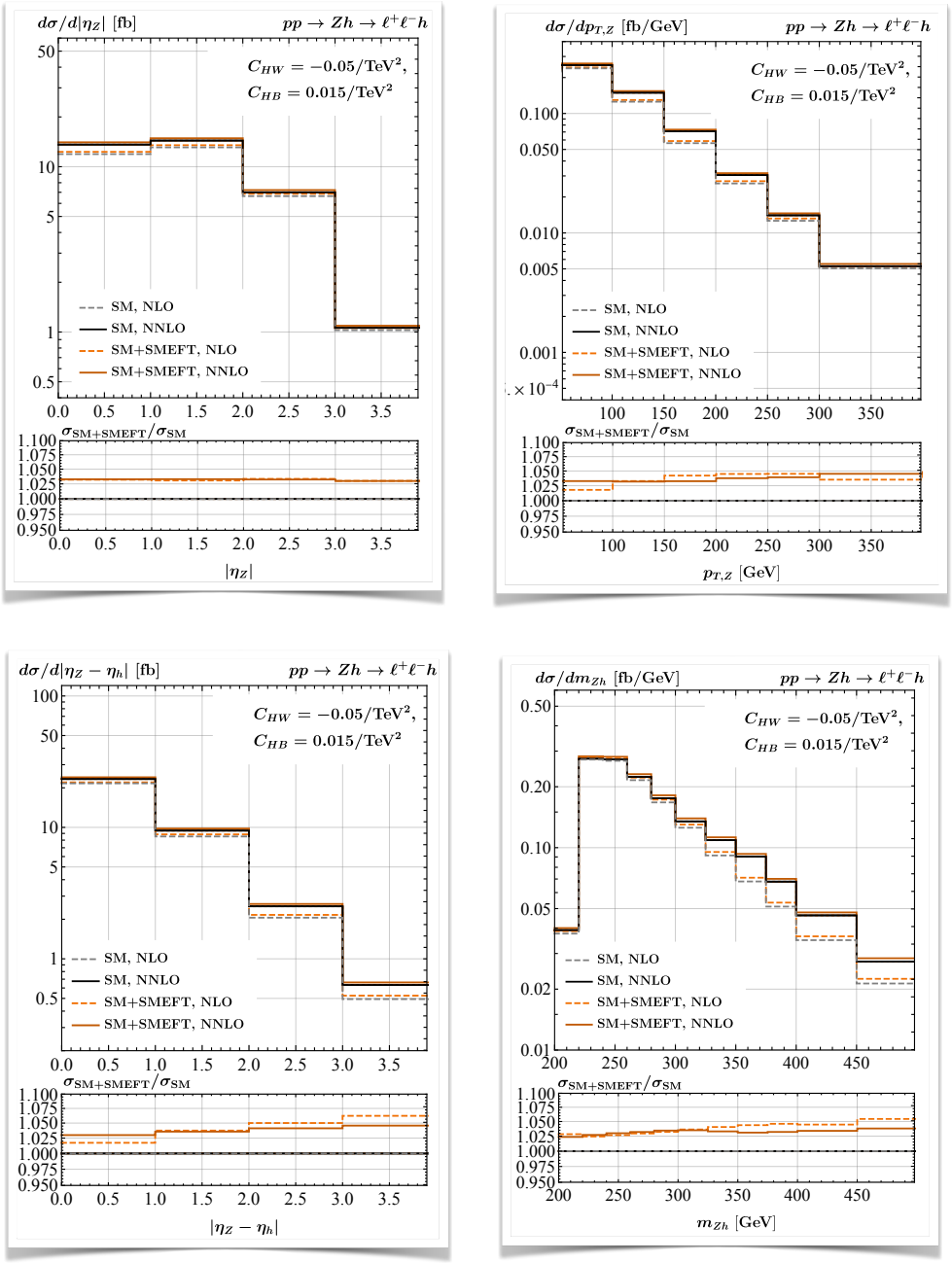

Figure B.2: As Figure B.1, but for benchmark scenario (5.28). The curves called SM+SMEFT correspond to the full squared matrix elements including the sum of both the SM and SMEFT contributions. The lower panels show the ratios between the SM+SMEFT and the SM predictions at the same order in QCD. For more details consult main text.

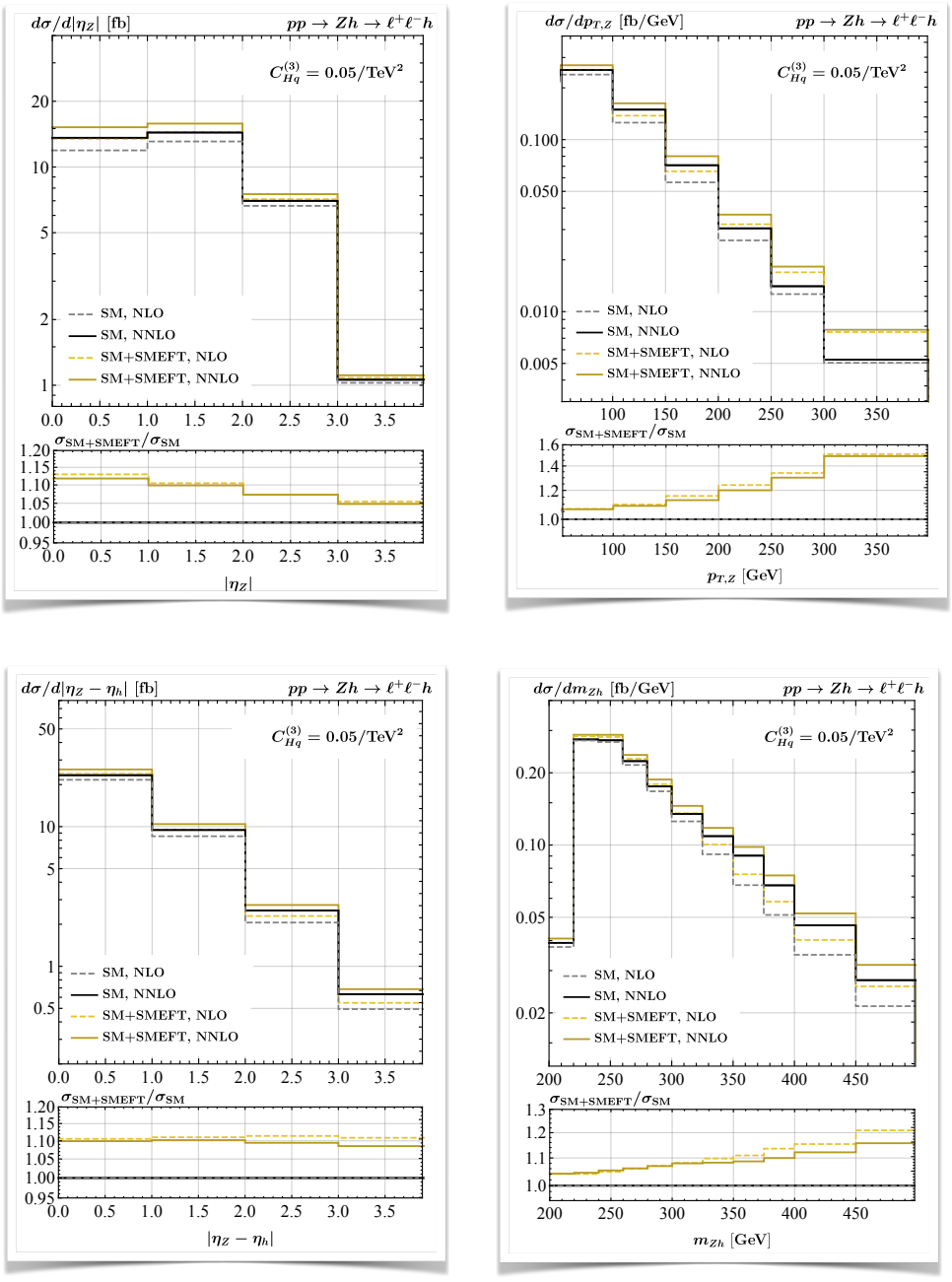

Figure B.3: As Figure B.2, but for benchmark scenario (5.29).

C

EXTENDED SCALAR SECTORS: RELIC DENSITY

In order to understand the physics of standard thermal relic freeze-out in 2HDM+a realizations with $\sin\theta \simeq 0$, we first write the cross section for annihilation of DM into a final state X as

$$\sigma\left(\chi\bar{\chi} \to X\right) v_{\rm rel} = \sigma_X^0 + \sigma_X^1 \, v_{\rm rel}^2 \,, \tag{C.1}$$

where $v_{\rm rel}$ is the relative velocity of the DM pair and the coefficient σ_X^0 (σ_X^1) describes the s-wave (p-wave) contribution.

In the alignment limit, the possible DM annihilation channels involving a pseudoscalar a are $\chi\bar{\chi} \to a \to f\bar{f}$, $\chi\bar{\chi} \to a \to ZH$, $\chi\bar{\chi} \to a \to ah$ and $\chi\bar{\chi} \to a \to aH$ for what concerns s-channel processes and $\chi\bar{\chi} \to aa$ with DM exchange in the t-channel (cf. also [219]). The annihilation cross sections (C.1) of the former two reactions are, however, proportional to $\sin^2\theta$, rendering them numerically irrelevant in the limit $\sin\theta \to 0$ unless $m_a = m_\chi/2$. Such highly tuned solutions to the DM miracle will not be considered in what follows. Similarly, all DM annihilation contributions involving the exchange of a heavy pseudoscalar A are suppressed by at least two powers of the sine of the mixing angle θ, so that only the processes depicted in Figure C.1 are relevant for the calculation of the DM abundance in the context of this work.

The annihilation process $\chi\bar{\chi} \to a \to ah$ proceeds via s-wave and we find for the corresponding coefficient the following analytic result

$$\sigma_{ah}^0 = \frac{y_\chi^2 \, g_{haa}^2 \cos^2\theta}{32\pi} \sqrt{1-\frac{\left(m_h+m_a\right)^2}{4m_\chi^2}} \sqrt{1-\frac{\left(m_h-m_a\right)^2}{4m_\chi^2}} \, \frac{v^2}{\left(m_a^2-4m_\chi^2\right)^2+m_a^2\Gamma_a^2} \,, \tag{C.2}$$

where the expression for g_{haa} in the limit $\sin\theta \to 0$ can be found in the first line of (7.5) and Γ_a denotes the total decay width of the pseudoscalar a. Since $\sigma_{ah}^0 \neq 0$, we ignore the p-wave coefficient σ_{ah}^1 below by setting it to zero. The result for the s-wave coefficient σ_{aH}^0 describing DM annihilation through $\chi\bar{\chi} \to a \to aH$ is simply obtained from (C.2) by the replacements $g_{haa} \to g_{Haa}$ and $m_h \to m_H$.

In the case of $\chi\bar{\chi} \to aa$, the annihilation cross section is instead p-wave suppressed (see [274] for the calculation of the t-channel contribution in the simplified pseudoscalar DM model) and the corresponding expansion coefficients take the form $\sigma_{aa}^0 = 0$ and

$$\sigma_{aa}^1 = \frac{y_\chi^4 \cos^4\theta}{24\pi} \sqrt{1-\frac{m_a^2}{m_\chi^2}} \, \frac{m_\chi^2 \left(m_a^2-m_\chi^2\right)^2}{\left(m_a^2-2m_\chi^2\right)^4} \,. \tag{C.3}$$

Using the velocity expansion (C.1), the DM relic density after freeze-out can be approximated by

$$\frac{\Omega h^2}{0.12} \simeq \frac{1.6\cdot 10^{-10}\,\text{GeV}^{-2}\, x_f}{\langle\sigma v_{\rm rel}\rangle_f} \,, \qquad \langle\sigma v_{\rm rel}\rangle_f = \sum_X \left(\sigma_X^0 + \frac{3\sigma_X^1}{x_f}\right) \,. \tag{C.4}$$

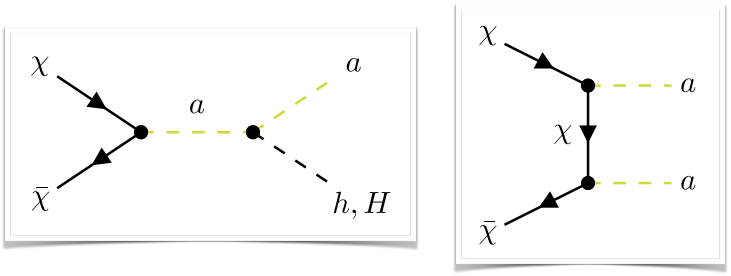

Figure C.1: Feynman diagrams that lead to DM annihilation via $\chi\bar{\chi} \to ah$ or $\chi\bar{\chi} \to aH$ (left) and $\chi\bar{\chi} \to aa$ in the 2HDM+a model. The possible decay modes of the pseudoscalar a, the SM-like Higgs h and the heavy $\mathcal{CP}$-even Higgs H are not shown. Further details are given in the main text.

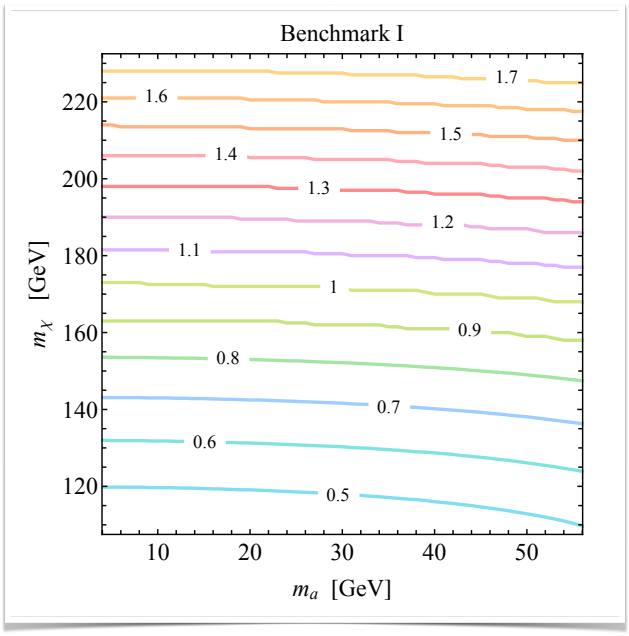

Figure C.2: Predicted DM relic abundance in the m_a–m_χ plane for the 2HDM+a benchmark I parameter choices (7.12). The contour lines indicated the value of $\Omega h^2/0.12$, meaning that the regions below (above) 1 correspond to a DM underabundance (overabundance) in today's Universe. For additional details we refer the interested reader to the main text.

Here $x_f = m_\chi/T_f \in [20, 30]$ with T_f the freeze-out temperature, and the sum over X in principle includes all possible final states. As we have explained above, for $\sin\theta \simeq 0$ and away from the exceptional points $m_a = m_\chi/2$, however, only the channels $X = ah, aH, aa$ are numerically important. In the limit of heavy DM, i.e. $m_\chi \gg m_a, m_h, m_H$, the velocity-averaged annihilation cross section at the freeze-out temperature can be further simplified:

$$\langle \sigma v_{\text{rel}} \rangle_f \simeq \frac{y_\chi^2}{128\pi m_\chi^2} \left[\frac{\left(g_{haa}^2 + g_{Haa}^2\right) v^2}{4m_\chi^2} + \frac{y_\chi^2}{x_f} \right] . \tag{C.5}$$

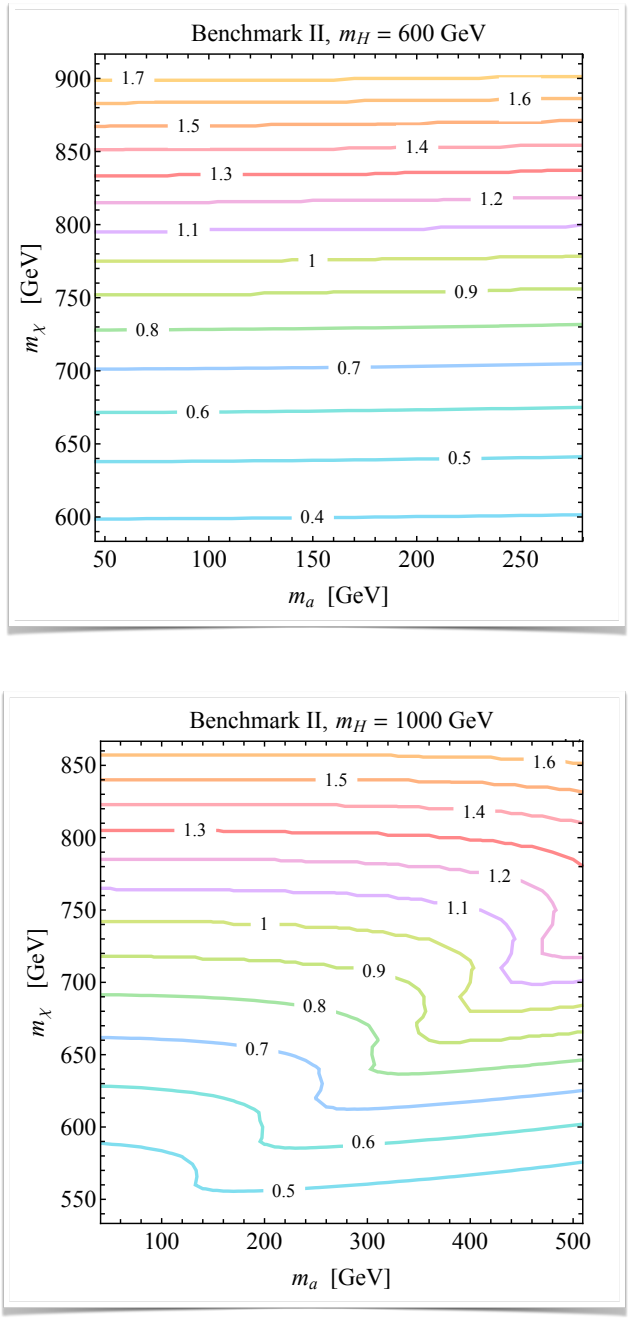

Figure C.3: As Figure C.2, but for the 2HDM+a benchmark II scenario with masses $m_H = 600\,\text{GeV}$ (upper panel) and $m_H = 1000\,\text{GeV}$ (lower panel), respectively. Additional details can again be found in the main text.

This approximation shows that the s-channel (t-channel) contributions to $\langle \sigma v_{\text{rel}} \rangle_f$ scale as $1/m_\chi^4$ $(1/m_\chi^2)$ in the limit of infinitely heavy DM.

The formulas (C.4) and (C.5) represent useful expressions to estimate Ωh^2. In the case of the benchmark I scenario (7.12) one has $g_{haa}^2 \simeq 6 \cdot 10^{-5}$ and $g_{Haa}^2 = 0$, and it is thus a good approximation to neglect the s-channel contributions to $\langle \sigma v_{\rm rel} \rangle_f$. It follows that

$$\frac{\Omega h^2}{0.12} \simeq \frac{0.9}{y_\chi^4} \left(\frac{x_f}{25}\right)^2 \left(\frac{m_\chi}{150\,\text{GeV}}\right)^2 . \tag{C.6}$$

Using $x_f \simeq 25$, the relic abundance of $\Omega h^2 = 0.120 \pm 0.001$, as determined by Planck [275], is therefore obtained in the case of (7.12) for DM masses $m_\chi \simeq 160\,\text{GeV}$ while for parameter regions with $m_\chi \lesssim 160\,\text{GeV}$ ($m_\chi \gtrsim 160\,\text{GeV}$) one expects DM underabundance (overabundance). These expectations agree quite well with the results of our exact relic calculation that have been obtained with `MadDM` [276] and are shown in Figure C.2. In fact, the exact computation for (7.12) and $m_a = 30\,\text{GeV}$ leads to $\Omega h^2 = 0.118$, while (C.6) naively predicts a value that is larger by around 15%. The observed difference can be traced back to the fact that the `MadDM` calculation gives $x_f \simeq 21$ in the parameter region of interest and correctly takes into account the phase-space suppression present in (C.3) due to the non-zero values of m_a^2/m_χ^2. We add that $\chi\bar{\chi} \to a \to ah$ annihilation represents a relative contribution to Ωh^2 of less than about 1% in the part of the m_a–m_χ plane that is depicted in the figure. Neglecting the s-channel contributions in the approximation (C.6) is hence fully justified.

In the case of our 2HDM+a benchmark II parameter scenario (7.17), the coupling g_{haa} is no longer small, in fact $g_{haa}^2 \simeq 35$ and we furthermore have $g_{Haa}^2 \neq 0$. On the other hand, $y_\chi^2/x_f \simeq 0.04$ and thus one can neglect the $\chi\bar{\chi} \to aa$ contribution to the velocity-averaged annihilation cross section at the freeze-out temperature (C.5) to first approximation. Doing this, one obtains the following simple expression

$$\frac{\Omega h^2}{0.12} \simeq \frac{43}{y_\chi^2 \left(g_{haa}^2 + g_{Haa}^2\right)} \frac{x_f}{25} \left(\frac{m_\chi}{800\,\text{GeV}}\right)^4 , \tag{C.7}$$

which approximately describes the resulting DM relic abundance for parameter choices à la benchmark II. From (C.7), one hence expects that the correct value of Ωh^2 is realized in the case of (7.17) for $m_\chi \simeq 770\,\text{GeV}$, while for smaller (larger) DM masses one should have $\Omega h^2 \gtrsim 0.12$ $\left(\Omega h^2 \lesssim 0.12\right)$ if $m_H = 600\,\text{GeV}$ which implies $g_{Haa}^2 \simeq 1.5$. The results of the corresponding `MadDM` computation is displayed in the upper panel of Figure C.3. We find that for the parameters (7.17) together with $m_a = 150\,\text{GeV}$ as well as $m_H = 600\,\text{GeV}$, the exact calculation predicts $\Omega h^2 = 0.117$, a value less than 5% below the naive expectation. Numerically, we furthermore obtain that the relative contribution of $\chi\bar{\chi} \to aa$ to the DM relic density is always below 1% in benchmark II with $m_H = 600\,\text{GeV}$, showing that it can be safely neglected in the derivation of (C.7).

The result of our `MadDM` scan in the 2HDM+a benchmark II parameter scenario with $m_H = 1000\,\text{GeV}$ is presented in the lower panel of Figure C.3. It is evident from the plot that in this case the above simplistic formula is not able to capture the more intricate behaviour of the contours of constant relic density. In fact, this is not a big surprise because in the derivation of (C.7) we have assumed that $m_\chi \gg m_a, m_h, m_H$, however, one has $m_\chi < m_H$ in the entire m_a–m_χ plane considered. Still, the values $m_\chi \in [680, 740]\,\text{GeV}$ of the DM mass that lead to the correct DM abundance for

$m_a \in [50, 500]$ GeV are only less than 10% smaller than what one would expect from (C.7). As previously, it turns out that the relative contribution of s-channel annihilation amounts to more than 99% of the predicted values of Ωh^2. This shows again that DM annihilation via $\chi\bar{\chi} \to aa$ is phenomenologically not relevant in 2HDM+a realizations of the type (7.17).

Before concluding, we add that DM direct detection experiments do not set relevant constraints on the 2HDM+a benchmarks (7.12) and (7.17) for the mixing angles $\theta \simeq 0$ necessary to have a long-lived a. This is a simple consequence of the fact that the SI DM-nucleon cross section is suppressed by both a loop factor and two powers of $\sin\theta$ – see the recent articles [218, 232, 277–279] for explicit formulas and further explanations.

BIBLIOGRAPHY

[1] O. Bruning, H. Burkhardt, and S. Myers. "The Large Hadron Collider." In: *Prog. Part. Nucl. Phys.* 67 (2012), pp. 705–734. DOI: 10.1016/j.ppnp.2012.03.001.

[2] Wesley H. Smith. "Triggering at the LHC." In: *Ann. Rev. Nucl. Part. Sci.* 66 (2016), pp. 123–141. DOI: 10.1146/annurev-nucl-102115-044713.

[3] F. Englert and R. Brout. "Broken Symmetry and the Mass of Gauge Vector Mesons." In: *Phys. Rev. Lett.* 13 (1964). Ed. by J. C. Taylor, pp. 321–323. DOI: 10.1103/PhysRevLett.13.321.

[4] Peter W. Higgs. "Broken Symmetries and the Masses of Gauge Bosons." In: *Phys. Rev. Lett.* 13 (1964). Ed. by J. C. Taylor, pp. 508–509. DOI: 10.1103/PhysRevLett.13.508.

[5] G. S. Guralnik, C. R. Hagen, and T. W. B. Kibble. "Global Conservation Laws and Massless Particles." In: *Phys. Rev. Lett.* 13 (1964). Ed. by J. C. Taylor, pp. 585–587. DOI: 10.1103/PhysRevLett.13.585.

[6] J. Goldstone. "Field Theories with Superconductor Solutions." In: *Nuovo Cim.* 19 (1961), pp. 154–164. DOI: 10.1007/BF02812722.

[7] Steven Weinberg. "The Making of the standard model." In: *Eur. Phys. J. C* 34 (2004). Ed. by G. 't Hooft, pp. 5–13. DOI: 10.1140/epjc/s2004-01761-1. arXiv: hep-ph/0401010.

[8] S. L. Glashow. "Partial Symmetries of Weak Interactions." In: *Nucl. Phys.* 22 (1961), pp. 579–588. DOI: 10.1016/0029-5582(61)90469-2.

[9] Abdus Salam and John Clive Ward. "Electromagnetic and weak interactions." In: *Phys. Lett.* 13 (1964), pp. 168–171. DOI: 10.1016/0031-9163(64)90711-5.

[10] Steven Weinberg. "A Model of Leptons." In: *Phys. Rev. Lett.* 19 (1967), pp. 1264–1266. DOI: 10.1103/PhysRevLett.19.1264.

[11] D. Abbaneo et al. "A Combination of preliminary electroweak measurements and constraints on the standard model." Dec. 1997.

[12] M. Spira and Peter M. Zerwas. "Electroweak symmetry breaking and Higgs physics." In: *Lect. Notes Phys.* 512 (1998). Ed. by H. Gausterer and C. B. Lang, pp. 161–225. DOI: 10.1007/BFb0106895. arXiv: hep-ph/9803257.

[13] J R Andersen et al. "Handbook of LHC Higgs Cross Sections: 3. Higgs Properties." In: *CERN-2013-004* (July 2013). Ed. by S Heinemeyer, C Mariotti, G Passarino, and R Tanaka. DOI: 10.5170/CERN-2013-004. arXiv: 1307.1347 [hep-ph].

[14] *The High-Luminosity LHC (HL-LHC) Project*. https://cds.cern.ch/record/2199189/files/English.pdf. Accessed: 2024-01-30. 2016.

[15] Patrick J. Fox, Ian Low, and Yue Zhang. "Top-philic Z' forces at the LHC." In: *JHEP* 03 (2018), p. 074. DOI: 10.1007/JHEP03(2018)074. arXiv: 1801.03505 [hep-ph].

[16] *Longer Term LHC Schedule*. https://lhc-commissioning.web.cern.ch/schedule/LHC-long-term.htm. Accessed: 2023-07-03. 2022.

[17] Stefan Höche. "Introduction to parton-shower event generators." In: *Theoretical Advanced Study Institute in Elementary Particle Physics: Journeys Through the Precision Frontier: Amplitudes for Colliders*. 2015, pp. 235–295. DOI: 10.1142/9789814678766_0005. arXiv: 1411.4085 [hep-ph].

[18] Stefano Frixione, Paolo Nason, and Carlo Oleari. "Matching NLO QCD computations with Parton Shower simulations: the POWHEG method." In: *JHEP* 11 (2007), p. 070. DOI: 10.1088/1126-6708/2007/11/070. arXiv: 0709.2092 [hep-ph].

[19] John C. Collins, Davison E. Soper, and George F. Sterman. "Factorization for Short Distance Hadron - Hadron Scattering." In: *Nucl. Phys. B* 261 (1985), pp. 104–142. DOI: 10.1016/0550-3213(85)90565-6.

[20] Hiren H. Patel. "Package-X 2.0: A Mathematica package for the analytic calculation of one-loop integrals." In: *Comput. Phys. Commun.* 218 (2017), pp. 66–70. DOI: 10.1016/j.cpc.2017.04.015. arXiv: 1612.00009 [hep-ph].

[21] Simone Alioli, Paolo Nason, Carlo Oleari, and Emanuele Re. "A general framework for implementing NLO calculations in shower Monte Carlo programs: the POWHEG BOX." In: *JHEP* 06 (2010), p. 043. DOI: 10.1007/JHEP06(2010)043. arXiv: 1002.2581 [hep-ph].

[22] William A. Bardeen, A. J. Buras, D. W. Duke, and T. Muta. "Deep Inelastic Scattering Beyond the Leading Order in Asymptotically Free Gauge Theories." In: *Phys. Rev. D* 18 (1978), p. 3998. DOI: 10.1103/PhysRevD.18.3998.

[23] T. Gehrmann, E. W. N. Glover, T. Huber, N. Ikizlerli, and C. Studerus. "Calculation of the quark and gluon form factors to three loops in QCD." In: *JHEP* 06 (2010), p. 094. DOI: 10.1007/JHEP06(2010)094. arXiv: 1004.3653 [hep-ph].

[24] Andrzej J. Buras. "Weak Hamiltonian, CP violation and rare decays." In: *Les Houches Summer School in Theoretical Physics, Session 68: Probing the Standard Model of Particle Interactions*. June 1998, pp. 281–539. arXiv: hep-ph/9806471.

[25] T. Kinoshita. "Mass singularities of Feynman amplitudes." In: *J. Math. Phys.* 3 (1962), pp. 650–677. DOI: 10.1063/1.1724268.

[26] T. D. Lee and M. Nauenberg. "Degenerate Systems and Mass Singularities." In: *Phys. Rev.* 133 (1964). Ed. by G. Feinberg, B1549–B1562. DOI: 10.1103/PhysRev.133.B1549.

[27] S. Frixione, Z. Kunszt, and A. Signer. "Three jet cross-sections to next-to-leading order." In: *Nucl. Phys. B* 467 (1996), pp. 399–442. DOI: 10.1016/0550-3213(96)00110-1. arXiv: hep-ph/9512328.

[28] S. Frixione. "A General approach to jet cross-sections in QCD." In: *Nucl. Phys. B* 507 (1997), pp. 295–314. DOI: 10.1016/S0550-3213(97)00574-9. arXiv: hep-ph/9706545.

[29] S. Catani and M. H. Seymour. "A General algorithm for calculating jet cross-sections in NLO QCD." In: *Nucl. Phys. B* 485 (1997). [Erratum: Nucl.Phys.B 510, 503–504 (1998)], pp. 291–419. DOI: 10.1016/S0550-3213(96)00589-5. arXiv: hep-ph/9605323.

[30] Richard D. Ball et al. "The path to proton structure at 1% accuracy." In: *Eur. Phys. J. C* 82.5 (2022), p. 428. DOI: 10.1140/epjc/s10052-022-10328-7. arXiv: 2109.02653 [hep-ph].

[31] D. B. Clark, E. Godat, and F. I. Olness. "ManeParse : A Mathematica reader for Parton Distribution Functions." In: *Comput. Phys. Commun.* 216 (2017), pp. 126–137. DOI: 10.1016/j.cpc.2017.03.004. arXiv: 1605.08012 [hep-ph].

[32] Torbjorn Sjostrand, Stephen Mrenna, and Peter Z. Skands. "PYTHIA 6.4 Physics and Manual." In: *JHEP* 05 (2006), p. 026. DOI: 10.1088/1126-6708/2006/05/026. arXiv: hep-ph/0603175.

[33] Torbjörn Sjöstrand, Stefan Ask, Jesper R. Christiansen, Richard Corke, Nishita Desai, Philip Ilten, Stephen Mrenna, Stefan Prestel, Christine O. Rasmussen, and Peter Z. Skands. "An introduction to PYTHIA 8.2." In: *Comput. Phys. Commun.* 191 (2015), pp. 159–177. DOI: 10.1016/j.cpc.2015.01.024. arXiv: 1410.3012 [hep-ph].

[34] G. Corcella, I. G. Knowles, G. Marchesini, S. Moretti, K. Odagiri, P. Richardson, M. H. Seymour, and B. R. Webber. "HERWIG 6: An Event generator for hadron emission reactions with interfering gluons (including supersymmetric processes)." In: *JHEP* 01 (2001), p. 010. DOI: 10.1088/1126-6708/2001/01/010. arXiv: hep-ph/0011363.

[35] Johannes Bellm et al. "Herwig 7.0/Herwig++ 3.0 release note." In: *Eur. Phys. J. C* 76.4 (2016), p. 196. DOI: 10.1140/epjc/s10052-016-4018-8. arXiv: 1512.01178 [hep-ph].

[36] T. Gleisberg, Stefan. Hoeche, F. Krauss, M. Schonherr, S. Schumann, F. Siegert, and J. Winter. "Event generation with SHERPA 1.1." In: *JHEP* 02 (2009), p. 007. DOI: 10.1088/1126-6708/2009/02/007. arXiv: 0811.4622 [hep-ph].

[37] Enrico Bothmann et al. "Event Generation with Sherpa 2.2." In: *SciPost Phys.* 7.3 (2019), p. 034. DOI: 10.21468/SciPostPhys.7.3.034. arXiv: 1905.09127 [hep-ph].

[38] Eric Laenen. "Resummation for observables at TeV colliders." In: *Pramana* 63 (2004), pp. 1225–1249. DOI: 10.1007/BF02704892.

[39] Andy Buckley and Debottam Bakshi Gupta. "Powheg-Pythia matching scheme effects in NLO simulation of dijet events." In: *MCNET-16-34* (Aug. 2016). arXiv: 1608.03577 [hep-ph].

[40] Stefano Frixione and Bryan R. Webber. "Matching NLO QCD computations and parton shower simulations." In: *JHEP* 06 (2002), p. 029. DOI: 10.1088/1126-6708/2002/06/029. arXiv: hep-ph/0204244.

[41] The Institute of Art and Ideas. *The future of particle physics*. https://www.youtube.com/watch?v=nF-xWJT4UuE. Accessed: 2024-04-30.

[42] Gino Isidori, Felix Wilsch, and Daniel Wyler. "The standard model effective field theory at work." In: *Rev. Mod. Phys.* 96.1 (2024), p. 015006. DOI: 10.1103/RevModPhys.96.015006. arXiv: 2303.16922 [hep-ph].

[43] Elizabeth E. Jenkins, Aneesh V. Manohar, and Michael Trott. "Renormalization Group Evolution of the Standard Model Dimension Six Operators I: Formalism and lambda Dependence." In: *JHEP* 10 (2013), p. 087. DOI: 10.1007/JHEP10(2013)087. arXiv: 1308.2627 [hep-ph].

[44] Wouter Dekens and Peter Stoffer. "Low-energy effective field theory below the electroweak scale: matching at one loop." In: *JHEP* 10 (2019). [Erratum: JHEP 11, 148 (2022)], p. 197. DOI: 10.1007/JHEP10(2019)197. arXiv: 1908.05295 [hep-ph].

[45] Céline Degrande, Gauthier Durieux, Fabio Maltoni, Ken Mimasu, Eleni Vryonidou, and Cen Zhang. "Automated one-loop computations in the standard model effective field theory." In: *Phys. Rev. D* 103.9 (2021), p. 096024. DOI: 10.1103/PhysRevD.103.096024. arXiv: 2008.11743 [hep-ph].

[46] B. Grzadkowski, M. Iskrzynski, M. Misiak, and J. Rosiek. "Dimension-Six Terms in the Standard Model Lagrangian." In: *JHEP* 10 (2010), p. 085. DOI: 10.1007/JHEP10(2010)085. arXiv: 1008.4884 [hep-ph].

[47] D. Barducci et al. "Interpreting top-quark LHC measurements in the standard-model effective field theory." In: *CERN-LPCC-2018-01* (Feb. 2018). Ed. by Juan Antonio Aguilar-Saavedra, C. Degrande, G. Durieux, F. Maltoni, E. Vryonidou, and C. Zhang. arXiv: 1802.07237 [hep-ph].

[48] Elizabeth E. Jenkins, Aneesh V. Manohar, and Michael Trott. "Renormalization Group Evolution of the Standard Model Dimension Six Operators II: Yukawa Dependence." In: *JHEP* 01 (2014), p. 035. DOI: 10.1007/JHEP01(2014)035. arXiv: 1310.4838 [hep-ph].

[49] Rodrigo Alonso, Elizabeth E. Jenkins, Aneesh V. Manohar, and Michael Trott. "Renormalization Group Evolution of the Standard Model Dimension Six Operators III: Gauge Coupling Dependence and Phenomenology." In: *JHEP* 04 (2014), p. 159. DOI: 10.1007/JHEP04(2014)159. arXiv: 1312.2014 [hep-ph].

[50] Alejandro Celis, Javier Fuentes-Martin, Avelino Vicente, and Javier Virto. "DsixTools: The Standard Model Effective Field Theory Toolkit." In: *Eur. Phys. J. C* 77.6 (2017), p. 405. DOI: 10.1140/epjc/s10052-017-4967-6. arXiv: 1704.04504 [hep-ph].

[51] Jason Aebischer, Jacky Kumar, Peter Stangl, and David M. Straub. "A Global Likelihood for Precision Constraints and Flavour Anomalies." In: *Eur. Phys. J. C* 79.6 (2019), p. 509. DOI: 10.1140/epjc/s10052-019-6977-z. arXiv: 1810.07698 [hep-ph].

[52] David M. Straub. "flavio: a Python package for flavour and precision phenomenology in the Standard Model and beyond." In: (Oct. 2018). arXiv: 1810.08132 [hep-ph].

[53] Jason Aebischer, Jacky Kumar, and David M. Straub. "Wilson: a Python package for the running and matching of Wilson coefficients above and below the electroweak scale." In: *Eur. Phys. J. C* 78.12 (2018), p. 1026. DOI: 10.1140/epjc/s10052-018-6492-7. arXiv: 1804.05033 [hep-ph].

[54] Peter Stangl. "smelli – the SMEFT Likelihood." In: *PoS* TOOLS2020 (2021), p. 035. DOI: 10.22323/1.392.0035. arXiv: 2012.12211 [hep-ph].

[55] Javier Fuentes-Martin, Pedro Ruiz-Femenia, Avelino Vicente, and Javier Virto. "DsixTools 2.0: The Effective Field Theory Toolkit." In: *Eur. Phys. J. C* 81.2 (2021), p. 167. DOI: 10.1140/epjc/s10052-020-08778-y. arXiv: 2010.16341 [hep-ph].

[56] Stefano Di Noi and Luca Silvestrini. "RGESolver: a C++ library to perform renormalization group evolution in the Standard Model Effective Theory." In: *Eur. Phys. J. C* 83.3 (2023), p. 200. DOI: 10.1140/epjc/s10052-023-11189-4. arXiv: 2210.06838 [hep-ph].

[57] Gino Isidori. "Flavor physics beyond the Standard Model and the Kobayashi-Maskawa legacy." In: Aug. 2023. arXiv: 2308.11612 [hep-ph].

[58] Joe Davighi and Gino Isidori. "Non-universal gauge interactions addressing the inescapable link between Higgs and flavour." In: *JHEP* 07 (2023), p. 147. DOI: 10.1007/JHEP07(2023)147. arXiv: 2303.01520 [hep-ph].

[59] R. Aaij et al. "Measurement of lepton universality parameters in $B^+ \to K^+\ell^+\ell^-$ and $B^0 \to K^{*0}\ell^+\ell^-$ decays." In: *Phys. Rev. D* 108.3 (2023), p. 032002. DOI: 10.1103/PhysRevD.108.032002. arXiv: 2212.09153 [hep-ex].

[60] Admir Greljo, Jakub Salko, Aleks Smolkovič, and Peter Stangl. "Rare b decays meet high-mass Drell-Yan." In: *JHEP* 05 (2023), p. 087. DOI: 10.1007/JHEP05(2023)087. arXiv: 2212.10497 [hep-ph].

[61] Javier Fuentes-Martín, Gino Isidori, Matthias König, and Nudžeim Selimović. "Vector leptoquarks beyond tree level. II. $\mathcal{O}(\alpha_s)$ corrections and radial modes." In: *Phys. Rev. D* 102.3 (2020), p. 035021. DOI: 10.1103/PhysRevD.102.035021. arXiv: 2006.16250 [hep-ph].

[62] Charalampos Anastasiou, Kirill Melnikov, and Frank Petriello. "A new method for real radiation at NNLO." In: *Phys. Rev. D* 69 (2004), p. 076010. DOI: 10.1103/PhysRevD.69.076010. arXiv: hep-ph/0311311.

[63] Javier Fuentes-Martín, Gino Isidori, Matthias König, and Nudžeim Selimović. "Vector Leptoquarks Beyond Tree Level." In: *Phys. Rev. D* 101.3 (2020), p. 035024. DOI: 10.1103/PhysRevD.101.035024. arXiv: 1910.13474 [hep-ph].

[64] R. L. Workman et al. "Review of Particle Physics." In: *PTEP* 2022 (2022), p. 083C01. DOI: 10.1093/ptep/ptac097.

[65] Michael E. Peskin and Daniel V. Schroeder. *An Introduction to quantum field theory*. Reading, USA: Addison-Wesley, 1995. ISBN: 978-0-201-50397-5.

[66] "A combination of measurements of Higgs boson production and decay using up to 139 fb^{-1} of proton–proton collision data at $\sqrt{s} = 13$ TeV collected with the ATLAS experiment." In: *ATLAS-CONF-2020-027* (Aug. 2020).

[67] Lei Wang, Jin Min Yang, and Yang Zhang. "Two-Higgs-doublet models in light of current experiments: a brief review." In: *Commun. Theor. Phys.* 74.9 (2022), p. 097202. DOI: 10.1088/1572-9494/ac7fe9. arXiv: 2203.07244 [hep-ph].

[68] G. C. Branco, P. M. Ferreira, L. Lavoura, M. N. Rebelo, Marc Sher, and Joao P. Silva. "Theory and phenomenology of two-Higgs-doublet models." In: *Phys. Rept.* 516 (2012), pp. 1–102. DOI: 10.1016/j.physrep.2012.02.002. arXiv: 1106.0034 [hep-ph].

[69] Martin Bauer, Ulrich Haisch, and Felix Kahlhoefer. "Simplified dark matter models with two Higgs doublets: I. Pseudoscalar mediators." In: *JHEP* 05 (2017), p. 138. DOI: 10.1007/JHEP05(2017)138. arXiv: 1701.07427 [hep-ph].

[70] G. Belanger, F. Boudjema, A. Pukhov, and A. Semenov. "Dark matter direct detection rate in a generic model with micrOMEGAs 2.2." In: *Comput. Phys. Commun.* 180 (2009), pp. 747–767. DOI: 10.1016/j.cpc.2008.11.019. arXiv: 0803.2360 [hep-ph].

[71] A. G. Grozin. "Integration by parts: An Introduction." In: *Int. J. Mod. Phys. A* 26 (2011), pp. 2807–2854. DOI: 10.1142/S0217751X11053687. arXiv: 1104.3993 [hep-ph].

[72] Vladyslav Shtabovenko, Rolf Mertig, and Frederik Orellana. "FeynCalc 10: Do multiloop integrals dream of computer codes?" In: – (Dec. 2023). arXiv: 2312.14089 [hep-ph].

[73] Vladyslav Shtabovenko, Rolf Mertig, and Frederik Orellana. "FeynCalc 9.3: New features and improvements." In: *Comput. Phys. Commun.* 256 (2020), p. 107478. DOI: 10.1016/j.cpc.2020.107478. arXiv: 2001.04407 [hep-ph].

[74] Vladyslav Shtabovenko, Rolf Mertig, and Frederik Orellana. "New Developments in FeynCalc 9.0." In: *Comput. Phys. Commun.* 207 (2016), pp. 432–444. DOI: 10.1016/j.cpc.2016.06.008. arXiv: 1601.01167 [hep-ph].

[75] R. Mertig, M. Bohm, and Ansgar Denner. "FEYN CALC: Computer algebraic calculation of Feynman amplitudes." In: *Comput. Phys. Commun.* 64 (1991), pp. 345–359. DOI: 10.1016/0010-4655(91)90130-D.

[76] Roman N. Lee. "LiteRed 1.4: a powerful tool for reduction of multiloop integrals." In: *J. Phys. Conf. Ser.* 523 (2014). Ed. by Jianxiong Wang, p. 012059. DOI: 10.1088/1742-6596/523/1/012059. arXiv: 1310.1145 [hep-ph].

[77] T. Gehrmann, T. Huber, and D. Maitre. "Two-loop quark and gluon form-factors in dimensional regularisation." In: *Phys. Lett. B* 622 (2005), pp. 295–302. DOI: 10.1016/j.physletb.2005.07.019. arXiv: hep-ph/0507061.

[78] J. Fleischer and O. V. Tarasov. "Calculation of Feynman diagrams from their small momentum expansion." In: *Z. Phys. C* 64 (1994), pp. 413–426. DOI: 10.1007/BF01560102. arXiv: hep-ph/9403230.

[79] O. V. Tarasov. "An Algorithm for small momentum expansion of Feynman diagrams." In: *4th International Workshop on Software Engineering and Artificial Intelligence for High-energy and Nuclear Physics*. Apr. 1995. arXiv: hep-ph/9505277.

[80] J. G. Korner, Z. Merebashvili, and M. Rogal. "Laurent series expansion of massive scalar one-loop integrals to $O(epsilson^{2})$." In: *Phys. Rev. D* 71 (2005), p. 054028. DOI: 10.1103/PhysRevD.71.054028. arXiv: hep-ph/0412088.

[81] Barak Kol. "Two-loop vacuum diagram through the Symmetries of Feynman Integrals method." In: – (July 2018). arXiv: 1807.07471 [hep-th].

[82] Lance J. Dixon. "Calculating scattering amplitudes efficiently." In: *Theoretical Advanced Study Institute in Elementary Particle Physics (TASI 95): QCD and Beyond*. Jan. 1996, pp. 539–584. arXiv: hep-ph/9601359.

[83] Keith Hamilton, Paolo Nason, and Giulia Zanderighi. "MINLO: Multi-Scale Improved NLO." In: *JHEP* 10 (2012), p. 155. DOI: 10.1007/JHEP10(2012)155. arXiv: 1206.3572 [hep-ph].

[84] S. Catani, F. Krauss, R. Kuhn, and B. R. Webber. "QCD matrix elements + parton showers." In: *JHEP* 11 (2001), p. 063. DOI: 10.1088/1126-6708/2001/11/063. arXiv: hep-ph/0109231.

[85] Keith Hamilton, Paolo Nason, Carlo Oleari, and Giulia Zanderighi. "Merging H/W/Z + 0 and 1 jet at NLO with no merging scale: a path to parton shower + NNLO matching." In: *JHEP* 05 (2013), p. 082. DOI: 10.1007/JHEP05(2013)082. arXiv: 1212.4504 [hep-ph].

[86] Pier Francesco Monni, Paolo Nason, Emanuele Re, Marius Wiesemann, and Giulia Zanderighi. "MiNNLO$_{PS}$: a new method to match NNLO QCD to parton showers." In: *JHEP* 05 (2020). [Erratum: JHEP 02, 031 (2022)], p. 143. DOI: 10.1007/JHEP05(2020)143. arXiv: 1908.06987 [hep-ph].

[87] Pier Francesco Monni, Emanuele Re, and Marius Wiesemann. "MiNNLO$_{\text{PS}}$: optimizing $2 \to 1$ hadronic processes." In: *Eur. Phys. J. C* 80.11 (2020), p. 1075. DOI: 10.1140/epjc/s10052-020-08658-5. arXiv: 2006.04133 [hep-ph].

[88] Simone Alioli, Christian W. Bauer, Calvin Berggren, Frank J. Tackmann, Jonathan R. Walsh, and Saba Zuberi. "Matching Fully Differential NNLO Calculations and Parton Showers." In: *JHEP* 06 (2014), p. 089. DOI: 10.1007/JHEP06(2014)089. arXiv: 1311.0286 [hep-ph].

[89] Simone Alioli, Christian W. Bauer, Calvin J. Berggren, Andrew Hornig, Frank J. Tackmann, Christopher K. Vermilion, Jonathan R. Walsh, and Saba Zuberi. "Combining Higher-Order Resummation with Multiple NLO Calculations and Parton Showers in GENEVA." In: *JHEP* 09 (2013), p. 120. DOI: 10.1007/JHEP09(2013)120. arXiv: 1211.7049 [hep-ph].

[90] Stefan Höche, Ye Li, and Stefan Prestel. "Drell-Yan lepton pair production at NNLO QCD with parton showers." In: *Phys. Rev. D* 91.7 (2015), p. 074015. DOI: 10.1103/PhysRevD.91.074015. arXiv: 1405.3607 [hep-ph].

[91] Stefan Höche, Ye Li, and Stefan Prestel. "Higgs-boson production through gluon fusion at NNLO QCD with parton showers." In: *Phys. Rev. D* 90.5 (2014), p. 054011. DOI: 10.1103/PhysRevD.90.054011. arXiv: 1407.3773 [hep-ph].

[LS1] Rhorry Gauld, Ulrich Haisch, and Luc Schnell. "SMEFT at NNLO+PS: Vh production." In: *JHEP* 01 (2024), p. 192. DOI: 10.1007/JHEP01(2024)192. arXiv: 2311.06107 [hep-ph].

[92] Morad Aaboud et al. "Observation of $H \to b\bar{b}$ decays and VH production with the ATLAS detector." In: *Phys. Lett. B* 786 (2018), pp. 59–86. DOI: 10.1016/j.physletb.2018.09.013. arXiv: 1808.08238 [hep-ex].

[93] A. M. Sirunyan et al. "Observation of Higgs boson decay to bottom quarks." In: *Phys. Rev. Lett.* 121.12 (2018), p. 121801. DOI: 10.1103/PhysRevLett.121.121801. arXiv: 1808.08242 [hep-ex].

[94] "Projections for measurements of Higgs boson cross sections, branching ratios, coupling parameters and mass with the ATLAS detector at the HL-LHC." In: *ATL-PHYS-PUB-2018-054* (2018).

[95] "Sensitivity projections for Higgs boson properties measurements at the HL-LHC." In: *CMS-PAS-FTR-18-011* (2018).

[96] W. Buchmuller and D. Wyler. "Effective Lagrangian Analysis of New Interactions and Flavor Conservation." In: *Nucl. Phys. B* 268 (1986), pp. 621–653. DOI: 10.1016/0550-3213(86)90262-2.

[97] Ilaria Brivio and Michael Trott. "The Standard Model as an Effective Field Theory." In: *Phys. Rept.* 793 (2019), pp. 1–98. DOI: 10.1016/j.physrep.2018.11.002. arXiv: 1706.08945 [hep-ph].

[98] Ken Mimasu, Veronica Sanz, and Ciaran Williams. "Higher Order QCD predictions for Associated Higgs production with anomalous couplings to gauge bosons." In: *JHEP* 08 (2016), p. 039. DOI: 10.1007/JHEP08(2016)039. arXiv: 1512.02572 [hep-ph].

[99] Celine Degrande, Benjamin Fuks, Kentarou Mawatari, Ken Mimasu, and Veronica Sanz. "Electroweak Higgs boson production in the standard model effective field theory beyond leading order in QCD." In: *Eur. Phys. J. C* 77.4 (2017), p. 262. DOI: 10.1140/epjc/s10052-017-4793-x. arXiv: 1609.04833 [hep-ph].

[100] Simone Alioli, Wouter Dekens, Michael Girard, and Emanuele Mereghetti. "NLO QCD corrections to SM-EFT dilepton and electroweak Higgs boson production, matched to parton shower in POWHEG." In: *JHEP* 08 (2018), p. 205. DOI: 10.1007/JHEP08(2018)205. arXiv: 1804.07407 [hep-ph].

[101] Fady Bishara, Philipp Englert, Christophe Grojean, Marc Montull, Giuliano Panico, and Alejo N. Rossia. "A New Precision Process at FCC-hh: the diphoton leptonic Wh channel." In: *JHEP* 07 (2020), p. 075. DOI: 10.1007/JHEP07(2020)075. arXiv: 2004.06122 [hep-ph].

[102] Fady Bishara, Stefania De Curtis, Luigi Delle Rose, Philipp Englert, Christophe Grojean, Marc Montull, Giuliano Panico, and Alejo N. Rossia. "Precision from the diphoton Zh channel at FCC-hh." In: *JHEP* 04 (2021), p. 154. DOI: 10.1007/JHEP04(2021)154. arXiv: 2011.13941 [hep-ph].

[103] Fady Bishara, Philipp Englert, Christophe Grojean, Giuliano Panico, and Alejo N. Rossia. "Revisiting Vh($\to b\bar{b}$) at the LHC and FCC-hh." In: *JHEP* 06 (2023), p. 077. DOI: 10.1007/JHEP06(2023)077. arXiv: 2208.11134 [hep-ph].

[104] Rhorry Gauld, Benjamin D. Pecjak, and Darren J. Scott. "One-loop corrections to $h \to b\bar{b}$ and $h \to \tau\bar{\tau}$ decays in the Standard Model Dimension-6 EFT: four-fermion operators and the large-m_t limit." In: *JHEP* 05 (2016), p. 080. DOI: 10.1007/JHEP05(2016)080. arXiv: 1512.02508 [hep-ph].

[105] Rhorry Gauld, Benjamin D. Pecjak, and Darren J. Scott. "QCD radiative corrections for $h \to b\bar{b}$ in the Standard Model Dimension-6 EFT." In: *Phys. Rev. D* 94.7 (2016), p. 074045. DOI: 10.1103/PhysRevD.94.074045. arXiv: 1607.06354 [hep-ph].

[106] Jonathan M. Cullen, Benjamin D. Pecjak, and Darren J. Scott. "NLO corrections to $h \to b\bar{b}$ decay in SMEFT." In: *JHEP* 08 (2019), p. 173. DOI: 10.1007/JHEP08(2019)173. arXiv: 1904.06358 [hep-ph].

[107] Jonathan M. Cullen and Benjamin D. Pecjak. "Higgs decay to fermion pairs at NLO in SMEFT." In: *JHEP* 11 (2020), p. 079. DOI: 10.1007/JHEP11(2020)079. arXiv: 2007.15238 [hep-ph].

[108] Ulrich Haisch, Darren J. Scott, Marius Wiesemann, Giulia Zanderighi, and Silvia Zanoli. "NNLO event generation for $pp \to Zh \to \ell^+\ell^- b\bar{b}$ production in the SM effective field theory." In: *JHEP* 07 (2022), p. 054. DOI: 10.1007/JHEP07(2022)054. arXiv: 2204.00663 [hep-ph].

[109] Fabio Maltoni, Kentarou Mawatari, and Marco Zaro. "Higgs characterisation via vector-boson fusion and associated production: NLO and parton-shower effects." In: *Eur. Phys. J. C* 74.1 (2014), p. 2710. DOI: 10.1140/epjc/s10052-013-2710-5. arXiv: 1311.1829 [hep-ph].

[110] Admir Greljo, Gino Isidori, Jonas M. Lindert, David Marzocca, and Hantian Zhang. "Electroweak Higgs production with HiggsPO at NLO QCD." In: *Eur. Phys. J. C* 77.12 (2017), p. 838. DOI: 10.1140/epjc/s10052-017-5422-4. arXiv: 1710.04143 [hep-ph].

[111] Wojciech Bizoń, Fabrizio Caola, Kirill Melnikov, and Raoul Röntsch. "Anomalous couplings in associated VH production with Higgs boson decay to massive b quarks at NNLO in QCD." In: *Phys. Rev. D* 105.1 (2022), p. 014023. DOI: 10.1103/PhysRevD.105.014023. arXiv: 2106.06328 [hep-ph].

[112] Imre Majer. "Associated Higgs Boson Production at NNLO QCD." PhD thesis. Zurich, ETH, 2020. DOI: 10.3929/ethz-b-000448848.

[113] G. Kramer and B. Lampe. "Two Jet Cross-Section in e+ e- Annihilation." In: *Z. Phys. C* 34 (1987). [Erratum: Z.Phys.C 42, 504 (1989)], p. 497. DOI: 10.1007/BF01679868.

[114] R. Hamberg, W. L. van Neerven, and T. Matsuura. "A complete calculation of the order $\alpha - s^2$ correction to the Drell-Yan K factor." In: *Nucl. Phys. B* 359 (1991). [Erratum: Nucl.Phys.B 644, 403–404 (2002)], pp. 343–405. DOI: 10.1016/0550-3213(91)90064-5.

[115] Thomas Gehrmann and Lorenzo Tancredi. "Two-loop QCD helicity amplitudes for $q\bar{q} \to W^{\pm}\gamma$ and $q\bar{q} \to Z^0\gamma$." In: *JHEP* 02 (2012), p. 004. DOI: 10.1007/JHEP02(2012)004. arXiv: 1112.1531 [hep-ph].

[116] John M. Campbell, R. Keith Ellis, and Ciaran Williams. "Associated production of a Higgs boson at NNLO." In: *JHEP* 06 (2016), p. 179. DOI: 10.1007/JHEP06(2016)179. arXiv: 1601.00658 [hep-ph].

[117] Oliver Brein, Robert Harlander, Marius Wiesemann, and Tom Zirke. "Top-Quark Mediated Effects in Hadronic Higgs-Strahlung." In: *Eur. Phys. J. C* 72 (2012), p. 1868. DOI: 10.1140/epjc/s10052-012-1868-6. arXiv: 1111.0761 [hep-ph].

[118] Silvia Zanoli, Mauro Chiesa, Emanuele Re, Marius Wiesemann, and Giulia Zanderighi. "Next-to-next-to-leading order event generation for VH production with H $\to b\bar{b}$ decay." In: *JHEP* 07 (2022), p. 008. DOI: 10.1007/JHEP07(2022)008. arXiv: 2112.04168 [hep-ph].

[119] D. Maitre and P. Mastrolia. "S@M, a Mathematica Implementation of the Spinor-Helicity Formalism." In: *Comput. Phys. Commun.* 179 (2008), pp. 501–574. DOI: 10.1016/j.cpc.2008.05.002. arXiv: 0710.5559 [hep-ph].

[120] Radja Boughezal, John M. Campbell, R. Keith Ellis, Christfried Focke, Walter Giele, Xiaohui Liu, Frank Petriello, and Ciaran Williams. "Color singlet production at NNLO in MCFM." In: *Eur. Phys. J. C* 77.1 (2017), p. 7. DOI: 10.1140/epjc/s10052-016-4558-y. arXiv: 1605.08011 [hep-ph].

[121] T. Hahn and M. Perez-Victoria. "Automatized one loop calculations in four-dimensions and D-dimensions." In: *Comput. Phys. Commun.* 118 (1999), pp. 153–165. DOI: 10.1016/S0010-4655(98)00173-8. arXiv: hep-ph/9807565.

[122] Thomas Hahn, Sebastian Paßehr, and Christian Schappacher. "FormCalc 9 and Extensions." In: *PoS* LL2016 (2016). Ed. by Luis Salinas and Claudio Torres, p. 068. DOI: 10.1088/1742-6596/762/1/012065. arXiv: 1604.04611 [hep-ph].

[123] Alejo Rossia, Marion Thomas, and Eleni Vryonidou. "Diboson production in the SMEFT from gluon fusion." In: *JHEP* 11 (2023), p. 132. DOI: 10.1007/JHEP11(2023)132. arXiv: 2306.09963 [hep-ph].

[124] Quentin Bonnefoy, Luca Di Luzio, Christophe Grojean, Ayan Paul, and Alejo N. Rossia. "Comments on gauge anomalies at dimension-six in the Standard Model Effective Field Theory." In: *JHEP* 05 (2021), p. 153. DOI: 10.1007/JHEP05(2021)153. arXiv: 2012.07740 [hep-ph].

[125] Ferruccio Feruglio. "A Note on Gauge Anomaly Cancellation in Effective Field Theories." In: *JHEP* 03 (2021), p. 128. DOI: 10.1007/JHEP03(2021)128. arXiv: 2012.13989 [hep-ph].

[126] Claudia Cornella, Ferruccio Feruglio, and Luca Vecchi. "Gauge invariance and finite counterterms in chiral gauge theories." In: *JHEP* 02 (2023), p. 244. DOI: 10.1007/JHEP02(2023)244. arXiv: 2205.10381 [hep-ph].

[127] Timothy Cohen, Xiaochuan Lu, and Zhengkang Zhang. "Anomaly cancellation in effective field theories from the covariant derivative expansion." In: *Phys. Rev. D* 108.5 (2023), p. 056027. DOI: 10.1103/PhysRevD.108.056027. arXiv: 2301.00827 [hep-ph].

[128] Timothy Cohen, Xiaochuan Lu, and Zhengkang Zhang. "Anomalies from the covariant derivative expansion." In: *Phys. Rev. D* 107.11 (2023), p. 116015. DOI: 10.1103/PhysRevD.107.116015. arXiv: 2301.00821 [hep-ph].

[129] J. Wess and B. Zumino. "Consequences of anomalous Ward identities." In: *Phys. Lett. B* 37 (1971), pp. 95–97. DOI: 10.1016/0370-2693(71)90582-X.

[130] Federico Buccioni, Jean-Nicolas Lang, Jonas M. Lindert, Philipp Maierhöfer, Stefano Pozzorini, Hantian Zhang, and Max F. Zoller. "OpenLoops 2." In: *Eur. Phys. J. C* 79.10 (2019), p. 866. DOI: 10.1140/epjc/s10052-019-7306-2. arXiv: 1907.13071 [hep-ph].

[131] J. Alwall, R. Frederix, S. Frixione, V. Hirschi, F. Maltoni, O. Mattelaer, H. S. Shao, T. Stelzer, P. Torrielli, and M. Zaro. "The automated computation of tree-level and next-to-leading order differential cross sections, and their matching to parton shower simulations." In: *JHEP* 07 (2014), p. 079. DOI: 10.1007/JHEP07(2014)079. arXiv: 1405.0301 [hep-ph].

[132] R. Gauld, U. Haisch, and L. Schnell. Vh Amplitudes. https://gitlab.com/lucschnell/vh-amplitudes. [Accessed: 2023-11-03].

[133] William Astill, Wojciech Bizoń, Emanuele Re, and Giulia Zanderighi. "NNLOPS accurate associated HZ production with $H \to b\bar{b}$ decay at NLO." In: *JHEP* 11 (2018), p. 157. DOI: 10.1007/JHEP11(2018)157. arXiv: 1804.08141 [hep-ph].

[134] Simone Alioli, Alessandro Broggio, Stefan Kallweit, Matthew A. Lim, and Luca Rottoli. "Higgsstrahlung at NNLL'+NNLO matched to parton showers in GENEVA." In: *Phys. Rev. D* 100.9 (2019), p. 096016. DOI: 10.1103/PhysRevD.100.096016. arXiv: 1909.02026 [hep-ph].

[135] Wojciech Bizoń, Emanuele Re, and Giulia Zanderighi. "NNLOPS description of the $H \to b\bar{b}$ decay with MiNLO." In: *JHEP* 06 (2020), p. 006. DOI: 10.1007/JHEP06(2020)006. arXiv: 1912.09982 [hep-ph].

[136] Paolo Nason. "A New method for combining NLO QCD with shower Monte Carlo algorithms." In: *JHEP* 11 (2004), p. 040. DOI: 10.1088/1126-6708/2004/11/040. arXiv: hep-ph/0409146.

[137] R. Gauld, A. Gehrmann-De Ridder, E. W. N. Glover, A. Huss, and I. Majer. "Associated production of a Higgs boson decaying into bottom quarks and a weak vector boson decaying leptonically at NNLO in QCD." In: *JHEP* 10 (2019), p. 002. DOI: 10.1007/JHEP10(2019)002. arXiv: 1907.05836 [hep-ph].

[138] Sally Dawson and Pier Paolo Giardino. "Electroweak and QCD corrections to Z and W pole observables in the standard model EFT." In: *Phys. Rev. D* 101.1 (2020), p. 013001. DOI: 10.1103/PhysRevD.101.013001. arXiv: 1909.02000 [hep-ph].

[139] Richard D. Ball et al. "Parton distributions from high-precision collider data." In: *Eur. Phys. J. C* 77.10 (2017), p. 663. DOI: 10.1140/epjc/s10052-017-5199-5. arXiv: 1706.00428 [hep-ph].

[140] Peter Skands, Stefano Carrazza, and Juan Rojo. "Tuning PYTHIA 8.1: the Monash 2013 Tune." In: *Eur. Phys. J. C* 74.8 (2014), p. 3024. DOI: 10.1140/epjc/s10052-014-3024-y. arXiv: 1404.5630 [hep-ph].

[141] Morad Aaboud et al. "Measurement of VH, $H \to b\bar{b}$ production as a function of the vector-boson transverse momentum in 13 TeV pp collisions with the ATLAS detector." In: *JHEP* 05 (2019), p. 141. DOI: 10.1007/JHEP05(2019)141. arXiv: 1903.04618 [hep-ex].

[142] Georges Aad et al. "Measurements of WH and ZH production in the $H \to b\bar{b}$ decay channel in pp collisions at 13 TeV with the ATLAS detector." In: *Eur. Phys. J. C* 81.2 (2021), p. 178. DOI: 10.1140/epjc/s10052-020-08677-2. arXiv: 2007.02873 [hep-ex].

[143] "Simplified template cross section measurements of Higgs boson produced in association with vector bosons in the $H \to b\bar{b}$ decay channel in proton-proton collisions at $\sqrt{s} = 13$ TeV." In: *CMS-PAS-HIG-20-001* (2022).

[144] *The POWHEG BOX*. Tech. rep. URL: http://powhegbox.mib.infn.it.

[145] J. R. Andersen et al. "Les Houches 2015: Physics at TeV Colliders Standard Model Working Group Report." In: *9th Les Houches Workshop on Physics at TeV Colliders*. May 2016. arXiv: 1605.04692 [hep-ph].

[146] Nicolas Berger et al. "Simplified Template Cross Sections - Stage 1.1." In: *LHCHXSWG-2019-003, DESY-19-070* (June 2019). arXiv: 1906.02754 [hep-ph].

[147] S. Amoroso et al. "Les Houches 2019: Physics at TeV Colliders: Standard Model Working Group Report." In: *11th Les Houches Workshop on Physics at TeV Colliders: PhysTeV Les Houches*. Mar. 2020. arXiv: 2003.01700 [hep-ph].

[148] APS News. *January 1976: From the Oops-Leon to the Upsilon Particle*. https://www.aps.org/publications/apsnews/202301/history.cfm. Accessed: 2024-05-30.

[LS3] Ulrich Haisch, Luc Schnell, and Stefan Schulte. "Drell-Yan production in third-generation gauge vector leptoquark models at NLO+PS in QCD." In: *JHEP* 02 (2023), p. 070. DOI: 10.1007/JHEP02(2023)070. arXiv: 2209.12780 [hep-ph].

[149] Nirmal Raj. "Anticipating nonresonant new physics in dilepton angular spectra at the LHC." In: *Phys. Rev. D* 95.1 (2017), p. 015011. DOI: 10.1103/PhysRevD.95.015011. arXiv: 1610.03795 [hep-ph].

[150] Admir Greljo and David Marzocca. "High-p_T dilepton tails and flavor physics." In: *Eur. Phys. J. C* 77.8 (2017), p. 548. DOI: 10.1140/epjc/s10052-017-5119-8. arXiv: 1704.09015 [hep-ph].

[151] B. C. Allanach, Ben Gripaios, and Tevong You. "The case for future hadron colliders from $B \to K^{(*)}\mu^+\mu^-$ decays." In: *JHEP* 03 (2018), p. 021. DOI: 10.1007/JHEP03(2018)021. arXiv: 1710.06363 [hep-ph].

[152] Ilja Doršner and Admir Greljo. "Leptoquark toolbox for precision collider studies." In: *JHEP* 05 (2018), p. 126. DOI: 10.1007/JHEP05(2018)126. arXiv: 1801.07641 [hep-ph].

[153] Yoav Afik, Jonathan Cohen, Eitan Gozani, Enrique Kajomovitz, and Yoram Rozen. "Establishing a Search for $b \to s\ell^+\ell^-$ Anomalies at the LHC." In: *JHEP* 08 (2018), p. 056. DOI: 10.1007/JHEP08(2018)056. arXiv: 1805.11402 [hep-ph].

[154] Saurabh Bansal, Rodolfo M. Capdevilla, Antonio Delgado, Christopher Kolda, Adam Martin, and Nirmal Raj. "Hunting leptoquarks in monolepton searches." In: *Phys. Rev. D* 98.1 (2018), p. 015037. DOI: 10.1103/PhysRevD.98.015037. arXiv: 1806.02370 [hep-ph].

[155] B. C. Allanach, Tyler Corbett, Matthew J. Dolan, and Tevong You. "Hadron collider sensitivity to fat flavourful Z′s for $R_{K^{(*)}}$." In: *JHEP* 03 (2019), p. 137. DOI: 10.1007/JHEP03(2019)137. arXiv: 1810.02166 [hep-ph].

[156] Tanumoy Mandal, Subhadip Mitra, and Swapnil Raz. "$R_{D^{(*)}}$ motivated $\mathcal{S}_1$ leptoquark scenarios: Impact of interference on the exclusion limits from LHC data." In: *Phys. Rev. D* 99.5 (2019), p. 055028. DOI: 10.1103/PhysRevD.99.055028. arXiv: 1811.03561 [hep-ph].

[157] Debajyoti Choudhury, Nilanjana Kumar, and Anirban Kundu. "Search for an opposite sign muon-tau pair and a b-jet at the LHC in the context of flavor anomalies." In: *Phys. Rev. D* 100.7 (2019), p. 075001. DOI: 10.1103/PhysRevD.100.075001. arXiv: 1905.07982 [hep-ph].

[158] Andrei Angelescu, Darius A. Faroughy, and Olcyr Sumensari. "Lepton Flavor Violation and Dilepton Tails at the LHC." In: *Eur. Phys. J. C* 80.7 (2020), p. 641. DOI: 10.1140/epjc/s10052-020-8210-5. arXiv: 2002.05684 [hep-ph].

[159] Andreas Crivellin, Claudio Andrea Manzari, and Marc Montull. "Correlating nonresonant di-electron searches at the LHC to the Cabibbo-angle anomaly and lepton flavor universality violation." In: *Phys. Rev. D* 104.11 (2021), p. 115016. DOI: 10.1103/PhysRevD.104.115016. arXiv: 2103.12003 [hep-ph].

[160] Andreas Crivellin, Dario Müller, and Luc Schnell. "Combined constraints on first generation leptoquarks." In: *Phys. Rev. D* 103.11 (2021). [Addendum: Phys.Rev.D 104, 055020 (2021)], p. 115023. DOI: 10.1103/PhysRevD.103.115023. arXiv: 2104.06417 [hep-ph].

[161] Andreas Crivellin, Martin Hoferichter, Matthew Kirk, Claudio Andrea Manzari, and Luc Schnell. "First-generation new physics in simplified models: from low-energy parity violation to the LHC." In: *JHEP* 10 (2021), p. 221. DOI: 10.1007/JHEP10(2021)221. arXiv: 2107.13569 [hep-ph].

[162] Bradley Garland, Sebastian Jäger, Charanjit K. Khosa, and Sandra Kvedaraitė. "Probing B anomalies via dimuon tails at a future collider." In: *Phys. Rev. D* 105.11 (2022), p. 115017. DOI: 10.1103/PhysRevD.105.115017. arXiv: 2112.05127 [hep-ph].

[163] Andreas Crivellin, Benjamin Fuks, and Luc Schnell. "Explaining the hints for lepton flavour universality violation with three S_2 leptoquark generations." In: *JHEP* 06 (2022), p. 169. DOI: 10.1007/JHEP06(2022)169. arXiv: 2203.10111 [hep-ph].

[164] Aleksandr Azatov, Francesco Garosi, Admir Greljo, David Marzocca, Jakub Salko, and Sokratis Trifinopoulos. "New physics in $b \to s\mu\mu$: FCC-hh or a muon collider?" In: *JHEP* 10 (2022), p. 149. DOI: 10.1007/JHEP10(2022)149. arXiv: 2205.13552 [hep-ph].

[165] Lukas Allwicher, Darius A. Faroughy, Florentin Jaffredo, Olcyr Sumensari, and Felix Wilsch. "Drell-Yan tails beyond the Standard Model." In: *JHEP* 03 (2023), p. 064. DOI: 10.1007/JHEP03(2023)064. arXiv: 2207.10714 [hep-ph].

[166] Georges Aad et al. "Search for heavy Higgs bosons decaying into two tau leptons with the ATLAS detector using pp collisions at $\sqrt{s} = 13$ TeV." In: *Phys. Rev. Lett.* 125.5 (2020), p. 051801. DOI: 10.1103/PhysRevLett.125.051801. arXiv: 2002.12223 [hep-ex].

[167] Georges Aad et al. "Search for pairs of scalar leptoquarks decaying into quarks and electrons or muons in $\sqrt{s}$ = 13 TeV pp collisions with the ATLAS detector." In: *JHEP* 10 (2020), p. 112. DOI: 10.1007/JHEP10(2020)112. arXiv: 2006.05872 [hep-ex].

[168] Albert M Sirunyan et al. "Search for singly and pair-produced leptoquarks coupling to third-generation fermions in proton-proton collisions at s=13 TeV." In: *Phys. Lett. B* 819 (2021), p. 136446. DOI: 10.1016/j.physletb.2021.136446. arXiv: 2012.04178 [hep-ex].

[169] Armen Tumasyan et al. "Searches for additional Higgs bosons and for vector leptoquarks in $\tau\tau$ final states in proton-proton collisions at $\sqrt{s}$ = 13 TeV." In: *JHEP* 07 (2023), p. 073. DOI: 10.1007/JHEP07(2023)073. arXiv: 2208.02717 [hep-ex].

[170] "The search for a third-generation leptoquark coupling to a τ lepton and a b quark through single, pair and nonresonant production at $\sqrt{s} = 13$ TeV." In: *CMS-PAS-EXO-19-016* (2022).

[171] Luca Buonocore, Ulrich Haisch, Paolo Nason, Francesco Tramontano, and Giulia Zanderighi. "Lepton-Quark Collisions at the Large Hadron Collider." In: *Phys. Rev. Lett.* 125.23 (2020), p. 231804. DOI: 10.1103/PhysRevLett.125.231804. arXiv: 2005.06475 [hep-ph].

[172] Luca Buonocore, Paolo Nason, Francesco Tramontano, and Giulia Zanderighi. "Leptons in the proton." In: *JHEP* 08.08 (2020), p. 019. DOI: 10.1007/JHEP08(2020)019. arXiv: 2005.06477 [hep-ph].

[173] Admir Greljo and Nudzeim Selimovic. "Lepton-Quark Fusion at Hadron Colliders, precisely." In: *JHEP* 03 (2021), p. 279. DOI: 10.1007/JHEP03(2021)279. arXiv: 2012.02092 [hep-ph].

[174] Luca Buonocore, Admir Greljo, Peter Krack, Paolo Nason, Nudzeim Selimovic, Francesco Tramontano, and Giulia Zanderighi. "Resonant leptoquark at NLO with POWHEG." In: *JHEP* 11 (2022), p. 129. DOI: 10.1007/JHEP11(2022)129. arXiv: 2209.02599 [hep-ph].

[175] Ulrich Haisch and Giacomo Polesello. "Resonant third-generation leptoquark signatures at the Large Hadron Collider." In: *JHEP* 05 (2021), p. 057. DOI: 10.1007/JHEP05(2021)057. arXiv: 2012.11474 [hep-ph].

[176] Darius A. Faroughy, Admir Greljo, and Jernej F. Kamenik. "Confronting lepton flavor universality violation in B decays with high-p_T tau lepton searches at LHC." In: *Phys. Lett. B* 764 (2017), pp. 126–134. DOI: 10.1016/j.physletb.2016.11.011. arXiv: 1609.07138 [hep-ph].

[177] Martin Schmaltz and Yi-Ming Zhong. "The leptoquark Hunter's guide: large coupling." In: *JHEP* 01 (2019), p. 132. DOI: 10.1007/JHEP01(2019)132. arXiv: 1810.10017 [hep-ph].

[178] Michael J. Baker, Javier Fuentes-Martín, Gino Isidori, and Matthias König. "High- p_T signatures in vector–leptoquark models." In: *Eur. Phys. J. C* 79.4 (2019), p. 334. DOI: 10.1140/epjc/s10052-019-6853-x. arXiv: 1901.10480 [hep-ph].

[179] Andrei Angelescu, Damir Bečirević, Darius A. Faroughy, Florentin Jaffredo, and Olcyr Sumensari. "Single leptoquark solutions to the B-physics anomalies." In: *Phys. Rev. D* 104.5 (2021), p. 055017. DOI: 10.1103/PhysRevD.104.055017. arXiv: 2103.12504 [hep-ph].

[180] Arvind Bhaskar, Diganta Das, Tanumoy Mandal, Subhadip Mitra, and Cyrin Neeraj. "Precise limits on the charge-2/3 U1 vector leptoquark." In: *Phys. Rev. D* 104.3 (2021), p. 035016. DOI: 10.1103/PhysRevD.104.035016. arXiv: 2101.12069 [hep-ph].

[181] Claudia Cornella, Darius A. Faroughy, Javier Fuentes-Martin, Gino Isidori, and Matthias Neubert. "Reading the footprints of the B-meson flavor anomalies." In: *JHEP* 08 (2021), p. 050. DOI: 10.1007/JHEP08(2021)050. arXiv: 2103.16558 [hep-ph].

[182] Alexandre Alves, Oscar J. P. Eboli, Giovanni Grilli Di Cortona, and Roberto R. Moreira. "Indirect and monojet constraints on scalar leptoquarks." In: *Phys. Rev. D* 99.9 (2019), p. 095005. DOI: 10.1103/PhysRevD.99.095005. arXiv: 1812.08632 [hep-ph].

[LS4] Ulrich Haisch, Luc Schnell, and Stefan Schulte. "On Drell-Yan production of scalar leptoquarks coupling to heavy-quark flavours." In: *JHEP* 11 (2022), p. 106. DOI: 10.1007/JHEP11(2022)106. arXiv: 2207.00356 [hep-ph].

[183] Luca Di Luzio, Admir Greljo, and Marco Nardecchia. "Gauge leptoquark as the origin of B-physics anomalies." In: *Phys. Rev. D* 96.11 (2017), p. 115011. DOI: 10.1103/PhysRevD.96.115011. arXiv: 1708.08450 [hep-ph].

[184] Javier Fuentes-Martín, Gino Isidori, Matthias König, and Nudžeim Selimović. "Vector Leptoquarks Beyond Tree Level III: Vector-like Fermions and Flavor-Changing Transitions." In: *Phys. Rev. D* 102 (2020), p. 115015. DOI: 10.1103/PhysRevD.102.115015. arXiv: 2009.11296 [hep-ph].

[185] Jason Aebischer, Andreas Crivellin, and Christoph Greub. "QCD improved matching for semileptonic B decays with leptoquarks." In: *Phys. Rev. D* 99.5 (2019), p. 055002. DOI: 10.1103/PhysRevD.99.055002. arXiv: 1811.08907 [hep-ph].

[186] Georges Aad et al. "Search for New Phenomena in Final States with Two Leptons and One or No b-Tagged Jets at $\sqrt{s} = 13$ TeV Using the ATLAS Detector." In: *Phys. Rev. Lett.* 127.14 (2021), p. 141801. DOI: 10.1103/PhysRevLett.127.141801. arXiv: 2105.13847 [hep-ex].

[187] Wolfgang Altmannshofer, P. S. Bhupal Dev, and Amarjit Soni. "$R_{D^{(*)}}$ anomaly: A possible hint for natural supersymmetry with R-parity violation." In: *Phys. Rev. D* 96.9 (2017), p. 095010. DOI: 10.1103/PhysRevD.96.095010. arXiv: 1704.06659 [hep-ph].

[188] Syuhei Iguro and Kazuhiro Tobe. "$R(D^{(*)})$ in a general two Higgs doublet model." In: *Nucl. Phys. B* 925 (2017), pp. 560–606. DOI: 10.1016/j.nuclphysb.2017.10.014. arXiv: 1708.06176 [hep-ph].

[189] Mohammad Abdullah, Julian Calle, Bhaskar Dutta, Andrés Flórez, and Diego Restrepo. "Probing a simplified, W' model of $R(D^{(*)})$ anomalies using b-tags, τ leptons and missing energy." In: *Phys. Rev. D* 98.5 (2018), p. 055016. DOI: 10.1103/PhysRevD.98.055016. arXiv: 1805.01869 [hep-ph].

[190] David Marzocca, Ui Min, and Minho Son. "Bottom-Flavored Mono-Tau Tails at the LHC." In: *JHEP* 12 (2020), p. 035. DOI: 10.1007/JHEP12(2020)035. arXiv: 2008.07541 [hep-ph].

[191] Motoi Endo, Syuhei Iguro, Teppei Kitahara, Michihisa Takeuchi, and Ryoutaro Watanabe. "Non-resonant new physics search at the LHC for the $b \to c\tau\nu$ anomalies." In: *JHEP* 02 (2022), p. 106. DOI: 10.1007/JHEP02(2022)106. arXiv: 2111.04748 [hep-ph].

[192] Marzia Bordone, Claudia Cornella, Javier Fuentes-Martin, and Gino Isidori. "A three-site gauge model for flavor hierarchies and flavor anomalies." In: *Phys. Lett. B* 779 (2018), pp. 317–323. DOI: 10.1016/j.physletb.2018.02.011. arXiv: 1712.01368 [hep-ph].

[193] Luca Di Luzio, Javier Fuentes-Martin, Admir Greljo, Marco Nardecchia, and Sophie Renner. "Maximal Flavour Violation: a Cabibbo mechanism for leptoquarks." In: *JHEP* 11 (2018), p. 081. DOI: 10.1007/JHEP11(2018)081. arXiv: 1808.00942 [hep-ph].

[194] Marzia Bordone, Claudia Cornella, Javier Fuentes-Martín, and Gino Isidori. "Low-energy signatures of the PS^3 model: from B-physics anomalies to LFV." In: *JHEP* 10 (2018), p. 148. DOI: 10.1007/JHEP10(2018)148. arXiv: 1805.09328 [hep-ph].

[195] Admir Greljo and Ben A. Stefanek. "Third family quark–lepton unification at the TeV scale." In: *Phys. Lett. B* 782 (2018), pp. 131–138. DOI: 10.1016/j.physletb.2018.05.033. arXiv: 1802.04274 [hep-ph].

[196] Claudia Cornella, Javier Fuentes-Martin, and Gino Isidori. "Revisiting the vector leptoquark explanation of the B-physics anomalies." In: *JHEP* 07 (2019), p. 168. DOI: 10.1007/JHEP07(2019)168. arXiv: 1903.11517 [hep-ph].

[197] Luc Schnell. *Drell-Yan LQ NLO*. https://gitlab.com/lucschnell/Drell-Yan-LQ-NLO. Accessed: 2024-05-30.

[198] Adam Alloul, Neil D. Christensen, Céline Degrande, Claude Duhr, and Benjamin Fuks. "FeynRules 2.0 - A complete toolbox for tree-level phenomenology." In: *Comput. Phys. Commun.* 185 (2014), pp. 2250–2300. DOI: 10.1016/j.cpc.2014.04.012. arXiv: 1310.1921 [hep-ph].

[199] Thomas Hahn. "Generating Feynman diagrams and amplitudes with FeynArts 3." In: *Comput. Phys. Commun.* 140 (2001), pp. 418–431. DOI: 10.1016/S0010-4655(01)00290-9. arXiv: hep-ph/0012260.

[200] Hiren H. Patel. "Package-X: A Mathematica package for the analytic calculation of one-loop integrals." In: *Comput. Phys. Commun.* 197 (2015), pp. 276–290. DOI: 10.1016/j.cpc.2015.08.017. arXiv: 1503.01469 [hep-ph].

[201] Richard D. Ball et al. "The path to proton structure at 1% accuracy." In: *Eur. Phys. J. C* 82.5 (2022), p. 428. DOI: 10.1140/epjc/s10052-022-10328-7. arXiv: 2109.02653 [hep-ph].

[202] Armen Tumasyan et al. "Identification of hadronic tau lepton decays using a deep neural network." In: *JINST* 17 (2022), P07023. DOI: 10.1088/1748-0221/17/07/P07023. arXiv: 2201.08458 [hep-ex].

[203] Matteo Cacciari, Gavin P. Salam, and Gregory Soyez. "FastJet User Manual." In: *Eur. Phys. J. C* 72 (2012), p. 1896. DOI: 10.1140/epjc/s10052-012-1896-2. arXiv: 1111.6097 [hep-ph].

[204] A. M. Sirunyan et al. "Identification of heavy-flavour jets with the CMS detector in pp collisions at 13 TeV." In: *JINST* 13.05 (2018), P05011. DOI: 10.1088/1748-0221/13/05/P05011. arXiv: 1712.07158 [physics.ins-det].

[205] Emil Bols, Jan Kieseler, Mauro Verzetti, Markus Stoye, and Anna Stakia. "Jet Flavour Classification Using DeepJet." In: *JINST* 15.12 (2020), P12012. DOI: 10.1088/1748-0221/15/12/P12012. arXiv: 2008.10519 [hep-ex].

[206] Eric Conte, Benjamin Fuks, and Guillaume Serret. "MadAnalysis 5, A User-Friendly Framework for Collider Phenomenology." In: *Comput. Phys. Commun.* 184 (2013), pp. 222–256. DOI: 10.1016/j.cpc.2012.09.009. arXiv: 1206.1599 [hep-ph].

[207] J. de Favereau, C. Delaere, P. Demin, A. Giammanco, V. Lemaître, A. Mertens, and M. Selvaggi. "DELPHES 3, A modular framework for fast simulation of a generic collider experiment." In: *JHEP* 02 (2014), p. 057. DOI: 10.1007/JHEP02(2014)057. arXiv: 1307.6346 [hep-ex].

[208] Georges Aad et al. "Search for neutral Higgs bosons of the minimal supersymmetric standard model in pp collisions at $\sqrt{s}$ = 8 TeV with the ATLAS detector." In: *JHEP* 11 (2014), p. 056. DOI: 10.1007/JHEP11(2014)056. arXiv: 1409.6064 [hep-ex].

[209] Georges Aad et al. "Search for new phenomena in pp collisions in final states with tau leptons, b-jets, and missing transverse momentum with the ATLAS detector." In: *Phys. Rev. D* 104.11 (2021), p. 112005. DOI: 10.1103/PhysRevD.104.112005. arXiv: 2108.07665 [hep-ex].

[210] Glen Cowan, Kyle Cranmer, Eilam Gross, and Ofer Vitells. "Asymptotic formulae for likelihood-based tests of new physics." In: *Eur. Phys. J. C* 71 (2011). [Erratum: Eur.Phys.J.C 73, 2501 (2013)], p. 1554. DOI: 10.1140/epjc/s10052-011-1554-0. arXiv: 1007.1727 [physics.data-an].

[211] Johan Alwall et al. "Comparative study of various algorithms for the merging of parton showers and matrix elements in hadronic collisions." In: *Eur. Phys. J. C* 53 (2008), pp. 473–500. DOI: 10.1140/epjc/s10052-007-0490-5. arXiv: 0706.2569 [hep-ph].

[LS2] Ulrich Haisch and Luc Schnell. "Long-lived particle phenomenology in the 2HDM+a model." In: *JHEP* 04 (2023), p. 134. DOI: 10.1007/JHEP04(2023)134. arXiv: 2302.02735 [hep-ph].

[212] Seyda Ipek, David McKeen, and Ann E. Nelson. "A Renormalizable Model for the Galactic Center Gamma Ray Excess from Dark Matter Annihilation." In: *Phys. Rev. D* 90.5 (2014), p. 055021. DOI: 10.1103/PhysRevD.90.055021. arXiv: 1404.3716 [hep-ph].

[213] Jose Miguel No. "Looking through the pseudoscalar portal into dark matter: Novel mono-Higgs and mono-Z signatures at the LHC." In: *Phys. Rev. D* 93.3 (2016), p. 031701. DOI: 10.1103/PhysRevD.93.031701. arXiv: 1509.01110 [hep-ph].

[214] Dorival Goncalves, Pedro A. N. Machado, and Jose Miguel No. "Simplified Models for Dark Matter Face their Consistent Completions." In: *Phys. Rev. D* 95.5 (2017), p. 055027. DOI: 10.1103/PhysRevD.95.055027. arXiv: 1611.04593 [hep-ph].

[215] Morad Aaboud et al. "Search for dark matter produced in association with bottom or top quarks in $\sqrt{s} = 13$ TeV pp collisions with the ATLAS detector." In: *Eur. Phys. J. C* 78.1 (2018), p. 18. DOI: 10.1140/epjc/s10052-017-5486-1. arXiv: 1710.11412 [hep-ex].

[216] Priscilla Pani and Giacomo Polesello. "Dark matter production in association with a single top-quark at the LHC in a two-Higgs-doublet model with a pseudoscalar mediator." In: *Phys. Dark Univ.* 21 (2018), pp. 8–15. DOI: 10.1016/j.dark.2018.04.006. arXiv: 1712.03874 [hep-ph].

[217] Patrick Tunney, Jose Miguel No, and Malcolm Fairbairn. "Probing the pseudoscalar portal to dark matter via $\bar{b}bZ(\to \ell\ell) + \not{E}_T$: From the LHC to the Galactic Center excess." In: *Phys. Rev. D* 96.9 (2017), p. 095020. DOI: 10.1103/PhysRevD.96.095020. arXiv: 1705.09670 [hep-ph].

[218] Giorgio Arcadi, Manfred Lindner, Farinaldo S. Queiroz, Werner Rodejohann, and Stefan Vogl. "Pseudoscalar Mediators: A WIMP model at the Neutrino Floor." In: *JCAP* 03 (2018), p. 042. DOI: 10.1088/1475-7516/2018/03/042. arXiv: 1711.02110 [hep-ph].

[219] Tomohiro Abe et al. "LHC Dark Matter Working Group: Next-generation spin-0 dark matter models." In: *Phys. Dark Univ.* 27 (2020), p. 100351. DOI: 10.1016/j.dark.2019.100351. arXiv: 1810.09420 [hep-ex].

[220] Albert M Sirunyan et al. "Search for dark matter produced in association with a Higgs boson decaying to a pair of bottom quarks in proton–proton collisions at $\sqrt{s} = 13\,\text{TeV}$." In: *Eur. Phys. J. C* 79.3 (2019), p. 280. DOI: 10.1140/epjc/s10052-019-6730-7. arXiv: 1811.06562 [hep-ex].

[221] Morad Aaboud et al. "Constraints on mediator-based dark matter and scalar dark energy models using $\sqrt{s} = 13$ TeV pp collision data collected by the ATLAS detector." In: *JHEP* 05 (2019), p. 142. DOI: 10.1007/JHEP05(2019)142. arXiv: 1903.01400 [hep-ex].

[222] Giorgio Arcadi, Giorgio Busoni, Thomas Hugle, and Valentin Titus Tenorth. "Comparing 2HDM + Scalar and Pseudoscalar Simplified Models at LHC." In: *JHEP* 06 (2020), p. 098. DOI: 10.1007/JHEP06(2020)098. arXiv: 2001.10540 [hep-ph].

[223] Albert M Sirunyan et al. "Search for dark matter produced in association with a leptonically decaying Z boson in proton-proton collisions at $\sqrt{s} = 13$ TeV." In: *Eur. Phys. J. C* 81.1 (2021). [Erratum: Eur.Phys.J.C 81, 333 (2021)], p. 13. DOI: 10.1140/epjc/s10052-020-08739-5. arXiv: 2008.04735 [hep-ex].

[224] Georges Aad et al. "Search for dark matter produced in association with a single top quark in $\sqrt{s} = 13$ TeV pp collisions with the ATLAS detector." In: *Eur. Phys. J. C* 81 (2021), p. 860. DOI: 10.1140/epjc/s10052-021-09566-y. arXiv: 2011.09308 [hep-ex].

[225] Georges Aad et al. "Search for dark matter in events with missing transverse momentum and a Higgs boson decaying into two photons in pp collisions at $\sqrt{s}$ = 13 TeV with the ATLAS detector." In: *JHEP* 10 (2021), p. 013. DOI: 10.1007/JHEP10(2021)013. arXiv: 2104.13240 [hep-ex].

[226] Georges Aad et al. "Search for dark matter produced in association with a Standard Model Higgs boson decaying into b-quarks using the full Run 2 dataset from the ATLAS detector." In: *JHEP* 11 (2021), p. 209. DOI: 10.1007/JHEP11(2021)209. arXiv: 2108.13391 [hep-ex].

[227] Georges Aad et al. "Search for associated production of a Z boson with an invisibly decaying Higgs boson or dark matter candidates at s=13 TeV with the ATLAS detector." In: *Phys. Lett. B* 829 (2022), p. 137066. DOI: 10.1016/j.physletb.2022.137066. arXiv: 2111.08372 [hep-ex].

[228] "Combination and summary of ATLAS dark matter searches using 139 fb-1 of $\sqrt{}$s = 13 TeV p p collision data and interpreted in a two-Higgs-doublet model with a pseudoscalar mediator." In: *ATLAS-CONF-2021-036* (2021).

[229] Tania Robens. "The THDMa Revisited." In: *Symmetry* 13.12 (2021), p. 2341. DOI: 10.3390/sym13122341. arXiv: 2106.02962 [hep-ph].

[230] Spyros Argyropoulos, Oleg Brandt, and Ulrich Haisch. "Collider Searches for Dark Matter through the Higgs Lens." In: *Symmetry* 13.12 (2021), p. 2406. DOI: 10.3390/sym13122406. arXiv: 2109.13597 [hep-ph].

[231] Shankha Banerjee, Geneviève Bélanger, Disha Bhatia, Benjamin Fuks, and Sreerup Raychaudhuri. "Phenomenological analysis of multi-pseudoscalar mediated dark matter models." In: *JHEP* 07 (2022), p. 111. DOI: 10.1007/JHEP07(2022)111. arXiv: 2110.15391 [hep-ph].

[232] Spyros Argyropoulos and Ulrich Haisch. "Benchmarking LHC searches for light 2HDM+a pseudoscalars." In: *SciPost Phys.* 13.1 (2022), p. 007. DOI: 10.21468/SciPostPhys.13.1.007. arXiv: 2202.12631 [hep-ph].

[233] "Search for dark matter produced in association with a Higgs boson decaying to tau leptons at $\sqrt{s} = 13$ TeV with the ATLAS detector." In: *ATLAS-CONF-2022-069* (2022).

[234] Georges Aad et al. "Search for dark matter produced in association with a single top quark and an energetic W boson in $\sqrt{s} = 13$ TeV pp collisions with the ATLAS detector." In: *Eur. Phys. J. C* 83.7 (2023), p. 603. DOI: 10.1140/epjc/s10052-023-11582-z. arXiv: 2211.13138 [hep-ex].

[235] "Search for dark matter in final states with a Higgs boson decaying to a pair of b-jets and missing transverse momentum at the HL-LHC." In: *CMS-PAS-FTR-22-005* (2022).

[236] Giorgio Arcadi, Nico Benincasa, Abdelhak Djouadi, and Kristjan Kannike. "Two-Higgs-doublet-plus-pseudoscalar model: Collider, dark matter, and gravitational wave signals." In: *Phys. Rev. D* 108.5 (2023), p. 055010. DOI: 10.1103/PhysRevD.108.055010. arXiv: 2212.14788 [hep-ph].

[237] "Dark matter summary plots for s-channel, 2HDM+a and Dark Higgs models." In: *ATL-PHYS-PUB-2022-036* (2022).

[238] David Curtin et al. "Long-Lived Particles at the Energy Frontier: The MATHUSLA Physics Case." In: *Rept. Prog. Phys.* 82.11 (2019), p. 116201. DOI: 10.1088/1361-6633/ab28d6. arXiv: 1806.07396 [hep-ph].

[239] Lawrence Lee, Christian Ohm, Abner Soffer, and Tien-Tien Yu. "Collider Searches for Long-Lived Particles Beyond the Standard Model." In: *Prog. Part. Nucl. Phys.* 106 (2019). [Erratum: Prog.Part.Nucl.Phys. 122, 103912 (2022)], pp. 210–255. DOI: 10.1016/j.ppnp.2019.02.006. arXiv: 1810.12602 [hep-ph].

[240] Juliette Alimena et al. "Searching for long-lived particles beyond the Standard Model at the Large Hadron Collider." In: *J. Phys. G* 47.9 (2020), p. 090501. DOI: 10.1088/1361-6471/ab4574. arXiv: 1903.04497 [hep-ex].

[241] R. Aaij et al. "Updated search for long-lived particles decaying to jet pairs." In: *Eur. Phys. J. C* 77.12 (2017), p. 812. DOI: 10.1140/epjc/s10052-017-5178-x. arXiv: 1705.07332 [hep-ex].

[242] M. Aaboud et al. "Search for the Higgs boson produced in association with a vector boson and decaying into two spin-zero particles in the $H \to aa \to 4b$ channel in pp collisions at $\sqrt{s} = 13$ TeV with the ATLAS detector." In: *JHEP* 10 (2018), p. 031. DOI: 10.1007/JHEP10(2018)031. arXiv: 1806.07355 [hep-ex].

[243] Morad Aaboud et al. "Search for long-lived particles produced in pp collisions at $\sqrt{s} = 13$ TeV that decay into displaced hadronic jets in the ATLAS muon spectrometer." In: *Phys. Rev. D* 99.5 (2019), p. 052005. DOI: 10.1103/PhysRevD.99.052005. arXiv: 1811.07370 [hep-ex].

[244] Morad Aaboud et al. "Search for long-lived neutral particles in pp collisions at $\sqrt{s} = 13$ TeV that decay into displaced hadronic jets in the ATLAS calorimeter." In: *Eur. Phys. J. C* 79.6 (2019), p. 481. DOI: 10.1140/epjc/s10052-019-6962-6. arXiv: 1902.03094 [hep-ex].

[245] Georges Aad et al. "Search for long-lived neutral particles produced in pp collisions at $\sqrt{s} = 13$ TeV decaying into displaced hadronic jets in the ATLAS inner detector and muon spectrometer." In: *Phys. Rev. D* 101.5 (2020), p. 052013. DOI: 10.1103/PhysRevD.101.052013. arXiv: 1911.12575 [hep-ex].

[246] Georges Aad et al. "Search for Higgs boson decays into two new low-mass spin-0 particles in the $4b$ channel with the ATLAS detector using pp collisions at $\sqrt{s} = 13$ TeV." In: *Phys. Rev. D* 102.11 (2020), p. 112006. DOI: 10.1103/PhysRevD.102.112006. arXiv: 2005.12236 [hep-ex].

[247] Albert M Sirunyan et al. "Search for long-lived particles using displaced jets in proton-proton collisions at $\sqrt{s} = 13$ TeV." In: *Phys. Rev. D* 104.1 (2021), p. 012015. DOI: 10.1103/PhysRevD.104.012015. arXiv: 2012.01581 [hep-ex].

[248] Armen Tumasyan et al. "Search for Long-Lived Particles Decaying in the CMS End Cap Muon Detectors in Proton-Proton Collisions at $\sqrt{s}$ =13 TeV." In: *Phys. Rev. Lett.* 127.26 (2021), p. 261804. DOI: 10.1103/PhysRevLett.127.261804. arXiv: 2107.04838 [hep-ex].

[249] Georges Aad et al. "Search for exotic decays of the Higgs boson into long-lived particles in pp collisions at $\sqrt{s} = 13$ TeV using displaced vertices in the ATLAS inner detector." In: *JHEP* 11 (2021), p. 229. DOI: 10.1007/JHEP11(2021)229. arXiv: 2107.06092 [hep-ex].

[250] Armen Tumasyan et al. "Search for long-lived particles decaying to leptons with large impact parameter in proton–proton collisions at $\sqrt{s} = 13$ TeV." In: *Eur. Phys. J. C* 82.2 (2022), p. 153. DOI: 10.1140/epjc/s10052-022-10027-3. arXiv: 2110.04809 [hep-ex].

[251] Armen Tumasyan et al. "Search for long-lived particles produced in association with a Z boson in proton-proton collisions at $\sqrt{s} = 13$ TeV." In: *JHEP* 03 (2022), p. 160. DOI: 10.1007/JHEP03(2022)160. arXiv: 2110.13218 [hep-ex].

[252] Armen Tumasyan et al. "Search for long-lived particles decaying into muon pairs in proton-proton collisions at $\sqrt{s} = 13$ TeV collected with a dedicated high-rate data stream." In: *JHEP* 04 (2022), p. 062. DOI: 10.1007/JHEP04(2022)062. arXiv: 2112.13769 [hep-ex].

[253] Georges Aad et al. "Search for events with a pair of displaced vertices from long-lived neutral particles decaying into hadronic jets in the ATLAS muon spectrometer in pp collisions at $\sqrt{s}$=13 TeV." In: *Phys. Rev. D* 106.3 (2022), p. 032005. DOI: 10.1103/PhysRevD.106.032005. arXiv: 2203.00587 [hep-ex].

[254] Georges Aad et al. "Search for neutral long-lived particles in pp collisions at $\sqrt{s}$ = 13 TeV that decay into displaced hadronic jets in the ATLAS calorimeter." In: *JHEP* 06 (2022), p. 005. DOI: 10.1007/JHEP06(2022)005. arXiv: 2203.01009 [hep-ex].

[255] Armen Tumasyan et al. "Search for long-lived particles decaying to a pair of muons in proton-proton collisions at $\sqrt{s}$ = 13 TeV." In: *JHEP* 05 (2023), p. 228. DOI: 10.1007/JHEP05(2023)228. arXiv: 2205.08582 [hep-ex].

[256] "Long-lived particle summary plots for Hidden Sector and Dark Photon models." In: *ATL-PHYS-PUB-2022-007* (2022).

[257] *Long-lived particle summary plots*. Tech. rep. Geneva: CERN, 2022. URL: https://twiki.cern.ch/twiki/bin/view/CMSPublic/SummaryPlotsEXO13TeV#Long_lived_particle_summary_plot.

[258] Albert M Sirunyan et al. "Measurements of properties of the Higgs boson decaying into the four-lepton final state in pp collisions at $\sqrt{s} = 13$ TeV." In: *JHEP* 11 (2017), p. 047. DOI: 10.1007/JHEP11(2017)047. arXiv: 1706.09936 [hep-ex].

[259] Morad Aaboud et al. "Measurement of the Higgs boson mass in the $H \to ZZ^* \to 4\ell$ and $H \to \gamma\gamma$ channels with $\sqrt{s} = 13$ TeV pp collisions using the ATLAS detector." In: *Phys. Lett. B* 784 (2018), pp. 345–366. DOI: 10.1016/j.physletb.2018.07.050. arXiv: 1806.00242 [hep-ex].

[260] P. A. Zyla et al. "Review of Particle Physics." In: *PTEP* 2020.8 (2020), p. 083C01. DOI: 10.1093/ptep/ptaa104.

[261] Ulrich Haisch, Jernej F. Kamenik, Augustinas Malinauskas, and Michael Spira. "Collider constraints on light pseudoscalars." In: *JHEP* 03 (2018), p. 178. DOI: 10.1007/JHEP03(2018)178. arXiv: 1802.02156 [hep-ph].

[262] Spyros Argyropoulos and Ulrich Haisch. *2HDM+a width calculator*. https://github.com/sargyro/2hdma_width_calculator. 2022.

[263] M. Cepeda et al. "Report from Working Group 2: Higgs Physics at the HL-LHC and HE-LHC." In: *CERN Yellow Rep. Monogr.* 7 (2019). Ed. by Andrea Dainese, Michelangelo Mangano, Andreas B. Meyer, Aleandro Nisati, Gavin Salam, and Mika Anton Vesterinen, pp. 221–584. DOI: 10.23731/CYRM-2019-007.221. arXiv: 1902.00134 [hep-ph].

[264] *BSM Higgs production cross sections at $\sqrt{s} = 13$ TeV (update in CERN Report4 2016)*. Tech. rep. Geneva: CERN, 2022. URL: https://twiki.cern.ch/twiki/bin/view/LHCPhysics/CERNYellowReportPageBSMAt13TeV.

[265] Morad Aaboud et al. "Search for Heavy Higgs Bosons A/H Decaying to a Top Quark Pair in pp Collisions at $\sqrt{s} = 8$ TeV with the ATLAS Detector." In: *Phys. Rev. Lett.* 119.19 (2017), p. 191803. DOI: 10.1103/PhysRevLett.119.191803. arXiv: 1707.06025 [hep-ex].

[266] Morad Aaboud et al. "Search for new phenomena in events with same-charge leptons and b-jets in pp collisions at $\sqrt{s} = 13$ TeV with the ATLAS detector." In: *JHEP* 12 (2018), p. 039. DOI: 10.1007/JHEP12(2018)039. arXiv: 1807.11883 [hep-ex].

[267] Albert M Sirunyan et al. "Search for heavy Higgs bosons decaying to a top quark pair in proton-proton collisions at $\sqrt{s} = 13$ TeV." In: *JHEP* 04 (2020). [Erratum: JHEP 03, 187 (2022)], p. 171. DOI: 10.1007/JHEP04(2020)171. arXiv: 1908.01115 [hep-ex].

[268] Albert M Sirunyan et al. "Search for production of four top quarks in final states with same-sign or multiple leptons in proton-proton collisions at $\sqrt{s} = 13$ TeV." In: *Eur. Phys. J. C* 80.2 (2020), p. 75. DOI: 10.1140/epjc/s10052-019-7593-7. arXiv: 1908.06463 [hep-ex].

[269] Georges Aad et al. "Evidence for $t\bar{t}t\bar{t}$ production in the multilepton final state in proton–proton collisions at $\sqrt{s} = 13$ TeV with the ATLAS detector." In: *Eur. Phys. J. C* 80.11 (2020), p. 1085. DOI: 10.1140/epjc/s10052-020-08509-3. arXiv: 2007.14858 [hep-ex].

[270] Georges Aad et al. "Measurement of the $t\bar{t}t\bar{t}$ production cross section in pp collisions at $\sqrt{s} = 13$ TeV with the ATLAS detector." In: *JHEP* 11 (2021), p. 118. DOI: 10.1007/JHEP11(2021)118. arXiv: 2106.11683 [hep-ex].

[271] "Evidence for the simultaneous production of four top quarks in proton-proton collisions at sqrts = 13 TeV." In: *CMS-PAS-TOP-21-005* (2022).

[272] Ilaria Brivio. "SMEFTsim 3.0 — a practical guide." In: *JHEP* 04 (2021), p. 073. DOI: 10.1007/JHEP04(2021)073. arXiv: 2012.11343 [hep-ph].

[273] Anke Biekötter, Benjamin D. Pecjak, Darren J. Scott, and Tommy Smith. "Electroweak input schemes and universal corrections in SMEFT." In: *JHEP* 07 (2023), p. 115. DOI: 10.1007/JHEP07(2023)115. arXiv: 2305.03763 [hep-ph].

[274] Andreas Albert et al. "Recommendations of the LHC Dark Matter Working Group: Comparing LHC searches for dark matter mediators in visible and invisible decay channels and calculations of the thermal relic density." In: *Phys. Dark Univ.* 26 (2019), p. 100377. DOI: 10.1016/j.dark.2019.100377. arXiv: 1703.05703 [hep-ex].

[275] N. Aghanim et al. "Planck 2018 results. VI. Cosmological parameters." In: *Astron. Astrophys.* 641 (2020). [Erratum: Astron.Astrophys. 652, C4 (2021)], A6. DOI: 10.1051/0004-6361/201833910. arXiv: 1807.06209 [astro-ph.CO].

[276] Mihailo Backovic, Antony Martini, Kyoungchul Kong, Olivier Mattelaer, and Gopolang Mohlabeng. "MadDM: New dark matter tool in the LHC era." In: *AIP Conf. Proc.* 1743.1 (2016). Ed. by Barbara Szczerbinska, Rouzbeh Allahverdi, Kaladi Babu, Baha Balantekin, Bhaskar Dutta, Teruki Kamon, Jason Kumar, Farinaldo Queiroz, Louis Strigari, and Rebecca Surman, p. 060001. DOI: 10.1063/1.4953318. arXiv: 1509.03683 [hep-ph].

[277] Nicole F. Bell, Giorgio Busoni, and Isaac W. Sanderson. "Loop Effects in Direct Detection." In: *JCAP* 08 (2018). [Erratum: JCAP 01, E01 (2019)], p. 017. DOI: 10.1088/1475-7516/2018/08/017. arXiv: 1803.01574 [hep-ph].

[278] Tomohiro Abe, Motoko Fujiwara, and Junji Hisano. "Loop corrections to dark matter direct detection in a pseudoscalar mediator dark matter model." In: *JHEP* 02 (2019), p. 028. DOI: 10.1007/JHEP02(2019)028. arXiv: 1810.01039 [hep-ph].

[279] Fatih Ertas and Felix Kahlhoefer. "Loop-induced direct detection signatures from CP-violating scalar mediators." In: *JHEP* 06 (2019), p. 052. DOI: 10.1007/JHEP06(2019)052. arXiv: 1902.11070 [hep-ph].